National Conference

on

Advances in Materials & Materials Processing

AMMP - 15

PROCEEDINGS

NIT SRINAGAR
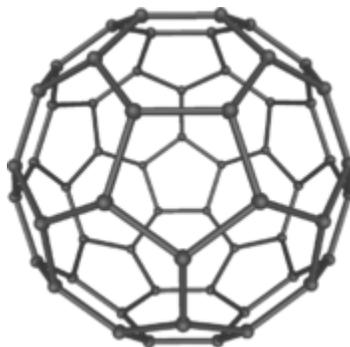
FOREWORD BY DIRECTOR

It gives me immense pleasure to mention that National Conference on Advances in Materials and Materials Processing (AMMP-15) was successfully conducted by the Department of Metallurgical & Materials Engineering, NIT Srinagar on 22-23 May, 2015.

When the whole valley of Kashmir was severely affected by the devastating flood in September'14 NIT Srinagar was no exception. Hostels, Library, Director's Lodge, Cafeteria, Hospital buildings were severely damaged. In spite of all these odds, I am happy to mention that we could complete our semester in time and the students did not suffer any session loss although all other institutions in the valley had to suspend their academic activities. This was possible mainly because of the constant support and service rendered by all--- right from the sanitary staff to the top management.

Under this backdrop, conducting a National Conference at NIT Srinagar is highly commendable. This only shows the commitment and dedication of the team. The previous Conference conducted by the department was about twenty years ago. To add to our pleasure, we had this time Dr. Srikumar Banerjee, Chancellor, Central University of Kashmir and Former Chairman, Atomic Energy Commission as the Chief Guest in the inaugural function, who delivered a lecture on Shape Memory Alloys.

61 abstracts were shortlisted for the conference of which 30 were selected for presentation. Abstract book was released during the inaugural function. In the Proceeding Volume 16 papers and a lecture presented by Prof. Indranil Manna, Director IIT Kanpur are accommodated.

The areas covered in this conference were vast including Laser Assisted Direct Manufacturing, Shape Memory Alloys, Low Temperature and Superconductor Materials.

I convey my sincere gratitude to the authors for choosing to send their papers in this Conference. I sincerely thank all the members of the Editorial Board for the support and cooperation.

PROF. RAJAT GUPTA
DIRECTOR
NIT SRINAGAR
PATRON (AMMP-15)

CONTENTS

Madeva Nagaral[1], Shivanand B K[2], V Auradi[3] and S A Kori[4]

[1]Design Engineer, ARDC, HAL, Bangalore and Research Scholar, Department of Mechanical Engineering,SIT, Tumkur-572103

[2]Department of Mechanical Engineering, MVJ Polytechnic, Bangalore-560067

[3]R&D Centre, Department of Mechanical Engineering, SIT, Tumkur-572103

[4]R&D Centre, Department of Mechanical Engineering, Basaveshwar Engineering College, Bagalkot, Karnataka

(Pg.175)

LASER ASSISTED DIRECT MANUFACTURING AND SURFACE ENGINEERING

INDRANIL MANNA, J C Bose Fellow

Indian Institute of Technology KANPUR and KHARAGPUR

imanna@iitk.ac.in; Web: www.imanna.org

- ❖ **Fundamentals of LMP**

- ❖ **Laser-matter interaction**

- ❖ **Laser assisted manufacturing**

- ❖ **Laser surface engineering (LSE)**

- ❖ **LSE of SAE 52100 ball bearing steel**

- ❖ **Laser cladding of AISI H13 tool steel**

- ❖ **LSA and LSM of Ti alloys (biomedical)**

Manufacturing

- ❖ **Manufacturing: Production of goods/services for use or sale using raw material, labor, design, tools/machines, processes.**

- ❖ **Manufacturing produces wealth, jobs, opportunities, trade, infrastructure, self reliance, stability and growth.**

❖ **Examples: synthesizing, casting, molding, forming, machining, joining, prototyping, polishing, surfacing, etc.**

❖ **Total worth of manufacturing worldwide is about $ 9.9 trillion (EU = ~ 22%, USA ~ 18%, China ~ 19%, Japan ~ 10%, Germany ~ 6%, India < 0.2%)**

❖ **Manufacturing contribution to GDP ~ 10% <*MAKE IN INDIA*>**

Evolution in Manufacturing

❖ **Science (know why?) to Engineering (know how?)**

❖ **Need/demand $\Rightarrow$ Utility $\Rightarrow$ Real time manufacturing**

❖ **Improvisation $\Rightarrow$ Design $\Rightarrow$ Innovation $\Rightarrow$ New approach**

❖ **Prototyping $\Rightarrow$ CAD/CAM $\Rightarrow$ Direct / Digital manufacturing**

Digital/Additive Manufacturing Process   **Direct manufacturing of complex**
components using CAD/CAM

Table I : Additive Manufacturing Technologies –

Name	Working Principle
Selective Laser Sintering (SLS)	**Uses CO_2 laser to selectively fuse polymer-coated metallic powder (stored in bed) one layer at time. Requires debinding, sintering, and infiltration**
Direct Metal Laser Sintering (DMLS)	**Similar to SLS. Patterns energy in powder bed but directly sinters a two-phase metallic powder system. Requires infiltration**
Selective Laser Melting (SLM)	**Selectively melts metallic powder with an focused laser. Does not require additional post-processing. Can make extremely small features**

Electron beam melting (EBM)	Uses a 4.8 kW electron beam to selectively scan and melt layers of metal powder
3D Printing (3DP)	Use of a printer head to print binder polymer over a metal powder bed. Requires sintering and infiltration
Multi phase jet solidification (MJS)	A metal powder-binder mixture is extruded through a heated nozzle to create layers (fused deposition modeling). Requires debinding, sintering, infiltration

–Table II Additive Manufacturing Technologies

Extrusion and Deposition of semi solid metals (EDSSM, or, SSM-SFF)	Deposition of semi-solid metal through a nozzle (similar to fused deposition modeling)
Laser Engineered Net Shaping (LENS) OR, Direct Metal Deposition (DMD)	Melting powdered metals with a high-powered Nd-YAG laser. Metal powder is fed into laser beam by nozzle .
Shape Deposition Manufacturing (SDM)	Combination of laser cladding (LENS process) with subtractive machining
Ultrasonic object consolidation (UOC)	Solid-state joining techniques deposit layers of tape to form solid aluminum parts, followed by trimming step
Layer object manufacturing (LOM)	Selectively cuts stacks of sheet metal and fuses the layer together
Computer –aided manufacturing of laminated engineering materials (CAM-LEM)	Similar to LOM, selectively cuts layers from green tapes, stacks the layers with robot arm, and offers more complex internal geometry and wide material selection

Light Amplification by Stimulated Emission of Radiation
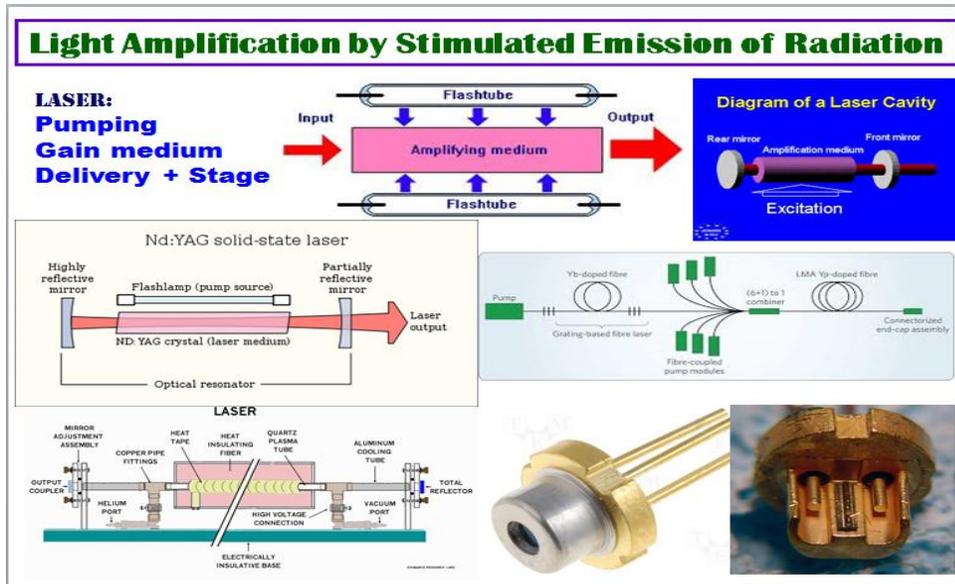
Light Amplification by Stimulated Emission of Radiation

Why is it different from ordinary light?

$\Rightarrow$ **Coherent (both spatially and temporarily)**

$\Rightarrow$ **Monochromatic (Dl/l = 10^{-10})**

$\Rightarrow$ **Low divergence (Straight line)**

$\Rightarrow$ **High power density is achievable**
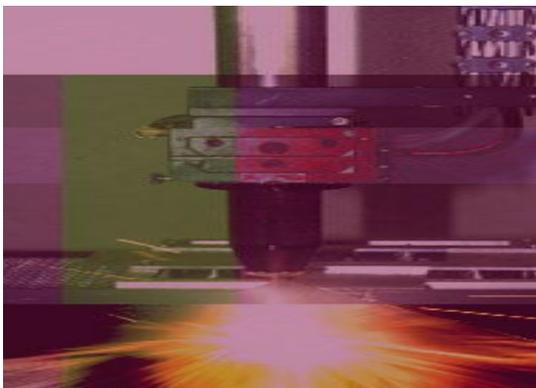
Laser-Matter Interaction Conversion of Photon to Lattice Heat
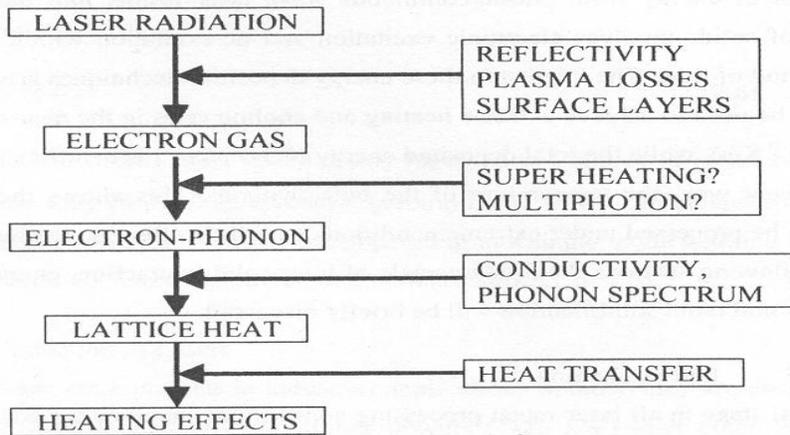
Directed Energy Beam Irradiation of Matter

$$I(z,t) = I_0(t)(1-R)\exp(-xz)$$
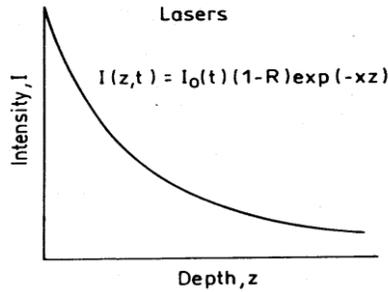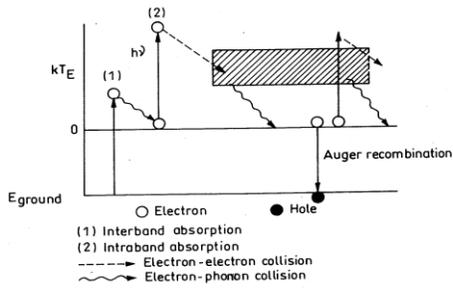
Electron excitation and carrier relaxation Spatial profile of deposited energy

Ion beam   **Electron beam**

$$C(z) = \frac{Q_T}{\sqrt{2\pi}\,\Delta R_P}\,\text{Exp}\left[-\left(\frac{z-R_P}{\sqrt{2}\,\Delta R_P}\right)^2\right]$$

$$I(z,t) = I_0(t)(1-R_E)\,f_E(X/X_P)$$
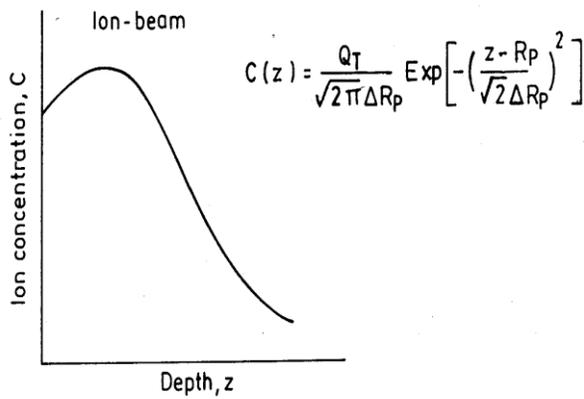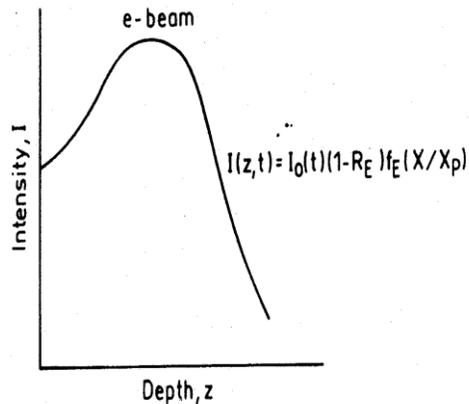
Laser Material Processing- Classification

Laser material processing
- Involving change of phase/state
  - solid → vapour
    - • Machining (cutting, drilling etc.)
    - • Deposition/coating
    - • Laser spectroscopy
    - • Laser-assisted purification
  - solid → liquid
    - • Joining (welding/brazing)
    - • Surface alloying/cladding
    - • Rapid prototyping
    - • Reclamation
- Involving no phase change
  - solid → solid
    - • Surface hardening
    - • Bending or forming
    - • Semiconductor annealing
    - • Shocking/shot-peening

- Forming
  - • Bending/straightening
  - • Manufacturing
  - • Colouring/deposition
  - • Rapid prototyping
- Joining
  - • Welding
  - • Brazing
  - • Soldering/sintering
  - • Repair/reclamation
- Machining
  - • Cutting
  - • Drilling
  - • Scribing/marking
  - • Cleaning
- Surface engineering
  - • Surface alloying/cladding
  - • Surface melting/remelting
  - • Surface amorphization
  - • Surface hardening/shocking

Laser Assisted Material Processing
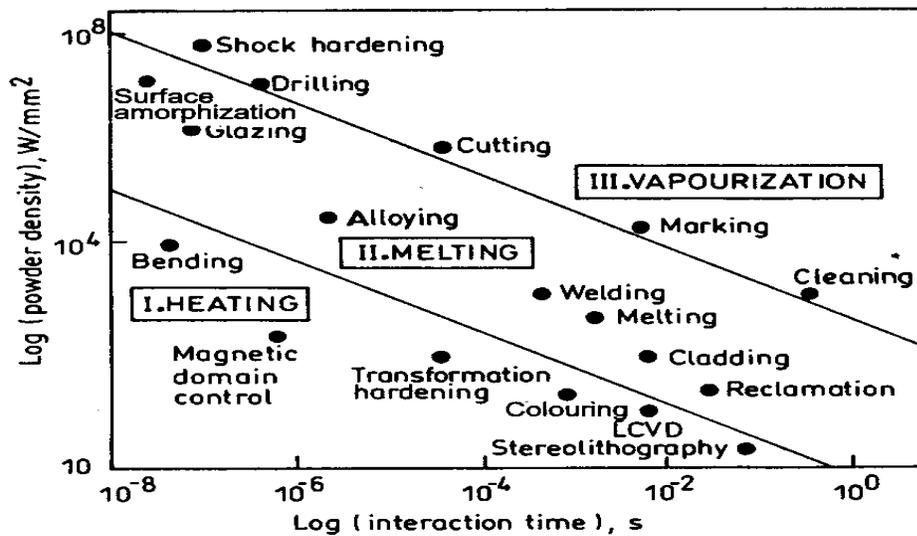
Processing window for laser material processing

12

Laser Assisted Machining

Machining processes:

$\Rightarrow$ **Cutting, drilling**

$\quad\Rightarrow$ **Marking, scribing**

$\quad\Rightarrow$ **Cleaning, polishing**

$\quad\Rightarrow$ **Patterning, texturing**

$\quad\Rightarrow$ **Rust / coating removal**

Characteristics:

$\quad\Rightarrow$ **Fast, automatic**

$\quad\Rightarrow$ **Remote operation**

$\quad\Rightarrow$ **No specimen claming**

$\quad\Rightarrow$ **Versatile, any material**

$\quad\Rightarrow$ **Negligible HAZ damage**
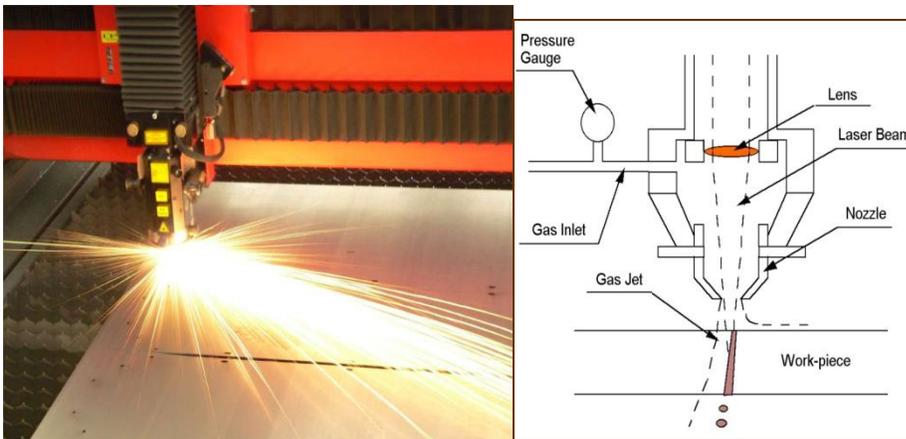
Laser cutting using (a) transmissive, (b) reflective optics

Laser assisted micromachining

Micro pattern machined on steel
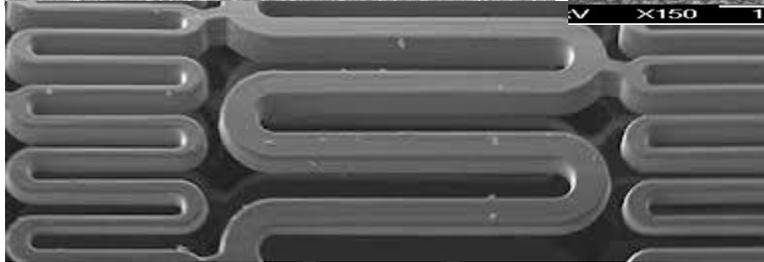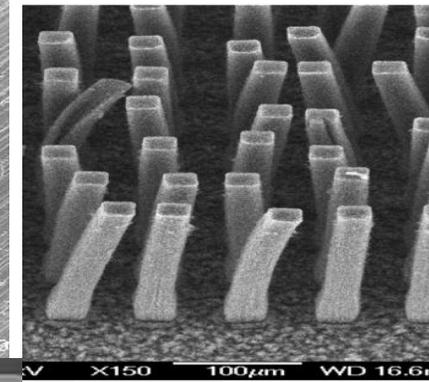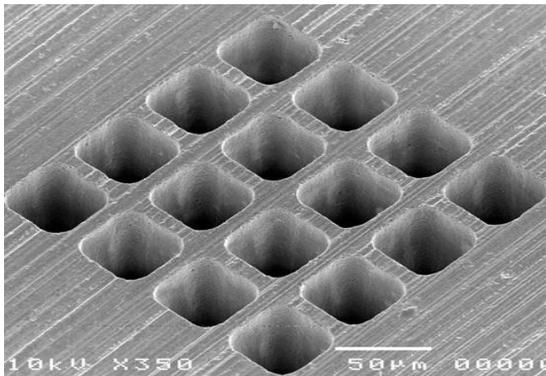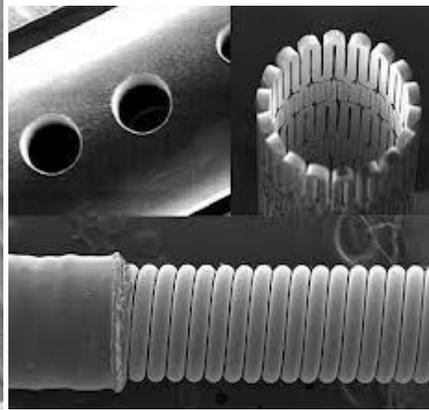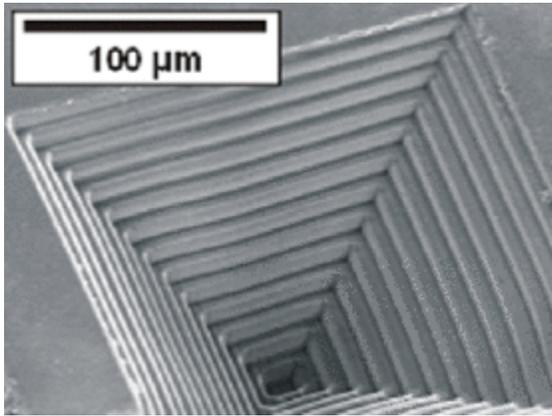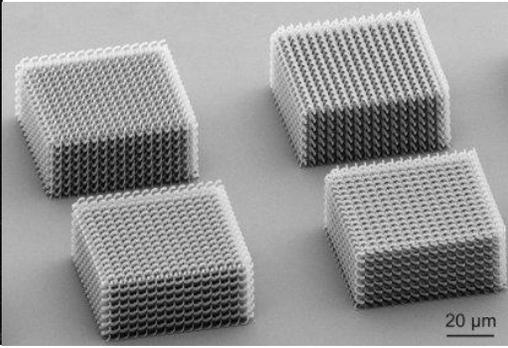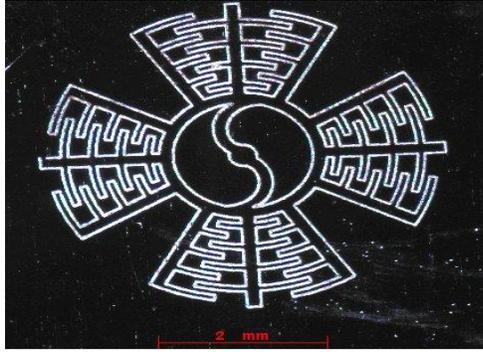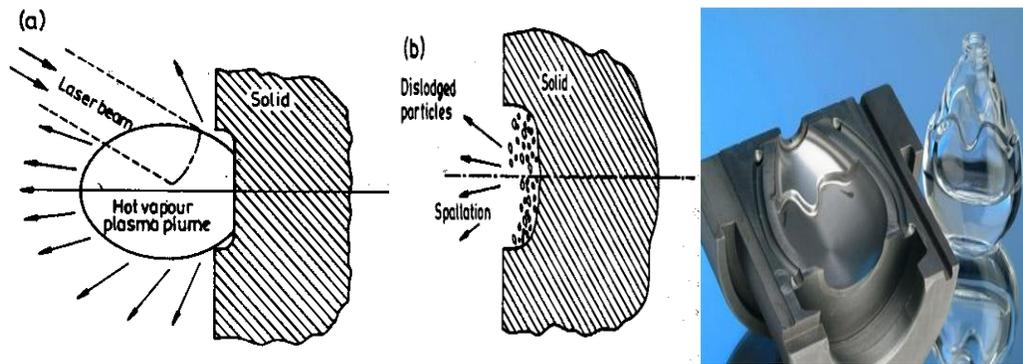
Scope: Removal of paint; cleaning of rust, cleaning of concrete

Laser assisted JOINING
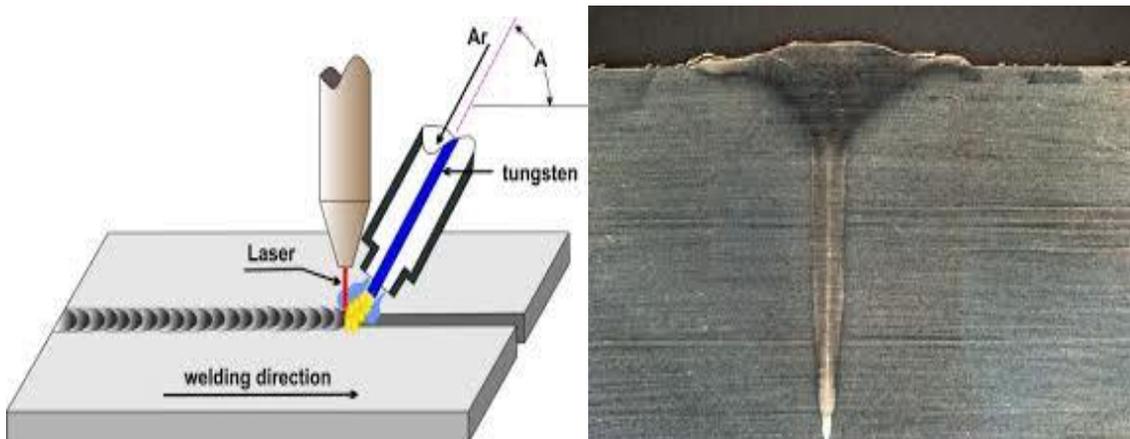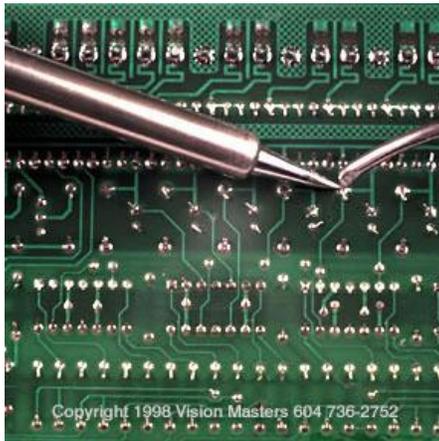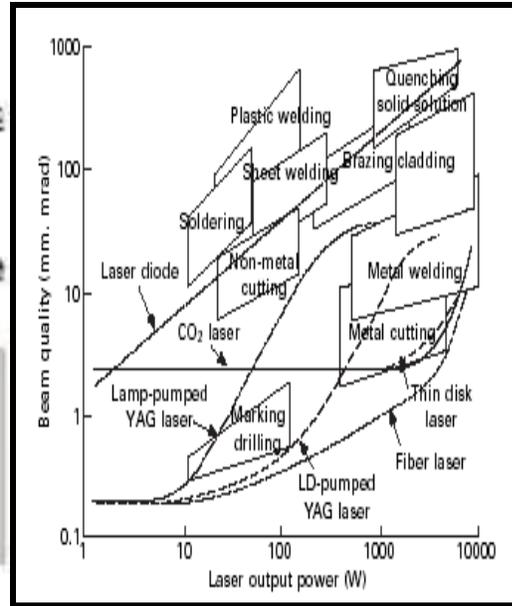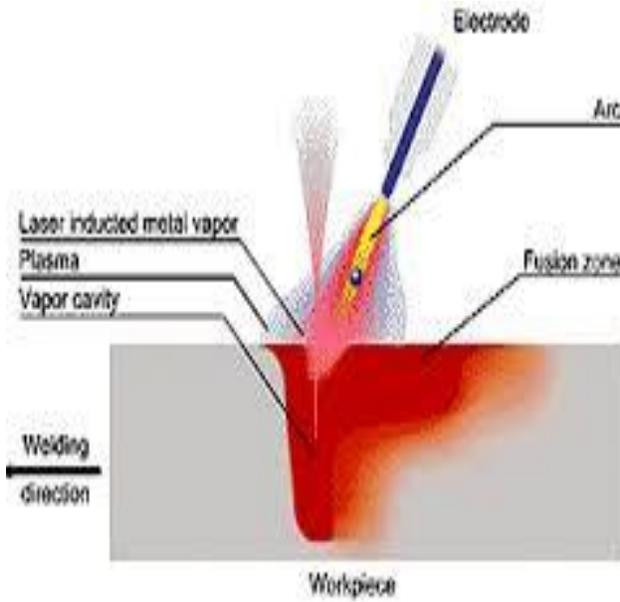
Soldering

Brazing

Laser Transmission Welding of Polymer
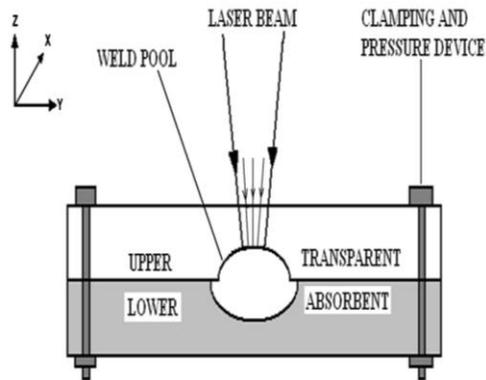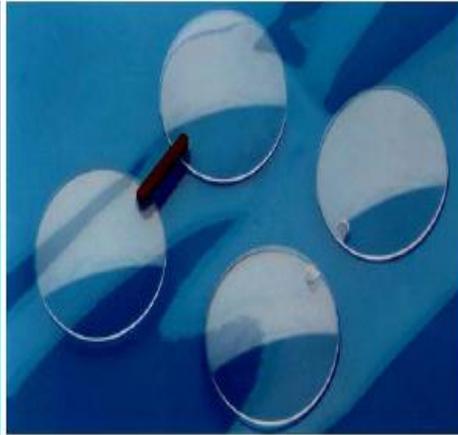
APPLICATIONS:

Filter cases of automobiles

Low weight polymeric spectacles

Keyless go card in luxury automobiles

Low cost high volume welding of components Examples: polymeric pump and plastic window

$$\rho \hat{C}_p \frac{\partial T}{\partial t} \quad = \quad -\rho \hat{C}_p \frac{\partial}{\partial x_i}(v_i T) \quad + \frac{\partial}{\partial x_i}\left(k \frac{\partial T}{\partial x_i} \right) \quad + S$$

| Rate of gain of energy per unit volume | Rate of energy input per unit volume by convection | Rate of energy input per unit volume by conduction | Source term |

$$K\left(\frac{dT}{dz} \right)_{u,b} = \frac{fQ\eta}{r_b^2} \exp\left(-\frac{f(x^2 + y^2)}{r_b^2} \right) - h_c\left(T_{u,b} - T_{l,t} \right) \qquad K\left(\frac{dT}{dz} \right)_{l,b} = h_{l,b}\left(T_{l,b} - T_a \right)$$

Limitation:

- **Requirement of pressure**

- **Material dependence**

- **Problem of contact**

- **Residual stress**

Experimental Results
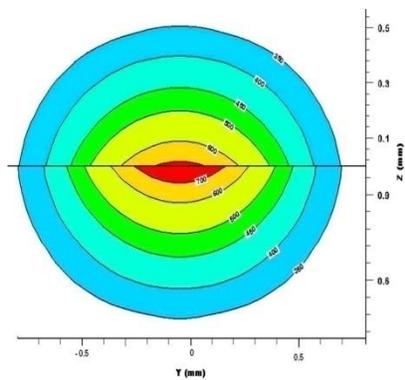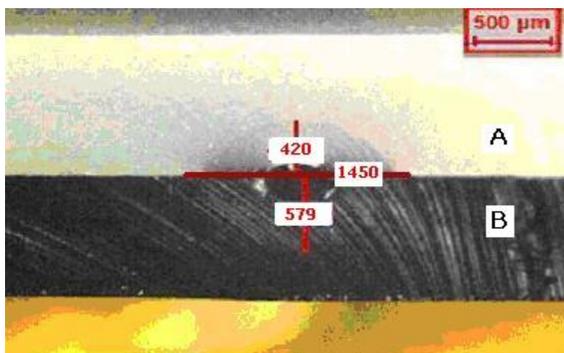
Shear strength of the joint (MPa)						
Pressure (kPa)	200	300	500	600	800	900
Speed (mm/s)						
1.6	5.2	5.4	6.5	7.0	7.0	5.2
2.7	4.7	4.9	5.5	6.0	7.3	5.3
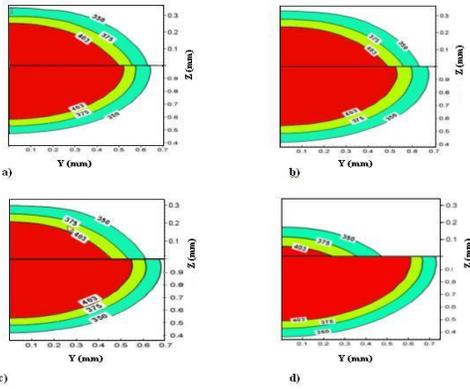
Laser Assisted Fabrication
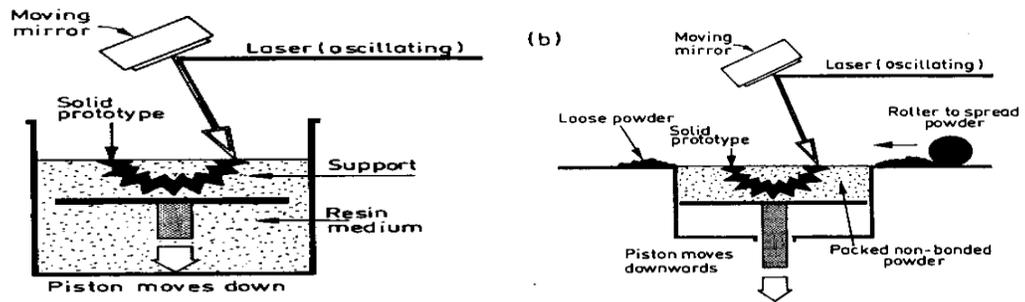
Schematic of LAF by (a) stereolithography and (b) selected laser sintering

J. Dutta Majumdar and I. Manna, Sadhana 28 (2003) 495-562

Low Density Cellular Materials
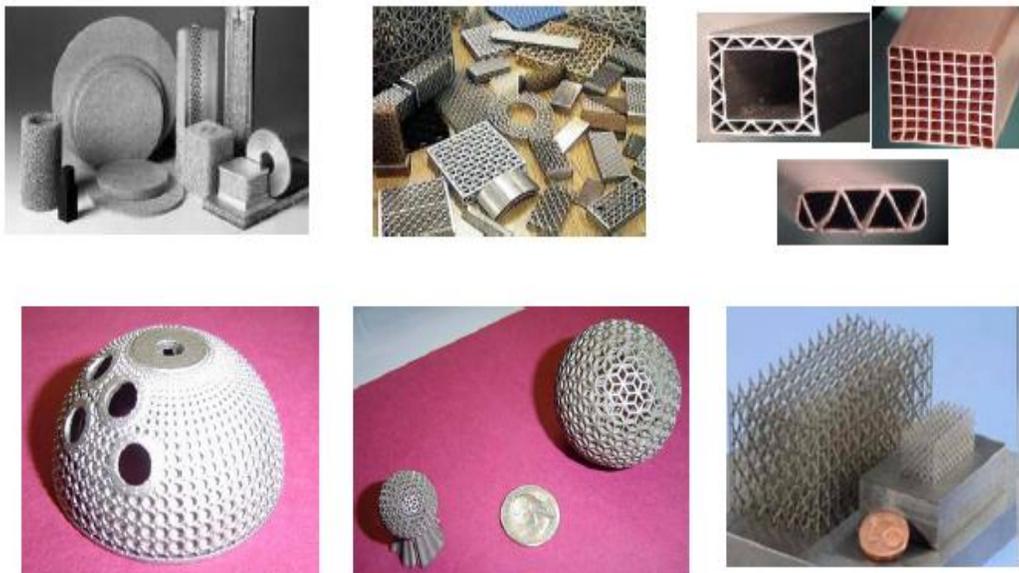
- **High-strength, low weight can be successfully applied for any type of structural components that require low moments of inertia, such as arms for industrial robots**

- **Ability to absorb impact can be used for lightweight armored plating on military vehicles, or bumpers on automobiles**

- **Fluid can be passed through the internal geometry of these structures for active cooling (satellites against solar heating)**

- **Body implants needs surface with porous structure**

Development of Compositionally Graded Component – Human Prosthesis/Implants
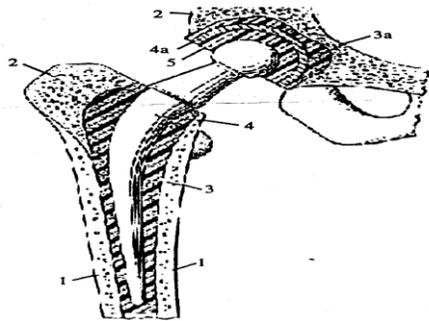
Artificial hip replacement
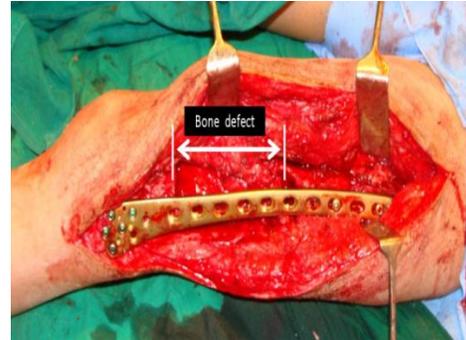
Neural Stimulation Electrode by LSA of Ti (Ir)
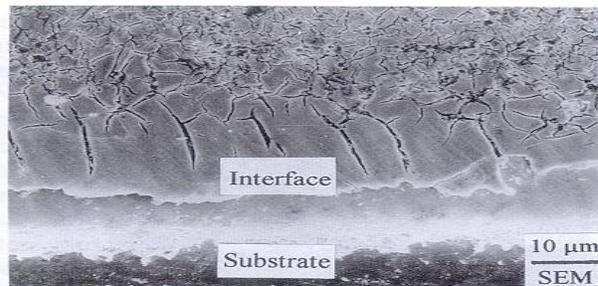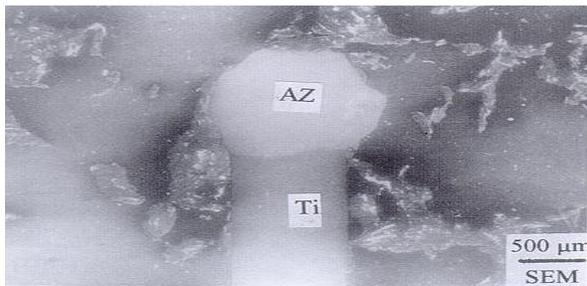
The Electrode   **Brittle Interface - Initial Trial**
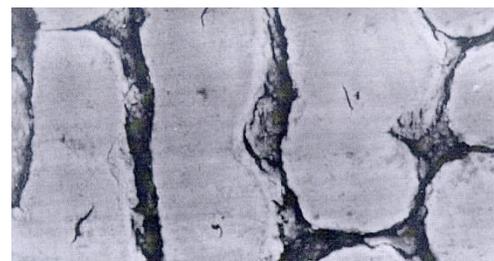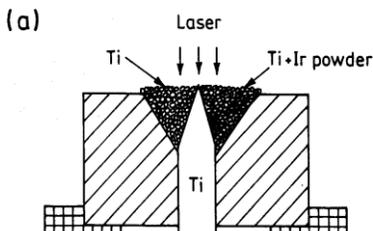
Columnar dendrites   **After deep etching**

I. Manna, W. M. Steen and K. G. Watkins, *Scripta mater.* **37 (1997) 561-568.**

The Tip Region - Front View
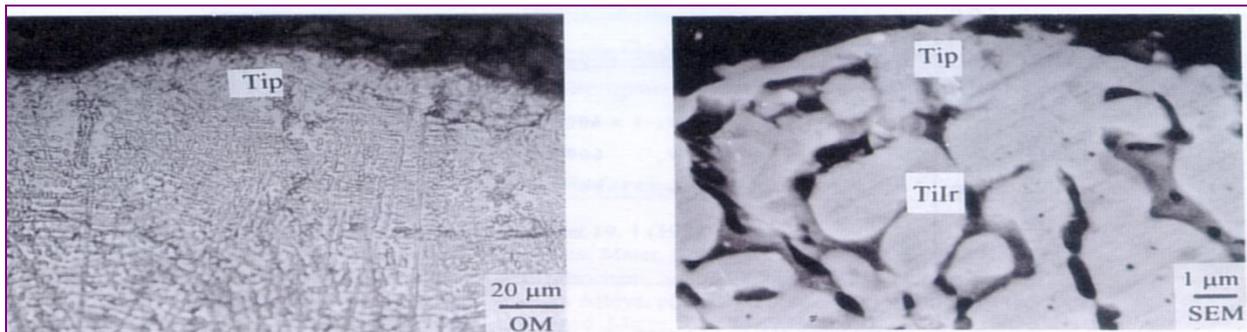
The Tip Region - Top View
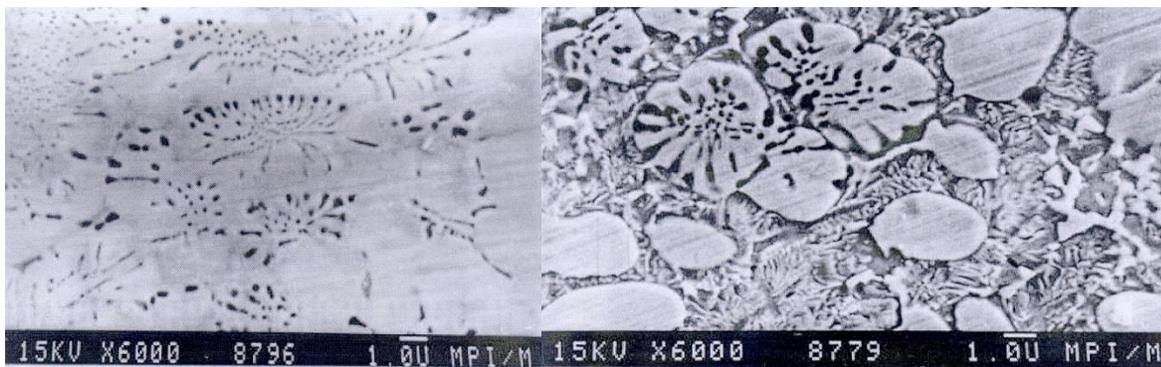
Engineering Components where Surface Matters

Su...

P...	**Che**...	...**echanical**
C...	**Cata**...	...**Wear, Erosion**
L...	**Chemisorption, Oxidation**	**Friction, Fretting**
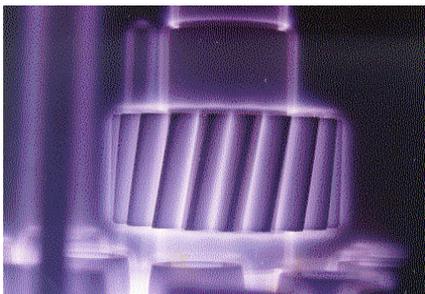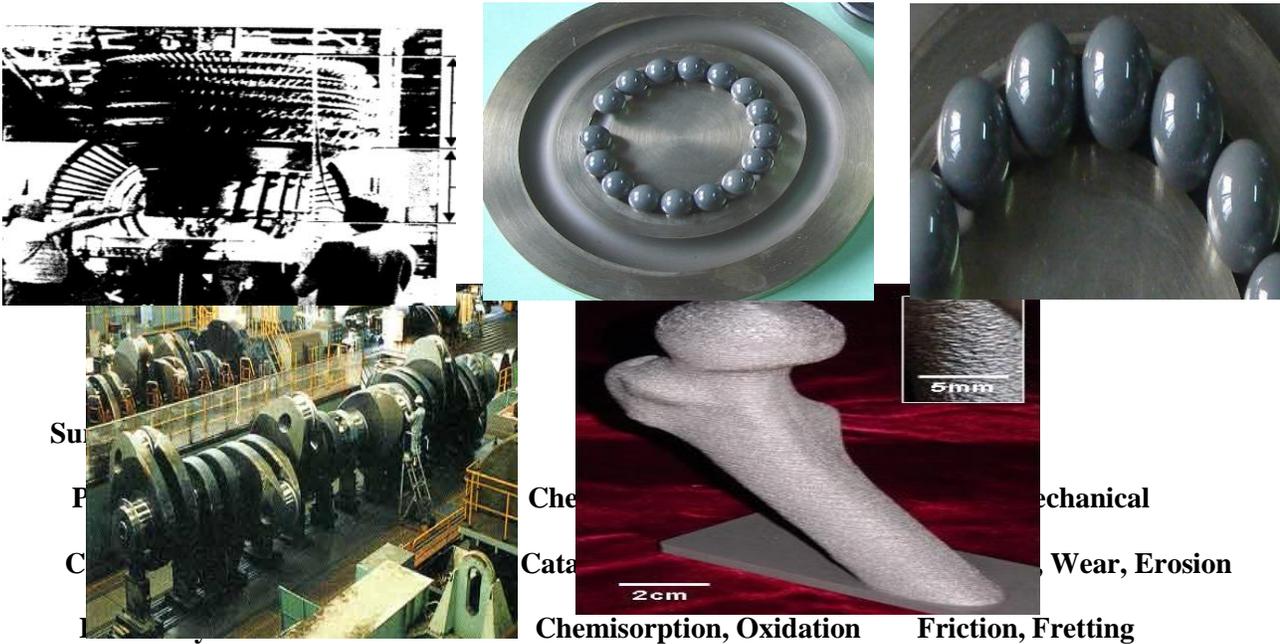
Surface Engineering Approach

| **Material Removal** | **Surface Modification** | **Material Addition** |
| **(Machining, Polishing)** | **(Alloying, Hardening)** | **(Deposition, Cladding)** |

Surface Engineering

Tailoring the microstructure/composition of the near-surface region (nm-mm) to enhance surface-dependent properties

Conventional

Carburizing, Nitriding, Electroplating, Painting, Calorizing, Diffusion Coating

Directed Energy Beam Techniques

Ion beam, Electron beam, Laser beam

LSH of Austempered Low Alloy Steel
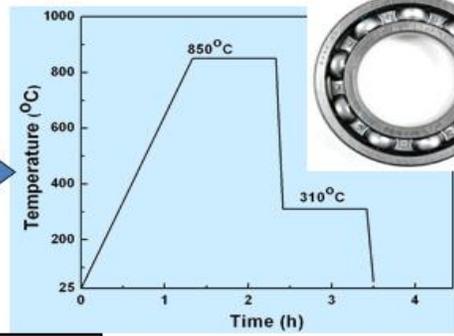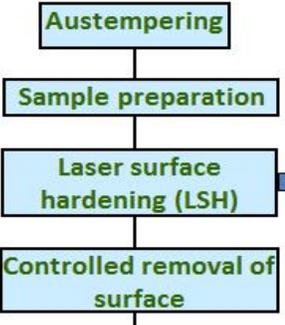
MICROSTRUCTURE and XRD

THERMAL PROFILE MODELING

$$T - T_0 = \frac{Aq/v}{2\pi\lambda\left[t(t+t_0)\right]^{1/2}} \exp\left[-\frac{1}{4\alpha}\left\{\frac{z^2}{t} + \frac{y^2}{t+t_0}\right\}\right]$$

T = Temperature of the substrate T_0 = Initial temperature of the substrate

A = Absorptivity at the sample surface q = Incident laser power

l = Thermal conductivity a = Thermal diffusivity ($=l/rc$)

r = Density c = Specific heat

v = Laser scan speed

r = Radius of the beam

$t_0 = r2/4a$

z = Vertical depth from the surface

y = Perpendicular distance

Temperature profile as a function of time at different depths (z) from surface for scan speed 16 mm/s and variation of temperature as a function of depth from surface (z)

Melt zone, ledeburitic, residual stress = 800 MPa, hardness = 900-1000 VHN, thickness = 10-30 μm
LSH zone, martensitic, residual stress = -400 MPa, hardness = ~850-900 VHN, thickness = 250-300 μm

Substrate, bainitic, hardness = ~600 VHN

Melt zone

LSH zone

10 μm
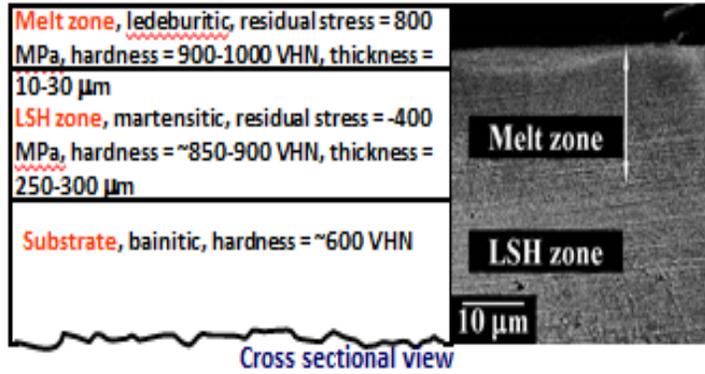
Basu et al, Scripta Mater. 56 (2007) 887-890

Cross sectional view

Mg Alloy Components in Automibile

Steering hanger beam
Steering wheel
Tailgate inner door panel
Cylinder head cover
Inner doorframe
Intake manifold
Seat frame
Transmission case
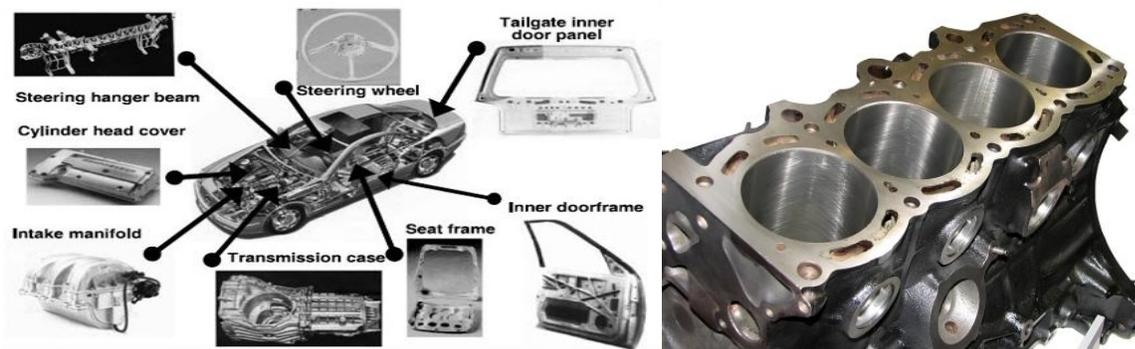
Surface Melting of Mg Alloy MEZ
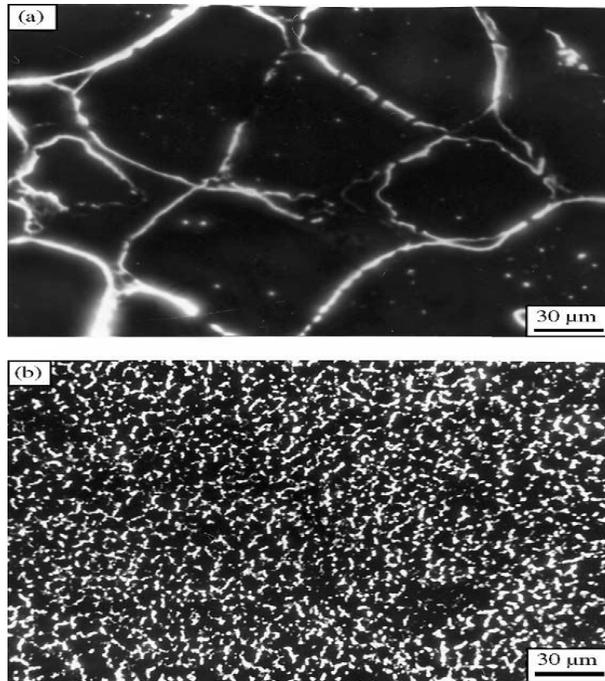
Mater Sci Eng A361 (2003) 119

Ti Alloy Components

LSA of Ti with Si/Al
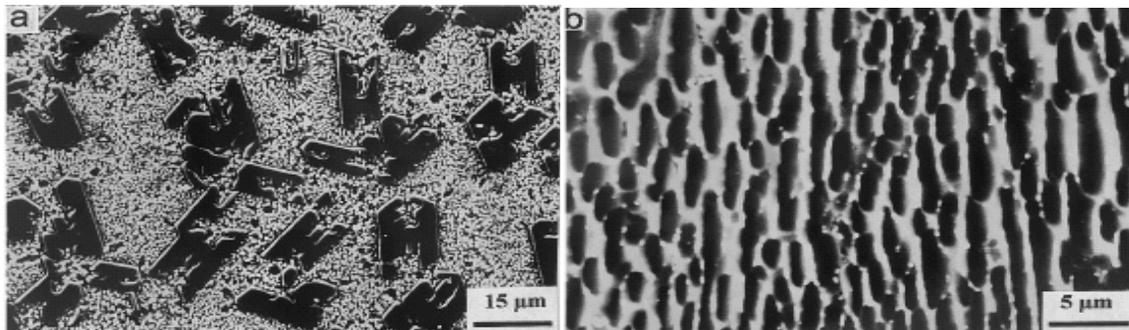
Dutta Majumdar et al, Mater. Sci. Eng., A266 (1999) 123

Oxidation Resistance Improvement
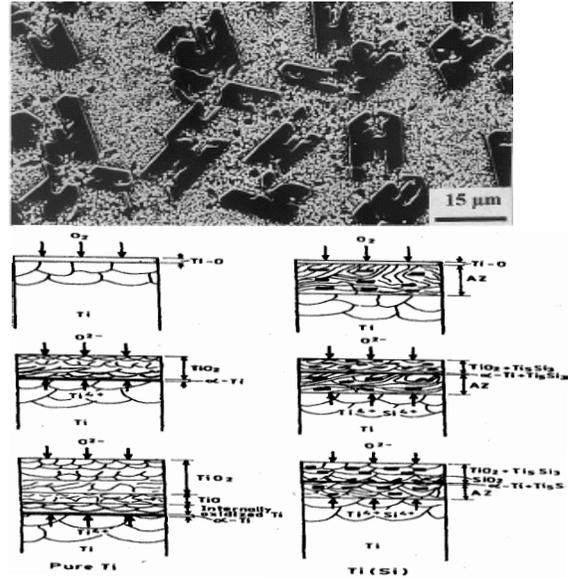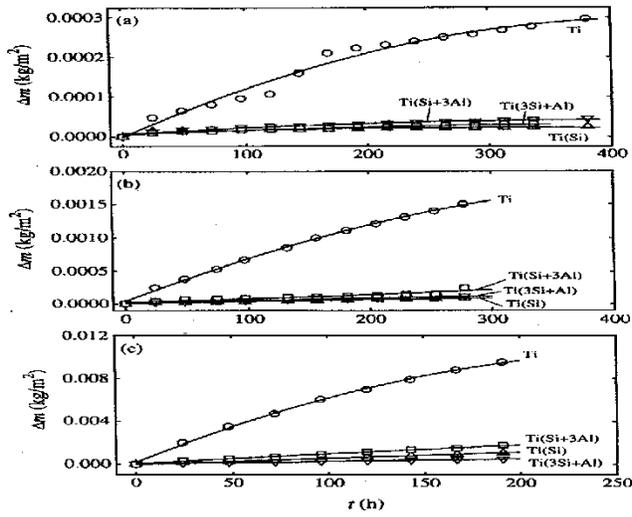
Kinetics of isothermal oxidation at (a) 950, (b) 1050, (c) 1150 K

LSC of Fe-Cr-Mo-Y-B-C BMG on SAE 52100 Steel
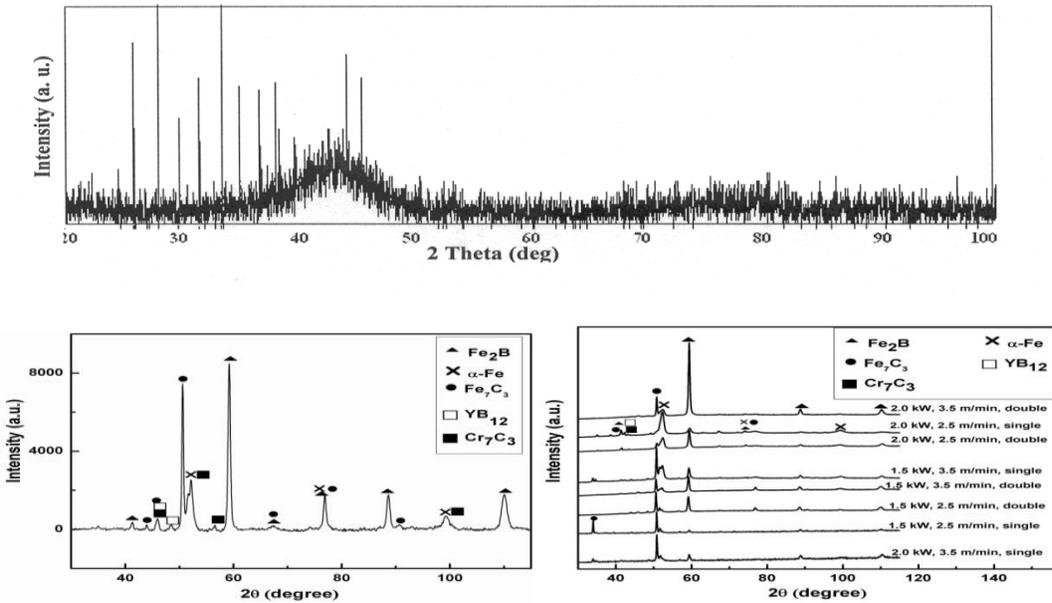
After cladding

Power: 1.5 kW power, Scan speed: 350 cm/min,Type: double scan

Basu et al., Surf Coatings Technol 202 (2008) 2623-2631

AISI H13 Tool Steel: Die Material for PDC

Powder: H13 tool steel

System: High power 6 KW diode laser

Spot Size: 3 mm
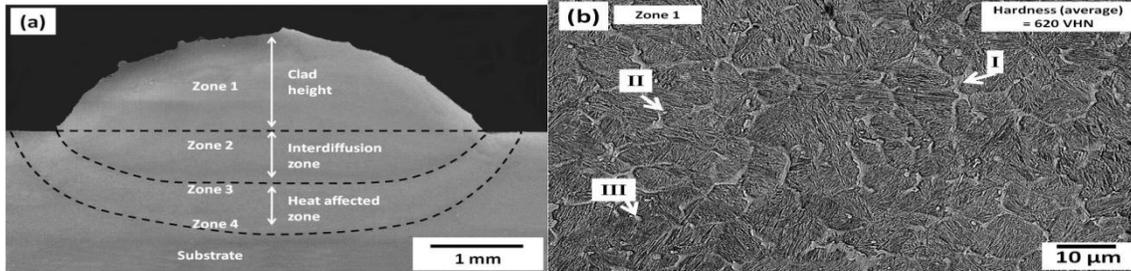
Single clad cross-section   **Clad microstructure**
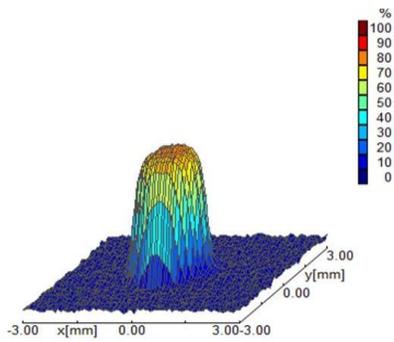
Laser energy density distribution
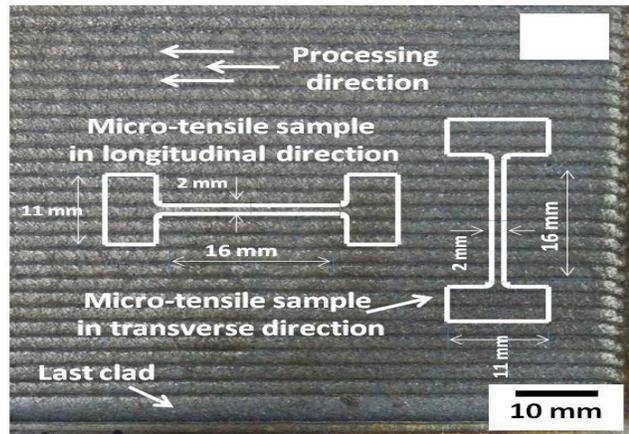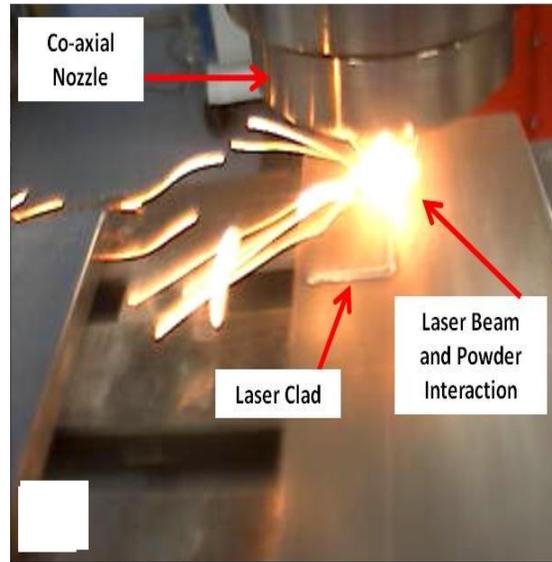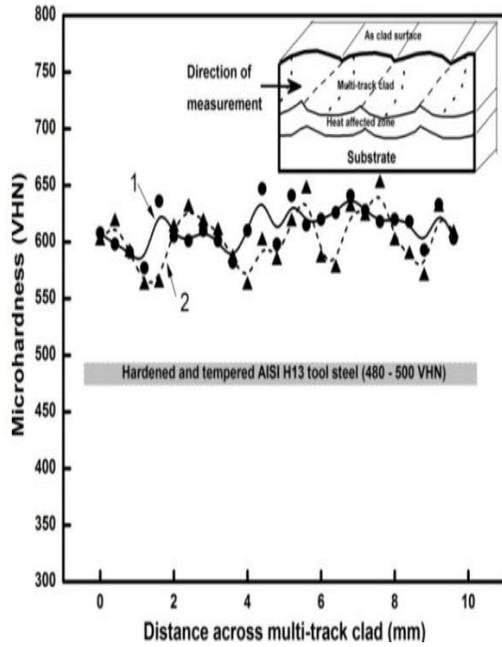
Laser cladding

Micro-Tensile Behavior of Laser Clad
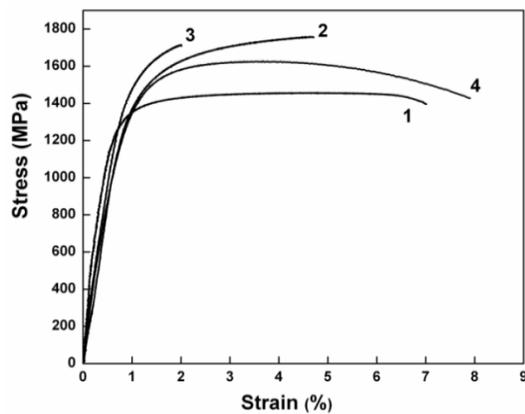
Sample ID	Y Strength (MPa)	UTS (MPa)	Elongation (%)
1	**1229**	**1457**	**7**
2	1379	1757	4.7
3	1425	1712	2
4	**1296**	**1622**	**8**
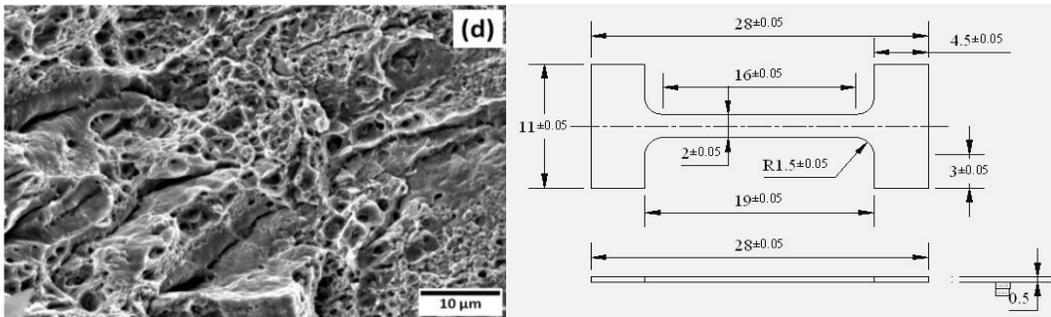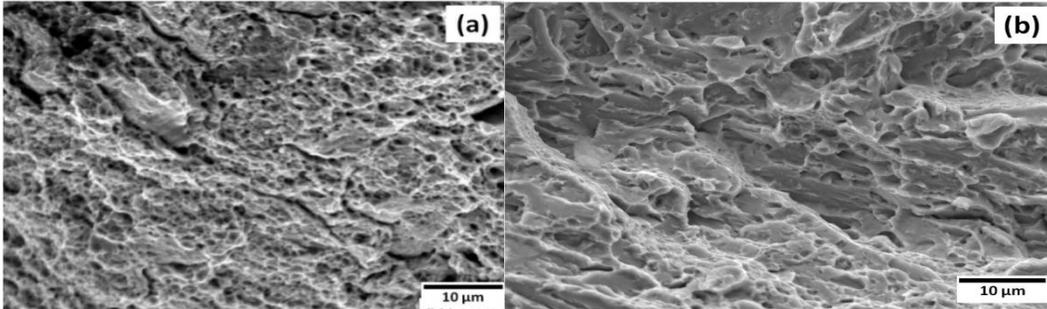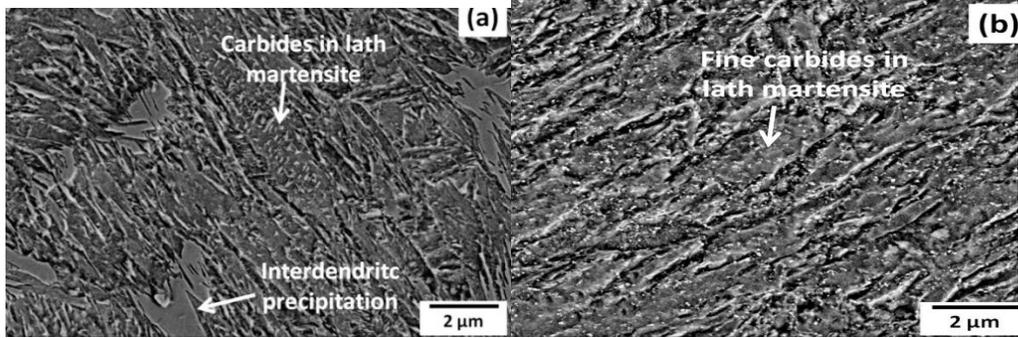
LSM: TiB-TiN Composite Coating on Ti

- BN powder (5/15 wt%) and Ti6Al4V alloy powder mixed with diluted polyvinyl alcohol solution

- Ti6Al4V powder: 50 – 150 μm

- BN powder: 0.5 – 2 μm

Ti6Al4V-EBN
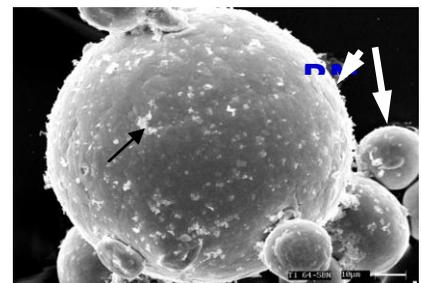
- ◆ **Strong peaks of $Ti_3N_{1.29}$ followed by TiB and TiN observed in all the coating**

- ◆ **No TiB_2 phase observed**
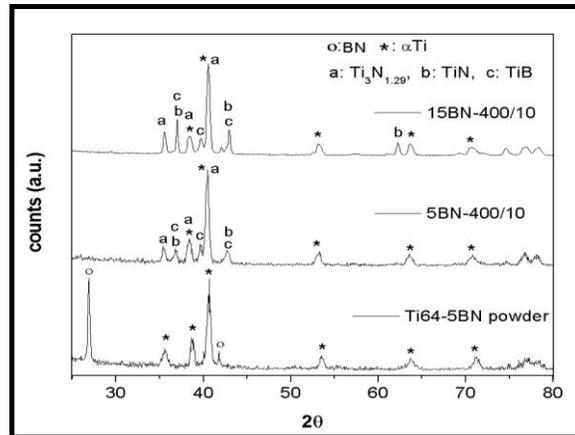
Das *et al*. Scripta Materialia 66 (2012) 578–581

Mechanical Properties
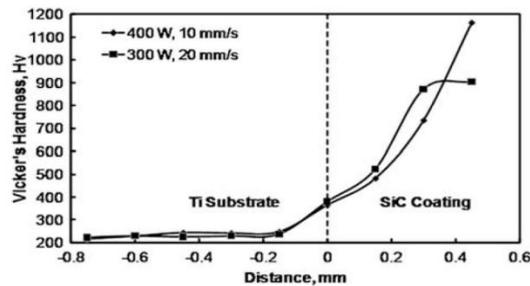
Cross section microhardness

- ❑ **Ti substrate: 232 ± 10 Hv**

- ❑ **300/20 coating: 976 ± 71 HV**

- ❑ **400/10 coating: 1167 ± 194 HV**

- ❑ **Hardness depends on reaction products, size, concentration and dispersion of hard SiC particle in the matrix**

- ❑ **Dry sliding against Si_3N_4 ball**

- ❑ **Wear resistance of Ti substrate improved by one order of magnitude due to incorporation of SiC on the surface**
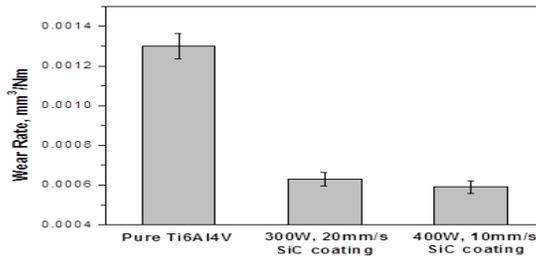
Effect of Laser Energy on Microstructure

[High]

Ti6Al4V-5BN-400W-
10mm/s

Coatings are

Mechanical Properties of TiB-TiN Composite Coatings

◆ **Hardness increases with increasing BN concentration in the coating**

◆ **Young's modulus significantly improve than titanium**

◆ **Wear rate significantly improve in coating containing 15 wt.% BN**

◆ **Chrome steel ball** [TiN] **simulated body fluid (SBF)**
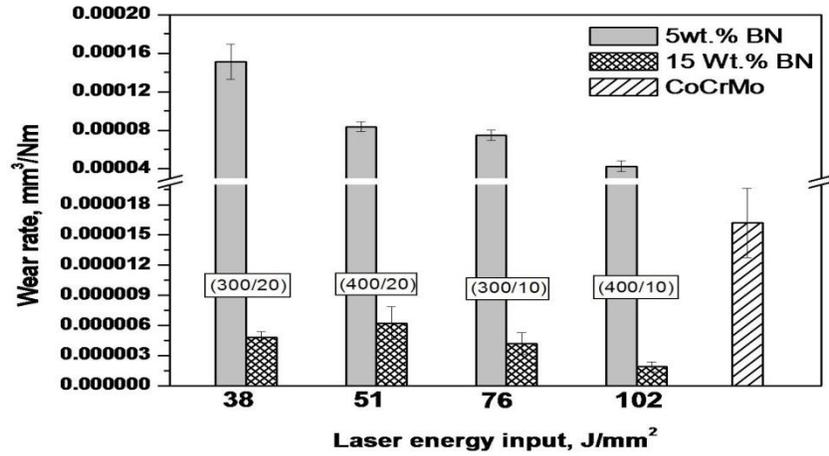
LSM: SiC Coating on Titanium
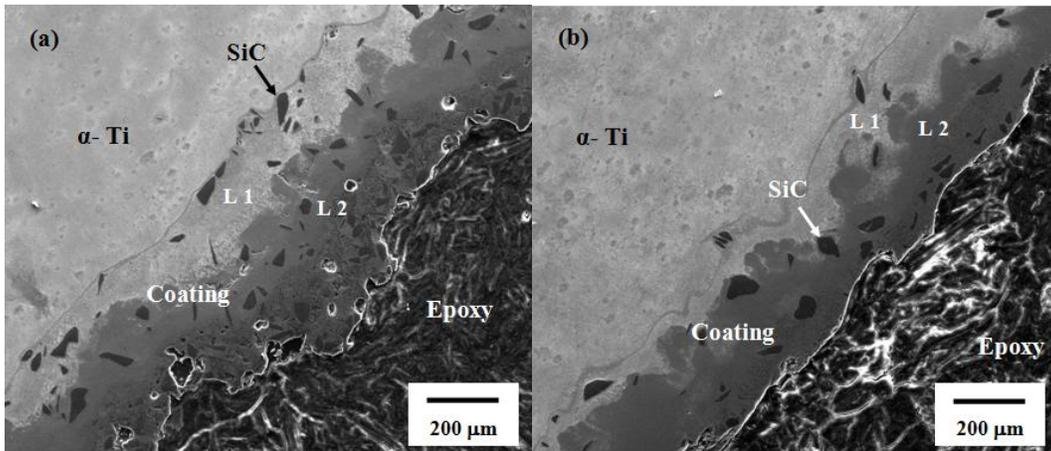
| Thicker coating | Thinner coating |

| Coarser aggregate | Finer aggregate |
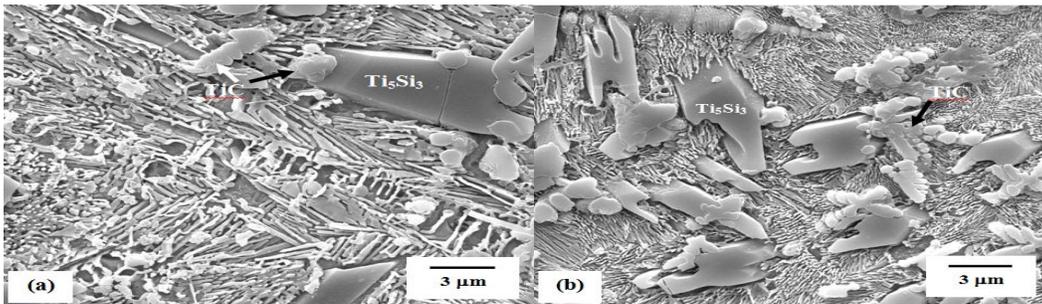
Cross Sectional Microstructure

Ti6A

Top Layer

TiC
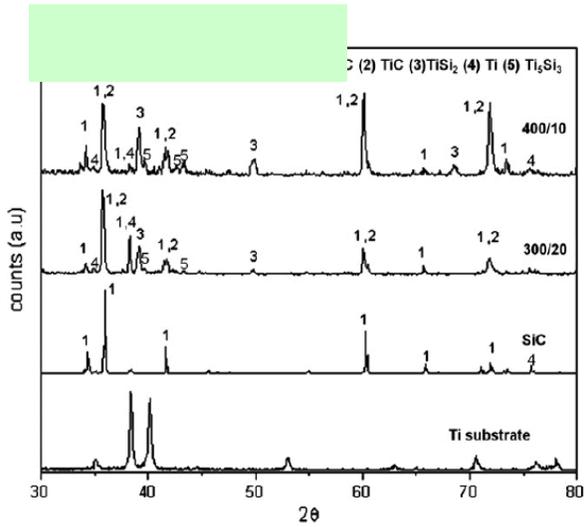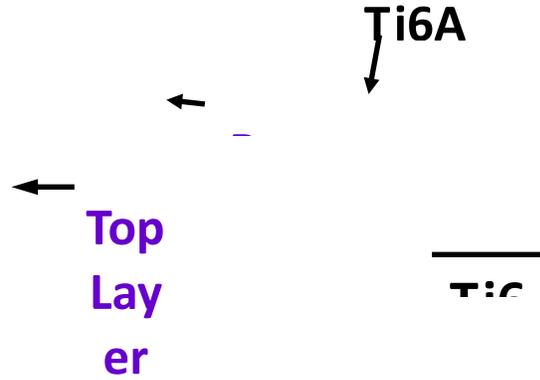
Bottom Layer:lamellar eutectic microstr ... dritic TiC phase

Low energy = 38.5 J/mm^2

Top Layer: cloud like TiCx phase embed

X-ray phase analysis: Coatings containing SiC, TiSi$_2$, TiC and Ti$_5$Si$_3$

Das *et. al.* Scripta Materialia 63 (2010) 438–441

Reaction Products

◆ **Injected SiC particles partially/ fully dissolve and formed new phases**

◆ **Exothermic reaction SiC + Ti → TiC + Si**

◆ **TiC layer formation around SiC particles**

◆ **Si reacts with Ti to form a variety of intermetallic compounds (Ti_5Si_3, $TiSi_2$).**

$$5Ti + 3Si \rightarrow Ti_5Si_3$$

$$Ti + 2Si \rightarrow TiSi_2$$
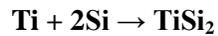
❑ **TEM images near the top surface of the composite coating**

❑ **Bright-field image of 300/20 coating**

❑ **Diffraction pattern from region A which is $TiSi_2$**

Ti

(b)

Ti SiC

Si

C

Ti

Si
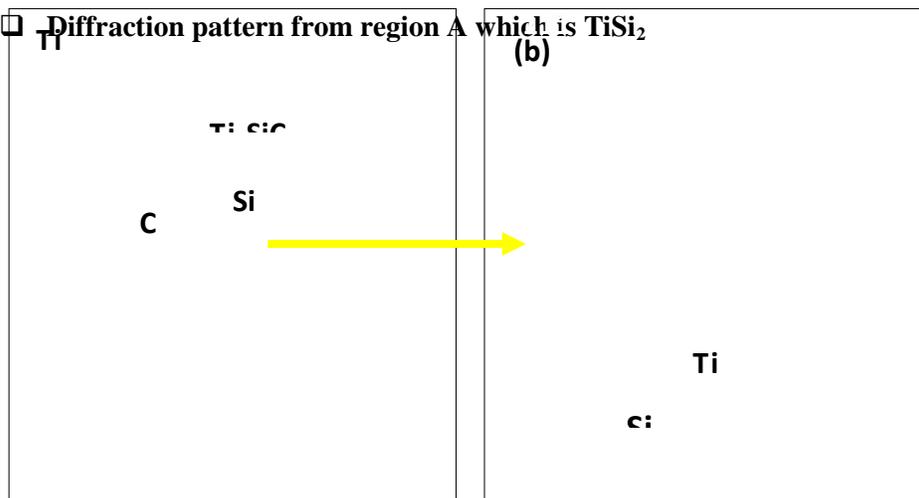
Summary of LAM:

1. **LSM of Mg: Improvement in wear and oxidation resistance is due to grain refinement and homogenization**

2. **LSA of Ti(Si,Al): Oxidation resistance improves due to silicide/aluminide layer**

3. **LSH of bearing steel: Martensitic layer with residual compressive stress for enhanced contact fatigue life**

4. **LSC of AISI H13: Homogeneity and hard carbides dispersed in predominantly martensitic surface**

5. **Ti6Al4V (SiC, TiN, TiB): Unique combination of mechanical and functional properties in the compositionally graded composite**

Metallic Materials for Body Implants

U.K. Chatterjee

Former Professor,Dept. of Metallurgical and Materials Engg.IIT Kharagpur 721302

ukc@metal.iitkgp.ernet.in

Abstract

Load-bearing joints in human body viz. hip, knee and shoulder joints, often require surgery to relieve pain due to degeneration and replacement of diseased joint surfaces by metal, plastic or ceramic implants to ensure increased mobility. Metallic materials are preferred as they can withstand all kinds of loading. Apart from joints, there is wide use of other metallic body implants.

Biocompatibility is an important consideration in human prosthesis. Though stainless steels and cobalt-chromium-molybdenum alloy (Vitallium) have been managing the show since 1950s, adverse tissue reactions, allergy and carcinogenic effects of the constituent elements of these alloys have led to the use of more biocompatible titanium alloys. Some compositions of stainless steels and cobalt-base alloys free from or low in nickel content have also found better acceptability as prosthetic materials.

Pure titanium and Ti-6Al-4V alloy have wide application in joint replacement parts, bone fixation and dental implants. Since vanadium and aluminium are respectively associated with potential cytotoxic effects and neurological disorders, alloys free from these adversities have been developed in the recent times. In order to achieve a modulus of elasticity comparable to that of the bone, the trend is towards the development of near beta and beta titanium alloys.

Surface modification to enhance the corrosion and wear resistance of the alloys has also proved to be beneficial.

Keywords: Biomedical metals, Mechanical properties, Corrosion, Biocompatibility

Introduction

Natural synovial joints, e.g., hip, knee or shoulder joints, are complex and delicate structures capable of functioning under critical conditions. Unfortunately, human joints are prone to degenerative and inflammatory diseases that result in pain and joint stiffness. It is estimated that about 90% of the population over the age of 40 suffer from some degree of degenerative joint diseases. Total joint replacement arthoplasty is recognized as a major achievement in orthopaedic surgery. The population ratio of the aged people is rapidly growing in all developed countries, with the growing need for replacement of failed tissues with artificial biomaterials. Apart from joint replacements, man-made materials are being widely used for fracture healing aids as bone plates and screws, spinal fixation devices, dental implants, vascular stents, catheter guide wires, orthodontic arch wires and others.

The material suited for human body implants should satisfy many requirements (Figure 1), but principally the features like strength, resistance to corrosion or wear, and biocompatibility. A material that does not produce any adverse reaction or inflammation and that is not rejected by the human system is said to be biocompatible. Polymers, ceramics and metallic materials are used for prosthetic and implant fabrication.

Ceramics and polymers are applicable in the construction of parts where high tensile stresses are absent, such as prosthesis heads or sockets of knee or hip joints. Polymers are suitable only for low stress conditions as the mechanical properties of polymers are poor under both tensile and compressive stresses. Polymers such as ultrahigh molecular weight polyethylene, polymethyl methacrylate, polylactide, polypropylene, polyacetal and polysulfone are commonly used. However, breakdown of these materials by embrittlement and excessive wear has often been experienced. Though the ceramics used for medicines like bioactive hydroxyapatite, $Ca_{10}(PO_4)_6(OH)_2$ and beta-tricalcium phosphate possess good biocompatibility and osteointegration (capable of rapid bone formation), they are seriously handicapped by their highly reduced fracture toughness and strength values. On the other hand, the metallic materials offer a wide range of mechanical properties, including resistance to fatigue and creep required in some prosthetic applications. Structural medical devices made of metals can be classified as low-loaded implants (e.g. plates, screws etc.) and high-loaded implants (e.g. hip and knee prostheses).

Early Developments

Metallic biomaterials have the longest history among the various biomaterials. The first metal/alloy used for implant application in the early 1900s was 'vanadium steel'. Iron and steel dissolve rapidly and induce erosion of adjacent bones. Copper and nickel embedded in bones led to discoloration of the adjacent tissues. Gold, silver and pure aluminium, although free from discoloration effect, were too soft for most applications. The first generation metallic biomaterials were implants made of stainless steels, cobalt-chromium and α+β titanium alloys. The chronological development of implant materials is shown in Figure 2.

Stainless steel with 18Cr-8Ni (Grade 304) was introduced as an implant material in 1926. It was found to be much stronger and more corrosion resistant to body fluids than vanadium steel. The molybdenum containing low carbon stainless steel (Grade 316L) was introduced in the 1950s. It is more resistant to pitting type corrosion, but was found to corrode inside the body in highly stressed and oxygen-depleted regions such as contact points under screws or fracture plates. Metal-on-metal hip prostesis was first introduced with the use of stainless steel, but was rapidly changed to a cobalt-chromium-molybdenum alloy to mitigate the excessive friction and rapid loosening of the stainless steel pair.

Two main types of cobalt-based alloys, CoCrMo alloy in the cast form and CoNiCrMo alloy usually obtained in wrought form by hot forging, were considered for surgical implants. The trade name, Vitallium, is applied to both the alloys. These alloys were considered superior to stainless steels as they displayed a balance between mechanical properties and biocompatibility. The chemical passivation of these alloys leads to the formation of complex chromium oxide which aids in the corrosion resistance of cobalt-based alloys. However, these alloys are not preferred for fracture-fixation purposes owing to their high cost.

Studies on toxicity have shown that elements such as aluminium, cobalt, nickel, molybdenum and chromium have long-term adverse effects in human body (Figure 3). These demerits led to the use of titanium and its alloys. Titanium as an element has extremely low toxicity, and is well tolerated by both bone and soft tissue. It is found to be safe for intravascular applications owing to its high electronegativity and passive surface. For the same reason titanium does not cause hypersensitivity, which makes it the best choice for patients suspected of being sensitive to metals. Pure titanium and its alloys such as Ti-6Al-4V, originally developed for chemical industry and aerospace structural application, made their inroad as

biomedical material in the late 1960s owing to their high strength, superior corrosion resistance, enhanced biocompatibility and relatively low modulus of elasticity. Titanium and its alloys are currently used for the following biomedical applications:

1) Joint replacement parts for hip, knee, shoulder, spine, elbow and wrist
2) Bone fixation devices such as nails, screws, nuts and plates
3) Dental implants and parts for orthodontic surgery and dental prosthesis
4) Heart pacemaker housings and artificial heart valves
5) Surgical instruments for heart and eye surgery
6) Components in high-speed blood centrifuges.

Recent Developments

Ti-6Al-4V is an α+β titanium alloy. Although this alloy possesses excellent corrosion resistance and biocompatibility, the toxicity of the β-stabilizing element of vanadium was pointed out in the early 1980s, and this led to the development of titanium alloys especially intended for use as prosthetic material. Vanadium is associated with potential cytotoxic effects in the human body. So, vanadium in the Ti-6Al-4V alloy has been replaced by other β-stabilizing elements, iron or niobium, both of which considered safer for the living body compared to vanadium. Specifically, Ti-5Al-2.5Fe and Ti-6Al-7Nb, which are also α+β alloys, have been introduced. Based on the same concept, other α+β type biomedical titanium alloys, such as Ti-6Al-6Nb-1Ta and Ti-6Al-2Nb-1Ta have been developed. Aluminium has been associated with potential neurological disorders. So, subsequently, α+β type titanium alloys that do not contain either V or Al, such as the Ti-15Zr-based and Ti-15Sn-based alloys were introduced.

Low modulus of elasticity is another important criterion to be considered in selection of materials for biomedical applications. Alloys with high modulus are very rigid and hence shield the stress to the bone. This is often referred to as 'stress shielding effect'. This results in the death of the bone cell and lead to the loosening of the implants with time. The elastic modulus of α+β type titanium alloys is much lower than those of stainless steel and cobalt-based alloy (Figure 4), but still much greater than that of cortical bone. The elastic moduli of β-type titanium alloys are known to be smaller than those of α- or α+β type titanium alloys. Therefore, mainly β-and near β-type titanium alloys have been introduced, and some of them are aimed at low modulus of elasticity. Niobium, when added either in the range of 10 to 20 wt%, or 30 to 50 wt%, has been found to reduce the modulus of elasticity. Figure 5 lists the titanium alloys, old and the newly developed ones with their elastic moduli. A near β-alloy, Ti-13Nb-13Zr, exhibits higher adhesion of osteoblasts and lower bacterial adhesion than Ti and Ti-6Al-4V. This alloy is also used for designing cardiovascular implants, as ZrO_2 passive film is thrombogenically compatible with blood. Further, corrosion resistance of this alloy is far superior due to the formation of ZrO_2 and Nb_2O_5 that strengthens the TiO_2 passive film formed on the surface of this alloy.

Co-Cr-based alloys have greater wear resistance as compared to stainless steels and titanium alloys. Therefore, in the case of artificial hip joints, they are used for the head of the hip prosthesis. Wrought Co-Cr-based alloys contain a large amount of nickel (9 to 37 wt%), which is a high risk element for allergy. Co-28Cr-6Mo is the nickel-free wrought alloy that has been developed in the recent years. A dispersion strengthened Co-Co-Mo alloy containing fine oxides of La and Al for medical implants has been reported.

Type 316L stainless steel has still remained a widely used prosthetic material. However, in order to avoid Ni allergy problems, high-N austenitic stainless steels with reduced nickel content or without nickel have been developed. One such nickel-free variety, EU-90, has the composition of: Cr 15.62, Mo 3.83, Mn

16.66, N 0.81, Ni 0.12, C 0.05 and Cu 0.04 (all wt%). Corrosion resistance of this alloy is superior to that of 316L, but inferior to that of CP titanium (Figure 6).

Surface Modification

Wear and corrosion are the most common causes of failure of metallic orthopaedic prostheses. This apart, enhanced biocompatibility, particularly in respect of fast tissue growth, is also demanded of them. Surface engineering can play a significant role in extending the performance of metallic orthopaedic devices several times beyond their natural capability. Various surface modification methods, conventional and newer ones, have been applied to achieve this.

The poor tribological properties of titanium and its alloys cause wear of the implants, and the wear debris produced have resulted in inflammatory reaction, loosening of implants and severe pain to the patient. The presence of high titanium and vanadium in the tissues and aluminium in surrounding muscle is often reported. The wear resistance of titanium alloys can be improved by forming compounds of high hardness e.g. titanium nitride, titanium carbide, titanium boride and titanium oxide on the surface. Nitriding and oxidizing are preferred as they possess better biocompatibility. Titanium nitride compounds can be formed by surface modification techniques such as ion implantation, plasma nitriding, plasma vapour deposition, chemical vapour deposition and laser nitriding.

Ion implantation has come out to be a versatile technique to modify the surface to improve the corrosion and wear resistance of the alloy. It has been observed that there is 100-fold increase in wear resistance in nitrogen implanted Ti-6Al-4V alloy than the un-implanted alloy. Enhanced corrosion resistance of nitrogen implanted CP titanium, Ti-6Al-4V alloy, 316L SS and Co-Cr-based alloys in Ringer's solution has been reported. The enrichment of nitrogen in the passive film and formation of oxynitrides in the passivated layers have improved the corrosion resistance.

Various cost-effective and simple treatments like electropolishing, ageing and thermal methods have a profound effect on the corrosion properties of metals. Commercial treatments such as ageing in nitric acid cause passivation of Ti alloys. Tensile strength of cast Co-Cr-Mo-C alloy was found to be improved by specific treatment in oxygen atmosphere and hot isostatic pressing. An anodic layer may also be formed on titanium by electrochemical oxidation (anodization).

An alternative technique used for surface modification is oxygen diffusion hardening (ODH). The abrasive wear of Ti-13Nb-13Zr is found to be comparable to that of Co-Cr alloys when its surface is hardened by ODH treatment. The improvement in abrasion resistance in other titanium alloys has also been reported. The corrosion rate of ODH treated titanium alloy was found to be about 12 times less than that of the Ti-6Al-4V alloy and 20 times less than that of the Co-Cr alloys.

Human bone is constituted by calcium phosphates (69 wt%), collagen (20 wt%) and water (9%). Calcium phosphates present in the form of crystalline hydroxyapatite (HAP) and/or amorphous calcium phosphate (ACP) provide stiffness to bone. This has led to the use of HAP as an implant material for bone surgery. However, owing to their poor mechanical properties, they are useful in applications where the mechanical forces are absent or primarily compressive. As an alternative, HAP coatings on metallic implants have gained wide use in clinical applications. The combined advantages of good biocompatibility (HAP) and good mechanical properties (metal) make them suitable materials for load-bearing parts of the skeleton.

The coatings have specific functions ranging from improving fixation by establishing strong interfacial bonds, shielding the metallic implant from environmental attack or leaching effects, promoting fast tissue growth and minimizing adverse reaction by the provision of a biocompatible phase. Several coating methods such as plasma spray, ion beam sputtering, blast coating, electrophoretic deposition, electrochemical deposition and coating through sol-gel process are available.

LOW TEMPERATURE SUPERCONDUCTORS –FABRICATION AND APPLICATIONS

M. M. Hussain, Atomic Fuels Division,Bhabha Atomic Research Centre Trombay, Mumbai – 85

Discovery of Superconductivity

- In 1911 superconductivity was first observed in mercury by Dutch physicist Heike Kamerlingh Onnes of Leiden University. When he cooled it to the temperature of liquid helium, 4 degrees Kelvin, its resistance suddenly disappeared!

Fig   Normal conductor $^v/_s$ Superconductor

The critical current density J_c, is a structure dependent property and depends very strongly on the density, size and distribution of imperfection such as dislocations, grain boundaries and precipitates which act as flux pinners.

α – hcp, normal

β – bcc, SC**Fig**
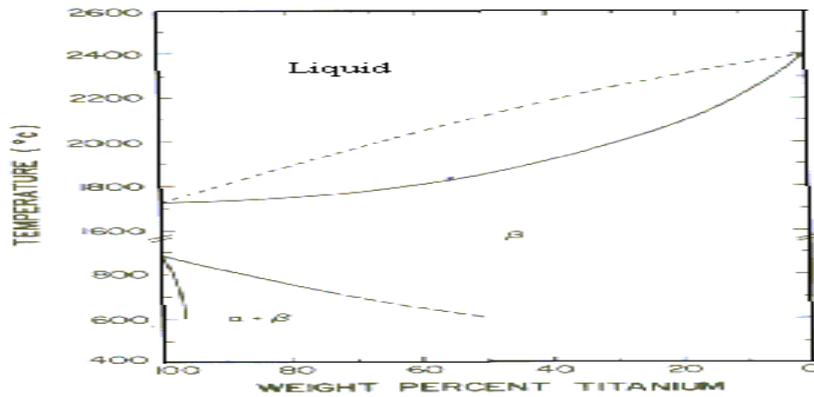
Fig The Nb-Ti phase diagram given by Hansen etal.
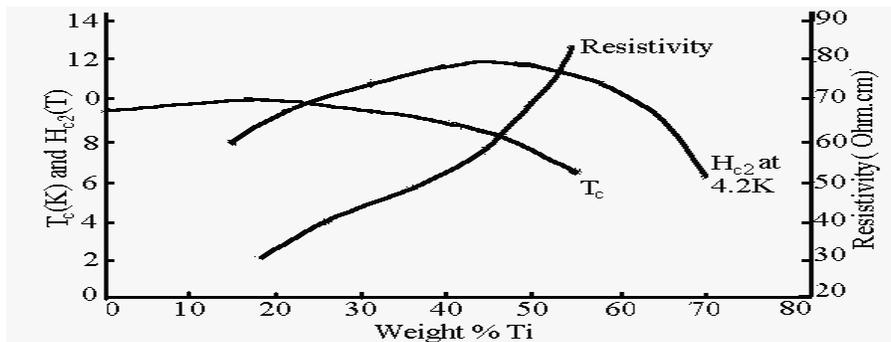
Fig   The variation in H_{c2} at 4.2 K, T_c and resistivity with composition for single phase b - Nb-Ti
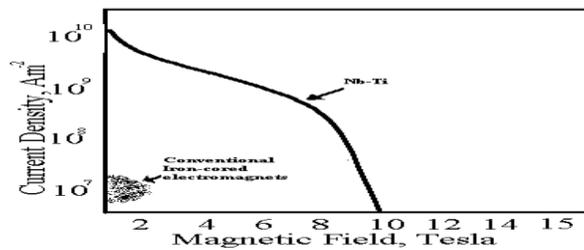
Fig   Conventional vs Nb-Ti SC at 4.2 K. The shaded area at bottom left representsthe usual range of conventional electromagnets

Fabrication at AFD

- Extensive development work has been carried out at AFD, which includes composite billet design, optimization of parameters for extrusion, drawing and ageing treatment to obtain suitable shape, size and distribution of α-Ti precipitates, which act as flux pinning centre. Fabrication route has been standardized for 1.30 mm dia. wire containing ~ 500 Nb-Ti filaments each of 40 micron size with Cu:SC ratio of 1.30:1.

- Soldering of 1.30 mm dia wire on to U-grooved rectangular OFHC copper channel has been carried out.

- Facility set up for development and fabrication of composite superconductor for various applications.

Technical Specification of SC Wire

- Wire Diameter   : 1.290 ± 0.127 mm

- Filament Size   :   40 micron

- Cu: Sc Ratio   : $1.3 \pm 0.15 : 1$

- Critical Current   :   1030 Amps at 5.5
                                                        Tesla and 4.2 K

NO. OF FILAMENT: 402
A/F SIZE: 5.5MM
Nb-Ti ROD DIA: 4.88MM
Cu:SC RATIO: 1.257
NO. OF Cu HEX: 97

EXTRUSION BILLET ASSEMBLY   18.11.98
FOR 150MM CONTAINER
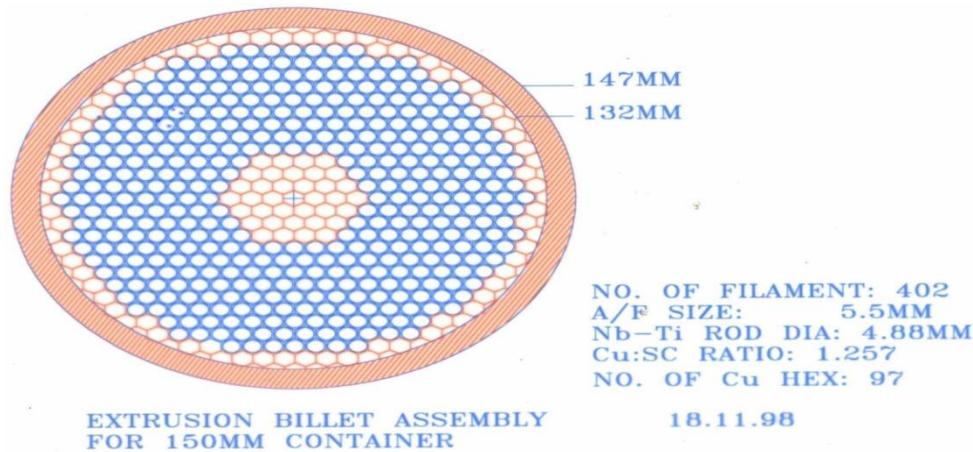
Components for SC billet assembly
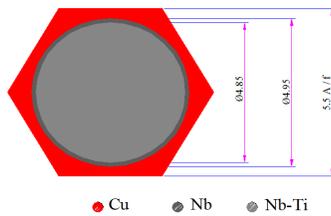
Fig.   Transverse Cross-section of a single rod

(Before being extruded and drawn into a filament)

Nb-Ti multi filamentary billet assembly developed at AFD, BARC.
It shall produce a 3 km single length superconducting wire of 1.3 mm dia.

Assembled Extrusion Billet

Extrusion temperature and pre-heating time

- The choice of extrusion temperature is very important parameter. The upper limit of applicable temperature is mainly given by chemical reaction of stabilizing copper with Nb-Ti to a brittle inter-metallic compound $(NbTi)_2Cu$ which causes wire interruption during further drawing.

- The lower limit is given by the deformation resistance of the Nb-Ti alloy and precipitation of α-Ti below 873 °C. In addition to this bonding is poor at lower temperature.

- Temperature constancy during processing can be achieved in the range between 3mm/sec – 6mm/sec.

Fig. Showing extrusion of superconducting billet

Cross-section of extruded Cu/Nb-Ti rod
(50 mm Dia.)
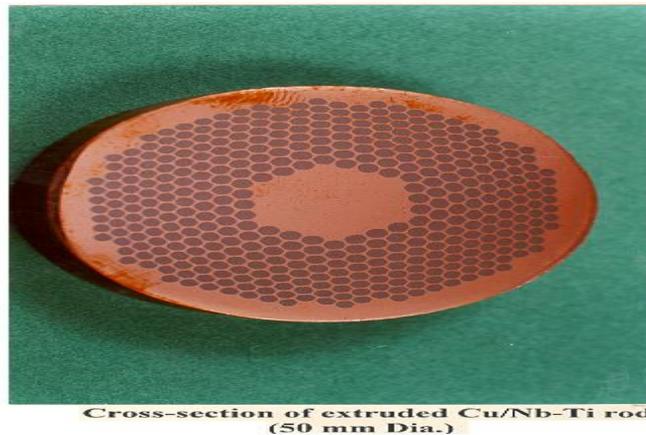
The cold work performs seven primary functions:

1. Encouraging the formation of the preferred precipitate phase and morphology.

2. Improving micro-chemical homogeneity by mechanical mixing both prior to heat treatment and after heat treatmentwhen local Ti depletion has occurred.

3. Increasing the density of precipitate nucleation sites.

4. Increasing the grain boundary density, thereby increasing diffusion rates (grain boundary diffusion being considerablyfaster than bulk inter-diffusion).

5. Reducing the average diffusion distance to the precipitate nucleation site.

6. Increasing the volume of precipitate by multiple strain/ heat treatment cycles.

7. Reducing the precipitate dimensions from the precipitationscale of 100 nm to 300 nm diameter to the pinning scale of 1nm to 5 nm.

Intermediate Annealing

- Annealing is required for precipitation of α-Ti.
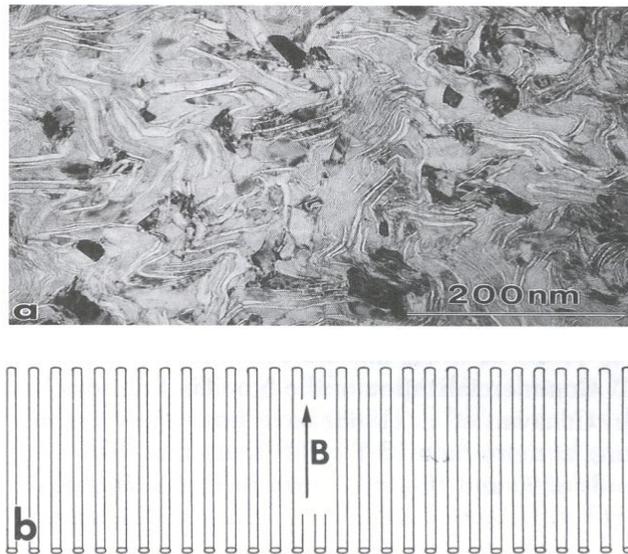
Fig   TEM micrograph of a transverse cross-section of Nb-46.5 wt%Ti filament from a composite manufactured by oxford superconductor Technology that achieved a J_c of 3700 A.mm^{-2} (4.2K, 5T).

1.3 mm dia Nb–Ti superconducting wire
(492 filaments, 40 micron size)
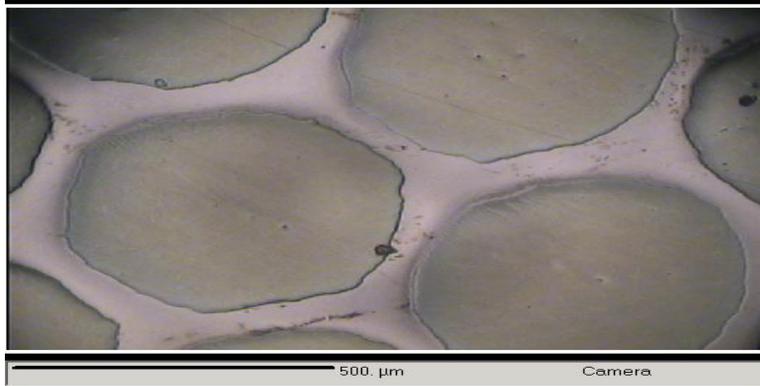
Fig.   Optical image of transverse cross-section of multi-filamentary Nb-47% Ti composite after third stage of heat Treatment. Φ = 17.4mm

1. mm   SE
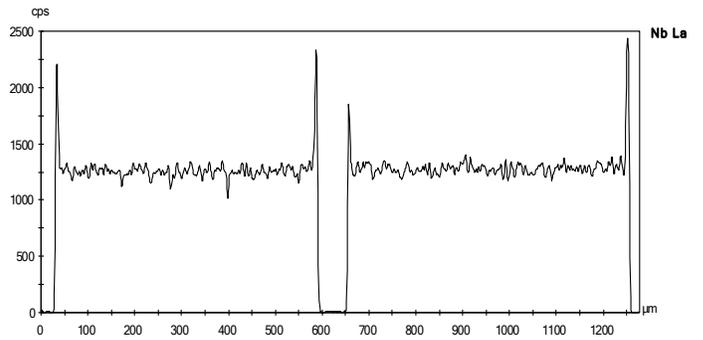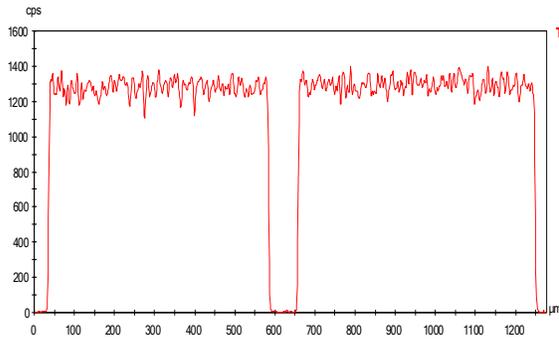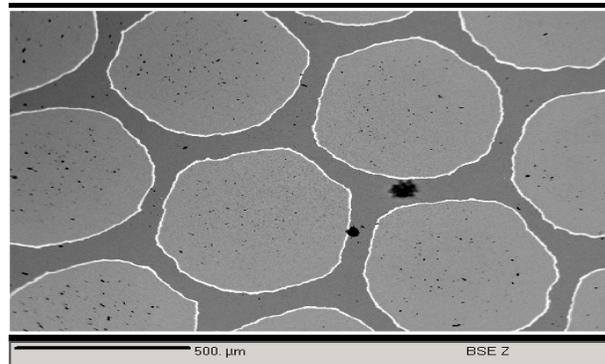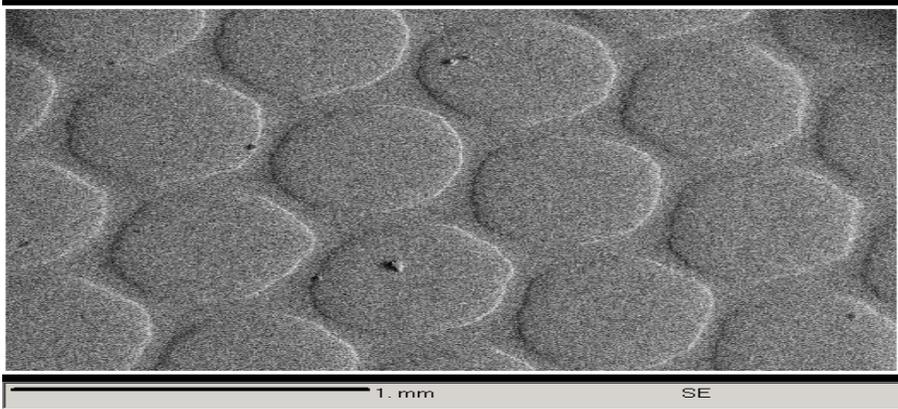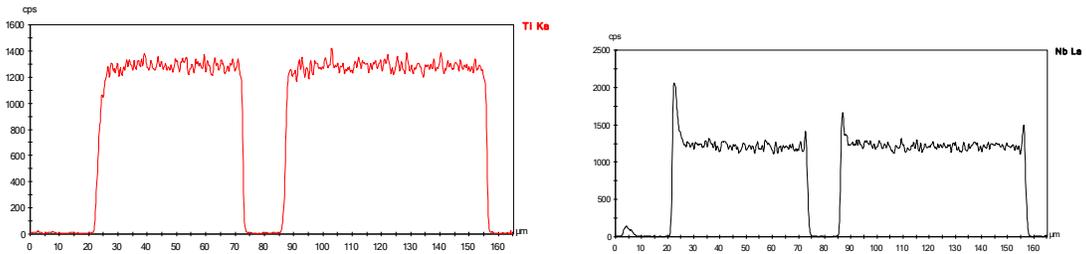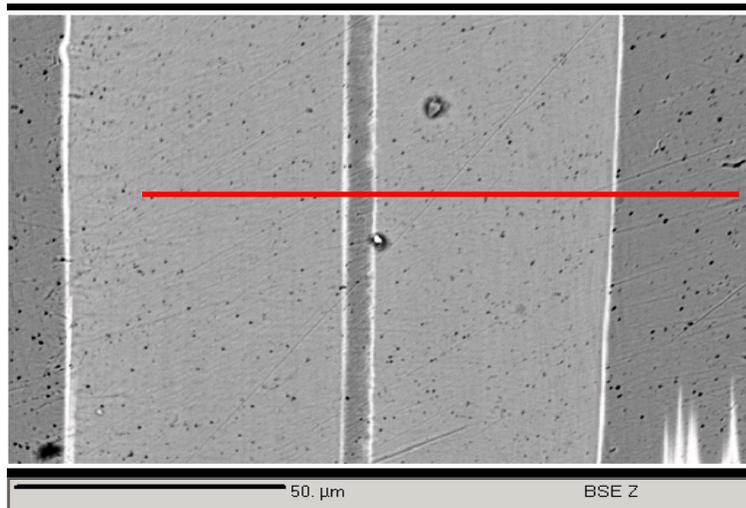
Fig.   EPMA micrograph showing Nb & Ti profile along line A-B (final wire 1.32mmΦ)

Test Results
A

1. **Metallography**

Sample	Filament number	Filament diameter, μm	Spacing, μm	Cu:SC ratio	Note
Sc. I	402	40.6	6.3	1.2:1	Geometry of cross section is slightly distorted
Sc. II	402	40.6	6.3	1.17:1	Right geometry of cross section
Sc. III	402	35.5	7.6	1.18:1	Strong distortion of cross section geometry

2. **RRR**

Sample	Residual Resistivity Ratio$_{293/10}$	
	As drawn	Annealed at 275°C for one hour
Sc. I	35	150
Sc. II	43	155
Sc. III	41	138

3. Critical current versus B on untwisted wires, n value, critical current density

I_c (0.1µV/cm), A/I_c (1.0µV/cm), A/n							
	Induction, T						
	4	5	5.5	6	7	8	9
Sc. I	1850/q*	1540/q	**1390/q**	1201/q	866/902/61	603/633/47	302/330/26
Sc. II	1710/q	1405/q	**1294/q**	1163/q	877/900/89	626/646/73	330/360/26
Sc. III	1790/q	1470/q	**1330/q**	1194/q	884/926/49	606/638/45	316/345/26
J_c (0.1 µV/cm), A/mm^2							
Sc. I	3025	2518	**2273**	1964	1416	986	494

Sc. II	2796	2297	**2116**	1902	1434	1024	540
Sc. III	2901	2383	**2156**	1935	1433	982	512

4. <u>Mechanical properties at Room Temperature</u>

No.	Sample	UTS, Kg/mm^2	YS, Kg/mm^2	δ, %	Note
1.	Sc I	95	58.0	1.2	Out of guage
2.		95	48.0	2.3	length
3.	**Sc II**	**95**	**54.0**	**1.5**	**Out of guage**
4.		**95**	**47.5**	**2.3**	**length**
5.	Sc III	94	45.0	2.4	
6.		96	46.0	2.4	

5. <u>Filament Breakage</u> : No filaments broken were revealed.

Flow sheet for Strand

Fabrication of Components

Assembly of Extrusion Billet

Hot Extrusion

Cold drawing with intermediate vacuum ageing treatments

Single wire Twisting

SOLDERING

Dip Soldering Process

- In this process SC wire is engaged into the U-groove of OFHC copper channel with the help of rollers.

- This assembly is passed through molten bath of Pb - Sn solder alloy continuously.

- Finally hot drawing is carried out to get the finished size and shape.
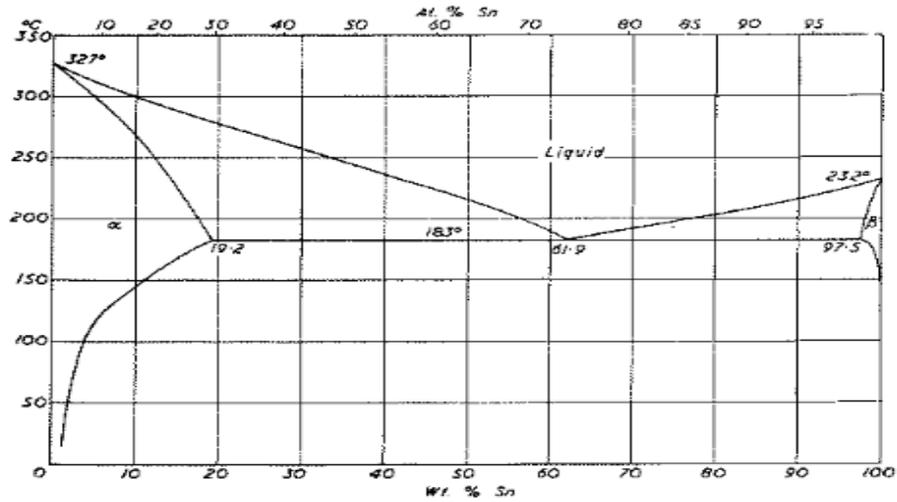
Pb – Sn Equilibrium Phase diagram

Continuous soldering unit for superconductor wire
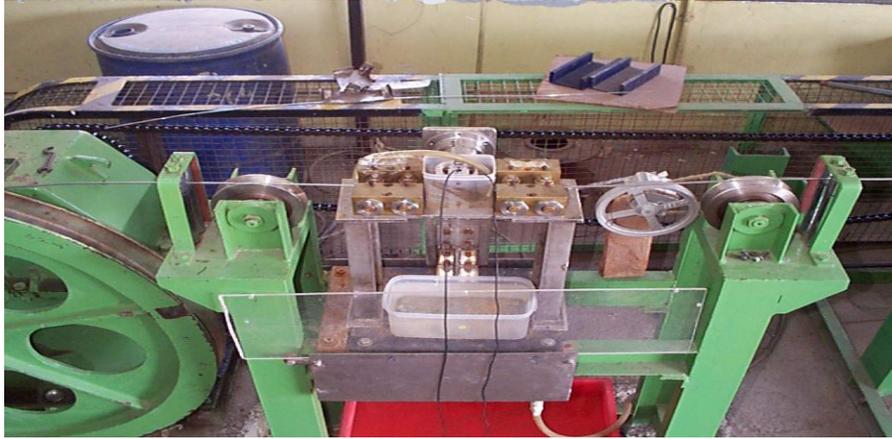
Fig.   An on-line UT system for continuous soldering unit
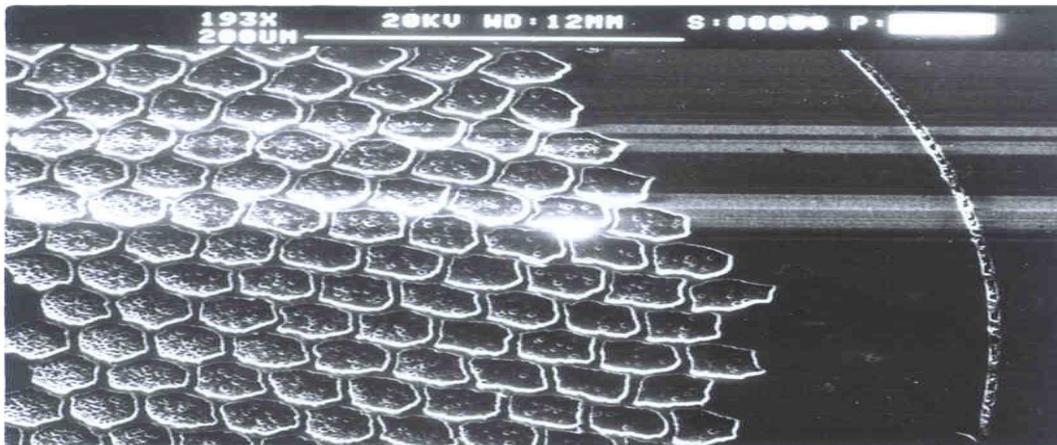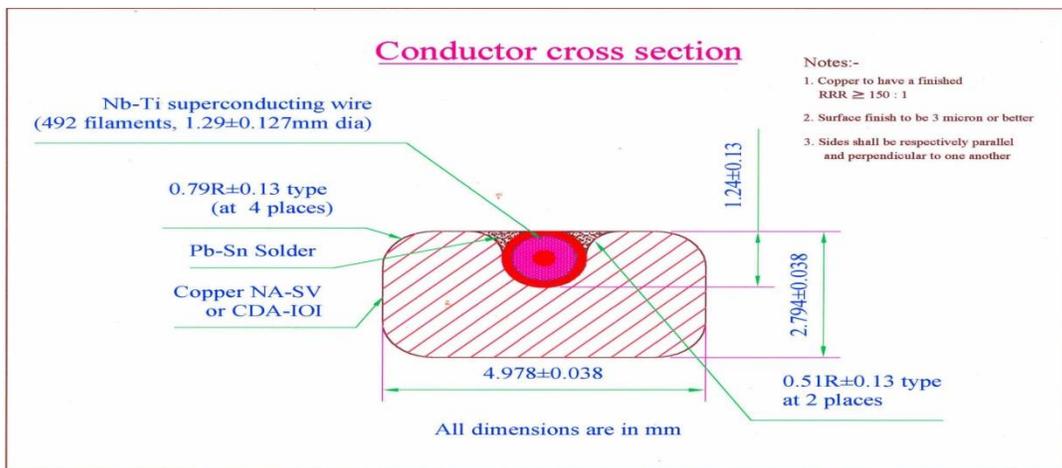
Fig.   SEM micrograph showing soldered cable section

Soldered Superconducting Wire
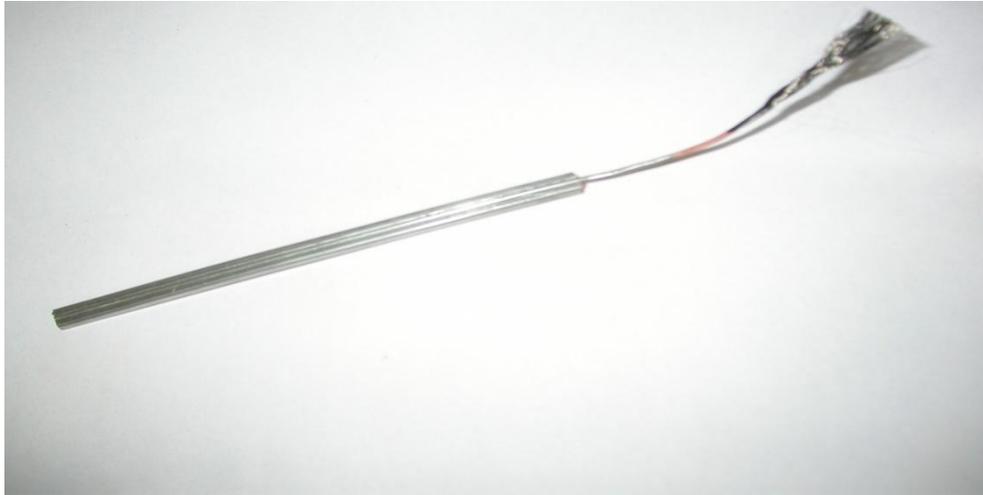
Summary of UT results for superconducting cable

Acceptance criteria

1) Continuous single flaw indication having length more than 8mm is not acceptable.

2) Cumulative length of flaw indications in any 100mm length shall not exceed 10mm.

Lot no.	Length (in M)	No. of flaw indications	No. of continuous indications	No. of unacceptable indications
3A	145	1	Nil	Nil
3B	185	8	Nil	Nil
4B	566	10	Nil	Nil

Flow Sheet for Continuous Soldering of   Nb-Ti Superconducting Wire

Wire and Channel

Degreasing

Pickling
(Pre-clean Soln)

Water rinsing with brush cleaning

Fluxing
Kester 645

Drying
(120 C)

On-line Hybrid Superconducting Cable-In-Conduit-Conductor (CICC) fabrication towards indigenous Fusion Programme

CICC fabrication consists of following stages:

- Fabrication of Nb-Ti strands of required configuration

- Cabling of Nb-Ti strands as well as copper wire

- Wrapping of final stage cable with SS304 Foil

- Jacketing of wrapped final stage cable using SS316LN tube

Thermo-nuclear Magnetically Confined Fusion

- Magnets system provide the basic magnetic bottle to keep the plasma confined.

- Superconducting Magnets provide steady state magnetic fields.

- In a Tokamak (a toroidal plasma confining device) the magnets aremade & placed in a such a manner that the magnetic fields are generated along the axis of the torous as well as in the plane perpendicular to it. These are called Toroidal Field Magnets and poloidal field magnets respectively.

STRAND FABRICATION

NbTi strand
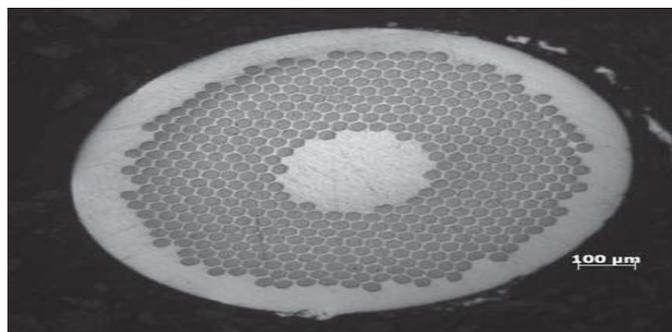
NbTi strand cross-section (0.8 mm) containing 492 filaments of 25 micron each. This strand has been used for 30 kA CICC
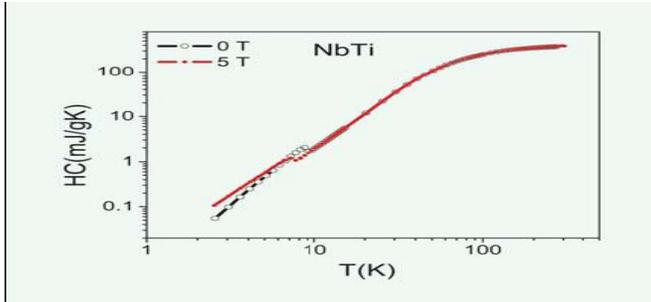
Second order phase transition (at 0 T and 5 T, the Tc can be seen) for 0.80mm dia SC strand.
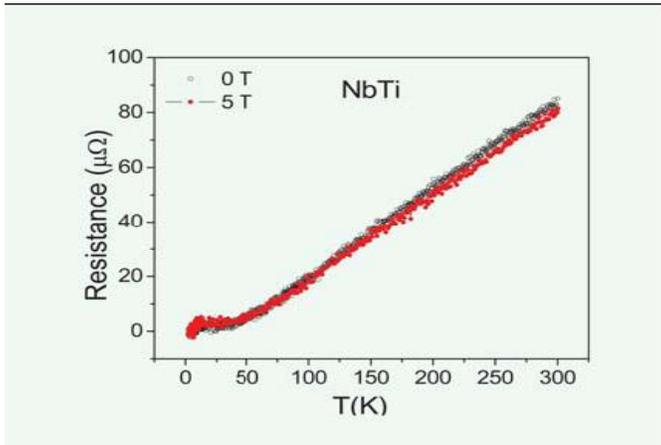
Resistance Drop with temperature (black: 0 T and red: 5 T)

CABLING TECHNOLOGY

Cabling scheme for 30kA hybrid conductor
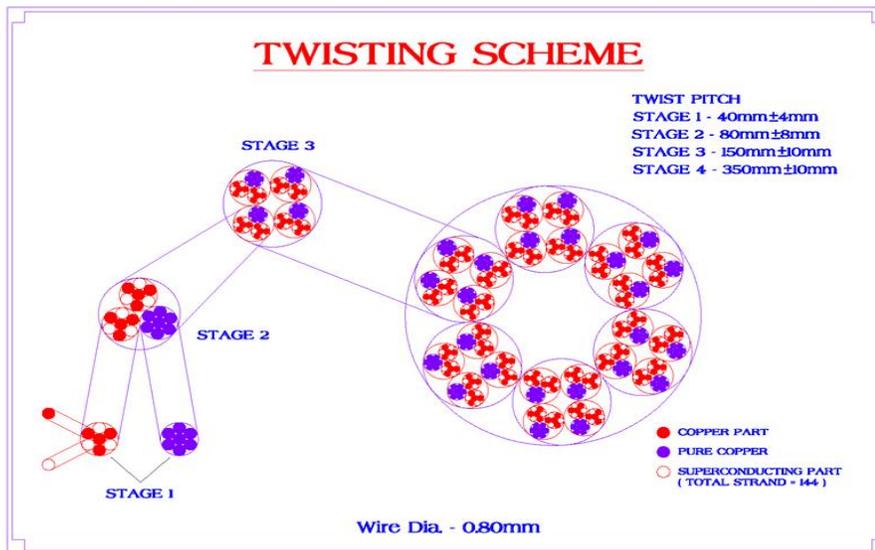
First Stage cablingFinal Stage cabling

Final Stage Cable Containing 504 wires of 0.8mm dia

Foil Wrapping

JACKETING

Fig: On-line CICC Fabrication Facility developed at AFD, BARC

Bending of CICC

100m long CICC on a bobbin

Total SC Wire – 14.4Km; 144Nos. Total OFHC Copper Wire – 52.80Km; 360Nos.

30mm X 30mm Square Cross Section Conductor

Results for 10kA CICC
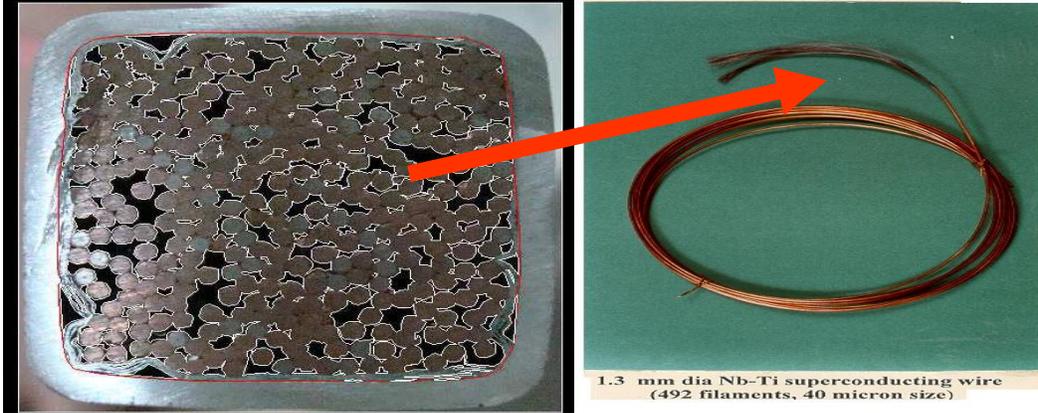
Cross section of 20x20mm CICC containing 336 wires of 0.8mm dia out of which 48 nos. are SC wires

- CICC developed at BARC have shown that 11000 A of current could be passed at 6 K against designed value of 10000 A at 4.5 K.

- This hybrid conductor has about 25% less superconductor compared to that of SST-I conductor.

Nb3Sn SUPERCONDUCTOR FABRICATION

Nb_3Sn Phase
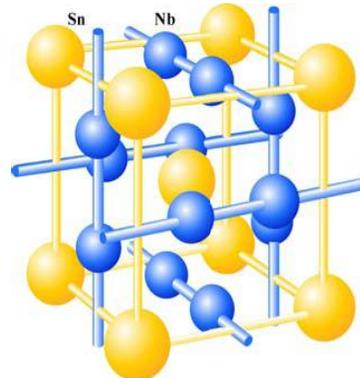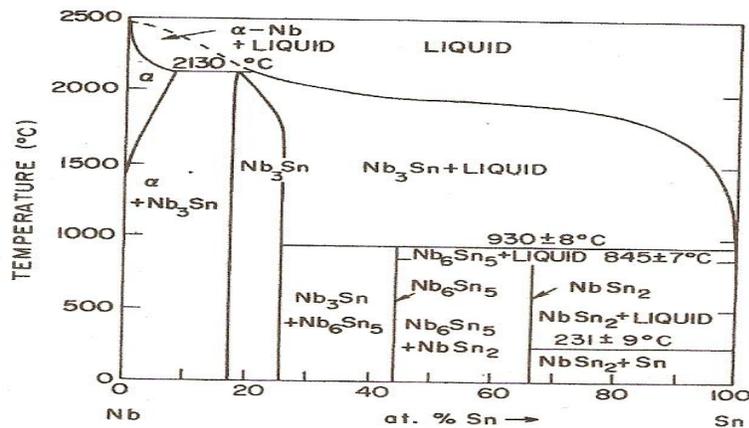
A15 Crystal Structure

Internal Tin process

This process was introduced to overcome the main limitation of tin content in bronze method.

A higher concentration of tin produces higher critical current densities in the Nb_3Sn layer.

The composite Cu tube containing several Nb rods around a central hole is first extruded, then filled with Sn and drawn into hexagonal sub-elements, which are cut into shorter lengths and reassembled into a new billet. The billet is then drawn to final wire size without intermediate annealing. Finished wire is reaction heat treated at 650 – 700 ^{o}C for several hours.
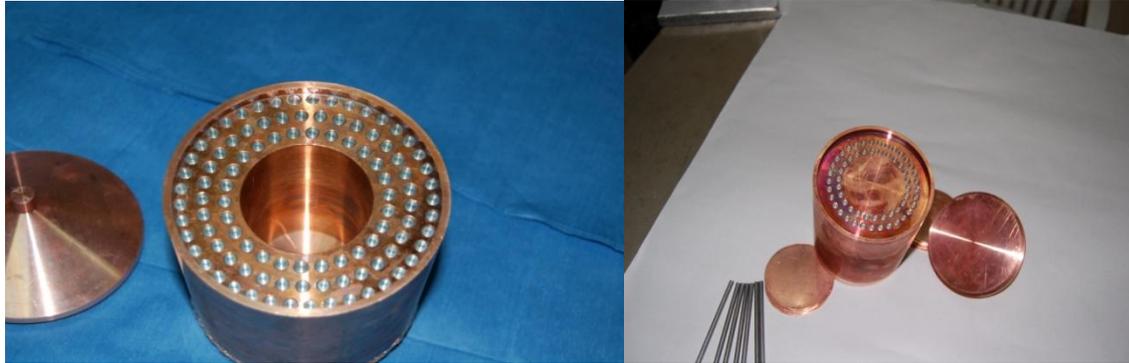
Billet Cross Section
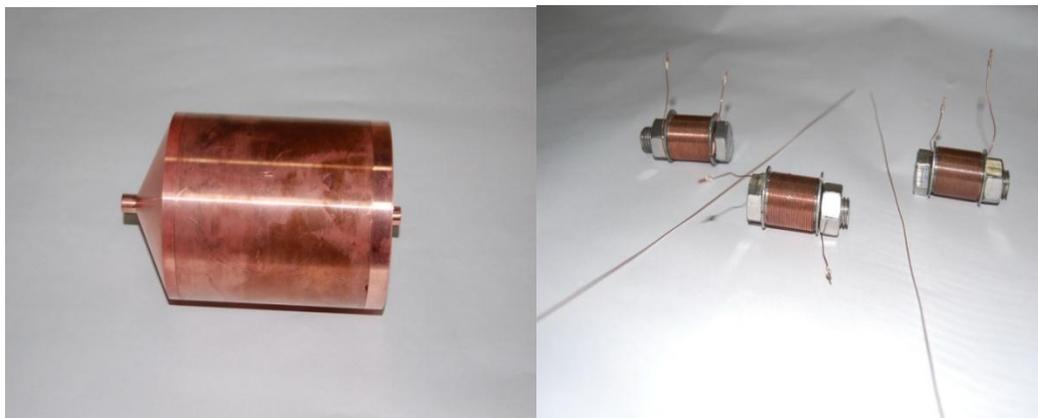
Assembled Extrusion BilletNb$_3$Sn wire samples on bobbin for reaction

heat treatment

Following samples were heat treated

- **59 filament Strand**

- **3589 filament Strand**

Heat Treatment:

200 ^{o}C/100 h followed by 650 ^{o}C

A- 160Hrs ;   C- 250Hrs

Comparison of micrographs before and after heat treatment

BEFORE HEAT TREATMENT   **AFTER HEAT TREATMENT**
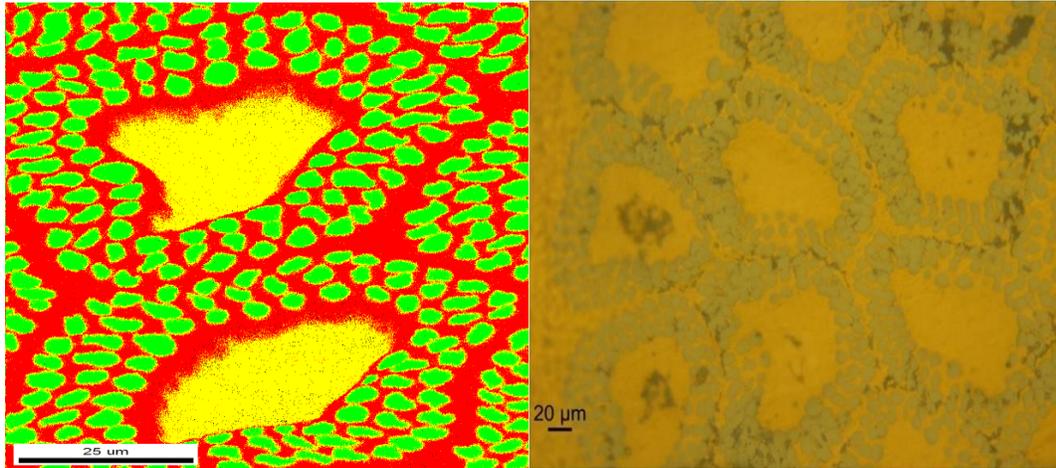
Cross section of 3589C sample
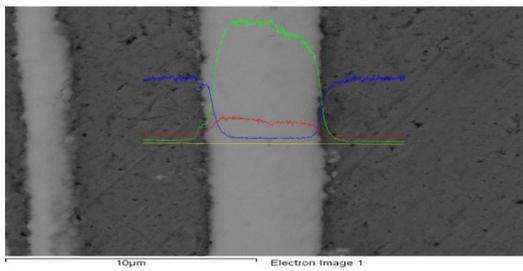
FEG-SEM Results

Sample: 3589C
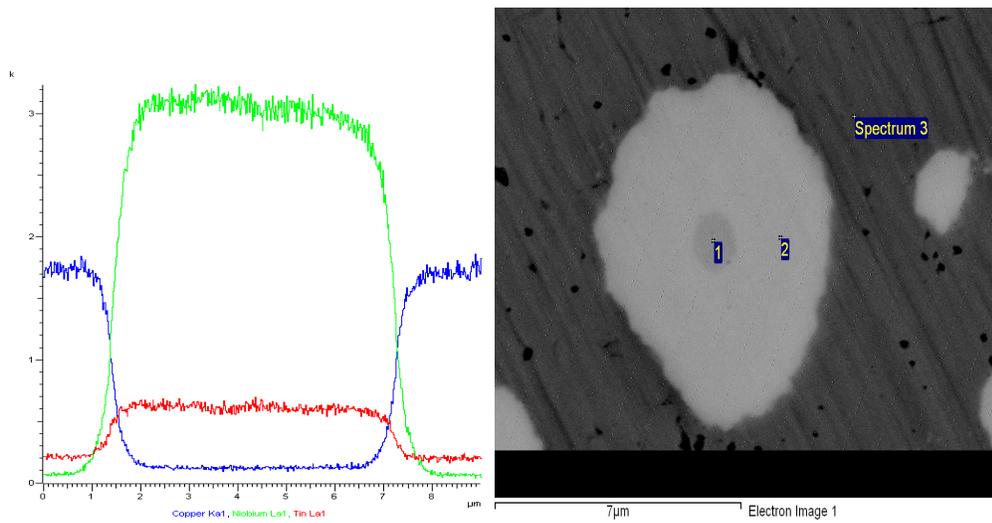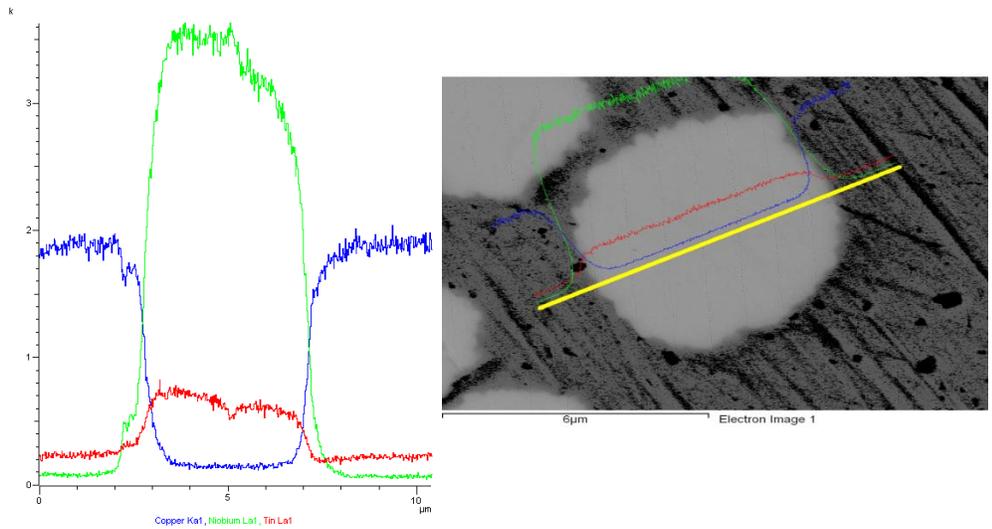
Spectrum	Cu	Nb	Sn
1	0.51	97.13	2.36
2	1.35	77.44	21.21
3	97.19		2.81

Grain Map 59A

RD

TD

Gray Scale Map Type:<none>

Color Coded Map Type: Confidence Index

	Min	Max	Total Fraction	Partition Fraction
	0.057	1.057	0.801	1.000

Boundaries: <none>
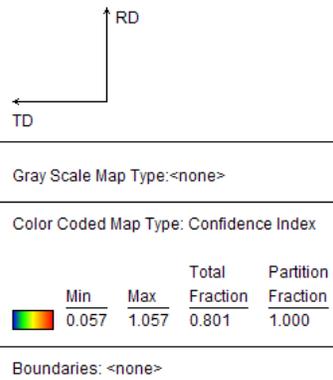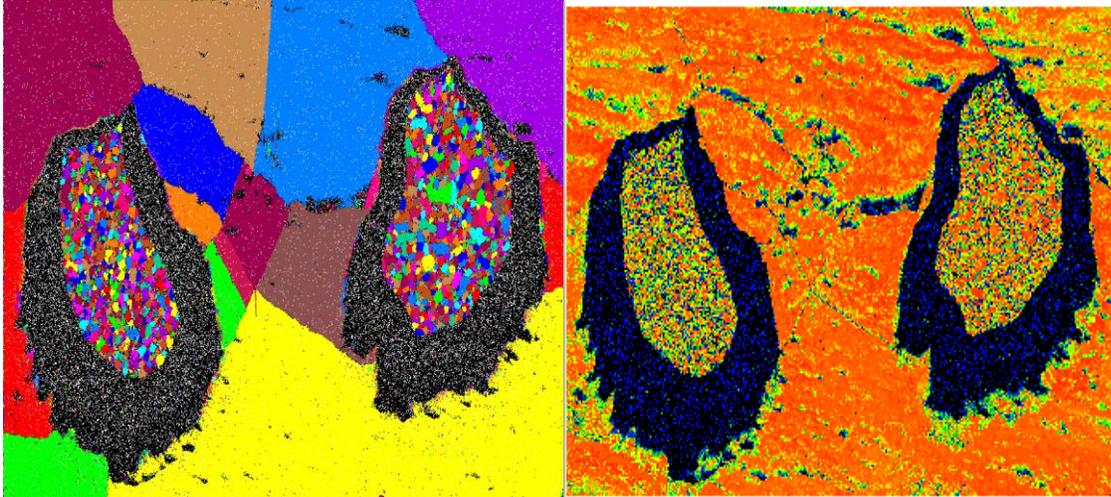
TEM Results

Sample: 3589C

1: <110>
2: <200>
3: <210>
4: <211>
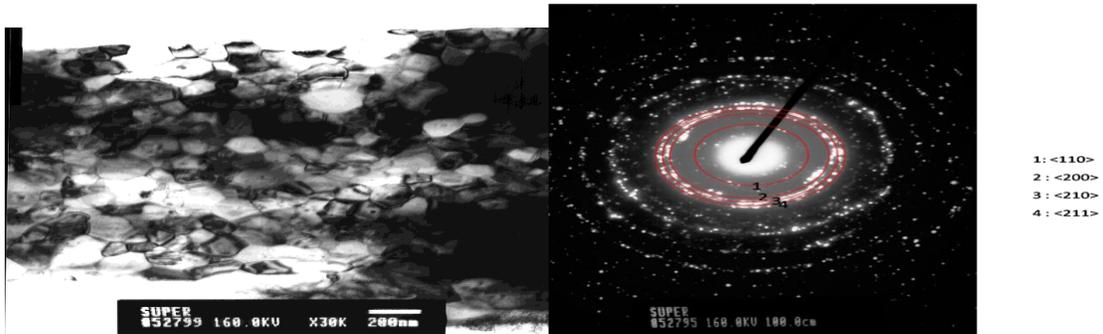
Application Areas   **Devices**

1. Physical research	Detection and beam handling in high energy physics, RF cavities for particle accelerators, High field for solid state physics
2. Measuring techniques	Superconducting electron microscope, Josephson

	junction as low field detectors and measuring oscillators
3. Energy technology	Superconducting eletric- generators (a.c. and d.c.), Superconducting magnetic energy storage system (SMES), Cryogenic power transmission, Fault limiter
4. Processing Technology	Magnetic ore separation, Particle accelerator for materials Investigation
5. Transportation	Levitation trains (MAGLEV), Electric motors for ship propulsion
6. Telecommunication and computing	RF telecommunication cable, Josephson junction for computer logic, Ultra-high-performance filters, E-bomb
7. Health	Particle accelerators for cancer therapy, MRI system and SQUID

Fig. Maglev test vehicle, 552 km/hr
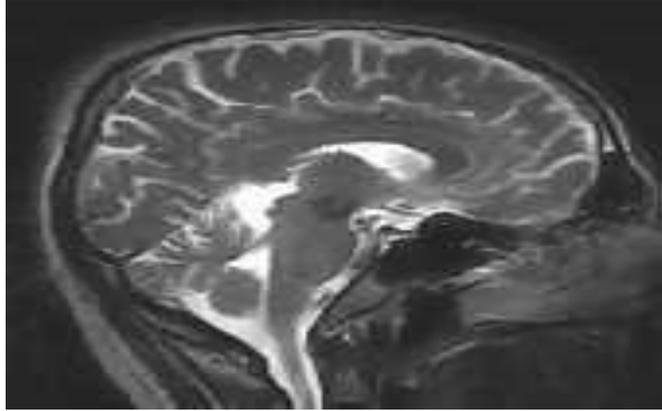
Fig.   MRI of a human skull

Comparison of electrospun CeO$_2$ and CuO/CeO$_2$ Nanofibers

D.B. Pal*[1], D.D. Giri[1],Harish Kumar[3],Pardeep Singh[2], P.K. Mishra[1]

[1] *Department of Chemical Engineering and Technology, Indian Institute of Technology, B.H.U.,Varanasi-221005, U.P., India,*

[2] *Department of Chemistry, Indian Institute of Technology, B.H.U., Varanasi- 221005, U.P., India*

[3] *Defense Research & Development Organization (DRDO), Jagdalpur, Chhattisgarh, India*

Abstract:

Synthesis of CeO$_2$ and Cu/CeO$_2$ nanofibers were electrospunned using Cu (CH$_3$COO)$_2$H$_2$O and Ce(NO$_3$)$_3$.6H$_2$O precursors, polyvinyl pyrrolidone fiber template and co-solvent mixture by volume 2/1 of C$_2$H$_5$OH/H$_2$O followed by thermal treatment (500°C, 3h). The fabricated nanofibers were characterized by SEM, XRD and FTIR for morphologies, structures, and functional group, respectively. We observed continuous line feature in CeO$_2$ nanofibers and Cu/CeO$_2$ with an average diameter of 125 nm, 98nm respectively and CeO$_2$ peaks were observed at 27.74°.

Key words: CeO$_2$, Cu/*CeO$_2$, electrospinning method, Nanofibers.*

1. INTRODUCTION

Cerium oxide (CeO$_2$) also known as ceric oxide, ceria or cerium dioxide is an oxide of the rare earth metal cerium. Ceria have pale yellow-whitish appearance and cubic fluorite crystal structure (MP 2400 ºC, density 7.215 gm/cc). The one-dimensional nanomaterials of ceria such as nanowires, nanobelts, nanoribbons, and nanorods, are a new class of nanomaterials that have been attracting a great research interest in the recent past [1-3].

CeO$_2$ have several applications e.g. electrolytes for solid oxide fuel cells [4, 5], abrasive materials for chemical mechanical planarization [6], catalysis, optical additive, cosmetic material [7, 8], UV protection , oxygen pumps, and automotive exhaust promoter [9]. Ceria is a key catalyst in CO oxidation [10], and low temperature water-gas shift reaction [11, 12].

The success of ceria in various applications is largely due to easy shift between Ce^{3+} and Ce^{4+} states and elevated oxygen transport capacity (OTC) [13]. However, pure CeO$_2$ have poor thermo-stability at high temperatures and loses its oxygen transport capacity [14]. The addition of other transition metal ions in the ceria cubic structure led to the formation of a defective fluorite-structured solid solution with novel properties to the materials e.g. better resistance to sintering, high OTC for various reactions and many other totally different catalytic behaviors [15]. There is an increased practical applications of nanocomposite metal oxides as the catalysts in organic synthesis [16]. Nanocomposites of CuO-CeO$_2$ have been used for the oxidation of CO and production of H$_2$-rich streams in water gas shift reaction [17].

In the present manuscript describes synthesis and characterization of cost effective ceria nanofibers and copper ceria nanofibers.

2. EXPERIMENTAL DETAILS

A. Preparation of the spinnable solution

The ceramic nanofiber of ceria has been prepared by electro-spinning sol solution containing an inorganic precursor and a solvent [18-22]. The sol-gel solution was prepared following Chaorong Li [23]. In brief, Polyvinyl pyrrolidone (1.2 g) was dissolved in 12mL 2:1 ethanol/water co-solvent by volume basis followed by addition of cerium nitrate hexa hydrate (0.434 g) and three or four drops of acetic acid. For preparation of composite $Cu-CeO_2$, copper acetate monohydrate (0.2g) was added in the above solution the solution was stirred at room temperature (6h) and loaded in syringe for electrospinning [24].

B. Electrospinning setup

Electrospinning is simple and widely used method for easy production of nanofiber. The electrospinning setup consists of a high voltage power supply, syringe pump, metallic needle and a conductive collector plate. The details of the set have been described elsewhere [20]. The basic schematic diagram of electrospinning setup is presented in Fig.1.
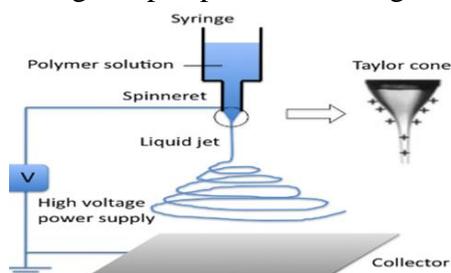
Fig.1**:** The Electrospinning setup

C. Electrospinning process

A polymer based sol-gel solution loaded into a 5mL syringe with blunt ended stainless steel needle (20-gauge) and syringe fitted in the syringe pump. The distance between needle tip and collector was adjusted to nine centimeter. The process was performed in ambient air at $25^{\circ}C$, relative humidity 65%, feeding rate 1 mLh^{-1} and applied positive high voltage of 13 kV between the needle tip and the collector. The moving accelerated jet from the needle converted into ultra thin fibers due to evaporation of solvents.

3. RESULTS & DISCUSSIONS

A. Scanning Electron Microscopy

The SEM analysis exhibited cylindrical nanofiber of varying diameter depending on PVP concentration. For 10% PVP solution diameter ranged between 80-125 nm for both CeO_2 and $Cu- CeO_2$ (Fig 2a, 2c). The diameter decreased about 30% after calcinations at $500^{\circ}C$ (Fig 2b, 2d). The occasional beads structures seen were most probably due to the viscoelastic relaxation or the work of surface tension upon partial discharge of the charged jet not dry enough before deposition on the collector plate.
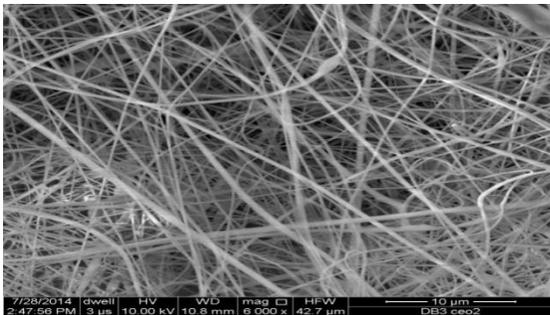
Fig. 2a: SEM analysis of CeO$_2$ nanofiber before calcinations, with 10% PVP and field strength 1.44 kV cm^{-1}.
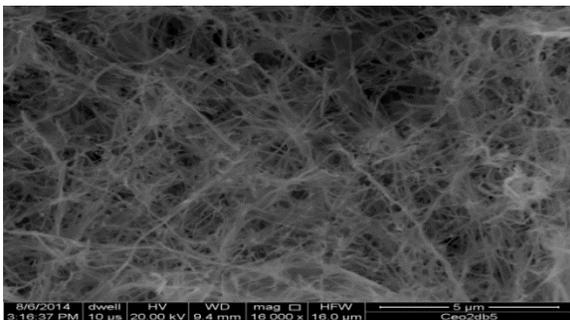
Fig. 2b: SEM analysis of CeO$_2$ nanofiber after calcinations with 10% PVP and field strength 1.44 kV cm^{-1}.
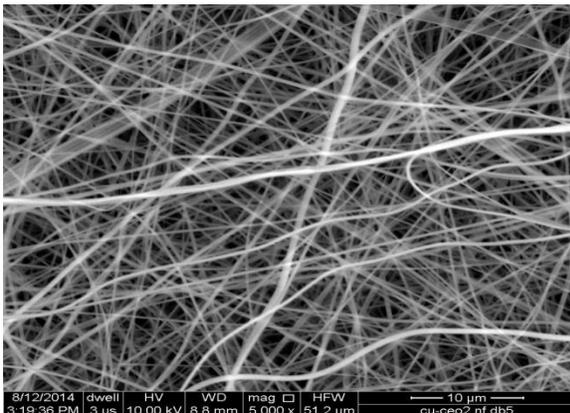
Fig .2c: SEM analysis of Cu-CeO$_2$ nanofiber before calcinations with 10% PVP and field strength 1.44 kV cm^{-1}.
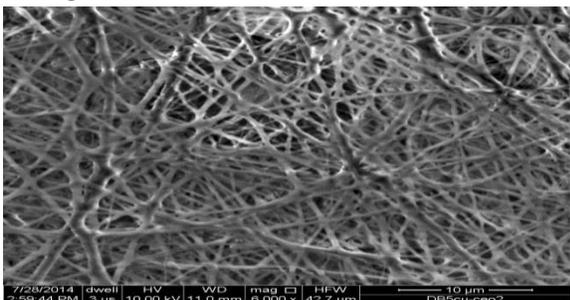
Fig .2d: SEM analysis of Cu-CeO$_2$ nanofiber after calcinations with 10% PVP and field strength 1.44 kV cm^{-1}.

B. X-Ray Diffraction Analysis

XRD data was recorded by 18KW rotating anode based powder diffract meter (Rigaku, Japan) fitted with a curved crystal monochromatic in the diffracted beam operating at 40KV and 150MA. Powder XRD data were collected in the two-theta range $10-80^0$ at scan rate of 2 degree/minute and scan step 0.02 degree. The diffraction patterns have been indexed by comparison with the JCPDS files. The XRD pattern of the CeO_2 and Cu/CeO_2 nanomaterial is presented in Fig.3a and Fig 3b respectively. The graph exhibit characteristic peaks of a fluorite-like cubic phase. The most intense reflections of CeO_2 at 2θ values of 46.83° are clearly visible and average crystalline size calculated by Debye Scherer formula around 10-14nm.
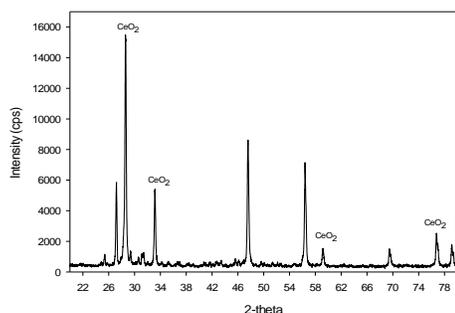
Fig.3a: XRD of CeO_2 nanofiber calcined at 500°C and prepared with 10% PVP and field strength 1.44 kV cm^{-1}.
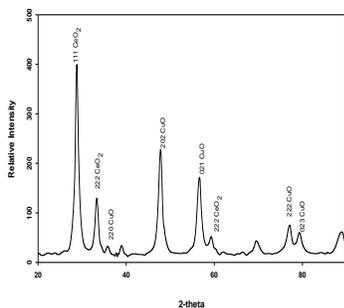
Fig. 3b: XRD of $Cu-CeO_2$ nanofiber calcined at 500°C, with 10% PVP and field strength 1.44 kV cm^{-1}.

C. Fourier Transforms Infrared Spectroscopy

The functional groups analysis of prepared nanofibers was identified by a FTIR analysis. Nanofiber mixed in KBr pellets was scanned in the range 400-1400 cm^{-1} for 16 times and spectrum was recorded. The FTIR spectra CeO_2 and Cu/CeO_2 nanomaterial is presented in Fig.4.
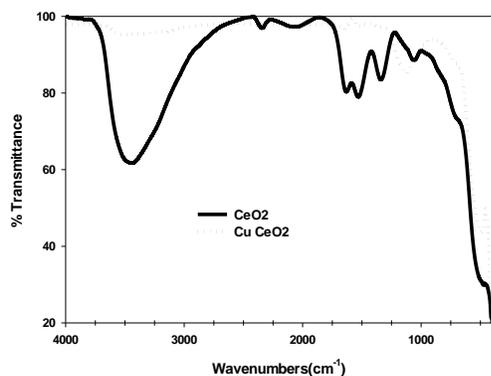
Fig.4: FTIRof CeO$_2$ and Cu-CeO$_2$ nanofiber calcined at 500°C and prepared with 10% PVP and field strength 1.44 kV cm^{-1}.

The broad band (3700 to 3000 cm^{-1}) was present due to the stretching vibration of hydroxyl (OH) of chemisorbed water. The disappearance of peak (900-1630 cm^{-1}) after calcinations of CeO$_2$ at 500°C denoting removal of most of the organic materials present in the sample. The significant enhancements in the absorption band (500-1060 cm-1) represent formation of CeO$_2$ nanofiber.

4. CONCLUSIONS

The electrospun nanofibers of CeO$_2$ andCu-CeO$_2$ in the average diameter range of 80 to 125 nm exhibit characteristic peaks of a fluorite-like cubic phase in the XRD analysis. The average crystalline size of calcined CeO$_2$and Cu/CeO$_2$ nanofiber were about 10-14nm in calculation of Debye Scherer formula.

ACKNOWLEDGEMENT

REFERENCES

[1] Yang A, Tao X M, Pang G K H and Siu K G G, J Am Ceram Soc **91(1)** (2008) 257.

[2] Panda P K and Ramakrishna S, J Mater Sci **42(6)** (2007) 2189.

[3] Kar S, and Chaudhuri S, J Phys Chem B **110(10)** (2006) 4542.

[4] Inaba H and Tagawa H, Solid State Ionics **83 (**1996) 1.

[5] Tullr H L and Nowick A S, J Electrochem Soc **122(2) (**1975) 255.

[6] Hoshino T, Kurata Y, Terasaki Y and Susa K, J Non-Cryst Solids **283 (**2001) 129.

[7] Bae D S, Lim B, Kin B I and Han K S, Mater Lett **56** (2002) 610.

[8] Tsuzuki T and Mccormick P, J Am Ceram Soc **84(7)** (2001) 1453.

[9] Lee J S, Lee J S and Choi S C, Mater Lett **59** (2005) 395.

[10] Monteiro RS, Dieguez LC and Schmal M, Catal Today **65** (2001) 77-89.

[11] Andreeva D, Idakiev V, Tabakova T, Bourlinos A, and Travlos A, Catal Today **72** (2002) 51-57.

[12] Andreeva D, Ivanov I, Ilieva L, and Abrashev M.V, Appl Catal A **302** (2006) 127-132.

[13] Jia LW, Shen MQ, Hao JJ, Rao T, and Wang J, J Alloys Compd **454** (2008) 321-326.

[14] Shen MQ, Wang JQ, Shang JC, An Y, Wang J, and Wang WL, J Phys Chem C **113** (2009) 1543-1551.

[15] Reddy BM, Khan A, Yamada Y, Kobayashi T, Loridant S, and Volta JC, J Phys Chem B **107** (2003) 5162-5167.

 [16] Samantaray S, Pradhan DK, Hota G, and Mishra BG, , Chem Eng J **193** (2012) 1-9.

[17] Razeghi A, Khodadadi A, Ziaie-Azad H, and Mortazavi Y, Chem Eng J **164** (2010) 214-220.

 [18] Yang X, Shao C, Liu Y, Mu R and Guan H, Thin Solid Films **478** (2005) 228-231

[19] Cui Q, Dong X and Wang J, J of Rare Earths **26** (2008) 664.

[20] Xu S, Sun D, Liu H, Wang X and Yan X, Catal Commun **12** (2011)514-518.

[21] Tang H, Sun H, Chen D and Jiao X, Mater Lett **77** (2012)7-9.

[22] Hwang A R, Park J and Yong C K, Bull. Korean. Chem. Soc. 32 (2011) 9.

[23] Li C, Chen R, Zhang X, Shu S, Xiong J, Zheng Y and Dong W, Mater Lett **65** (2011)1327-1330.

[24] Pal   D B, Kumar H, Giri D D, Singh P, Mishra P K,   Adv. Sci. Lett **20** (2014)1582-15.

Effect of ruthenium complex dye sensitizer on photo-conversion efficiency of ZnO nanoparticles based dye sensitized solar cells

Padmini Pandey, Mohammad Ramzan Parra and Fozia Z. Haque*

Optical Nanomaterials Lab, Department of Physics,

Maulana Azad National Institute of Technology, Bhopal 462051, India

Corresponding author. E-mail address: foziazia@rediffmail.com

(Mobile No. +919300687943)

ABSTRACT

In this study, we report on an insight into the influential factor of the photo-conversion efficiency of ZnO-based dye sensitizedsolar cells. ZnO nanoparticles were prepared via simple and cost effective sol gel technique. Crystallographic analysis was done using X-ray diffraction, followed by morphology determination through scanning electron microscopy and transmission electron microscopy instruments. Dye-sensitization was achieved by immersing ZnO nanoparticles based photoelectrodes into different ruthenium based dye solutions. Further dye-sensitized electrodes were assembled in typical sandwich-type cells. It has been found that DSSC made with N719 dye is the most efficient with current density (J_{sc}) 5.92mA/cm^2 and photo-conversion efficiency (η) of approximately 1.7% compared to the other dyes. Such ZnO nanoparticles with ruthenium dyes resulted in significant improvement of the device performance. This work would explore feasible routes to synthesize efficient metal-oxide nanoparticles for opto-electronic or other related applications.

Keywords: ZnO, nanoparticles, dye sensitized solar cell, photo-conversion efficiency.

1. Introduction

As a clean solar-to-electricity conversion system, dye-sensitized solar cells (DSSCs) are considered viable substitutes to the conventional silicon-based photovoltaic devices since the pioneering work reported by O'Regan and Grätzel [1], and then attracted much more attention due to its low cost and simple fabrication process [2, 3]. The porous electrode in DSSC is crucial and the overall energy conversion efficiency strongly depends on its surface and electronic properties [4]. Recently metal oxide nanostructure electrodes have been of interest for potential applications in many fields of technologies, such as electric transistors [5], photovoltaic devices [6-8] and sensors [9, 10].

Among the various semiconductor oxides, ZnO with bandgap of ~3.37eV and high excitonic binding energy (60meV) [11-13] should be an alternative electrode material for the DSSCs due to its electronic properties similar to TiO$_2$. The properties of ZnO depend on its morphology and microstructure. Application of ZnO in solar cells as an optoelectronic material makes it essential to have control on its size, shape and microstructure [14]. There are various methods available to form ZnO nanostructures from either physical or chemical method. The fabrication costs of the chemical routes which include hydrothermal, chemical bath deposition and sol-gel method are lower than those of physical routes. The advantages of sol-gel method are larger area and feasible to form various ZnO nanostructures with excellent physical properties [15]. In addition sol-gel method allows the hybridization of inorganic, organic and metallic materials at low-temperature [16]. Studies have shown that the surface of ZnO nanocrystals can play an important role in carrier transport.

Compared with organic dyes, inorganic metal complex dyes have high thermal and chemical stability. Among these complexes, polypyridyl ruthenium sensitizers were widely used and investigated for their high stability and outstanding redox properties and good response to natural visible sunlight. The sensitizers anchored on the surface of semiconductor film electrode with carboxylate or phosphonate group enable the electron injection into the conduction band of the semiconductor. Most well-known Ru complexes for DSCs are N3, N719, N749 and Z907. N3 has two bipyridine and two thiocyanato (NCS) ligands. It absorbs up to 800 nm radiation due to loosely attached NCS groups, even though the dye provides high J_{sc} (short circuit current), it does not give high V_{oc} (open circuit voltage). N719 dye has the same structure as N3 dye but has TBA^+ (tetrabutylammonium) instead of H^+ at two carboxyl groups. The difference in V_{oc} is rationalized as due to the difference in proton concentrations at the surfaces. Since N3 dye can provide at most four protons per dye, which can absorb at the basic sites of the metal oxide surface and shift the E_{cb} (conduction-band-edge energy level) to positive.

In this article, we systematically investigated the effect of ruthenium complex dye sensitizers such as N3, N719 and Z907 on power conversion efficiency of ZnO nanoparticles based DSSCs.

2. Experimental Details

2.1. Synthesis of ZnO nanoparticles

Zinc acetate dihydrate $[Zn(CH_3COO)_2.2H_2O]$ (0.2M) of AR grade having 99.99% purity procured from Sigma Aldrich, used as starting material, dissolved in 75ml ethanol and resulting solution was stirred continuously. Tartaric acid was added dropwise to the solution until a thick, white gel was obtained with pH 3. The gels was slowly dried for several hours and calcined at 500°C for 3 hours in the muffle furnace. The as-synthesized ZnO nanoparticles were further subjected to characterization in terms of its morphological and structural properties analysis, followed by the study of its optical properties.

2.2. Fabrication of dye sensitized solar cell

Doctor-blade technique was adopted to prepare the porous electrodes on Fluorinated tin oxide (FTO, 15 Ω cm^{-2}, Solaronix SA, Switzerland), which were rinsed ultrasonically in acetone, ethanol and distilled water for 15min, respectively. Paste of ZnO nanoparticles was prepared by grinding the samples with acetylacetone and DI water with a subsequent addition of a small amount of Triton X-100. The resulting pastes were dropped onto one large area FTO glass with adhesive tapes (Scotch, approximately 3μm) served as spacers, and spread evenly using a glass rod. After drying in the air the films were then annealed at 500^{0}C for 1 h. Dye-sensitization was achieved by immersing the electrodes into (0.5mM) cis-bis (isothiocyanato) bis (2,2'-bipyridyl-4,4'-dicarboxylato) ruthenium (II) (N3) dye, di-tetrabutylammonium cis-bis (isothiocyanato) bis (2,2'-bipyridyl-4,4'-dicarboxylato) ruthenium (II) (N719) dye and cis-bis(isothiocyanato) (2,2'-bipyridyl-4,4'-dicarboxylato) (4,4'-dinonyl-2'-bipyridyl) ruthenium (II) (Z907) dye procured from Solaronix SA, Switzerland, followed byrinsing in ethanol and drying. The dye-sensitized electrodes were assembled in typical sandwich-type cells; the identical Pt counter-electrodes were placed over the dye-sensitized working electrodes, and the electrolyte (Iodolyte AN-50, Solaronix SA), containing 50mM tri-iodide and 0.5M 4-tert-Butylpyridine in anhydrous acetonitrile was sandwiched between the photoanode and the counter electrode by the firm press in both the cases.

2.3. Characterizations

The X-ray diffraction (XRD) data was collected through Bruker D8 Advance X-ray diffractrometer with CuK$_\alpha$ radiation operating at 40 kV and 40 mA and a position sensitive detector (Lyn xEye) based on Bruker AXS compound silicon strip technology was used. Scanning has been performed from 20º to

80° 2θ range. Diffraction peaks of the crystalline phase were compared with those of the standard compound reported in the JCPDS data files No. 361451. The morphology of the sample was determined using Scanning electron microscopy (SEM) JEOL-JSM-6390 and Transmission Electron Microscopy (TEM) TECNAI G2. The sample was prepared by dispersing the drop of colloid on the copper grid, covered with the carbon film and the solvent was evaporated. The photoresponse of DSSC prototypes was measured with a solar simulator (91545 Newport, USA) equipped with an AM1.5G filter, where the light energy was adjusted with calibrated Si solar cell (Newport-69907), for approximating one-sun light intensity (100mW/cm^2). A Computer-controlled Keithley-2420 source meter was employed to collect the current density-voltage curves.

3. Results and Discussion

3.1. Determination of lattice parameters from XRD

XRD can be utilized to evaluate peak broadening with crystallite size and lattice strain due to dislocation. The crystallite size of as-synthesized ZnO nanoparticles was determined by the X-ray line broadening method using the Scherrer equation:

$$D = \frac{k\lambda}{\beta_{hkl}cos\theta} \ldots\ldots\ldots\ldots\ldots\ldots (1)$$

where D is the crystallite size in nanometers, λ is the wavelength of the radiation (1.54056 Å for CuK$_\alpha$ radiation), k is a constant equal to 0.94, β_{hkl} is the full width at half-maximum intensity and θ is the scattering angle. The breadth of the Bragg peak is a combination of both instrument- and sample dependent effects. The instrument-corrected broadening β_{hkl} corresponding to the diffraction peak of ZnO was estimated using the relation:

$$[\beta_{hkl}^2 = \beta_{hkl\,(measured)}^2 - \beta_{hkl\,(instrumental)}^2]\ldots\ldots\ldots\ldots\ldots\ldots (2)$$

XRD patterns of ZnO have been depicted in figure 1. The analysis of the diffraction peaks revealed the presence of hexagonal wurtzite structure of pure ZnO with lattice constants a = b = 3.234Å, c = 5.281Å. The peaks observed in XRD pattern are well indexed to pure hexagonal wurtzite-phase ZnO (JCPDS Card, No. 361451). No other diffraction peaks are detected except ZnO peaks, which indicate the presence of ZnO nanocrystals without any amorphous component.
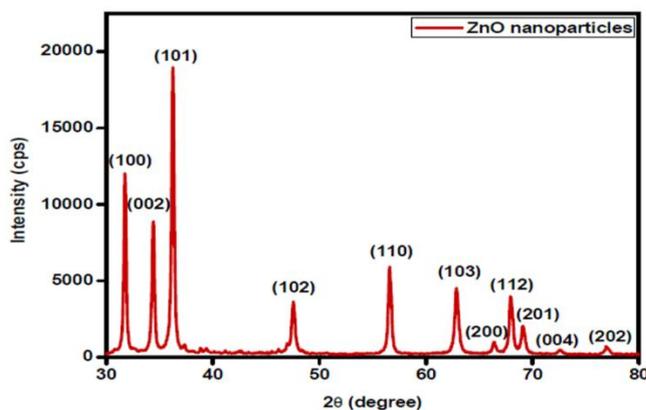
Figure 1: X-Ray Diffraction pattern of ZnO nanoparticles

3.2. Scanning and Transmission Electron Microscopic analysis

Surface structure plays an important role in determining the structural and optical properties of nanomaterials. Accordingly, SEM and TEM studies were carried out and these have been depicted in figure 2. SEM micrograph shows the presence of nanoparticles with certain agglomeration for as-

synthesized ZnO (figure 2a). Figure 2b shows the TEM image of ZnO nanoparticles. Diffraction rings corresponding to (100), (101), (102), (110) and (112) planes were observed in selected-area electron diffraction (SAED) pattern, revealing the highly crystalline nature of these nanoparticles. Particle sizes observed from TEM measurement is in range of 40nm, this result is in good agreement with the XRD result.
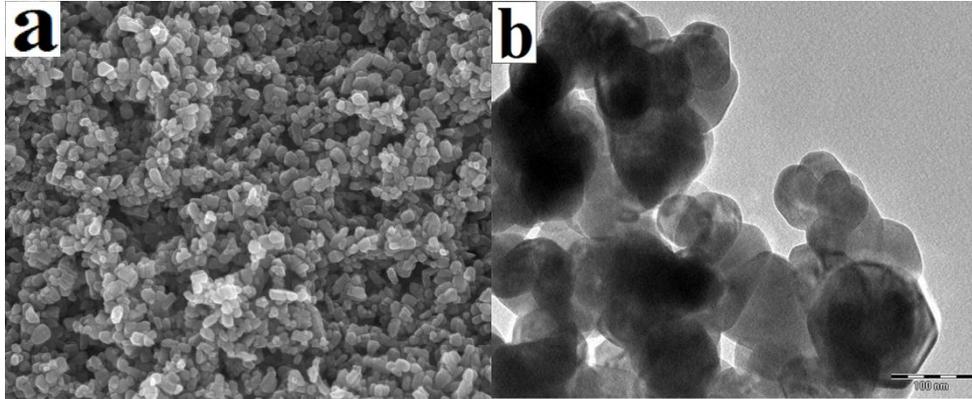
Figure 2: (a) Scanning electron microscopic image and (b) Transmission electron microscopic image of as-synthesized ZnO nanoparticles

3.3. *Photovoltaic performance of ZnO nanoparticles*

The photocurrent density-voltage (J–V) characteristics of dye sensitized solar cells (DSSCs) fabricated by using ZnO nanoparticles based photoanode under 100 mW/cm^2 light illumination, are shown in figure 3. The fill factor of DSSCs was calculated by using the following equation:

$$F = \frac{I_{max} \times V_{max}}{V_{oc} \times I_{sc}} \dots \dots \dots \dots \dots \dots (3)$$

Where I_{max} and V_{max} are the maximum current and voltage obtained, respectively, at the maximum power point on the photovoltaic power output curve. The solar conversion efficiency (η) was calculated by the following equation:

$$\eta = \frac{V_{oc} \times J_{sc} \times FF}{P_{in}} \dots \dots \dots \dots (4)$$

where J_{sc} is the short-circuit current density, V_{oc} is the open-circuit voltage, FF is the fill-factor and P_{in} is the incident light power.

All the data from the J-V curves are summarized in 'Table 1'. From the J–V curves under light illumination, it was found that the cell sensitized with N719 dye showed the largest area of the current–density curve, indicating that this cell generated the highest output power.
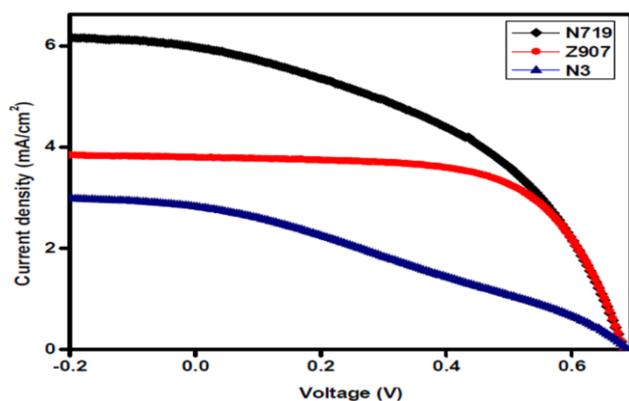
Figure 3: Photocurrent density-voltage (*J–V*) curves of DSSCs for ZnO nanoparticles based photoanode with different sensitizers under 100 mW/cm^2 light illumination.

Meanwhile, the cell utilizing the N3 dye showed the smallest area of the current–density curve, generating the lowest power. However, it was noticeable that the J–V curve areas of the cells were not much different, leading to small differences in the photovoltaic parameters. From the table, it can be seen that the DSSC with N719 dye performed with the highest J_{sc} and η. Meanwhile, the device sensitized with the N3 demonstrated the lowest J_{sc} and η. This leads to more electrons being injected from N719 dye molecules to the conduction band of ZnO upon light illumination, resulting in an enhancement of the photovoltaic parameters of the cell such as J_{sc} and η.

Table 1: Photovoltaic parameters of the ZnO nanoparticles based DSSCs with various dyes.

Dye	V_{oc} (V)	J_{sc} (mA/cm^2)	Maximum Power P_{max} (mW)	Fill factor (FF %)	Efficiency (η%)
N719	0.64	5.92	0.42	44.94	1.70
Z907	0.57	3.15	0.33	62.22	1.20
N3	0.76	2.83	0.16	29.90	0.64

Conclusion

ZnO nanoparticles as photovoltaic material in DSSCs was successfully prepared via simple and cost effective sol-gel method and utilized in solar cell sensitized with N719, N3 and Z907 dyes. The cells sensitized with N719 and Z907 dye demonstrated the best photovoltaic performance compared with the cell sensitized with N3 dye. The cell sensitized with N719 dye performed at the highest short-circuit density, J_{sc} of 5.92 mA/cm^2 and power conversion efficiency η of 1.70%. Further research needs to be carried out to find a dye that will absorb light ina broader visible region, thus enhancing the performance of the cell.

Acknowledgments

for kindly providing the experimental facilities for dye sensitized solar cell fabrication and device testing.

References
[1] Regan B O and Grätzel M, *Nature* 353 (1991) 737.
[2] Chiba Y, Islam A, Watanabe Y, Komiya R, Koide N and Han L Y, *Jpn J Appl Phys* 45 (2006) L638.
[3] Wang Z S, Yanagida M, Sayama K and Sugihara H, *Chem Mater* 18 (2006) 2912.
[4] Grätzel M, *J Photochem Photobiol* C 4 (2003) 145.
[5] Heo Y W, Tien L C, Kwon Y, Norton D P, Pearton S J, Kang B S, Ren F and Roche J R La, *Appl Phys Lett* 85 (2004) 2274.
[6] Martinson A B F, Elam J W, Hupp J T and Pellin M J, *Nano Lett* 7 (8) (2007) 2183.
[7] Nayeri F D, Soleimani E A and Salehi F, *Renew Energ* 60 (2013) 246.
[8] Meng Y, Lin Y, Lin Y, *Ceram Int* 40 (2014) 1693.
[9] Xu J, Zhang Y, Chen Y, Xiang Q, Pan Q and Shi L, *Mater Sci Eng* B 150 (1) (2008) 55.
[10] Zhang H, Du N, Chen B, Li D and Yang D, *Sci Adv Mater* 1 (2009) 13.
[11] Parra M R and Haque F Z, *Optik* 125 (2014) 4629.
[12] Pandey P, Singh N and Haque F Z, *Optik* 124 (2013) 1188.
[13] Haque F Z, Singh N, Pandey P and Parra M R, *Optik* 124 (2013) 4167.
[14] Baxter B, Walker A M, Ommering K Van and Aydil E S, *Nanotechnol* 17 (2006) S304.
[15] Chen Z, Li X X, Chen N, Wang H, Du G P and Suen Andy Y M, *J Sol-Gel Sci Technol* 62 (2012) 252.
[16] Prastomo N, Muto H, Sakai M and Matsuda A, *Mater Sci Eng* B 173 (2010) 99.

Study of graphite oxide reinforced nitrile rubber composite as insulating material for solid propellant rocket motor

Sriniwas Panda[*], Lakshmikanth, Nirmal C, Samir Kumar Das, Mathew Daniel, S S Manna

Vikram Sarabhai Space Centre, Thiruvananthapuram-695022, India

Corresponding Author:

SRINIWAS PANDA ,SCIENTIST/ENGINEER "SE",QDPC/QGCP/QRPG/SR,VSSC/ISRO, TRIVANDRUM,

KERALA-695022

Email: skynsrinu@gmail.com. Sriniwas_panda@vssc.gov.in

Phone: 09037949989 (M), 0471-2563386 (O)

Abstract

Materials used as insulators for solid rocket motors usually are identified by a hybrid name that identifies a filler or reinforcement material in a matrix or binder. Elastomers find widespread use as matrix or binder in insulators. Composites of NBR (Copolymer of Acrylonitrile and Butadiene Rubber) & EPDM (Ethylene Propylene Diene Methylene) rubbers with various reinforcing fillers are most commonly used as insulating materials for space applications. The present paper deals with the evaluation of rheological, physical, mechanical, thermal, interface and electrical properties of NBR based graphite oxide (GO) reinforced rubber composites based on NBR containing different concentrations of GO along with silica.

Improvement in heat of ablation, decrease in erosion rate and increase in electrical conductivity is observed on incorporation of GO to NBR-silica composite. Other rheological, physical, mechanical, thermal and interface properties of the composite meets the requirement of conventional insulation material.

Keywords:NBR, EPDM, GO, interface properties

1 Introduction

Acrylonitrile butadiene rubber (NBR) composites find widespread use as insulating material in solid propellant rocket motors for Indian space and defense applications [1]. Silica is used as reinforcing filler in the NBR matrix composite along with other additives like plasticizers, cure accelerators, cure activators, cure catalyst and curing agent. An attempt is made in the present study to incorporate graphite oxide (GO) as additional filler along with silica to improve the thermal and electrical properties without deteriorating other physical, mechanical and interface properties [2].

2 Experimental

2.1 Materials

Acrylonitrile butadiene rubber (acrylonitrile content 30%), supplied by JSR Co Ltd, Japan. Industrial grade graphite oxide was purchased from Ander Labs, Mumbai and named as "GO". All other raw materials (process aids, plasticizer, cure catalyst, activators, curing agents) used after evaluation of

required properties are from identified sources.The typical composition of NBR based insulation system is given in Table-1.

Table 1: Composition of NBR based insulation system

Ingedient	Phr
NBR	100
Reinforcing filler	10-80
Vulcanizing agent	0.5-5.0
Cure activator	2-15
Plasticizer/ processing aid	5-30
Cure accelerator	0-5
GO	0.5-10

Nomenclature of the composites is made based on the concentration of fillers (silica and GO). The composites identification is given in Table-2.

Table 2: Composite identification

Composite	Name
NBR+50 phr Silica (without GO)	A1
NBR+ 50 phr Silica + 1 phr GO	A2
NBR+ 50 phr Silica + 2.5 phr GO	A3
NBR+ 50 phr Silica +5 phr GO	A4
NBR+ 50 phr Silica + 2.5 phr GO (Solution method)	A5
NBR+30phr Silica + 5 phr GO (Solution method)	A6
NBR+30phr Silica+ 5 phr GO+10 phr HTPB	A7

2.2 Mixing and Vulcanization

Rubber compounding was carried out in an open two roll mill under identical conditions of time, temperature, rotor speed and sequence of mixing of all ingredients. Curing was carried out at 145 ^{0}C for 30 minutes under identical pressure by compression molding. These cure sheets were then conditioned before testing (24 hour maturation under AC condition). In solution mixing method, the required phr of GO and a small amount of NBR was dispersed in suitable solvents. The mixture was dried and used for preparing the composite by mixing in open two roll mill.

3 Results and Discussion

Rheological, physical, mechanical, thermal and interface properties achieved for the best composite [A3] compared to conventional insulation composite [A1] is given in Table-3

Table 3: Comparison of properties of A4 composite and A1 composite

Property	A3	A1	Requirement
Cure time(min) (from Rheogram)	8.19	6.44	---
Tensile strength (ksc)	164	168	100 minimum
Elongation (%)	1275	1354	600 minimum
Density (g/cc)	1.18	1.19	1.17-1.21
Heat of ablation (cal/g)	3742	3250	---
Erosion rate (mm/s)	0.14	0.15	0.20 maximum
Thermal conductivity (cal/cm/g/^{0}C)	6.45×10^{-4}	6.10×10^{-4}	6.5×10^{-4} maximum
Specific heat (cal/cm/g/^{0}C)	0.46	0.42	0.35 minimum
Residue after TGA upto 800^{0}C under N_2 atmosphere (%)	30.47	34.48	---
Electrical volume resistivity (Ω. cm)	1.14×10^{12}	5.73×10^{15}	---
Rubber to metal peel strength (kg/cm)	10.5	11.0	5.0 minimum

4 Conclusions

The new NBR composite with 50 phr silica and 2.5 phr graphite oxide [A3] has shown higher heat of ablation & lower erosion rate and volume resistivity without deteriorating other required physical, mechanical, thermal and interface properties. These improvements in properties can help in reduction of net insulation requirement for a motor and hence improvement in payload mass of launch vehicle.

5. References

[1] Solid rocket motor internal insulation, *NASA* December, 1976, NASA SP-8093.

[2] Ahmed, Ashraf Fathy, and Suong V. Hoa. "Thermal insulation by heat resistant polymers for solid rocket motor insulation." *Journal of Composite Materials* 46.13 (2012): 1549-1559.

An Investigation into Genesis of Surface Cracks in TMT Reinforcement Bars

B Singh, M Deepa, G Sahoo and A Saxena.

R&D Centre for Iron and Steel, Steel Authority of India Limited,Ranchi, Jharkhand, India

E-mail: bsingh@sail-rdcis.com

ABSTRACT

TMT bars used for concrete reinforcement are produced through TMCP route. Due to partial quenching and auto tempering the bars acquire a microstructural gradient across the diameter consisting of tempered marensite near to the surface and bainite/ ferrte-pearlite microstructures in the subsequent layers. In spite of conforming to the specifications, the reinforcement bar, sometimes contain surface defects such as longitudinal surface cracks. In the present investigation, such a defect visible on the bar surface has been analyzed through optical microscopy, scanning electron microscopy using EDS and microhardness measurements. The observations identified the presence of adherent iron oxide layer entrapped within the crack. Along one side of the crack, a decarburized layer was also observed which most probably developed due to carbon depletion during reheating a pre-existing defect in the input material, i.e. 100x100 mm^2 continuous cast billets. Such defects in continuous cast billets usually occur in the heats having high superheat giving rise to reheating cracks or a deep blow hole in the billet. The crack gets oxidized during reheating the billets in furnace forming a hard oxide layer which at later stage on rolling the billets to reinforcement bars manifests as rolled-in scale. Thus, the imperfection running parallel to the rod axis appears like a crack after the billet is rolled to reinforcement bar in the last stand where rib pattern is inscribed.

Key words: TMT rebars, reinforcement wire rods, surface defects, TMCP.

1.0 INTRODUCTION

TMT bars used for concrete reinforcement are produced through thermo-mechanical controlled processing (TMCP) route which consists of partial quenching of bar diameter just after finish rolling the billets between 1000-950°C. Subsequently, the bars are cut to required lengths and allowed to cool on cooling beds. During the cooling process, heat retained within the core helps in tempering the martensite formed on the bar surface due to high pressure water quenching. Simultaneously, the core transforms to equilibrium transformation products such as ferrite, pearlite and/or bainite. This results in developing a composite microstructural gradient across the diameter, leaving the harder surface around a ductile core. In order to ascertain the product quality the bar surface is inspected to identify the surface defects, if any. However, many a times surface defects such as longitudinal cracks, blow holes, under cuts, scratch marks, etc. are observed on the bar surface, which are identified in the mill or at the customer's end [1, 2]. Under such circumstances the material is rejected, incurring monetary losses to the producer as well as the user. In this paper attempt has been made to present an investigation carried out to identify the cause of formation of a longitudinal crack on the surface of TMT bar produced at Durgapur Steel Plant. The investigation consisted of determination of chemical composition, visual inspection of surface, microstructural evaluation, measurement of micro-hardness, and elemental analysis within and around the defect through energy dispersive spectroscopy (EDS). The results are presented in the following sections.

2.0 EXPERIMENTAL

2.1 Material

The present investigation was carried out on 16 mm diameter reinforcement rod/ bar which was hot rolled from 100x100 mm^2 billets through TMCP route. Mechanical property-wise as well as chemistry-wise the bar conformed to Fe-500 grade as stipulated in IS:1786-2008 specification. As observed at the customer's end the reinforcement rod contained a surface crack running parallel to the bar length as shown in Fig.1. The chemical composition of the reinforcing steel under investigation was assessed through optical emission spectroscopy (OES) with a view to verify the grade of reinforcement rod and elements present in the steel.

Fig. 1 TMT rebar with a parallel surface crack
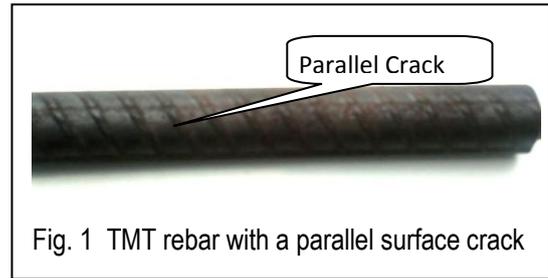
2.2 Optical Metallography

In order to examine the microstructure and characteristics of the surface crack a disc specimen of height about 15 mm was cut from the rod in transverse direction and polished in usual manner on grinding wheel and using alumina suspension. The specimen after final polishing was etched with 2% nital solution to reveal the microstructure. Polished surface was observed under Olympus optical microscope in both the un-etched as well as the etched conditions. Additionally, the etched specimen was photographed at low magnification for examining different microstructural zones present across the diameter and also the shape and size of pre-existing crack (Fig.2).

Fig.2 Cross-section of TMT rebar showing tempered martensitic rim and the core
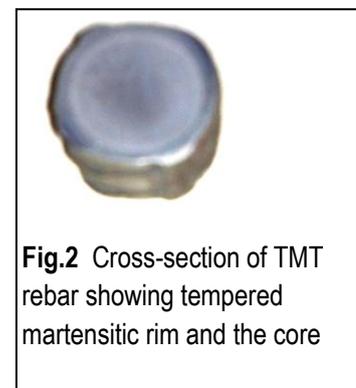
2.3 Microhardness

Microhardness was measured under Litz-MM6 microhardness tester on both sides of the crack as well as beyond the crack at different locations along the crack length using 100 gm weight. This would help to study the characteristics of the crack formed during manufacturing the bar.

2.4 SEM - Electron Dispersive Spectroscopy

The polished specimen prior to etching was examined under EVO MA-10 scanning electron microscope through electron dispersive spectroscopy (EDS) technique to analyze elemental composition of material, in particular, oxides present within the crack.

3.0 RESULTS AND DISCUSSION

3.1 Chemical Composition

The chemical composition as determined through OES is given in Table-1. It is observed from the table that various elements present in the defective rebar are within the specified range conforming the reinforcement to Fe-500 grade, (IS:1786-2008) specification.

Table-1 Chemical composition of TMT rebar

	C	Si	Mn	P	S
TMT bar having surface crack	0.22	0.32	0.92	0.014	0.014
Specified for Fe 500 grade (IS:1786-2008)	0.25 max	-	-	0.40 max	0.40 max

3.2 Visual Inspection

The 16 mm diameter reinforcement rod was inspected visually wherein a longitudinal/ parallel crack of about 1.0 mm opening was observed as shown in Fig.1. On examining the polished and subsequently etched specimen at low magnification three different microstructural zones could be seen as depicted in Fig.2. These zones were identified later under optical microscope as tempered martensitic rim and combinations of bainite with ferrite-pearlite morphologies. Presence of this type of microstructural gradient across the diameter confirmed the bar under investigation as belonging to TMT grade.

3.3 Microstructure

The microstructure of TMT bar was observed under optical microscope after etching the polished specimen with 2% nital solution. The structure was examined near to the crack in the martensitic rim zone as well as the central core of the TMT bar. As per the observations peripheral layers contained tempered martensitic structure of thickness about 2.0 mm followed by another zone of bainite microconstituent of similar thickness. The central core, however consisted of ferrite-pearlite microstructures with some amount of bainite (Fig.4). It may also be seen from Fig.3 that a crack of about 2-3 mm depth is distinctly visible. On examining the microstructure carefully around the crack it was revealed that upper side of the crack is decarburized while the other side has microstructure similar to the one present in rest of the tempered martensitic zone. This implied that the decarburized part was exposed to atmosphere during reheating the input material, i.e. the billet. It is also observed from Fig.5(a-c) that the crack contains a grayish colour layer adequately adherent to both sides of the crack. The layer has been identified as iron oxide through SEM-EDS analysis presented at later stage in this paper.
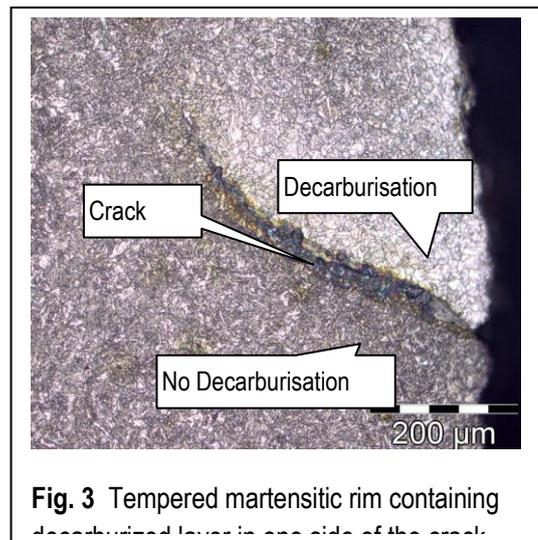
Fig. 3 Tempered martensitic rim containing decarburized layer in one side of the crack

Fig. 4 Ferrite+pearlite+bainite
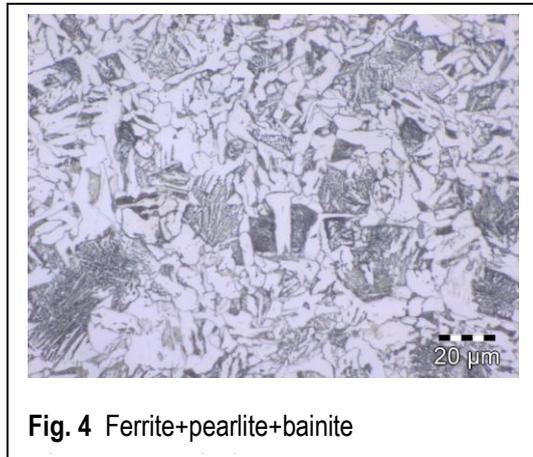
Fig. 5 (a-c) The crack containing iron oxide layer with coherent interface
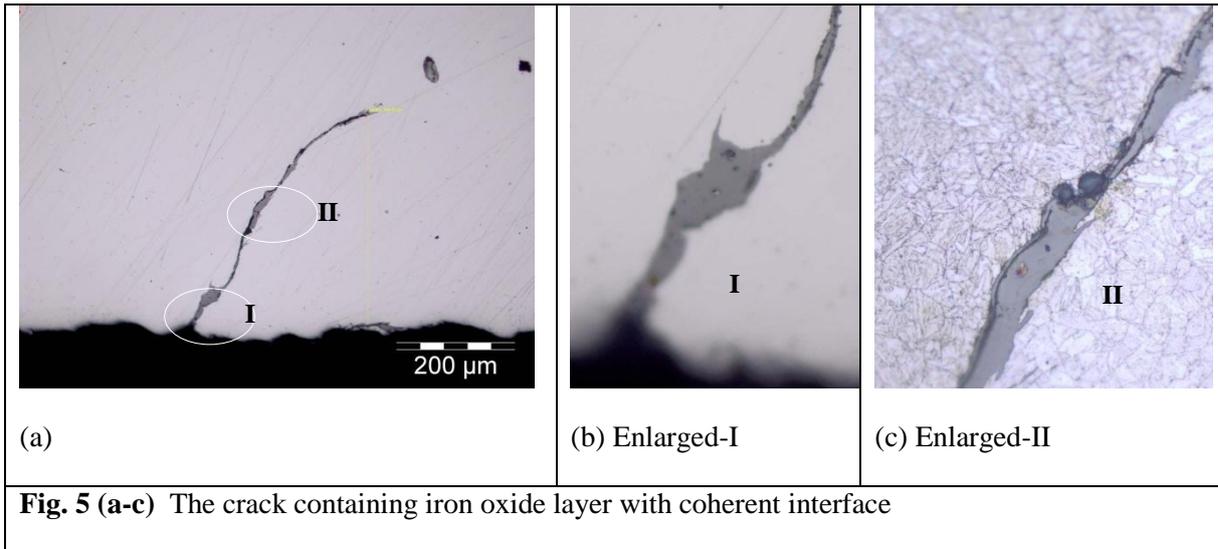
3.4 SEM-EDS analysis

In order to identify the composition of material present within the crack, EDS analysis was carried out in SEM. As shown in Fig.6 point analysis revealed presence of rich concentrations of Fe and O elements in the layer suggesting iron oxide (FeO) as the bearing material within the crack. Moreover, presence of iron oxide with coherent interface indicates that the oxide layer was present at this location prior to rolling the billets into rebars. This observation therefore helps in strengthening the fact that the crack has not originated by rupturing the surface but folding two surfaces together. This may happen during rolling process when material passes through rolling stands having different sizes and shapes.

3.5 Microhardness

In order to support occurrence of decarburization that has taken place along the crack, micro-hardness was measured along both sides of the crack as well as away from the crack. The locations of indentations obtained on the sample are shown in **Fig.7** and the values are given in **Table-2**. It may be observed from the table that average hardness value on right side of the crack (244 VHN) is lower than the left side (265 VHN). This may occur due to presence of softer phases designated by decarburization. However, both the values are still lower than the values away from the crack in tempered martensitic zone, i.e. 293 VHN. Thus, the difference in average hardness on both sides of the crack supported the optical microscopic observation of decarburized layer seen along the crack length in Fig.3. As stated earlier the possible reason of carbon depletion and formation of decarburized layer along the crack seems to be due to exposure of the surface to high temperatures during reheating of billets.

Element	Wt%	Atomic%
O K		22.00

Fig 7 Location of indentations for micro-hardness measurement
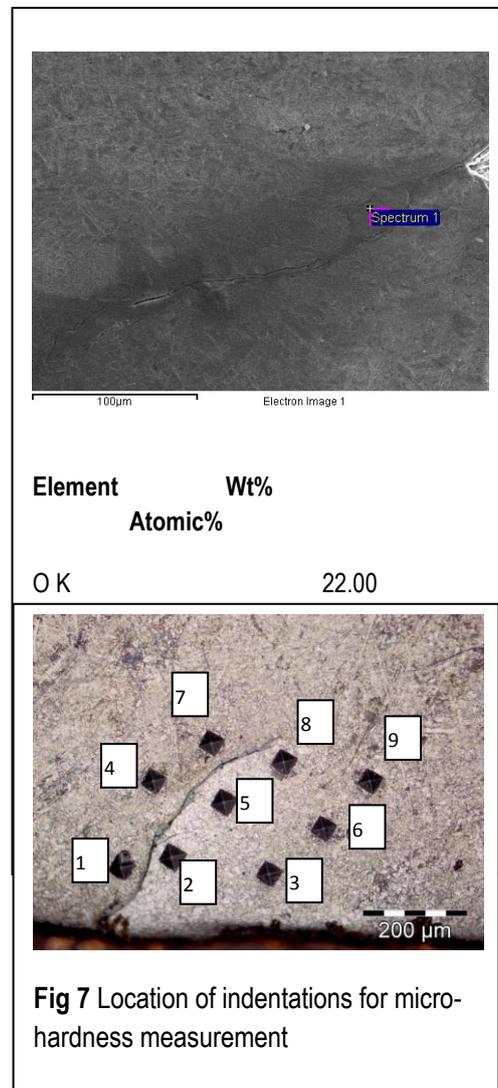
Table-2 Micro-hardness values along the crack and away from the crack

	Micro-Hardness Values (VHN)			Average Hardness
Left Side	250 (Location-1)	272 (Location-4)	273 (Location-7)	265
Right Side (decarburized)	232 (Location-2)	233 (Location-5)	268 (Location-8)	244
Away from Crack	274 (Location-3)	304 (Location-6)	300 (Location-9)	293

The results obtained through optical microscopy, energy dispersive spectroscopy (EDS) and hardness measurements along the crack helped in inferring that the crack containing adherent FeO layer with one side metal decarburized was formed most probably due to folding of two surfaces during rolling the billets into reinforcement bars or presence of imperfections in the input material. As decarburization has also been observed in one side of the crack, pre-existing defect in billets seems to be more probable to generate longitudinal crack in the bar. The defects such as heating cracks and deep blow holes in continuous cast billets usually occur in heats having high super heat. The cracks/ imperfections thus formed in billets get oxidized during reheating the billets in furnace forming a hard oxide layer which at later stage on rolling the billets to reinforcement bars manifests as rolled-in scale. Although, minor cracks if present in the material get welded during rolling due to heavy deformations imparted at high temperatures. However, in case a pre-existing oxide layer gets sandwiched between two surfaces it hinders welding as iron oxide is harder than the plastic metal at rolling temperatures of about 950ºC. Thus, the imperfection running parallel to the rod axis appears like a crack after the billet is rolled to reinforcement bar in the last stand where rib pattern is inscribed.

3.0 CONCLUSIONS

• The amounts of various elements in the 16 mm diameter TMT rebar were found within the specified ranges. Therefore the steel conformed to Fe-500 grade TMT reinforcement bar as per IS:1786 specification.

• The rebar consisted of a rim of tempered martensite near to the surface and ferrite+pearlite+bainite microstructures within the central regions of the cross section.

• The crack running parallel to the bar axis contained iron oxide (FeO) having coherent interface with the parent metal.

• The parent metal in one side of the crack was decarburized while other side contained microstructure similar to that of the tempered martensitic zone.

• Average micro-hardness of the decarburized layer present on one side of the crack was observed to be 244 VHN, while on the other side the value found to be 265 VHN. Tempered martensitic rim on other locations was observed to have micro-hardness of 293 VHN away from the crack.

• Based on the characteristics of adherent iron oxide present within the crack and also decarburization in one side of the crack helped in inferring that the imperfection/ crack was developed not because of material rupturing but due to pre-existing defect in the input material, i.e. continuous cast billets of 100x100 mm^2 cross-section.

REFERENCES

1. Minimization of surface defects on bars and wire rod originated in billet casting. By Cristian Genzano et al.; Paper presented in the 34th International Conference held during 19-21 May 2003 at Belo Horizonte, Brazil.

2. Study and Minimization of Surface Defects on Bars and Wire Rod Originated in Continuous Cast Billets. By Dinesh Dekate, B.D. Deshmukh and Sarang Khedkar. Paper published in the International Journal of Modern Engineering Research (IJMER) www.ijmer.com Vol.3, Issue.2, March-April, 2013, pp-736-738; ISSN: 2249-6645.

Effect of Titanium and Boron Addition on High Temperature

Dry Sliding Wear Behaviour of A356 Alloy

M. S. Prabhudev1, V. Auradi2, V. Bharath3, K. Venkateswarlu4 and S. A. Kori5

1Department of Mechanical Engg, Government Polytechnic, Kalgi-585 312, Karnataka, India

2bDepartment of Mechanical Engg, Siddaganga Institute of Technology, Tumkur- 572 103, Karnataka, India

3CSIR-National Aerospace Laboratory, Bangalore-560 017, Karnataka, India

4Department of Mechanical Engg, Basaveshwar Engg College, Bagalkot-587 102, Karnataka, India

In the present paper, effect of additions of Titanium (Ti) and Boron (B) content in theform of master alloys on the high temperature dry sliding wear behaviour for A356 alloy hasbeen reported. Alloy composition, normal pressures and sliding distances on A356 alloy atconstant temperature of 300oC was also studied. The cast alloys and worn surfaces werecharacterized by SEM/EDX microanalysis. The results indicate that, the wear rate of A356 alloyincreases with increase in normal pressures and sliding distances in all the cases and decreaseswhen Ti and B are added to A356 alloy. The decrease in wear rate after addition of Ti and B ismainly due to changes in microstructure which lead to improvement in mechanical properties. Afurther, worn surface study indicates that, the formation of iron-rich oxide layer between themating surfaces during sliding improves sliding wear performance.

***Corresponding author:** Tel./fax: +919449381159, E-mail: prabhudevms@yahoo.com or kori.shivu@gmail.com

1. Introduction

Dry sliding performance at high temperature is a critical problem in many industrial sectors, inwhich formation of oxide layers controls friction and wears [1]. Advancement of technology, ledto the increased use of Aluminium (Al) alloys in industries [2]. A356 (Al-7%Si) is one of theimportant alloy finds wide applications in automotive, marine, aerospace, automotive sectors andgeneral engineering industries possessing excellent properties such as good fluidity, lowcoefficient of thermal expansion, high strength-to-weight ratio and good corrosion resistance [3].The dry sliding wear performance of A356 (Al-7%Si) depends on a number of mechanical

properties such as hardness, ultimate tensile strength and ductility and microstructural propertieslike shape and size of Alpha Aluminium (_-Al) dendrites and morphology of eutectic silicon inaddition to load, speed, temperature and counter face, etc [3, 5]. It is a common practice thatmechanical properties of these alloys were improved by subjecting to suitable melt treatmentssuch as grain refinement, modification, addition of cover fluxes & mould vibration etc [4].Thewear performance of eutectic, hypoeutectic and hypereutectic Al-Si alloys at room temperaturewas reported by [5] and improvements in wear properties which are mainly due tomicrostructural changes.

Kori and Chandrashekariah [6] have investigated the room temperature dry sliding behaviour ofgrain refined and modified hypoeutectic Al-Si (Al-0.2, 2 and 7Si) alloys and reported that wearresistance is improved with the addition of (Al-Ti-B) grain refiner and Al-Sr modifier to the melteither individually or in combined addition of both. They also suggested that the combinedaddition of grain refiner and modifier to Al-7Si shows a better wear resistance than individualadditions. Prasad Rao et al. [7] have investigated the effect of grain size of Al and dendritic armspacing (DAS) of _-Al in Al-7Si alloy on

wear behaviour of Al and Al-7Si alloys under drysliding condition. Al-7Si alloy was grain refined using various grain refiners such as Al-1Ti-3B,Al-3Ti and Al-3B, while Al was grain refined with Al-5Ti-1B master alloy. It was reported thatthe wear rate decreases with the decrease in the grain size and DAS of Al and Al-7Si alloysrespectively. The results suggested that wear properties are not dependent on the type of grainrefiner used but depend on grain size/DAS of the metal and alloys.

From the literature review it is clear that, limited/no information is available on high temperaturedry sliding wear and friction behaviour of A356 alloy with and without the addition of grainrefiner. Some of the high temperature applications include pistons, cylinder heads and blocks forcar engines where temperatures above 200-300°C can be expected [8-11]. Therefore, in thepresent investigation attempt has been made to study the effect of Titanium and Boron (added inthe form of master alloy) additions on the high temperature wear behaviour of A356 alloy andalso to investigate the possible wear mechanisms involved at varying wear parameters.

2. Materials and Methods

2.1. Specimen preparation for wear

Melting of the charge was carried out at 720oC in an electric resistance furnace under a coverflux containing NaCl, KCl and NaF. To expel all the absorbed gases, degassing of the melt isdone using C2Cl6 in tablet form. To incorporate Ti and B into the melt, Al-3Ti and Al-3B masteralloy are used. Chips of Al-3Ti and Al-3B master alloy packed in Al foil were added to liquid Al.

Manual Stirring of the melt is carried out with zirconia coated steel rod after Ti and B addition.Two castings at different times of 0 and 5 min. were produced by pouring liquid Al in to mouldhaving dimensions of 12.5mm dia and 125 mm height. From these castings of wear specimens ofdimensions 10mm dia and 32mm length (ASTM G99) were machined [12]. Compositionalanalysis of the alloys used in the present study was done using spectrometer (model Varian AA-240, Netherlands) which is given in Table 1.

Table 1 showing chemical composition of pure Al, base alloy, Al-3Ti and Al-3B master alloy

2.2. Dry sliding wear experiments

Wear studies were performed using pin-on-disc high temperature wear testing machine attachedwith information acquirement system. During wear tests specimens were positioned in colletwhich is clamped to the holder. Wear specimen is mounted on to the disc with weight.Measurement of roughness of the surface is done using SJ-201 tester (Make: Mitutoyo, Japan)and was lying between 0.30-0.72 μm. En-32 steel disc of dimensions 165mm and 8mm thick,with roughness value of 0.47 – 0.87 μm and with hardness of HRc61was used in the presentwork. In order to maintain dry sliding conditions both wear specimens and steel disc weretreated with emery papers, acetone before every test. Further, the Pin-On Disc machine used forwear studies has a loading capacity of 200N and tests were conducted with a track dia. of 90mm.

Weight loss method is adopted to study the wear behaviour and weight of the wear specimenbefore and after each test was measured using balance with an accuracy of 0.0001g. A sensor isused for measuring frictional force. Wear behavior of A356 alloy before and after addition of Ti,B was studied at various applied normal pressures and sliding distances at a constant temperatureof 300oC. For every specimen three tests were conducted and average value is reported.SEM/EDX was used for characterization of the wear specimens before and after the test and withand without addition of Ti and B.

Alloy

Composition

Composition (in wt.%)

Si Cu Mg Fe Ti Mn Zn B Pb Al

Al 0.11 - - 0.18 - - - - - Rest

A356 6.95 0.11 0.29 0.51 0.24 0.32 0.11 - 0.2 Rest

Al-3Ti 0.15 - - 0.20 2.98 - - - - Rest

Al-3B 0.15 - - 0.16 - - - 2.83 - Rest

3. Results and Discussions

3.1. Effect of normal pressures

The effect of varying normal pressures (0.143, 0.286, 0.429, 0.572, 0.716 and 0.858N/mm2) onthe wear rate of A356 alloy under constant sliding distance of 1696.460m and at constant slidingspeed of 1.884m/s is shown in Fig.1. From the figure it is clear that, wear rate of A356 alloyincreases with increase in normal pressures in all the cases studied and the wear rate is higher incase of untreated alloy. The increasing trend is as per basic wear law. It is also clear from thefigure that addition of 0.60% of Al-3B grain refiner to A356 alloy has resulted in minimum wearrate as compared to the 0.65% Al-3Ti and in an untreated condition. This is due to the change inmicrostructure of A356 alloy resulting from conversion of coarse columnar dendrites to equiaxeddendrites with grain refiners which results in increased hardness, strength and ductility values ofA356 alloy. Figure 1b shows the effect of normal pressures on the frictional force of A356 alloy,it is clear that higher frictional force was observed in case of as cast alloy due to its softness.Because of which, there is an intimate contact of specimen with the rotating disc leading toincrease in the values of frictional force. The present results suggest that, the frictional forcedecreases with grain refined, Al-3Ti, Al-3B additions to A356 alloy in order.Fig.1 (a) Shows effect of normal pressure on the wear rate of commercial A356 alloy (b) Showseffect of normal pressure on the frictional force of commercial A356 alloy
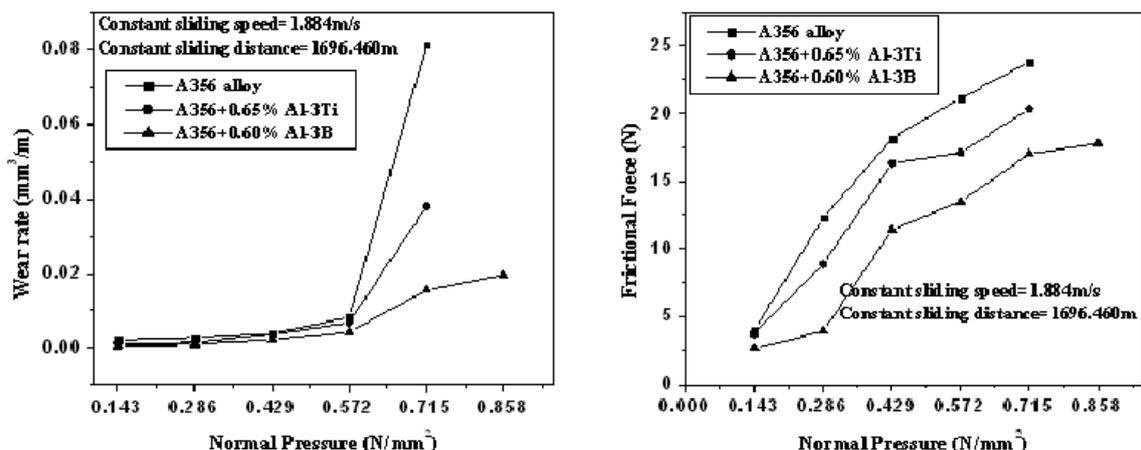
3.2 Effect of sliding distances

The effect of grain refinement of A356 alloy on the wear rate under different sliding distances(565.486, 1130.973, 1696.460, 2261.94 and 3392.92m) under constant normal pressure(0.716N/mm2) and at constant sliding speed (1.884m/s) are shown in Fig. 2(a). The wear

rate(expressed as volume loss) increases with increasing sliding distances in all the cases studied.Similar kind of increasing trend is observed by previous researchers at higher temperatures foraluminium alloys [8]. Also this could be due to the fact that, volume loss is directly proportionalto sliding distances as per basic wear equation. It is commonly known that with increasingsliding distances, the volume loss increases due to more intimate contact time between thecontact surfaces of the sample pin and with the counterface. However, less wear rate (volumeloss) was observed in case of the alloys containing Ti, B grain refiner compared to the absence ofgrain refiner due to the change in microstructure of

The effect of varying sliding distances on the frictional force of A356 alloy is shown in Fig.2(b). It is clear from the figure that the frictional force increases with the increase in slidingdistances in all the cases studied at the test temperature. The frictional force for A356 alloy withgrain refiner addition increases with increasing sliding distances and is less than that of additionof grain refiner, and for as cast alloy. The reason for improvement in wear resistance is due tochange in microstructure, improved hardness, strength properties of A356 alloy and formation ofFe-rich oxide layer between the sliding contact surfaces.
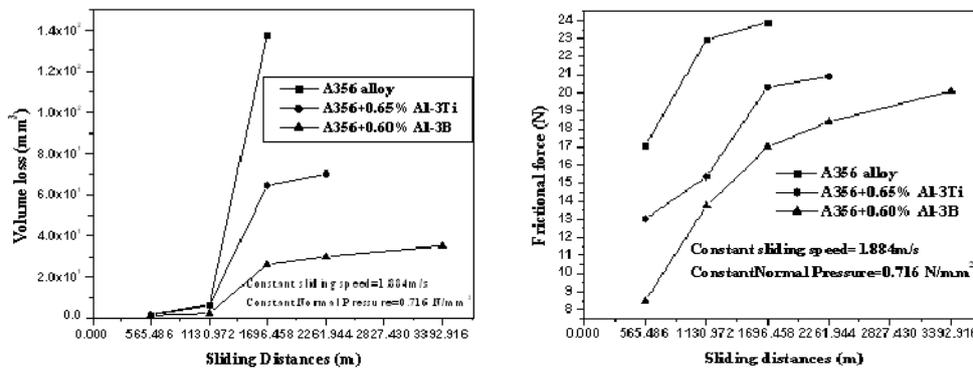
Fig.2 (a) Shows effect of sliding distances on the wear rate of commercial A356 alloy (b) Showseffect of sliding distances on the frictional force of commercial A356 alloy

3.3 Worn surface studies

Figure 3a shows the SEM photomicrograph of the worn surface of A356 alloy at an appliedpressure of 0.143N/mm2 tested at a temperature of 300°C. It is clear from the Fig.3a that, the wornsurface consists of fine grooves and surface covered with fractured oxide layer. This indicates mildoxidative wear at lower applied pressure. With the increase of normal pressure to 0.716N/mm2, theworn surface shows abrasive, oxidative and delaminative type of wear as shown in Fig.3b andindicating it as severe wear. Figure 4 shows the SEM photomicrograph of the worn surface ofA356 alloy with 0.65% of Al-3Ti addition at applied normal pressure 0.716 N/mm2 tested at atemperature of 300°C. It is clear from the Fig. 4 that, the worn surface consists of few fine parallelgrooves with most of the surface covered by delamination. For similar tested conditions A356alloy with 0.60%Al-3B shows less damage and with the increase of normal pressure to0.858N/mm2 the worn surface shows abrasive grooves, oxide debris and delaminatie on of oxidelayer as shown in Fig. 5.

Figure 6 shows the SEM photomicrographs of worn surface of A356 alloy with 0.65% of Al 3Tiaddition at 2262.940m respectively with constant normal pressure of 0.716N/mm2, constant slidingspeed of 1.884m/s at a constant temperature of 300°C. The worn sample shows fine grooves, Ferichoxide layer clearly indicating mild wear operating at the tested conditions. Figure 7 shows theSEM photomicrograph and EDS analysis of worn surface of A356 alloy with 0.60% of Al-

3Baddition at 3392.92m sliding distances respectively with constant normal pressure of 0.716N/mm2,constant sliding speed of 1.884m/s. Figure 7 shows fine abrasive grooves with iron-oxide layer onthe worn out surface. It also shows the delamination of oxide layers indicating near mild wearconditions.
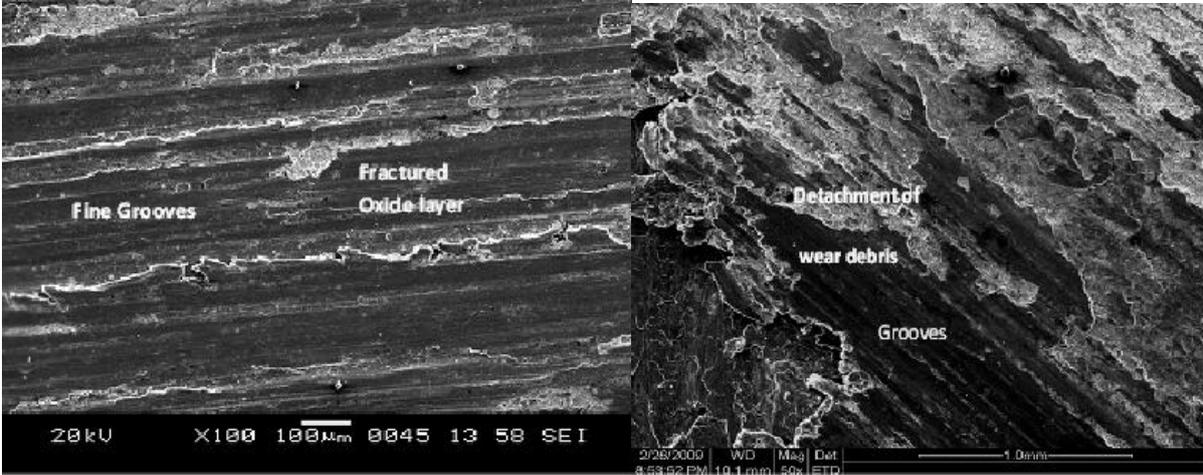
Fig. 3(a-b) Shows SEM photomicrograph of worn surface of A356 alloy at normal pressures of (a)at 0.143N/mm2 (b) 0.716N/mm2; under constant sliding distance of 1696.460m and at constant sliding speed of 1.884m/s
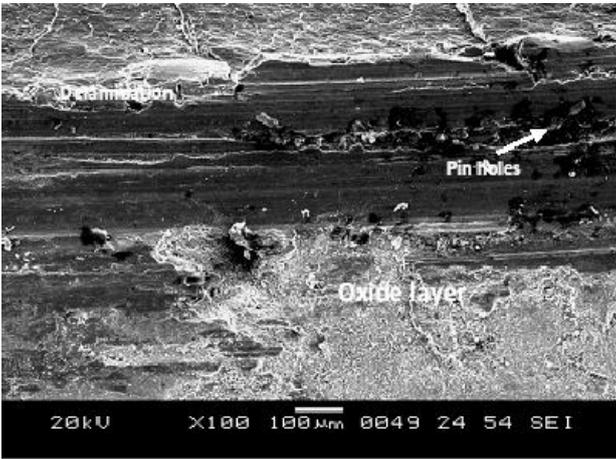
Fig. 4 Shows SEM photomicrograph of worn surface of A356 alloy with 0.65% of Al-3Ti additionat normal pressures of 0.716N/mm2; under constant sliding distance of 1696.460m and atconstant sliding speed of 1.884m/s
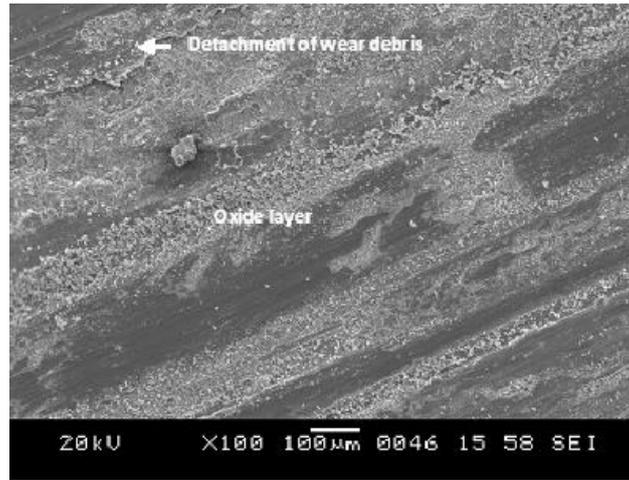
Fig.5 Shows SEM photomicrographs of worn surface of A356 alloy with 0.60% of Al-3B additionat a normal pressure of 0.858N/mm2; with constant sliding distance of 1696.460m and atconstant sliding speed of 1.884m/s
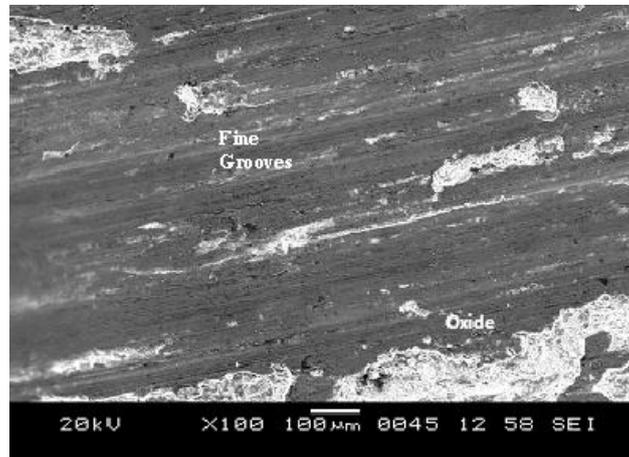
Fig.6 Shows SEM photomicrographs of worn surface of A356 alloy with 0.65% of Al-3Ti at2262.940m with constant normal pressure of 0.716N/mm2, at constant sliding speed of1.884m/s
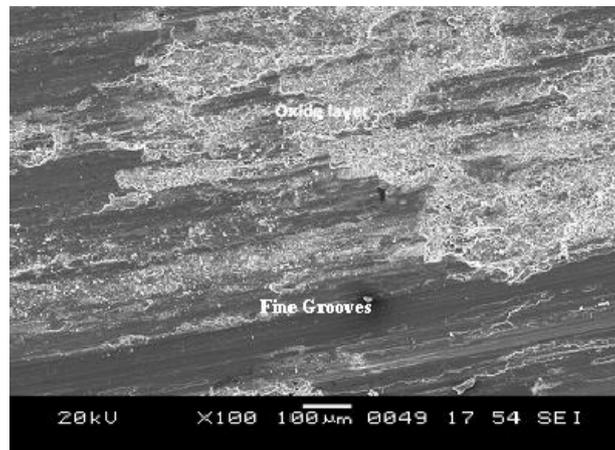
Fig. 7 Shows SEM photomicrographs of worn surface of A356 alloy with 0.60% Al-3B at 3392.92m with constant normal pressure of 0.716N/mm2, at constant sliding speed of 1.884m/s

4. Conclusions

Wear rate of A356 alloy increases with increases in normal pressures and sliding distances at the test temperature of 300°C. The frictional force showing the same trend as wear rate and is lower than the as cast alloy in all the cases studied. Addition of grain refiners changed the coarse columnar _-Al dendrites into fine equiaxed dendrites. An improvement in mechanical properties and microhardness values are obtained due to the addition of grain refiners to A356 alloy. Addition of grain refiner (Al-3B) to A356 alloy has shown maximum improvement in mechanical properties as compared to the Al-3Ti addition of grain refiners and in as cast condition. Formation of Fe-rich oxide layer between the sliding contact surfaces controls friction and wear in the present studies.

References

[1] Cui X H, Mao Y S, Wei M X and Wang S Q, *Wear characteristics Ti-6Al-4V alloy at 20-400oC*, Tribology Transactions 55(2), (2012) 211-14.

[2] Yavuz Sun, *Wear behaviour of AA6063 Aluminium alloys reinforced with insitu Al3Ti particles*, Tribology Transactions, 55(2), (2012) 224-229.

[3] Kori S A, *Grain refinement and modification of some hypoeutectic and eutectic Al-Si alloys,* Doctoral Thesis, IIT Kharagpur, India (2000).

[4] Gruzleski J E, and Closset B M, Liquid treatment to Al-Si alloys, AFS, Illinois,(1990.

[5] Chandrashekharaiah T M, *Studies on the sliding wear behaviour of grain refined and modified hypoeutectic, eutectic and hypereutectic Al-Si alloys*, Doctoral Thesis, VTU, Karnataka, India (2008).

[6] Kori S A, and Chandrashekharaiah T M, "*Studies on the dry sliding wear behaviour of hypoeutectic and eutectic Al-Si alloys,*" Int. J. of Wear, Special issue, (2007), 745-755.

[7] Prasad Rao A K, Karabi Das, Murty B S, Chakraborty M, "*Effect of grain refinement on wear properties of Al and Al-7Si alloy*," Wear, 257, (2004), 148-153.

[8] Kumar S, Subramanya Sarma V, and Murty B S "*Effect of temperature on the wear behavior of Al-7Si-TiB2 in-situ composites,*" Metall.& Mat. Trans., A, 40 A, (2009), 223-231.

[9] Kori S A, and Prabhudev M S, "*Sliding wear characteristics of Al–7Si–0.3Mg alloy with minor additions of copper at elevated temperature,*" Wear 271, (2011), 680– 688.

[10] Alpas A T, and Zhang J, "*Wear rate transitions in cast aluminium-silicon alloys reinforced with SiC particles,*" Scripta Metallurgica et Materilia, 26, (1992), 505-509.

[11] Singh J and Alpas A T, "*Elevated temperature wear of Al6061 and Al6061-20%Al2O3,*" Scripta Metallurgica et Materilia, 32(7), (1995), 1099-1105.

[12] ASTM Standards, "*Standard test method for wear testing with a pin- on-disc apparatus*" Designation G99-90", ASTM, 1916 Raco St. Philadolphia, PA19103, (1993), 1-5.

Transport Properties of Solid Polymer Nanocomposite Films for Energy Device Applications

M. Sadiq[1] and Dr. A. L.Sharma[2*],

Centre for Physical and Mathematical Science, Central University of Punjab (CUPB), Mansa, Road, Bathinda -151001(Punjab)

Presenting author; E-mail: sadiqjk.89@gmail.com **sadiqphy@gmail.com.**

[*]**Correspondence Author**: Email: alsharmaiitkgp@gmail.com Phone No: 91-164-2864220

Abstract

Sample preparation of high quality new series polymer nanocomposite (PNC) films based on (PAN-PEO)-LiPF$_6$+xwt. %DMMT has been prepared via solution cast technique. Keeping in view of applications of solid state PNC films, Fourier transform infrared (FTIR) spectroscopy is done for understanding of microscopic interaction among the different composite component present in the material system. The impedance and electrochemical analysis have been done to fulfill the objective of the materials for the energy storage/conversion device applications. Thermo gravimetric analysis (TGA) has been done to estimate the thermal stability of the prepared polymer nanocomposite films.

Keywords: FT-IR, Nanocomposites; Thermogravimetric analysis (TGA), Complex Impedance Analysis, Conductivity.

1. INTRODUCTION:

Solid state ionic is a new class of solid polymeric systems which exhibit several advantages compared to liquid electrolytes [1]. To fast ionic deal with the motion of ions in solid system, also known as solid electrolytes and super ionic conductors are solids in which ions are highly mobile and these materials are essential in the area of solid state Ionics [2]. These materials of solid polymer nanocomposite electrolytes show great technological promises and its uses in all solid-state electrochemical devices viz. such as high energy density lithium ion batteries, fuel cells, super-capacitors, gas sensors, and electrochromic display devices etc. [3]. In general the fast ion conductors and ionically conducting polymers in a dimensionally flexible film form in particular have attracted worldwide attention for device applications in view of their unique properties such as; possibility of miniaturization in shape, design flexibility, easier synthesis routes, simplicity of processing and mouldability, optimum performance-cost ratio etc [4]. The most important challenging aspect in the development of ion conducting solid polymers (also known conventionally as the solid polymer electrolytes; SPEs) till date that imposes serious limitations on their utility for applications in devices are; ambient conductivity, poor mechanical, thermal and voltage stability under desired operating conditions of the device. In addition, the presence of both cations and anions in the solid polymer matrix causes inherent problems of concentration polarization arising due to ion-pairing effect leading to immobilization of the conducting species and consequent lowering of electrical conductivity at an unacceptable level. A lot of polymeric membranes based on various combinations of polymer salt complex such as poly (ethylene oxide) e.g. PEO- LiPF$_6$, PEO-LiClO$_4$, PEO-LiCF$_3$SO$_3$, Poly (acrylonitrile) e.g. PAN/PEGME- LiClO$_4$, PAN-LiCF$_3$SO$_3$, PAN/LiClO$_4$, PAN-LiBF$_4$, PAN-LiAsF$_6$ [5-12] and various composite based on polymer/salt/clay such as; PEO/LiMMT, PEO/ LiClO$_4$/DMMT, PEO//Li-MMT, PEO/MMT, PEO/MMT, Polyacrylonitrile (PAN) e.g. PAN/NaMMT/SiO$_2$, PAN/MMT /Bentonite, PAN/Na-MMT/ solutions electro spun, PAN /MMT, PANI/MMT, Polyvinylidene fluoride e.g. PVDF/MMT, PVDF/MMT [13-24] have been found in literature report.

A lot of approaches have been put in vogue to overcome the present difficulties with solid polymer electrolytes (SPEs). Among them, intercalated type polymer nanocomposite seems best in reducing the

concentration polarization which is big hurdle in such devices. In the present work, we report polymer nanocomposite (PNC) film contains a blend of host polymer based on Polyacrylonitrilre-Polyethylene oxide (PAN-PEO), a lithium salt (LiPF$_6$) and modified clay (DMMT). On the basis of this study, we may expected that the promising ways to improve the electrochemical performance and thermal stability of polymer electrolytes is to form a nanocomposite electrolyte by adding inorganic (ceramic) powder or modified montmorillonite clays to such an electrolyte, retaining an ionic conductivity of 10^{-3}. These polymer nanocomposite electrolytes are associated with considerably better capacity and efficiency of circulation in lithium polymer secondary batteries, while inhibiting the formation of passivation films between the electrolyte and the electrodes.

2. EXPERIMENTAL

2.1. Material Preparation

Polymer blend-based solid electrolyte separator films have been prepared by a standard solution cast technique reported elsewhere [25, 29]. Polyacrylonitrile (PAN; M/S Aldrich, average molecular weight 1.5×10^5 ,(USA); 0.7gm) and polyethylene oxide (PEO; M/S Aldrich, average molecular weight 6×10^5 ,(USA); 0.3gm) , N,N-dimethylformamide (10 ml), (E-Merck Germany) was used as organic solvent, Lithium hexaflorophosphate (LiPF$_6$; Sigma Aldrich) as the salt and sodium-montmorillonite (SWy-2 variety) procured from Clay Minerals Society (USA). The modification process of montmorillonite clay is reported elsewhere [32]. In the first step, the 0.7 gram of polyacrylonitrile and adding the 10 ml of N, N-dimethylformamide (DMF) was used as solvent has been stirred using magnetic stirrer for 6 hours. And also adding the 0.3 gram of polyethylene oxide in the polyacrylonitrile solution was stirred for 7 hours to make complete polymer solution. In the second steps an optimized amount ($\frac{\ddot{N}}{Li^+}$=6) of (LiPF$_6$)(x= 0.336 gm)was added into the PAN-PEO solution and stirred for 13 hours to make polymer salt complex. In the third steps the clay was added into the polymer salt complex in concentration (x=15 wt.%; x refers to clays concentration with respect to PAN by wt,) and stirred for 13 hours. The obtained film was visually examined for its dryness and free standing nature. Finally free standing films polymer nanocomposites having general formula (PAN-PEO)$_6$LiPF$_6$ +xwt DMMT were obtained.
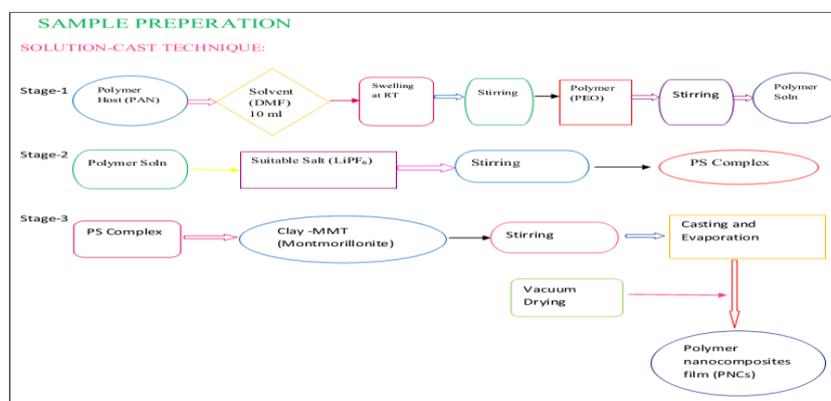
Fig.1 Flow chart of sample preparation by solution –cast technique.

2.2 Material Characterization

The typical vibrational technique of FTIR analysis has been carried out to investigate the role of clay concentration on the polymer - ion interaction. In the present investigation, FTIR spectra of all the polymer nanocomposites films were recorded in the frequency range of 600 – 4000 cm^{-1} at resolution of .4 cm^{-1} by using a Bruker Tensor 27 Spectroscopy. The FTIR spectra were recorded in the absorbance mode. The ionic conductivity of polymer nanocomposite film (PNC) electrolytes were measured by DC impedance methods in the temperature ranging from 30 ^{o}C to 100 ^{o}C and over the frequency range 100Hz to 5MHz. The sample were placed in a cell configuration: SS│PAN-PEO/MMT SPNCEs│SS cell (i.e., SS stands for stainless steel blocking electrodes) and placed in a temperature-controlled oven. The experiments were performed in a constant area cylindrical cell of an electrode diameter of 1.06 cm^{2}. The complex impedance/admittance plots of PNCEs have been fitted using the computer program and instrument model is connected to Wayne Kerr Precession Impedance Analyzer, Model 6500B series U.K. The thermal stability of the nanocomposites was analyzed by thermogravimetric analysis (TGA) using a SHIMDZU–DTG-60H under dynamic conditions from 30 ^{o}C temperature to 600 ^{o}C, in nitrogen atmosphere.

3. RESULTS AND DISCUSSION

3.1 Fourier Transforms Infrared (FTIR) Analysis

The Fourier transform infrared (FTIR) spectroscopy has been used as an important tool to characterize the organics, inorganic and polymer nanocomposite materials. Infrared spectra can be identifying the nature of bonding and different functional groups present in a sample by monitoring the vibrational energy levels of the molecules, which are essentially the fingerprint of different molecules [3]. The films were subjected to structural, thermal, and electrical characterization for their possible use in electrochemical devices. Fourier transform infrared (FT-IR) spectra were recorded in the absorbance mode with the resolution of .4cm^{-1} in the vibrational frequency range of 600-4000 cm^{-1}. FTIR spectrum of free standing PNC films based on (PAN-PEO)$_6$ LiPF$_6$ + xwt % MMT having varying clay concentration (x) and bands assignment of DMMT is shown in the below. The sample spectrum recorded under room temperature condition shows FTIR bands that has been identified and assigned to various constituent groups of the composite polymer film. The detailed assignment of the experimentally observed FTIR band and effect of clay on change in their position with increasing the concentration of clay are record in the (table 1) of various groups can changes be attributed to the polymer host (PAN-PEO)$_6$LiPF$_6$ in and montmorillonite DMMT clay with varying concentration suggests strong confirmation of interaction among polymer– salt–clay components in the polymer nanocomposite electrolytes films (PNCEs) film. The bands that appear at 600 to 670 cm^{-1} correspond to deformation of CH$_2$ band of polymer (PAN-PEO) Def(CH$_2$).The bands that appear from 700 and 1000 cm^{-1} correspond to rocking mode of CH$_2$ (ρ (CH$_2$)) , and those between 1200-1300 cm^{-1} correspond to twisting mode of CH$_2$(τ(CH$_2$)), the bands around 1300 to 1390 cm^{-1} correspond to wagging mode of CH$_2$(ω(CH$_2$)), the bands from 1400 and 1500 cm^{-1} correspond to scissoring mode of CH$_2$(δ(CH$_2$)), wave number is 2200 and 2300 cm^{-1} correspond to nitrile groups of (–C$\equiv \ddot{N}$) , the peak appear in wave number 800 and 900 cm^{-1} correspond to salt (ν (PF$_6^-$)), respectively of polymer- salts complex [26-28] . For polymer nanoccomposites electrolyte films, the band appear in 1100 and 1150 cm^{-1} correspond to the clay of ν (SiO) [29].

Table 1 FTIR Spectral Band Assignment of PNC Films Based on (PAN-PEO)$_6$ LiPF$_6$ + xwt. % MMT Film.

FTIR SPECTRUM OF ASSIGMENT OF (PAN-PEO) $_6$ LIPF$_6$ + xwt. % DMMT FILM					
Pure PAN-PEO	**x=0 wt. %**	**x=15 wt. %**	**Assignments mode**	**Source**	**Reference**
-	-	670.21	Def(CH$_2$)	PAN	29
	833.74	-	ν_a(PF$_6^-$)	Salt	5
-	845.43	832.98	ν_a(F$_2$P)	Salt	29
943.54	905.55	-	ρ (CH$_2$)	PEO	5
1099.40	1081.37	944.55	Bend(CH$_2$)	PAN	29
-	-	1046.33	ν(SiO)	Clay	29
1247.24	1247.24	1104.00	τ(CH$_2$)	PAN	29
1300.02	1301.75	1248.68	τ (CH$_2$)	PAN	29
1357.04	1357.04	1300.41	ꞷ (CH$_2$)	PAN-PEO	29, 30
1446.59	1453.60	1339.90	δ(CH$_2$)	PAN-PEO	29, 30
1635.82	1632.70	1390.52	ν(C=O)	Solvent	29
1977.67	1949.64	1451.26	ν_{as}(CH$_2$)	PEO	32
2239.32	2264.33	1663.85	ν(C=N)	PAN	28
2863.07	2887.21	1977.67	ν_s(CH$_2$)	PAN	28
-	2932.55	2241.44	ν_{as}(CH$_2$)	PAN	29

The below figure shows the general description of FTIR spectrum of polymer nanocomposite film PNCs based on(PAN-PEO)$_6$LiPF$_6$ + xwt.% of DMMT with different concentration of organ modified clay (x= 0 and 15 wt.%) in the wave number region. A comparison of the band position clearly suggested that FTIR bands attributed to both the anion and the polymer chain groups undergo change with different concentration of sorganoclay in the composite phase . The characteristic absorption peak observed in the spectral pattern at the wave number ~   669, ~ 741, ~ 839, ~ 843, ~ 963, ~1050, ~1,100, ~1112, ~ 1153, ~ 1252, ~ 1304, ~ 365, ~ 1391, ~ 1452, ~ 1658, ~ 2245, ~ 2872, ~ 2939 are

attributed to $\delta(CH_2)$, $\nu(C=O)$, $\nu(C\equiv N)$, $\nu(PF_6^-)$, bend(CH_2), $\omega(CH_2)$, $\nu(C=O)$, $\nu_a(CH_2)$ etc. of the polymer nanocomposite film is shown in the previous reports in literature respectively [29 -30]. It clearly shows that the $LiPF_6^-$ group of salt can be observed peak is calculated in the wave numbers 833.74, 838.41, 838.41, 826.73, 835.47. 832.98, 809.90, 845.43, 846.53, 846.75, 841.98, 847.66 cm^{-1}. These observations give us the information of role salt in the polymer ion interaction in polymer nanocomposite film.
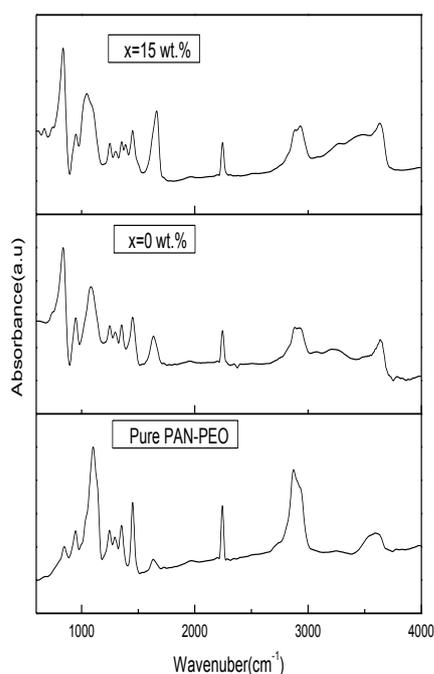
Fig.3.1. FTIR spectrum of PNCs film   Fig. 3.2. Band profile of ν (Si-O) +τ (CH$_2$) mode.
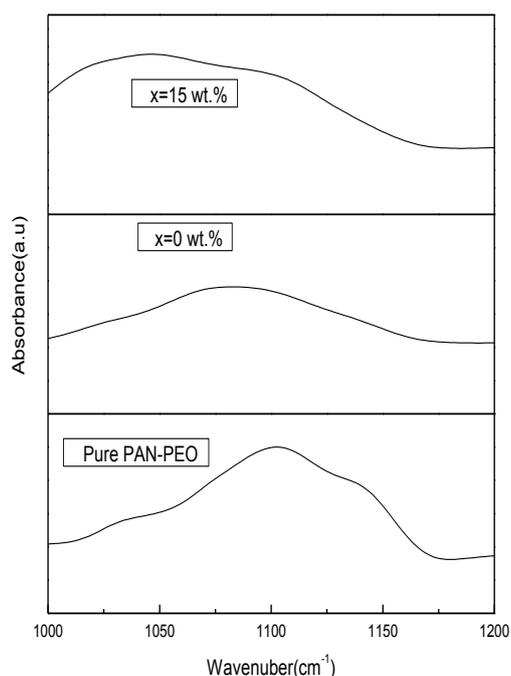
The spectral band pattern of polymer- clay interaction indicated by change in the ν (Si-O) +τ (CH$_2$) twisting mode in PNC film based on (PAN-PEO)$_6$ LiPF$_6$ + xwt% DMMT clay is shown in Fig. 3.2. The addition of clay in polymer salt has drastically change in the profile of FTIR spectrum of of PAN-PEO as host polymer indicated by clay concentration dependence of the spectral changes recorded in the wave number range from ν= 1000–1200 cm^{-1}, 1410–1500 cm^{-1}, 1310-1390 and 2200–2300 cm^{-1}, 2800-2990 cm^{-1} attributed to CH$_2$ twisting, CH$_2$ scissoring, CH$_2$ Wagging, –C$\equiv \ddot{N}$ nitrile group and symmetric stretching and asymmetric stretching mode of CH$_2$ respectively. The spectrum of twisting vibration mode [τ(CH$_2$)] in PAN-PEO is shown in above Figure 3.2. It consist of a peak at 1102 cm^{-1} in pure PAN-PEO [Fig.3.2.(Pure PAN-PEO)] and 1081.01 cm^{-1} in PS [Fig.3.2.(x=0)]. The significant modification in its profiles of the host polymer PAN-PEO exhibits the [τ (CH$_2$)] mode. Its evidences the strong interaction between polymer-salt complex and clay layer is significant change intercalation. The peaks appear observed in the wave number range is 1000-1200 cm^{-1}. The peak appearing at 1110.55 cm^{-1} attributed to bending mode of CH$_2$ changes its profile on cation coordination with polymer backbone. The detailed can be analyzed and recorded of spectrum in PNCs film is done by above table. On the addition of salt and clay in the host polymer matrix, the shoulder at 1036.40 cm^{-1} can be become visible in the content of salt and clay at the x=15 wt.% concentrations. To observe if such a change is the effect of ν(Si-O) vibration of the clay. This result can be shown that the interaction is possibility strong in the polymer –ion-clay interaction.

Further, some new peaks (~ 1004.05 , 3252.43 ,3231.40, 3275.01 ,3248.53 ,3285.13 ,3208.43 ,3348.53 ,3285.13 , 4357.71 ,3482.93 ,3468.91,3489.81 ,3522.67 , 3664.36, 3645.68 cm^{-1}) are observed in the polymer–polymer solution, polymer salt complex and polymer nanocomposite complex film. From the above analysis the complexation of (PAN-PEO)$_6$ LiPF$_6$ + x wt.% DMMT clay has been confirmed.

3.3. Thermogravimetric Analysis

The result of thermogravimetric analysis (TGA) suggested a wide change in the mass of the polymer nanocomposite films PNCs relative to their initial mass. Thermogravimetric analysis of the (PAN-PEO)$_6$ LiPF$_6$ + xwt.% of Na-DMMT investigated over a temperature 30-600 ^{o}C indicate significant changes in the thermal stability of the polymer nanocomposite films PNCs [fig.3.3.(c-j)] in comparison to pure polymer PP film [fig.3.3.(a)] and clay free polymer salt PS film[fig.3.3.(b)]. The above TGA patterns of PP, PS and PNC indicate that each can be classified in to three regions and the TGA patterns of PP, PS and PNC film are shown in the below figures.
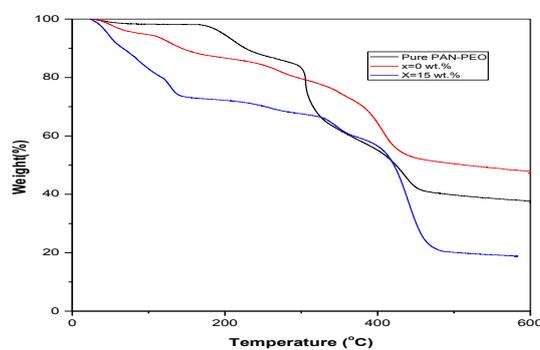
Fig. 3.3. Thermogravimetric analysis of (TGA) pattern of PNC (PAN-PEO) $_6$ LiPF$_6$ +xwt. % of MMT films.

Fig.3.3(a) Shows the TGA curves of the polymer nanocomposite film with weight of PAN -PEO has been investigated to add solvent such as DMF content. In the first region at a temperature up to 178 ^{o} C that can be extended from 74 to 178 ^{o} C show very slowly varying flat region. Now the second region can be extended from the temperature range of 176 to 300°C provides a signal of thermal transition. Finally the third region show the steadily decreasing weight loss region at temperature range of 300 ^{o}C to 600 ^{o}C. In the region third the TGA pattern show thermal degradation has been clearly appear with slight fall in the mass with temperature. This mass loss may be related to the release of surface absorbed moisture and solvent were trapped in the PAN-PEO chain.

As seen from TGA curves of fig 3.3 (b), of the polymer salt complex the content of the salt can be significant changes in the thermal stability of the polymer nanocomposite film in the clay free polymer salt film. The temperature and the percentage of total weight loss of the PAN–PEO-LiPF$_6$ samples can be obtained from TGA. In the first region there is rapid decrease in the weight loss from sample between 25 °C to 108 °C. In this way the evaporation of moisture absorbed during loading or evaporation of solvent left in the samples. In the second stage the around 110-355 ^{o}C is due decomposition of PAN-PEO-salt membrane. So the temperature is quite stable from the sample but it is observed that the total weight loss after 355 °C decreases as the concentration of the LiPF$_6$ salt increases. The higher the weight loss, the less stable the polymer electrolyte and the more non-heat resistant. Now in the third stage indicates the thermal stability of the polymer increases with the increase in the concentration of salt [1]. Due to this the thermal transition can be slowly down and the stability of salt starts to melt and the system is no longer stable.

In the addition of clay the thermal stability property of the polymer nanocomposite film has been analyzed systematically in the different concentration of modified clay and the TGA plot of the PNC films are shown in above in fig3.3(c) reveals three types region of changes suggested three distinct thermal transitions noticeable as I, II, and III region. The occurring of physical process with the system indication of different. In the first region up to 150 ^{o}C can extends from 27 to 150 ^{o}C show the rapid decrease in the loss of mass at a lower and higher concentration of clay. The second region can be extended from the temperature range of 150 ^{o}C to 336 ^{o}C show the linear decrease in the temperature and therefore the stabilization of polymer backbone of adjacent –CN group formation. It may be related to chain flexibility of the polymer backbone near its melting temperature (317 ^{o}C). However, the possibility of evolution of volatile component from PAN backbone cannot be ruled out by past report [31]. So the weight loss can depend on the concentration of clay. In fact the third region show the flat region is shown. The evolution of gaseous product having different condensation temperature shows that these products are a combination of some compound such as CO, CH_2O, CH_3CHO, in agreement with data reported by [4]. In the third region show the above 330 ^{o}C temperature, there is sharp decrease in the mass .This may be the polymer chain scission and thero-oxidative degradation, So the thermal stability continuously increase after the adding of organo modified montmorillonite clay in the polymer salt matrix.

Table 2 Summary of thermogravimetric analysis of (PAN-PEO) $_6$ LiPF$_6$ +xwt. % of MMT for PNCs films.

Sample Name	% wt loss vs. temperature (^{o}C)					
	Temperature $^\circ$ C Range in Region-1	Weight Loss (%)	Temperature ($^\circ$ C) Range in Region-2	Weight in Loss (%)	Temperature ($^\circ$ C) Range Region-3	Weight Loss (%)
PAN-PEO	31-172	2	172-298	18	298-454	59
x= 0	26-110	6	110-245	16	245-343	24
x=15	16-131	26	131-332	24	332-476	78

3.4. Ionic Conductivity Study

The impedance spectroscopic technique is new and powerful method which be used to calculate the electrical properties of polymer blend and polymer electrolyte membranes. The impedance spectra of PNCEs films with pure PAN-PEO, PAN-PEO + LiPF$_6$, and (PAN – PEO)$_6$ LiPF$_6$ + various concentration at x (i.e x= 0 and 15 wt. %) of DMMT clay .Its show a typical response, comprising a semicircular arc in the higher frequency region followed by steeply rising spike in the low-frequency region. The intercept of the semicircular arc with the spike on real axis gives an estimate of the sample bulk resistance (R$_b$).   The impedance measurements were performed by sandwiching the films between the conductivity values (σ) were calculated from the bulk resistance (R$_b$) of the material. The ionic conductivity of (PAN – PEO) $_6$ LiPF$_6$ +x wt% DMMT clay-based films is calculated by the following equation

$$\sigma = G \frac{l}{A}$$

Where 'l' is the thickness (cm) of the polymeric film, A is the area of the stainless steel electrode (cm^2) and G= $1/R_b$ is the bulk resistance of the sample. This process has been followed for all the PNCEs samples and their measurement of conductivity (30 ^{o}C and 100 ^{o}C) has been observed as a function of clay concentration. However the larger the conductivity higher is the availability of the mobile charges. Therefore the intercept of the semicircle with the real axis (Z') in the low frequency part give rise to the sample bulk ionic resistance (R_b). Though there are various reasons for departure from gives the ideal behaviours, some of them are explained as follows: Most of polymer electrolytes are often heterogeneous (with both amorphous and crystalline regions) and the distribution of the salt concentration may vary throughout the polymer electrolytes. This is the main reason of broadening and distortion of semicircle. The non-vertical spike (i.e. spike inclined at an angle less than 100 ^{o}C to the real axis) in the impedance plane is due to the roughness of the electrode–electrolytes interface. The systematic representation CIS pattern is common used to analyzes impedance spectroscopy because it is simpler and can provide the complete picture of the system is shown in the below figures.
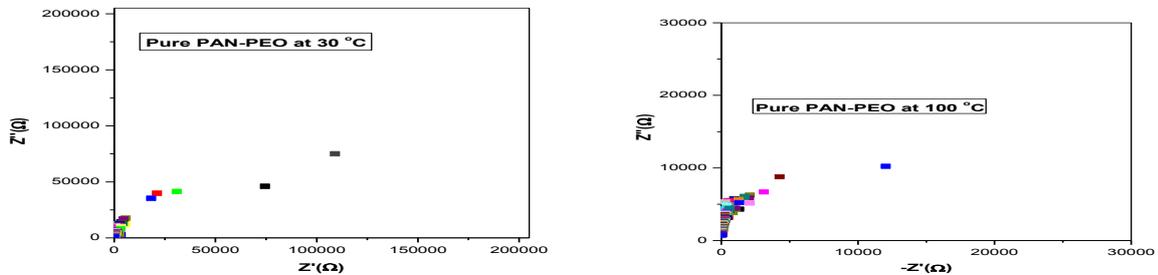
Fig.3.4 (a). Impedance Plot of PAN-PEO + at 30 ^{o}C and 100 ^{o}C
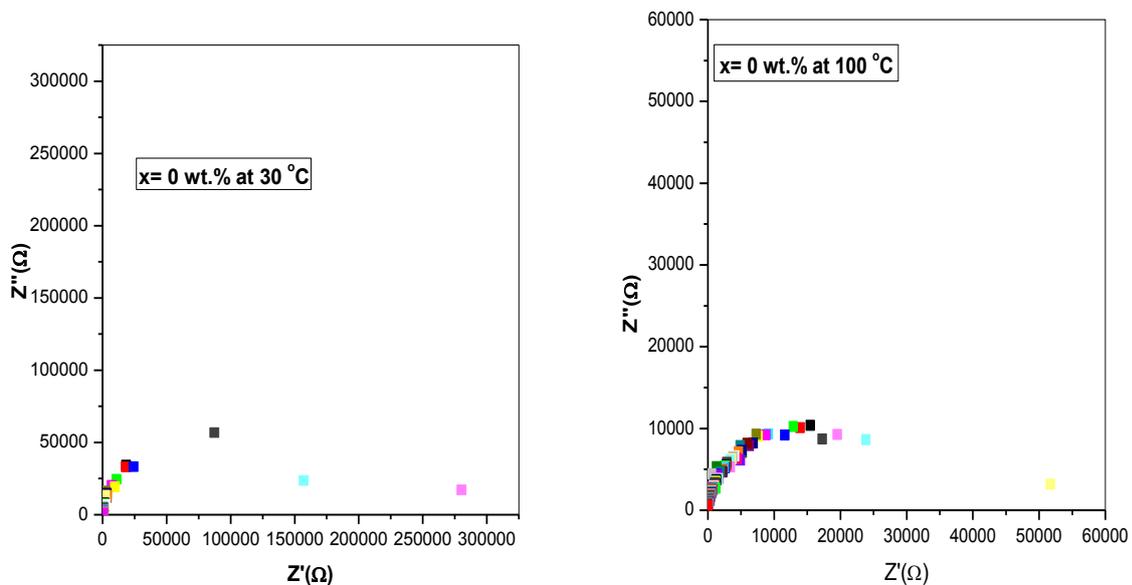
Fig.3.4(b). Impedance Plot for (PAN – PEO) $_6$ LiPF$_6$ +x = 0 wt.% at 30 ^{o}C and 100 ^{o}C
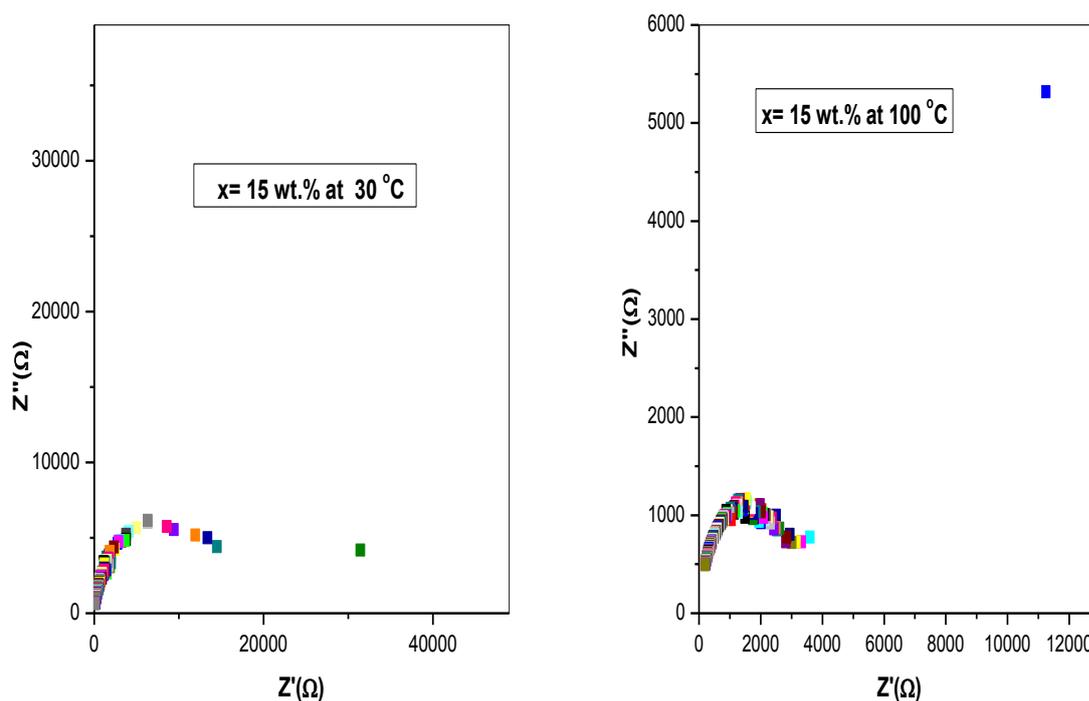
Fig.3.4(c). Impedance Plot for $(PAN - PEO)_6 LiPF_6 + x=15wt.\%$ of DMMT at 30 and 100 ^{o}C

The above results suggested that the electrical conductivity was calculated by using the above formula. The typical response of high frequency arc followed by real axis of the impedance spectrum for PAN-PEO as pure polymer complex, PAN-PEO+$LiPF_6$ as polymer salt complex and for PNC as a (PAN–PEO) $LiPF_6$+xwt. % of DMMT at clay concentrations at the different temperature range from 30 ^{o}C and 100 ^{o}C are given in tabular form in given below. The highest room temperature (T= 100°C) conductivity of the electrolyte system is 2.4×10^{-5} S cm^{-1}, has been observed at x= 15 wt. % for the polymer based on composition. It lies in the desirable limit for energy storage devices. Furthermore the enhancement of ionic conductivity in the PNC films appears good correlation with the described previously report. At both the temperatures (30 °C and 100 °C), all the PNC films show significantly higher conductivity than the PS film. This enhancement in conductivity at higher temperature is due to an increase in flexibility of polymer chain in addition to the clay assisted ion dissociation. The observed enhancement in σ_{dc} due to the availability of more mobile charge carriers in the PNC matrix agrees well with the FTIR results on polymer–clay interaction. The enhancement in ionic conductivity results appear to be well correlated with structural phase composition/microstructure as evidenced in the TGA analysis described above.

Table 3 Measurement of ionic conductivity and activation energy of polymeric film having composition of Pure PAN-PEO +DMF, (PAN – PEO) $_6$ + $LiPF_6$ with (X= 0 and 15 wt% montmorillonite clay DMMT at some selected temperature

Sample Name	dc conductivity(S cm^{-1})		Activation energy (eV)
	30 ^{o}C	100 ^{o}C	

Pure PAN-PEO	4.7×10^{-7}	2.7×10^{-6}	.460
X=0 wt.%	6.0×10^{-8}	1.7×10^{-5}	.210
X=15 wt.%	4.6×10^{-6}	2.4×10^{-5}	.445

3.5. Variation of ionic conductivity with temperature

Figure shows the variation of DC conductivity (σ_{dc}) evaluated from impedance spectrum results and observed as a function of temperature for PNC films with different clay concentration. The nature of variation of conductivity indicates that (σ_{dc}) increase with rise in temperature for the entire sample. The typical temperature dependent of the ionic conductivity of the solid polymer nanocomposite electrolytes is generally expressed by Arrhenius equation: $\sigma = \sigma_o \exp(-E_a/K_B T)$; where σ_o is the pre-exponential factor, E_a is the activation energy in eV, $K_B T$ is Boltzmann constant and T is the temperature in k. The corresponding conductivity values obtained at different temperature are listed in the above tables.
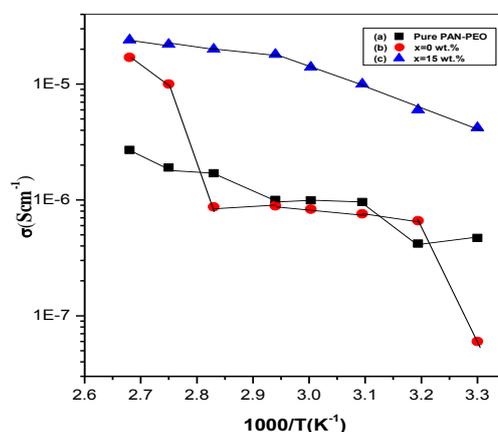
Fig.3.5. Variation of dc conductivity as a function of temperature with Pure polymer, Polymer salt complex and various concentration (x) of DMMT: (a). Pure PAN-PEO, (b). x=0 wt. % (c). x=15 wt.% in the range of 30 ^{o}C- 100 ^{o}C.

It shows that the temperature dependence of ionic conductivity for pure PAN-PEO, PAN-PEO + LiPF$_6^-$ and (PAN-PEO)LiPF$_6^-$ +DMMT. In both cases, conductivity appears to obey the Arrhenius law in both the low and high temperature regions. Our objective here to develop a high conductivity material, which satisfies the requirements application in high energy lithium ion batteries. The highest ionic can be observed at 30 ^{o}C is 2.4×10^{-6} and at clay loading (15 wt.%) and 2.4×10^{-5} s/cm for x= 15 wt.% at 100 ^{o}C respectively. This increase on ionic conductivity at higher temperature to be achieved .The increasing on clay concentration, show activation energy value goes down drastically. It may be due to the lowering of lattice energy and faster transport of charge carriers.

It has been experimental found that the electrical conductivity of the PNCs is high at glass transition temperature (T= Tg). The results indicate that the directly due to flexibility of the polymer- clay and polymer –salt system is primarily subject by local motion in the PNC films of the polymer chain.

Summary and conclusions

A new series of Polymer Nanocomposite film expressed by the blend polymer electrolytes based on Polyacrolynitrile PAN($CH_2 – CH - CN$) $_n$ - Polyethylene oxide PEO $(CH_2\text{-}CH_2\text{-}O)_n)_6$ LiPF$_6$+ xwt%

montmorillonite were prepared by solution cast technique with fix N to Li ratio ($\frac{\ddot{N}}{Li^+}$ =6) where Lithium hexafluorophosphate (LiPF$_6^-$) was taken as salt and MMT as the modified montmorillonite clay. The electrical measurement, thermal, and ion transport properties of the polymer electrolyte have been studied using different experimental techniques. The main conclusions drawn from the results obtained may be summarized as follows:

1. FTIR results suggested that the strong evidence of polymer–ion-clay interaction in the PNC films that gets change significantly on nanocomposite formation controlled by clay concentration. In the presence of polymer–ion-clay interaction and changes occurring in it on composite formation has been analyzed in the present. It may be due the polymer-ion interaction in the polymer salt film.

2. The solid polymer nanocomposites electrolytes film was visible and flexible with ionic conductivity in the range of at 4.7×10^{-7} S cm^{-1} 30 ^{o}C at blend polymer of Pure PAN-PEO. The highest conductivity value 2.4×10^{-5} S cm^{-1} has been observed at 100 ^{o}C is found for a film of (x= 15 wt. %). The temperature dependent of the (PAN–PEO)$_6$ LiPF$_6$+xwt.% of DMMT blend polymer nanocomposites obeys the Arrhenius equation and the activation energy (Ea) of this solid electrolyte is estimated.

3. The thermal stability has been observed to improve in polymer–clay nanocomposite films evidenced by weight loss of material on continuously increase after the adding of organo modified montmorillonite clay in the polymer salt matrix.

We conclude that intercalation of PP, PS complex into nanometric clay channels of the modified MMT clay has resulted in a very strong interaction among components (blend polymer–salt–clay) of PNC films

Reference

1. Ramesh S , Ng H , Solid State Ionics*192* (2011) 2-5.

2. Choudhary S, Sengwa R J, Indian Journal of Physics**86**(2012) 335-340

3. Kuo C W , Huang C W , Chen B K , Li W B , Chen P R , Ho T H , Wu T Y, Int. J. Electrochem. Sci**8**(2013) 3834-3850

4. Pradhan D K , Choudhary R , Samantaray B , Thakur A K , Katiyar R ,*Ionics 15*(2009) 345-352.

5. Ibrahim S, Yassin M M , Ahmad R , Johan M R , Ionics **17** (2011) 399-405

6. Guilherme L , Borges R , Moraes E M S , Silva G G , Pimenta M , Marletta A ,Silva R , Electrochimica Acta **53** (2007) 1503-1511.

7.Kumar Y , Hashmi S, and Pandey G, Solid State Ionics **201**(2011) 73-80.

8. Kuo C W , Huang C W , Chen B K, Li W B, Chen P R , Ho T H , Tseng C G , Wu T Y, Int. J. Electrochem. Sci **8**(2013) 3834-3850.

9. Sharma L A , Thakur A. K , Journal of applied polymer science **118** (2010) 2743-2753.

10. Huang B., Wang Z , Chen L , Xue R , Wang F. Solid State Ionics **91** (1996) 279-284.

11. Chong W , Osman Z , Journal of Polymer Research **21** (2014) 1-9.

12. Perera K , Dissanayake M , Bandaranayake P , Electrochimica acta **45** (2000)1361-1369.

13. Erceg M , Jozić D , Banovac I , Perinović S , Bernstorff S ,Thermochimica Acta **579** (2014) 86-92.

14. Fan L , Nan C W , Li M , Chemical physics letters **369** (2003) 698-702.

15. Choudhary S, Sengwa R J, Journal of Pure & Applied Physics**49**(2011)204-213.

16. Stefanescu E A , Stefanescu C , Negulescu Daly W H , Macromolecular Chemistry and Physics, **209** (2008) 2320-2330.

17. Manoratne C , Rajapakse R, Dissanayake M, Int J Electrochem Sci **1** (2006)32-46.

18. YuT , Lin J , Xu J , Chen T , Lin S. Novel polyacrylonitrile nanocomposites containing Na-montmorillonite and nano SiO_2 particle. Polymer **46** (2005) 5695-5697.

19. Moreno, M., Ana, M. A. S., Gonzalez, G., and Benavente, E , Electrochimica Acta **55** (2010) 1323-1327.

20. Shami Z , Sharifi Sanjani N , Fibers and Polymers **11**(2010) 695-699.

21. Chuntao G , Qingqing W , Xiaolin X , Yibing C , Qufu W , Technology of Water Treatment **7** (2012)010.

22. Kulhánková L , Tokarský J, Matějka V, Peikertová P, Vallová S, Mamulová Kutláková K, Stýskala V, Čapková P , Thin Solid Films **562** (2014) 319-325.

23. Deka M , Kumar A,Journal of Power Sources **196** (2011) 1358-1364.

24. Prasanth R , Shubha N , Hng H H, Srinivasan M , European Polymer Journal **49** (2013) 307-318.

25. Avirup Das, Awalendra K Thakur , K Kumara , Solid State Ionics 262 (2014) 815–820

26. Ibrahim S , Yassin M M , Ahmad R , Johan M R , Ionics **17** (2011) 399-405.

27.Pradhan D K , Choudhary R , Samantaray B , Thakur A K , Katiyar R , Ionics **15** (2009) 345-352.

28. Sharma L A , Shukla N., and Thakur A K , Journal of Polymer Science Part B: Polymer Physics **46** (2008) 2577-2592.

29.Sharma A ,Thakur A K Journal of materials science **46** (2011) 1916-1931.

30. Oliveira J E , Mattoso L H , Orts W J , Medeiros E S , Advances in Materials Science and Engineering **2013** (2013).

31.Sharma A , Thakur A K(2013) ,*Ionic* **19** (2013) 795-809.

32. Rajendran S , Mahalingam T , Kannan R ,***130*** (2000) 143-148.

33. Singla P, Mehta R, and Upadhyay S N. (2012). Green and Sustainable Chemistry **2:** 21.

Optimization of Optical Gain in GaAsP/AlGaAs Nano-Heterostructures

H. K. Nirmal[1], M. J. Siddiqui[2], P. A. Alvi*[1]

[1]Department of Physics, Banasthali Vidyapith-304022, Rajasthan (INDIA)

[2]Department of Electronics, Aligarh Muslim University, Faculty of Engineering and Technology, Aligarh Muslim University, Aligarh-202022, UP (INDIA)

*E-mail corresponding author: drpaalvi@gmail.com

Abstract

In this paper, we have optimized the optical gain in the Type-I GaAsP/AlGaAs nano heterostructure grown on GaAs substrate. In order to calculate the optical gain of the structure, first the 4 x 4 Kohn-Luttinger Hamiltonian is solved for finding the energies of electrons in conduction band and holes (Light and Heavy holes) in valence sub-bands; and then transition matrix elements calculations is designed to perform calculations of momentum matrix elements and dipole moments of selected transitions. The calculated optical gain corresponding to maximum intensity meets at photonic energy ~ 1.64 eV and at corresponding wavelength ~ 756 nm. The simulated results are found to match with experimental results.

Keywords: Nano-heterostructure, Optical gain, GaAsP, AlGaAs, K.P Method, Type-I structure

INTRODUCTION

Heterostructures are very important for opto-electronic device applications [1]. There has been progressive evolution and radical changes in the history of semiconductor lasers. The idea of degenerately doped p-n junction based semiconductor laser was introduced in 1961 [2]. A very important point was marked that lower current densities could be obtained if the semiconductors forming the p-n junction have different forbidden gaps. Later on the concept of double heterostructure was proposed and developed [3]. In the double heterostructures (DHs) based lasing structures, an active media of extremely thin quantum well layer of narrow gap semiconductor were embedded in a wide gap barrier. Researchers have approached a lot of techniques to study the performance of semiconductor lasing heterostructures. These include numerical modeling, analytical solution or circuit modeling of rate equations determining the physical line of action of lasing heterostructures [4-6]. Recently, R. Yadav et al. [7] have simulated the optical gain of $In_{0.90}Ga_{0.10}As_{0.59}P_{0.41}$/InP lasing nano-heterostructure and found that the maximum gain is corresponding to the wavelength lying in the near infra red region.

The present paper focuses on the numerical simulation of optical gain and analysis of the gain spectrum of p- $Al_{0.45}Ga_{0.55}As$/$GaAs_{0.84}P_{0.16}$/n- $Al_{0.45}Ga_{0.55}As$ diode structure that consists of QW (quantum well) of thickness 140 Å and material GaAsP sandwiched between AlGaAs layers of thickness 100 Å; see the figure 1. The overall structure is supposed to be grown on GaAs. The reason behind the selection of GaAs substrate is the matching of lattice constants between the substrate and AlGaAs layers in order to avoid the strain factor.
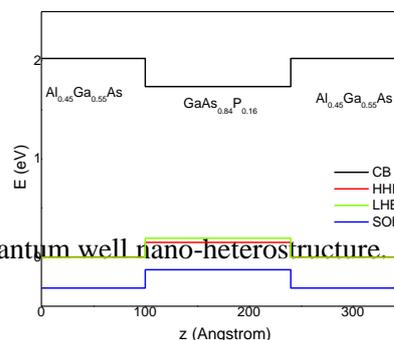
Figure 1. Energy band diagram of GaAsP/AlGaAs quantum well nano-heterostructure.

THEORETICAL BACKGROUND

The valence and conduction band profiles, as well as size quantized levels and wave functions of electrons and holes in the $GaAs_{0.84}P_{0.16}$ QW under investigation were numerically calculated. The numerical calculations were performed in the framework of the program "Heterostructure Design Studio 2.25" in the vicinity of the zone centre at the Γ point. There was used the model developed in [8], which considers the 4×4 Luttinger-Kohn Hamiltonian and describes the conduction band, light and heavy hole subbands but doesn't take into account the valence split-off subband because it does hang about 300 meV below the top of the valence band in $GaAs_{0.84}P_{0.16}$ [9].

In the calculations, the hole wave functions were expanded in basis functions of Luttinger-Kohn representation with the total angular momentum J = 3/2, and its projections m_J = ± 1/2 and m_J = ± 3/2 correspond to light holes and heavy holes respectively [8]. From the electron and hole wave functions, matrix elements of electron-photon interaction operator for interband transitions and, further, optical gain may be calculated. The optical gain was calculated for the TE (Transverse Electric) mode using the standard gain expression [10-13].

RESULTS AND DISCUSSION

The band dispersion for the bulk GaAsP material (on substrate AlGaAs) has been calculated by using eight-band Kane model along k_z with setting k_x and k_y = 0. The dispersion curve of bulk GaAsP has been shown in figure 2 (a). In figure 2 (a), it is clear that conduction band is almost parabolic while the valence subbands (Light, Heavy and Split off holes) are not. It has also been shown that light hole subband is above the heavy hole subband indicating that there is little lattice mismatch between the substrate GaAs and GaAsP QW. This mismatching shows the tensile strain in the QW.

After studying the band structure of bulk GaAsP material, the calculations have been performed for $GaAs_{0.84}P_{0.16}$ QW. The performed calculations shows that in the strained $GaAs_{0.84}P_{0.16}$ QW within the heterostructure, the first light hole (LH1) level is the ground state in valence band while the first heavy hole (HH1) level is the next one in the energy scale; refer to figure 2 (b). Next, from the electron and hole wave functions, matrix elements of electron-photon interaction operator for interband transitions and, further, optical gain have been calculated.

The dipole matrix elements and momentum matrix elements for the transitions occurring in between conduction band and valence subbands (i.e. light holes and heavy holes) in the heterostructure have been calculated and plotted in figure 3 (a and b). In general, the dipole matrix elements give information about the strengths of dipole formations between the conduction band and valence subbands. The Optical transitions between the lowest electron level E1 and the highest hole level LH1 in the valence band determine an optical gap that is equal to the experimentally observed emitted photon energy.

a)

(b)
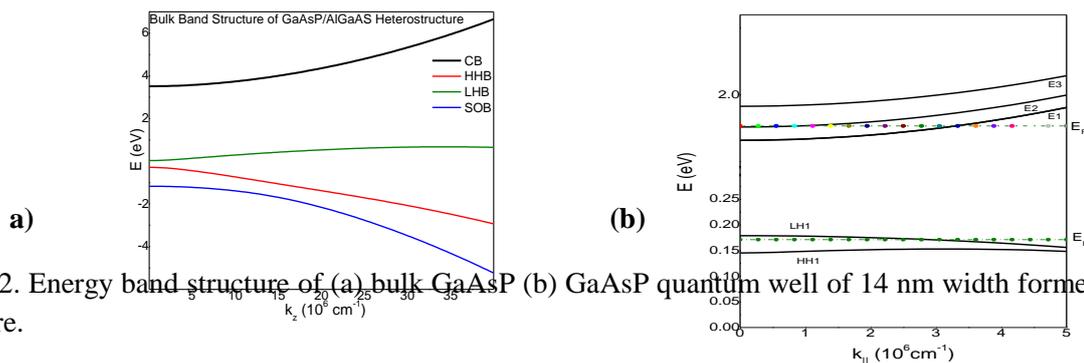
Figure 2. Energy band structure of (a) bulk GaAsP (b) GaAsP quantum well of 14 nm width formed in structure.
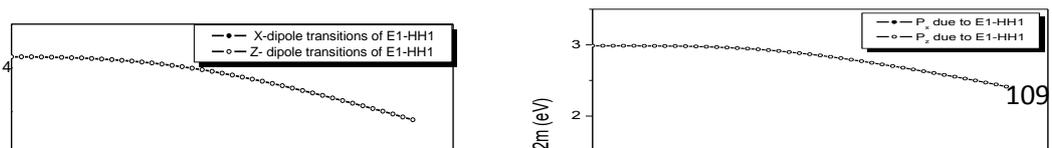
Figure 3. Behaviour of dipole matrix and momentum matrix elements for the transitions in the structure.

The calculated optical gain has been shown in figure 4. In figure 4, the spin dependent optical gain due to individual electrons and holes having parallel and anti-parallel spins is shown. The total optical gain has also been shown. The total optical gain corresponding to maximum intensity has been optimized at photonic energy ~ 1.64 eV and at corresponding wavelength ~ 756 nm (NIR region), that is found agreed with the experimental result; see figure 5.
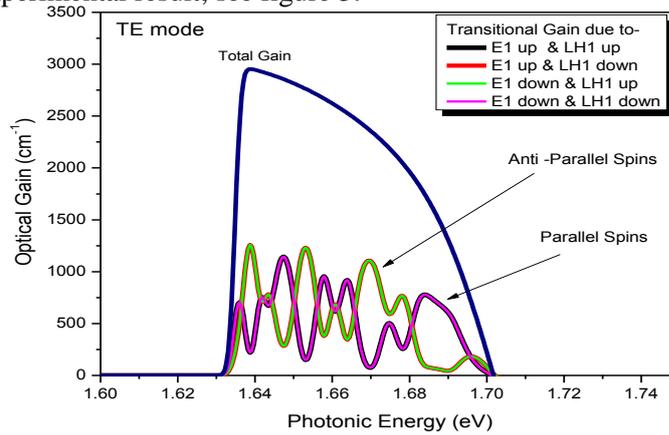
Figure 4. Optical gain of p- $Al_{0.45}Ga_{0.55}As/GaAs_{0.84}P_{0.16}/n$- $Al_{0.45}Ga_{0.55}As$ nano-heterostructure.

$$\lambda(nm) = \frac{1240}{E(eV)}$$
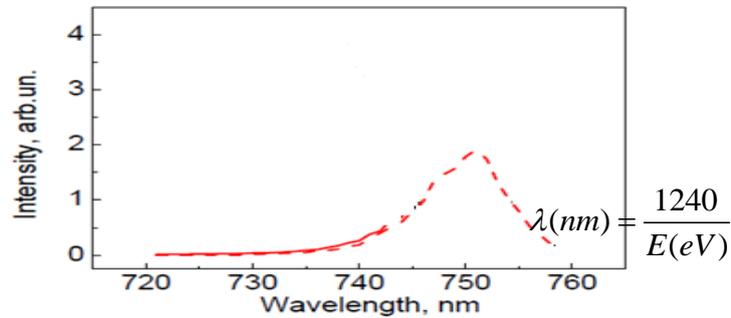
Figure 5. Plot of Intensity versus wavelength (Experimental result; ref. 8)

CONCLUSION

We have solved 4 x 4 Kohn-Luttinger Hamiltonian to determine the sub-band dispersion and corresponding envelope wave functions for p-$Al_{0.45}Ga_{0.55}As/GaAs_{0.84}P_{0.16}$/n- $Al_{0.45}Ga_{0.55}As$ nano-heterostructure. Taking into account spin concept of electron and hole, the transition matrix elements

calculations is designed to perform calculations of momentum matrix elements and dipole moments of selected transitions. Finally, the optical gain for the structure has been calculated. The calculated optical gain corresponding to maximum intensity meets at photonic energy ~ 1.64 eV and at corresponding wavelength ~ 756 nm (NIR region), that is found agreed with the experimental result.

ACKNOWLEDGEMENT

References

Alvi P A, Gupta S, Vijay P, Sharma G, Siddiqui M J, *Physica B: Condensed Matter*, **405**, Issue 17 (2010) 3624.

Basov N G, Krokhin O N, and Popov Yu M, *JETP*, **40** (1961) 1320.

Alferov Zh I and Kazarinov R F, *"Double heterostructure laser",* Authors Certificate no. 27448, Application no. 950 840, priority from March 30 (1963).

Carr T W and Erneux T, *IEEE J. Quantum Electron.*,**37**, (2001) 1171.

Ansari L, Zarifkar A, and Moravvej-Farshi M K, *in Proc. 4th Int. Conf Optical Communications and Networks (ICOCN)*, Bangkok, Thailand, (2005) 332.

Salehiand M R, Cabon B, *IEEE J. Quantum Electron*,**38**, (2002) 1510.

Yadav R, Lal Pyare, Rahman F, Dalela S, and Alvi P A, *International Journal of Modern Physics B*, **28**, No. 10 (2014) 1450068.

Kolokolov K I, Savin A M, Beneslavski S D, Minina N Ya and Hansen O P, *Phys. Rev. B,***59** (1999) 7537.

Vurgaftman I, Meyer J R and Ram-Mohan L R, *J. Appl. Phys.,* **89** (2001) 5815.

Chuang S L, *Physics of Optoelectronic Devices*, Wiley, New York (1995).

Alvi P A, Lal Pyare, Dalela S, Siddiqui M J, *Physica Scripta,***85** (2012) 035402.

Alvi P A, Lal Pyare, Yadav R, Dixit S, Dalela S, *Superlattices and Microstructures,***61** (2013) 1.

Alvi P A, *Materials Science in Semiconductor Processing*, **31** (2015) 106.

MICROSTRUCTURE AND MECHANICAL PROPERTIES OF Cu-COATED Al_2O_3 PARTICULATE REINFORCED 6061 Al ALLOY COMPOSITE

MITHUN B R, MADEVA NAGARAL, BHARATH V, V AURADI

Department of Mechanical Engineering, Siddaganga Institute of Technology, Tumkur – 572103, Karnataka, India

E-mail:mithunbr44@gmail.com,madev.nagaral@gmail.com,bharathv88@gmail.com, vsauradi@gmail.com

Abstract

In the present work an attempt is made to synthesize 6061Al – Cu coated Al_2O_3 particulate metal matrix composite by two stage melt stirring method. Ceramic particulates such as TiB_2, SiC, Al_2O_3, B_4C can be reinforced with aluminum matrix for better strength and wear resistance properties. In the present investigation 6061Al alloy were reinforced with copper coated Al_2O_3 particulate through two stage melt stirring process. Two stage melt stirring is adopted over single stage melting stirring process as this avoids agglomeration of particulates and results in better properties of MMC. Microstructural analysis reveals that Cu coatings around Al_2O_3 particulates have improved the wettability at the interface resulting in better incubation of particulates into melt which are evident from SEM microphotographs. Mechanical properties like density, hardness and tensile strength were studied for both copper coated and uncoated Al_2O_3 reinforced composite at room temperature. Significant increase in mechanical properties was observed for copper coated Al-Al_2O_3 composite due to improved wettability and uniform distribution of particulates within 6061Al matrix compared with Al-Al_2O_3 composite without Cu coatings.

Keywords: Al/Al_2O_3 composite, Cu coatings, Microstructure, Tensile strength.

I. Introduction

Aluminium alloys are extensively used in advanced engineering application such as aerospace and automotive industry due to its high strength, machinability, low density, easy availability and cost effectiveness compared to other materials. The scope of aluminium can be further extended by using it as a matrix material in the production of MMC. Aluminium metal matrix composites (AMMCs) possess significantly improved properties including high strength to weight ratio, higher elastic modulus, damping capacity and good wear resistance compared to unreinforced alloys [1] & [2].

Among aluminium alloys, 6061 Al is an Al-Si-Mg alloy widely used in structural and engineering applications due to its good strength to weight ratio, weldability, machinability, corrosion resistance, heat treatability – forms precipitates on heat treatment and thus increasing strength with the cost of ductility. Harder ceramic particles such as B_4C, Al_2O_3 and SiC are widely used as reinforcement in composites. Among this, Al_2O_3 facilitates high strength and stiffness, good thermal conductivity, excellent size and shape capability and good wear resistance [3]. Al_2O_3 is most commonly used in the applications such as pistons, connecting rods etc., where tribological properties of the material are important [4]. But from studies and experiments it is observed that Al_2O_3 particle has poor wettability with 6061Al matrix.

Interface between the matrix and reinforcement strongly affect the properties of MMC's. Wettability between the matrix and reinforcement is the main factor which influences on the interfacial properties [5]. If the interface is not tailored properly it leads to lack of wettability, chemical reaction at the interface and degradation of reinforcement. Techniques used to obtain the desired interface include surface treatment of reinforcement, coating the reinforcement, optimizing process parameters and

altering the matrix composition. Among the various techniques to improve the interface, coating is important one and widely investigated in the recent years [6] & [7].

Coating of the reinforcement restricts the diffusion of molten matrix material into the surface of the reinforcement. Thus, in the absence of diffusion chemical reaction at the interface is minimized [8]. Coating also plays an important role in increasing the wettability of the reinforcement in the molten matrix. Chemical vapor deposition, Physical vapor deposition, thermal spraying, electroless and electrolytic deposition etc., are the various techniques adopted to coat the reinforcement particles. Among these techniques electroless deposition is gaining importance due to its easy set up, low cost, uniform and continuous coating [9] & [10].

In present work an attempt is made to synthesize 6061Al based composites with reinforcements of un-coated Al_2O_3 / Cu-coated Al_2O_3 particulates with 6 weight % by two stage Stir casting route and to study the mechanical properties of the MMC.

II. Experimental Details
A. Materials Used

6061Al is used as the matrix material and Al_2O_3 is used as the reinforcement in the current work. Particle size of Al_2O_3 various between 100-125 micro meter. Chemical composition of 6061Al is as given below. The properties of matrix material and reinforcing material are given below.

Table 1: Chemical composition of 6061 Al alloy

Components	Amount (wt%)
Aluminium	Balance
Magnesium	0.8-1.2
Silicon	0.4-0.8
Iron	Max 0.7
Copper	0.15-0.40
Zinc	Max 0.25
Titanium	Max 0.15
Manganese	Max 0.15
Chromium	0.04-0.35
Other	0.05

Material/Properties	Density gm/cc	Hardness (HB500)	Strength (Tensile/Compressive) (MPa)	Elastic modulus (GPa)
Matrix – 6061 Al	2.7	30	115(T)	70-80
Reinforcement Al_2O_3 Particulate	3.69	1175	2100(C)	300

Table 2: Properties of matrix and reinforcement

B. Electroless Cu-Coating

Electroless Cu-coating ofAl_2O_3 particle is carried out as follows: Al_2O_3 is cleansed with acetone and acetone is separated. Cleaned Al_2O_3 is sensitized with stannous chloride & Conc. HCL and Al_2O_3 is separated from the mixture. Sensitized Al_2O_3 is treated with $PdCl_2$ and Conc. HCL to activate the surface of inactive Al_2O_3. In the activation process Pd is adsorbed on to the surface of Al_2O_3. Dried Al_2O_3 is dispersed in the electrolytic bath containing $CuSO_4$, distilled water, sodium hydroxide and Al_2O_3. 11-13 ph of the solution is maintained in the electrolytic bath. Thus Cu- coating is obtained on the surface of Al_2O_3 particulates.

C. Processing

Stir casting method is used to prepare the metal matrix composites of required dimensions. 6061Al alloy is melted in graphite crucible using resistance furnace. Meanwhile Al_2O_3 particles are preheated at 400°C for 30 minutes. The furnace temperature is maintained at 750°C, which is above the liquidous temperature of 6061Al alloy in order to increase the viscosity of the melt. Mechanical stirrer maintained at 200rpm is used to stir the melt to form the vortex. Once the vortex is created, the preheated weighed reinforcing Al_2O_3 particle is introduced in 2 stages. The melt is stirred for 10 minutes and the furnace temperature is maintained at 750°C i.e. pouring temperature. The melt is poured into permanent mould made of cast iron containing the cavity as per requirement. The test samples are prepared in the same procedure for different weight percentages.

D. Testing

Microstructure of prepared specimen is studied by taking the central part of the composite block. The face of the specimen to be examined is prepared by polishing through220, 400, 600, 800 & 1000 grit emery papers and polished using diamond paste. The specimen is etched using Keller's reagent before it is examined using optical microscopy and scanning electron microscopy. Specimen for hardness test and tensile test are prepared as per ASTM standards. Hardness test is done on the polished surface of the specimen using Micro- Vickers hardness testing machine consisting of diamond cone indentor and with the application of 30N load. Tensile test is done using computerized universal testing machine as per ASTM standards and four specimens are tested for each composition of composite.

III. Results and Discussions

A. Microstructural Studies

The properties of MMC's are mainly influenced by the dispersion of reinforcement in the matrix material. Uniform dispersion of reinforcement leads to better mechanical properties compared to non-uniform dispersion.

Figure (a) shows the SEM micrographs of 6061 Al alloy. Figure (b) show the SEM micrographs of 6 weight % of un-coated Al_2O_3 reinforced 6061Al alloy. This reveals the agglomeration of Al_2O_3 particulates at the inter-dendritic region of matrix alloy and also the presence of porosity which intern reduces the properties of MMC's.

Figures (c) show the SEM micrograph of 6 weight% of Cu-coated Al_2O_3 reinforced 6061Al alloy. The SEM micrograph reveals the homogeneous distribution of reinforcement in the matrix. This homogeneous distribution of reinforcement shows that Cu-coating of the reinforcement has increased its wettability with the matrix material effectively.

(b)   (c)
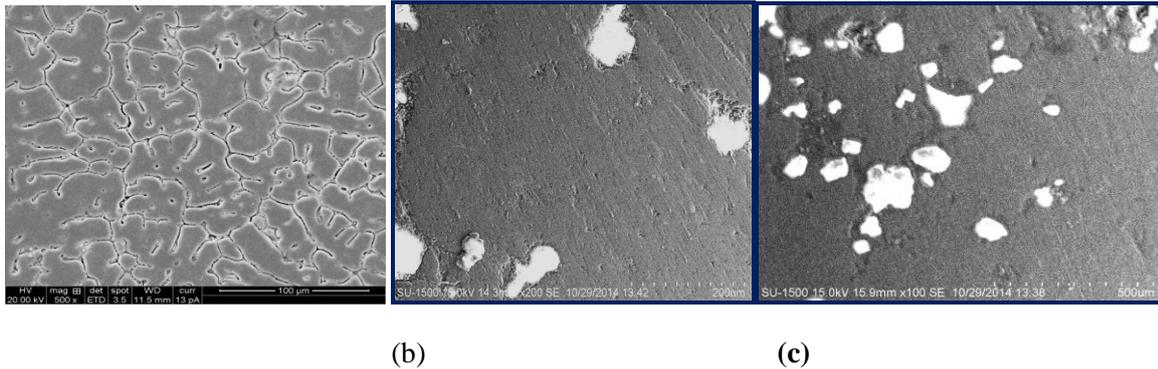
Fig 3: Shows the SEM micrographs of (a) 6061 Al alloy (b) 6061 Al reinforced with 6 wt% un-coated Al$_2$O$_{3P}$ (c) 6061 Al reinforced with 6 wt% Cu-coated Al$_2$O$_{3P}$

B. Hardness Observations

The polished samples are taken to perform Micro- Vickers hardness test using diamond cone indentor. 30N load is applied on the polished samples and 3 reading are reported at different locations and average of these 3 reading is considered. The experiment is repeated for all the samples. Thus obtained hardness value of base material (6061Al alloy) and the prepared composites (6061Al reinforced Cu-coated Al$_2$O$_3$ / non-coated Al$_2$O$_3$) is plotted in the below graph (Figure 3.1). The obtained values reveal that there is noticeable raise in the hardness value with increasing weight percentage of Al$_2$O$_3$ particles. It is observed that the hardness of prepared composite with Cu-coated Al$_2$O$_3$ is higher than that of composite containing non-coated Al$_2$O$_3$. The increase in hardness is due to the presence of stiffer and harder Al$_2$O$_3$ reinforcement particulates which acts as a constraint to plastic deformation of the softer matrix material. The presence of copper coating prevents the formation of brittle intermetallics at the interface thus facilitating effective transfer of load from matrix to reinforcement.
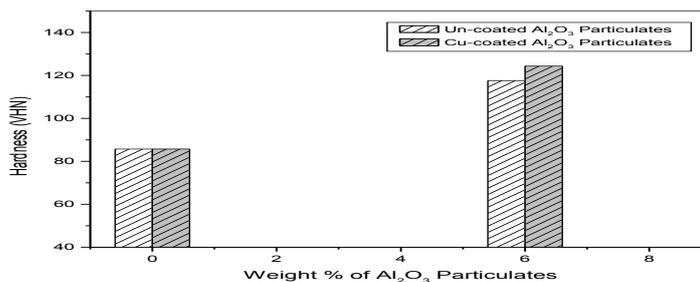
Fig 3.1: Graph showing the variation in hardness of 6061 Al and 6061 Al reinforced with 6 wt% of Un-coated/ Cu-coated Al$_2$O$_3$

C. Tensile Properties

Investigation of mechanical behavior of the composite is done by conducting the tensile test on computerized universal testing machine as per ASTM standards. Four test specimens are used for each run. The tensile properties such as yield strength, percentage elongation and tensile strength are extracted from the test results. The test is carried out for the samples of base material and 6 wt % of Un-coated & Cu-coated Al$_2$O$_3$ particulates. The obtained results revels that there is appreciable increase in the fracture strength of composites but ductility of the material decreases when compared to 6061Al alloy. It is observed that composites of Cu-coated Al$_2$O$_3$ have more strength than that of the

composites containing non-coated Al_2O_3. From the test results we can conclude that there is increase in tensile strength of the composites but the ductility of the material containing Cu-coated Al_2O_3 is higher than material containing non-coated Al_2O_3.

(a)   (b)
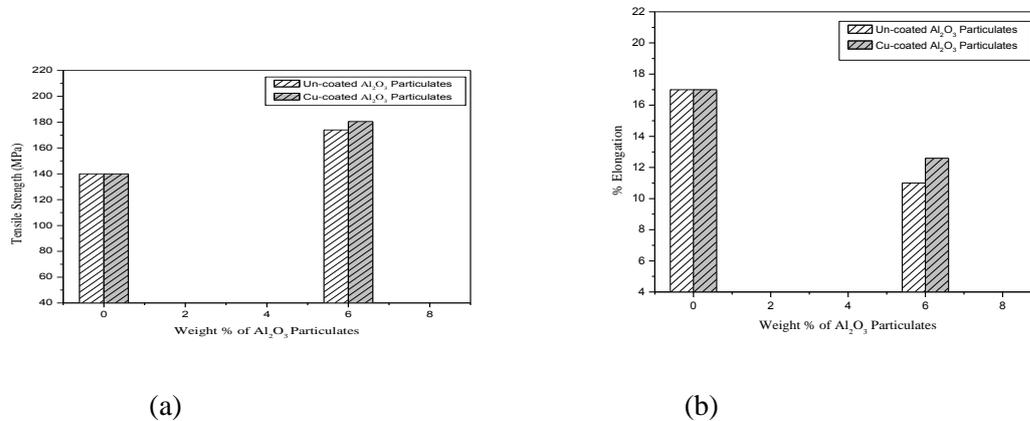
Fig 3.2: Graph showing the tensile test result of 6061 Al base alloy before and after the addition of Un-coated / Cu-coated Al_2O_3 (a) Variation in ultimate tensile strength (b) Variation in % elongation

Conclusion

1. Successful synthesis of 6061 Al and Cu-coated Al_2O_3 by two stage stir casting method.
2. Microstructural analysis reveals the uniform distribution of Cu-coated Al_2O_3 in matrix metal.
3. The hardness of composite containing Cu-coated Al_2O_3 is 7.9% greater than that of composite consisting non-coated Al_2O_3.
4. Tensile strength of the prepared composites with non-coated & Cu-coated Al_2O_3 is found to increases by 24.2% & 28.9% respectively.
5. Ductility of Cu-coated Al_2O_3 reinforced 6061 Al matrix composite is increased by 9.33% than that of composite prepared with non-coated Al_2O_3.

Reference

[1] *Rajeshkumar Gangaram Bhandare, Parshuram M. Sonawane*, Preparation of Aluminium Matrix Composite by Using Stir Casting Method @ International Journal of Engineering and Advanced Technology (2013) 2249 – 8958

[2] *Dr. Virupaxi Auradi,* Composite material tutorials (2012), Department of mechanical Engineering, Siddaganga Institute of Technology , Tumkur , Karnataka, INDIA.

[3] *Bharath V, Madeva Nagaral, V Auradi,* Preparation of 6061Al-Al_2O_3 Metal Matrix Composite by Stir Casting and Evaluation of Mechanical Properties @ International Journal Of Metallurgical & Materials Science and Engineering (2012) 2278-2516

[4] *Prakash Gadade, Arun L.R,* Characterization Of Aluminium-Flyash-Alumina Composite for Piston analysis By CAE Tools @ International Journal of Innovative Research in Science, Engineering and Technology (2013) 2319-8753

[5] *Hashim. J, Looney. L, Hashim. M.S.J,* The wettability of SiC particles by molten aluminium alloy @Journal material processing Technology, Vol. 119 (2001)

[6] *Rajan. T.P.D., Pillai. R.M., Pai. B.C.,* Review reinforcement coatings and interfaces in aluminium metal matrix composites @ Journal of Material Science, Vol.33 (1998)

[7] *Rams. J, Urena. A, Campo. J,* Sol-gel coatings as active barriers to protect ceramic reinforcement in aluminium matrix composites @ Advanced Engineering Materials, Vol.6 (2004)

[8] *H. Beygi, S.A. Sajjadi, S.M. Zebarjad,* Microstructural analysis and mechanical properties of aluminum matrix nano composites reinforced with uncoated and Cu-coated alumina particles @ Elsevier Journal of Material Science and Engineering (2014)

[9] *R. Karthigeyan, S.Ezhil vannan, G. Ranganath, S.Paul vizhian, K.Annamalai,* Effect of Coating Parameters on Coating Morphology of Basalt Short Fiber for Reinforcement Preparation of Al/Basalt Metal Matrix Composites @ International Journal of Electrochemical Science (2013) 10138 – 10148

[10] *Burak Dikici, Cagri Tekmen, Mehmet Gavgali, Umit Cocen,* The Effect of Electroless Ni Coating of SiC Particles on the Corrosion Behavior of A356 Based Squeeze Cast Composite @ Journal of Mechanical Engineering (2011)

Solar Water Heater with Implementation of Phase change Material

Ahsan Moazzam and Rakesh Kumar

Department of ME, Sant Longowal Institute of Engineering and Technology 148106, Sangrur, Punjab

India.

Abstract- **Developing efficient and inexpensive energy storage devices is as important as developing new sources of energy. Energy storage can reduce the time between energy supply and energy demand, thereby playing a vital role in energy conservation. It improves the energy systems by smoothing the output and thus increasing the reliability. This paper deals with storage of solar thermal energy in materials undergoing phase changes. PCMs, which include salt hydrates, paraffin's, no paraffin's, and eutectics of inorganic, are discussed. Heat storage in phase change materials (PCM) has an advantage of compactness and heat supply at constant temperature.**

Keywords— reliability; CTS; solar thermal energy; PCMs; hydrates; paraffin; constant temperature

I.   Introduction

Energy is essential for the existence of human life and plays vital role in the progress of the nation. However the past few years have witnessed a rapid growth in global population putting a tremendous burden on energy resources .In the present scenario the importance of available energy can't be under Estimated. The country's energy demand has grown to an average of 3.65% per annum over the past 30 years. So it has become a need to harness alternate and renewable energy sources. Today India has one of the highest potential for the effective use of renewable energy sources .The country has also invested heavily in recent years in renewable energy utilization. Solar energy being simple to use, clean, non-polluting and inexhaustible has received wide spread attention in recent times. It provides well abundant energy source if utilized efficiently. But this energy is time dependent energy source with an intermittent character. Hence some form of thermal energy storage is necessary for more effective utilization of this energy source.

A.   Phase Change Material

  PCMs absorb and emit heat while maintaining a nearly constant temperature. Within the human comfort range of 68° to 86°F (20° to 30℃), latent thermal storage materials are very effective. They store 5 to 14 times more heat per unit volume than sensible storage materials such as water, masonry, or rock.

Thermal energy can be stored in well-insulated fluids or solids. It can be generally stored as latent heat-by virtue of latent heat of change of phase of medium. In this the temperature of the medium remains more or less constant since it undergoes a phase transformation. Phase change storages with higher energy densities are more attractive for small storage.

The PCMs fall in three categories:-

i. Salt Hydrates-These materials are preferred because of their high latent heat storage density. Salt hydrates have suitable phase change temperatures for use as storage in space heating systems. The storage of heat in salt hydrates is in form of heat of fusion, which is latent heat of reaction. If latent heat of reaction is large latent heat storage has the advantage of making smaller systems. At certain

temperature these materials release their water of crystallization and the solid remainder dissolves in it or in part.

ii. Paraffin's-Heat -of- fusion storage materials due to their availability in large temperature range and their reasonable high heat of fusion. Due to cost consideration, only technical grade paraffin's may be used as PCMs in latent heat stores. Paraffin like other mineral oil products are complicated mixtures of several organic compounds and contain one major component called alkanes.

iii. Non paraffin organic-This is the largest category of candidate materials for phase change storage. The hot storage capacity of non-paraffin organics 125-200 kJ/dm3.

Compared to different storage techniques for solar space heating and hot water production applications the operating temperature range for PCM is large, depending on the choice of material .The reason so as to why PCM is a suggested alternative to conventional storage mediums are:-

i. Thermal storage capacity per unit mass and unit volume for small temperature differences is high.

ii. A thermal gradient during charging and discharging is small.

iii. Simultaneous charging and discharging is possible with appropriate selection of heat exchanger.

B. Solar Water Heater with PCM

The one of the most important part of a solar collector system is the solar tank. The solar collectors work daytime only, and its power depends on the weather. The hot water consumption in family houses is generally bigger in the evening and in the morning, so it is necessary to store the utilized energy. The collectors transform but not store the solar energy. The storage is necessary to accomplish in a heat-insulated tank, placed in tempered space. According the current architectural tendencies the boiler rooms are smaller, so the putting of the currently available solar tanks is very difficult. It is necessary to store the energy in a little space. The solution of the problem is the solar tank particularly filled with phase change material. This tank has smaller dimensions and bigger heat capacity than the conventional tanks. The other important advantage of a PCM solar tank is the possibility of the operating of the collectors at lower temperature. It could result a higher efficiency of the solar collector system.

The storage system consists of two simultaneously functioning heat-absorbing units. One of them is a solar water heater and the other a heat storage unit consists of PCM. The solar water heater functions normally and supplies hot water during the day. The storage unit stores the heat in PCM.s during the day and supplies hot water during the night and overcast periods. The storage unit utilizes small cylinders made of filled with paraffin (PCM) as the heat storage medium and integrated with a solar collector to absorb solar energy. The performance of this PCM based thermal energy storage system is compared with conventional sensible heat storage system and the conclusions drawn from them are presented.

II. experimental Setup

For human comfort or to increase the efficiency of a system, temperature maintenance is very important. The ambient temperature of a place tends to increase due to the heat from the outside or due to the heat produced in-house. To capture the excess heat some equipment like chillers, refrigerated air, etc. are being used. This heat can also be captured by energy storage device. PCM is a good energy storage material, which absorbs such excess heat. This excess heats melts the PCM. This character of the PCM does not allow the temperature of the product to increase until the PCM melts completely. Thus for a particular period of time (until the PCM melts completely) we can maintain the temperature. Similarly when a heat source is being used for human comfort like solar water heater, a material like PCM that has high energy storage capacity (latent heat) than water (specific heat) can be used to increase the storage capacity in the same volume.

The water heater is a simple design, and uses a flat panel collector connected to a plastic water tank. There is also a header tank to replace the hot water as it is used. A lot of the material used in the project was recycled. This included both of the water tanks and the metal sheet used in the collector.

C. Solar Energy Collector

Solar energy collectors are special kind of heat exchangers that transform solar radiation energy to internal energy of the transport medium. The major component of any solar system is the solar collector. This is a device which absorbs the incoming solar radiation, converts it into heat, and transfers this heat to a fluid (usually air, water, or oil) flowing through the collector. The solar energy thus collected is carried from the circulating fluid either directly to the hot water or space conditioning equipment or to a thermal energy storage tank from which can be drawn for use at night and/or cloudy days.

There are basically two types of solar collectors: non-concentrating or stationary and concentrating. A non-concentrating collector has the same area for intercepting and for absorbing solar radiation whereas a sun-tracking concentrating solar collector usually has concave reflecting surfaces to intercept and focus the sun's beam radiation to a smaller receiving area, thereby increasing the radiation flux. Solar energy collectors are also distinguished by their motion, i.e., stationary, single axis tracking and two-exes tracking, and the operating temperature.

The performance of a solar collector depends mainly on its optical and thermal efficiencies, determined according to various methods outlined in international standards.

D. Solar Tank

The tank used in this design, the main storage tank, which holds the heated water. Tank is made from HDPE (high density polyethylene) plastic drums, the type often used for water and chemical storage. It is a 10 litre drum.

E. Pump

To circulate the water into the system, diaphragm pump (12 V DC, 1/12 horsepower, rated at 1500 RPM). An on-off switch and inline fuse are mounted next to the flow meter on the solar collector's frame.

F. Transformer

A transformer is an electrical device that transfers energy from one circuit to another by magnetic coupling with no moving parts. A transformer comprises two or more coupled windings, or a single tapped winding and, in most cases, a magnetic core to concentrate magnetic flux. A changing current in one winding creates a time-varying magnetic flux in the core, which induces a voltage in the other windings. Michael Faraday built the first transformer, although he used it only to demonstrate the principle of electromagnetic induction and did not foresee the use to which it would eventually be put.

G. Copper Tube

It contains phase change material in it. Phase change material circulates in this spiral copper tubes with the help of a pump.

III.   ASSEMBLING THE COMPONENT

I made a frame out of 42 x 35mm pine from the local hardware store. This consisted of eight 400mm lengths assembled into a base similar in shape to a stool or tiny table. I used 6mm diameter x 100mm long coach bolts to hold it all together.
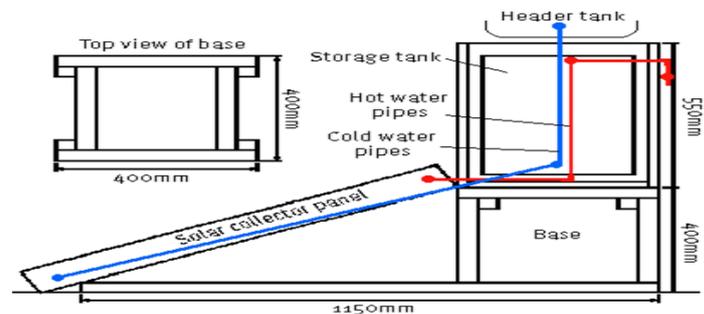
Figure1. The dimensions and assembly of the solar water heater

From the legs of the base ran two horizontal lengths of the same material. This increased the base size enormously and allowed me to attach the collector to the frame at about a 30° angle, making it all one unit. The tank box mounts on top of the frame, with the header tank sitting on top of the box (see figure 1). The tank was connected to the collector using 13mm poly pipe and fittings. As the outlets from the tank and collector were 10mm pipe, I had to slide some 25mm lengths of clear plastic tube over them so the poly pipe would be a snug fit. Use petroleum jelly on the fittings if they feel too tight. You will need to do this to the tank before you assemble it into its box. The inlet and outlet on the tank both had a short length of poly pipe attached, just long enough to bring it outside the box, and a T-fitting was inserted into each of these. The bottom outlet was connected to the bottom inlet of the collector panel, and also to the outlet of the header tank. This allows the main tank to fill with cold water from the bottom. The top tank connections went to the top of the collector panel, and also to a plastic tap mounted on the back of the frame. All of the connections had a crimp-on hose clamp fitted so that they couldn't be pulled off. All right angles were achieved using poly pipe angle connectors, as you can't bend poly pipe very far without it kinking. That is about all there was to it. The header tank was filled with water, and refilled until the main tank had filled. I then gently rocked the whole unit lightly to allow any trapped air to escape.

IV.   conclusions

Solar energy holds the key to future's non-exhaustive energy source. Effective utilization of these resources requires effective storage. Heat storage using 'phase change materials' is a wise alternative. The main applications for PCMs are when space restrictions limit larger thermal storage units in direct gain or sunspace passive solar systems. Research is being conducted on methods of incorporating PCMs into other lightweight building materials such as plywood, as well as ceiling and floor tiles. The systems with PCM are viable option for solar heat energy storage. Possessing considerable advantages over the systems without PCM, it can be used as an alternative to current domestic sensible solar water heating technologies.

References

[1] Leon Freris, David Infield, "Renewable energy in power systems", John Wiley & Sons, 2008.
[2] Rashid .M. H "power electronics Hand book", Academic press, 2007.
[3] Rai. G.D, "Non conventional energy sources", Khanna publishes, 2010.
[4] Ali Keyhani, Design of Smart Power Grid Renewable Energy Systems, John Wiley & Sons, 2011
[5] Wind Electric Systems: S.N.Bhadra,D.Kastha, OXFORD university press, 2005.
[6] Kreith, F. and Kreider, J. F., "Principles of Solar Engineering," McGraw Hill, 1978.
[7] Duffie, J. A., Beckman, W. A., "Solar Engineering of Thermal Processes," John Wiley, 1980.
[8] Veziroglu, N., "Alternative Energy Sources," Volume 5 & 6, McGraw-Hill, 1978.
[9] Sukhatme, S. P., "Solar Energy: Principles of Thermal Collection and Storage," 2nd ed., Tata McGraw-Hill, 2001.
[10]Garg, H.P. and Prakash, J., "Solar Energy: Fundamentals and Applications," Tata McGraw-Hill, 2001.

Analysis of Functionally Graded Variable Thickness Rotating Disc Under Thermo-Mechanical Loading

Manish Garg[1], Dharmpal Deepak[2] and V. K. Gupta[2]

[1]Department of Physics, S.D.College, Barnala-148101

[2]Department of Mechanical Engg.,PunjabiUniversity, Patiala-147002

Abstract: The study investigates thermo-mechanical response of variable thickness rotating disc made of functionally graded materials (FGM). The properties of the disc material, viz. density, young's modulus and coefficient of thermal expansion are assumed as power functions of disc radius. The closed form solutions for stresses and strains in rotating disc are obtained by solving compatibility equations, constitutive equations governing elastic deformations and force equilibrium equation for rotating disc. The effect of varying disc thickness profile and distribution of reinforcement gradient, and radial thermal gradient in the disc are investigated on the elastic stresses and strains in the disc. It is noticed that the distributions of stresses and strains in the disc are significantly affected by varying disc thickness profile and reinforcement gradient in the disc, and on imposing radial temperature distribution. The FGM disc having radially decreasing thickness exhibits the lowest stresses and strains, which are further reduced with the increase in disc thickness gradient. The FGM disc, operating under radially increasing temperature profile exhibits lower radial and and tangential strains over a larger portion of the disc.

Key words: Rotating disc, Functionally graded material, Stress analysis, Thermal gradient, Variable thickness

1. INTRODUCTION

Rotating disc is a widely used component in many engineering applications like turbine rotors, flywheels, automobiles brakes and computer disc drives. In most of these applications, the disc is subjected to several mechanical and/or thermal loadings, thereby causing significant deformations. Therefore, it attracts the attention of many researchers [1-6]. Functionally Graded Material (FGM) is a kind of composite material in which the constituent and/or their structure vary gradually along certain directions so as to achieve the desired variation in properties, satisfying the given application [7-9]. The properties of FGM that may be tailored for desired functionality include chemical, mechanical, thermal and electrical properties. The concept of FGMs has led to the development of superior heat resistant materials while keeping the cost under control.

Several investigators have analyzed elastic stresses in rotating FGM discs. Horgan and Chan [10] investigated the effects of material inhomogeneity on the stresses in linearly elastic, isotropic, constant thickness, solid circular discs rotating at constant angular velocity. They observed that the stresses in inhomogeneousdisc are significantly different from those observed in their homogeneous counterparts. Durodala and Attia [11] performed elastic analysis for rotating hollow and solid FGM discs of constant thickness, subjected to centrifugal load. The study also reveals that for a given total amount of reinforcement, the different forms of reinforcement gradation modify the stresses and displacements fields in the FGM discs, when compared to those observed in disc having uniform distribution of reinforcement. Yeh and Han [12] proposed a symmetric formulation to predict elastic stresses in an inhomogeneous rotating disc with arbitrary thickness, operating under thermal loading. Zenkour [13-14] presented a solution procedure to estimate the distribution of elastic stresses in rotating FGM disc of constant thickness. The study indicates that the stresses and deformations in the FGM disc are lower when the material of the disc is tailored in such a way that the elastic modulus and density are more near the inner radius than those noticed towards the outer radius. Callioglu [15-16] obtained closed-

form solutions for rotating annular FGM disc subjected to internal as well as external pressure. The elastic modulus and density of the disc were assumed to vary radially according to different power law functions. It is observed that with the increase in property gradient, the stresses and deformations in the disc change significantly. Afsar [17] carried out finite element analysis of rotating FGM disc subjected to thermal load. It is observed that thermo-elastic characteristics of the FGM disc are significantly influenced by temperature and thickness profile of the disc, apart from angular speed of the disc. Peng and Li [18] performed elastic analysis for a constant thickness rotating sandwich solid disc made of FGM. The numerical results obtained are observed to be in excellent agreement with the exact solution, for some specific power-law gradients. Callioglu *et al* [19] analyzed elastic stresses in constant thickness rotating FGM disc subjected to internal pressure and radially varying temperature distribution. It is revealed that the tangential stress in the disc increases at the inner surface and decreases at the outer surface, with the increase in values of T_0 (uniform average temperature in the disc) and T_b (temperature at the outer disc surface). The radial stress reduces gradually with increasing values of T_0 and T_a (temperature at the inner surface) but increases with increase in T_b. It is also revealed that the radial displacement in FGM disc subjected to uniform temperature is higher than the FGM disc subjected to temperature gradient.

The literature consulted so far reveals that attempts have been made to analyze elastic stresses in FGM disc having constant thickness. In most of these analyses, the disc has been assumed to operate under uniform temperature. The variable thickness disc performs better than a constant thickness disc [20]. Further, the analyses carried out, mostly assume the disc to operate at constant temperature. However, in numerous applications of rotating disc, viz. turbine rotor and disc brake, the disc is subjected to radial thermal gradient, in addition to mechanical load caused by disc rotation [8, 21]. Keeping this in view, it has been decided to analyze elastic stresses and strains in a variable thickness rotating FGM disc subjected to constant temperature and radially varying temperature distributions. An attempt is also made to investigate the effects of varying disc thickness gradient, reinforcement gradient and radial temperature profile on the elastic stresses and strains in disc.

2.   DISC PROFILE AND MATERIAL PROPERTIES

Let us consider a variable thickness functionally graded rotating disc with the inner radius a (=0.04 m) and the outer radius b (=0.1 m). The thickness $h(r)$ of the disc is assumed to vary radially, according to the following equation,

$$h(r) = h_b \left(\frac{r}{b} \right)^k \tag{1}$$

where h_b is thickness of disc at the outer radius and k is the disc thickness gradation index. The thickness of the disc is assumed to be significantly small compared to its diameter, therefore condition of plane stress (σ_z =0) can be assumed [20].

In this study, we have compared the elastic stresses in variable thickness FGM disc with a similar FGM disc of uniform thickness (t). For the purpose of comparison, the volume of both the FGM discs are kept equal *i.e.*,

$$\int_a^b 2\pi\, rh(r)dr = \pi(b^2 - a^2)t \tag{2}$$

Substituting $h(r)$ from Equation (1) into above equation and simplifying, we get,

$$h_b = \frac{(b^2 - a^2)\,t\,(2+k)\,b^k}{2\,(b^{2+k} - a^{2+k})}$$

(3)

Assuming thickness of uniform disc (t) = 5 mm, one may estimate the value of h_b from equation (3), after substituting the numerical values of a, b and k, as mentioned earlier.

The FGM disc under investigation is assumed to be made of Al-SiC$_p$ composite. The content, $V(r)$, of silicon carbide particles (SiC$_p$) in the FGM disc is assumed to decrease with increasing radial distance (r) according to the following relation,

$$V(r) = V_o \left(\frac{r}{b} \right)^n$$

(4)

Where V_o is the content of SiC$_p$ at the outer disc radius and n is SiCp gradation index. The value of n is chosen -0.5 in this study.

If V_{av} is average SiC$_p$ content in the FGM disc then on equating total SiC$_p$ content in variable thickness FGM disc with that in uniform thickness FGM disc, we get,

$$\int_a^b 2\pi r h(r) V(r) dr = V_{av} \left[\pi (b^2 - a^2) t \right]$$

(5)

Substituting the values of $h(r)$ and $V(r)$, respectively from equations (1) and (4), into equation (5), the minimum SiC$_p$ content (V_o) at the outer radius of FGM disc may be estimated as,

$$V_o = \frac{V_{avg}\, b^n\, (2+k+n)(b^{2+k} - a^{2+k})}{(b^{2+k} - a^{2+k})(2+k)}$$

(6)

The properties of disc material, like density, Young's modulus, coefficient of thermal expansion and thermal conductivity, denoted by a common variable $P(r)$, are assumed to vary radially, according to the following relation,

$$P(r) = P_o \left(\frac{r}{b} \right)^{n_i}$$

(7)

where P_o is the value of property $P(r)$ at the outer radius ($r = b$) and n_i is the property gradation index.

Following equation (7), the density, young's modulus and coefficient of thermal expansion, denoted respectively by $\rho(r)$, $E(r)$ and $\alpha(r)$, at any radius (r) of the FGM disc are given by,

$$\rho(r) = \rho_0 \left(\frac{r}{b} \right)^{n_1}, \quad E(r) = E_0 \left(\frac{r}{b} \right)^{n_2}, \quad \alpha(r) = \alpha_0 \left(\frac{r}{b} \right)^{n_3}$$

(8)

where ρ_o, E_o and α_o are respectively the values of density, young's modulus and coefficient of thermal expansion at the outer radius of FGM disc. The exponents n_1, n_2 and n_3 denotes gradation indices respectively for density, young's modulus and coefficient of thermal expansion. In this study, we have assumed that the FGM disc is subject to linearly varying thermal gradient along the radial directions, as given by,

$$T(r) = T_a + (T_b - T_a)\frac{(r-a)}{(b-a)}$$

(9)

where T_a and T_b respectively denote temperatures, at the inner and outer disc radii.

3. Mathematical formulation

The radial strain (ε_r) and tangential strain (ε_θ) are related to the radial displacement (u_r) by,

$$\varepsilon_r = \frac{du_r}{dr}, \quad \varepsilon_\theta = \frac{u_r}{r}$$

(10)

The above relations yield the following compatibility equation,

$$\varepsilon_r = \varepsilon_\theta + r\frac{d\varepsilon_\theta}{dr}$$

(11)

For elastic deformations, the constitutive equations between elastic stresses and strains for an isotropic FGM disc under plane stress condition are given by [16],

$$\varepsilon_r = \frac{1}{E(r)}(\sigma_r - v\sigma_\theta) + \alpha(r)T(r)$$

(12)

$$\varepsilon_\theta = \frac{1}{E(r)}(\sigma_\theta - v\sigma_r) + \alpha(r)T(r)$$

(13)

where σ_r and σ_θ are respectively the radial and tangential stresses in the disc and v (=0.3) is the Poisson's ratio.

The force equilibrium equation for a variable thickness rotating FGM disc is given as [5],

$$\frac{d}{dr}\left[rh(r)\sigma_r\right] - h(r)\sigma_\theta + \rho(r)\omega^2 r^2 h(r) = 0$$

(14)

where $\rho(r)$ is the density and ω is angular velocity of the disc. The angular velocity (ω) is taken 1570 *rad/s* in this study.

The equilibrium equation (14) is satisfied by the stress function F, defined as,

$$\sigma_r = \frac{F}{rh(r)}, \quad \sigma_\theta = \frac{1}{h(r)}\frac{dF}{dr} + \rho(r)\omega^2 r^2$$

(15)

Substituting the values of ε_r and ε_θ from equations (12) and (13) respectively and using equation (15) into the compatibility equation (11), we can get on simplification,

$$r^2\frac{d^2F}{dr^2}+r\frac{dF}{dr}\left[1-\frac{r}{h(r)}\frac{dh}{dr}-\frac{r}{E(r)}\frac{dE}{dr}\right]+F\left[\frac{vr}{h(r)}\frac{dh}{dr}+\frac{vr}{E(r)}\frac{dE}{dr}-1\right]=-\rho(r)\omega^2r^3h(r)\left[3+\upsilon-\frac{r}{E(r)}\frac{dE}{dr}\right]$$

$$-\omega^2r^4h(r)\frac{d\rho}{dr}-r^2h(r)E(r)\alpha(r)\frac{dT}{dr}-r^2h(r)E(r)T(r)\frac{d\alpha}{dr} \tag{16}$$

Substituting the values of properties from equation (8) into equation (16), we get,

$$r^2\frac{d^2F}{dr^2}+r\frac{dF}{dr}\left[1-k-n_2\right]+F\left[vk+vn_2-1\right]=-\frac{\rho_o\omega^2h_br}{b^{n_1+k}}(3+\upsilon+n_1-n_2)r^{3+n_1+k}$$

$$-\frac{E_o\alpha_oh_b(1+n_3)}{b^{n_2+n_3+k}}\left[\frac{(T_b-T_a)}{(b-a)}\right]r^{2+k+n_2+n_3}-\frac{E_o\alpha_oh_bn_3}{b^{n_2+n_3+k}}\left[T_a-\frac{(T_b-T_a)}{(b-a)}\right]r^{1+k+n_2+n_3} \tag{17}$$

Solving the above this differential equation, the stress function (F) can be obtained as,

$$F=C_1r^{\frac{n_2+k+m}{2}}+C_2r^{\frac{n_2+k-m}{2}}+Ar^{3+n_1+k}+Br^{1+k+n_2+n_3}+Cr^{2+k+n_2+n_3} \tag{18}$$

where C_1 and C_2 are the constants of integration and A, B, C and m are given by,

$$A=\frac{-\rho_o\omega^2h_b(3+v+n_1-n_2)}{b^{n_1+k}(8+n_1{}^2+n_1k+3k+6n_1-n_1n_2-n_2k-3n_2+vn_2+vk)}\quad;\quad m=\sqrt{(n_2+k)^2-4(vn_2+vk-1)}$$

$$B=\frac{E_o\alpha_oh_bn_3}{b^{n_2+n_3+k}(n_3{}^2+n_2n_3+n_3k+k+n_2+2n_3+vn_2+vk)}\left[T_a-\frac{(T_b-T_a)}{(b-a)}\right]$$

$$C=\frac{-E_o\alpha_oh_b(1+n_3)}{b^{n_2+n_3+k}(n_3{}^2+3+n_2n_3+n_3k+2k+2n_2+4n_3+vn_2+vk)}\left[\frac{(T_b-T_a)}{(b-a)}\right]$$

The radial and tangential stresses can be obtained by substituting the values of stress function (F) in equation (15) as,

$$\sigma_r=\frac{1}{h(r)}\left[C_1r^{\frac{n_2+k+m-2}{2}}+C_2r^{\frac{n_2+k-m-2}{2}}+Ar^{2+n_1+k}+Br^{n_2+n_3+k}+Cr^{n_2+n_3+1+k}\right] \tag{19}$$

$$\sigma_\theta=\frac{1}{h(r)}\left[\begin{array}{l}\left(\dfrac{n_2+k+m}{2}\right)C_1r^{\frac{n_2+k+m-2}{2}}+\left(\dfrac{n_2+k-m}{2}\right)C_2r^{\frac{n_2+k-m-2}{2}}+(3+n_1+k)Ar^{2+n_1+k}\\[4pt]+(1+n_2+n_3+k)Br^{n_2+n_3+k}+(2+k+n_2+n_3+)Cr^{1+k+n_2+n_3+}\end{array}\right]+\rho(r)r^2\omega^2 \tag{20}$$

It is assumed that the FGM disc under investigation is fitted on a splined shaft where small axial movement is permitted. Thus, we may use the following free-free boundary conditions [8],

$\sigma_r = 0$ at $r = a$ and $\sigma_r = 0$ at $r = b$ (21)

Using the above boundary condition in equation (19), we get,

$$C_1 = \frac{D_2 b^{\frac{2+m-n_2-k}{2}} - D_1 a^{\frac{2+m-n_2-k}{2}}}{(b^m - a^m)} \quad \text{and} \quad C_2 = \frac{D_1 b^m a^{\frac{2+m-n_2-k}{2}} - D_2 b^{\frac{2+m-n_2-k}{2}} a^m}{(b^m - a^m)}$$ (22)

where,

$$D_1 = -Aa^{2+n_1+k} - Ba^{n_2+n_3+k} - Ca^{n_2+n_3+1+k} \quad D_2 = -Ab^{2+n_1+k} - Bb^{n_2+n_3+k} - Ca^{1+k+n_2+n_3}$$ (23)

4. Results and Discussion

Based on the mathematical formulation presented in previous section, a computer code has been developed to estimate the distributions of elastic stresses and strains in variable thickness FGM disc made of Al-SiC$_p$. The results are estimated for different FGM discs with different thickness profile (refer Table 1). The results obtained for variable thickness FGM discs are compared with those estimated for a similar FGM disc, but of constant thickness. The values of various constants and properties used during the computation process are summarized in Table 2. In order to estimate the values of property gradation indices n_1, n_2 and n_3 (refer equation 8), we have first estimated the variation of SiC$_p$ content, $V(r)$, in different FGM discs, mentioned in Table 1, from equation (4) after substituting the value of V_o from equation 6 for the corresponding disc. Knowing the radial variation of SiC$_p$ in various FGM discs, the radial variation of properties $\rho(r)$, $E(r)$ and $\alpha(r)$ in the FGM discs is estimated by applying rule of mixture [8].

It is important to mention here that unlike earlier works [16, 19], wherein the properties of disc material are assumed to vary in an arbitrary manner, according to power law function having a constant value of power index for all the properties, the present work uses realistic variation of properties. The estimation of material properties at different radial locations of various FGM disc is based on the actual amount of reinforcement (SiCp) present in the given disc. Knowing the radial variation of various properties (ρ, E and α), the values of gradation indices n_1, n_2 and n_3 are estimated by fitting the curve of form $Y = A(X)^N$, available in DATA-FIT software, for various properties. In the preceding regression equation, Y is the property, $X = r/b$, N is the property index and A is the value of property at $r = b$ (i.e. ρ_o, E_o, α_o).

Table 1 Description of FGM discs with varying thickness gradient (TG)

Disc Notation	k	h_a (mm)	h_b (mm)	TG (h_a- h_b) (mm)	SiC$_p$ Content (vol %)			SiC$_p$ Gradient (vol %)
					$V_i (r = a)$	V_{av}	$V_o (r = b)$	($V_i - V_0$)
Disc (D1)	0.5	3.69	5.80	-2.11	27.07	20	17.12	9.95
Disc (D2)	0	5.00	5.00	0	26.66	20	16.86	9.80

Disc (D3)	-0.25	5.78	4.60	1.18	26.45	20	16.73	9.72
Disc (D4)	-0.50	6.66	4.21	2.45	26.25	20	16.60	9.65
Disc (D5)	-0.75	7.65	3.84	3.80	26.02	20	16.46	9.56
Disc (D6)	-1	8.75	3.50	5.25	25.80	20	16.32	9.48

Table 2 Values of material properties and constants

Disc Notation	ρ_o	n_1	E_o	n_2	α_o (x10⁻⁶)	n_3
Disc (D1)	2784.95	-0.01958	134.51	-0.2696	1.9890	0.1045
Disc (D2)	2783.64	-0.01929	133.53	-0.2677	1.9940	0.1026
Disc (D3)	2782.98	-0.01915	133.04	-0.2668	1.9960	0.1016
Disc (D4)	2782.33	-0.01900	132.55	-0.2658	1.9990	0.1007
Disc (D5)	2781.63	-0.01885	132.02	-0.2647	2.0010	0.0997
Disc (D6)	2780.92	-0.01870	131.49	-0.2637	2.0040	0.0987

Before presenting the results obtained in this study, it is necessary to validate the current analysis scheme performed and the software developed. To accomplish this task, the radial stress has been computed for a constant thickness rotating disc having uniform material properties throughout the disc. The values of parameters used for validation are given in Table 3. The results obtained are compared with those estimated earlier [16] by using ANSYS software, for the same kind of disc. A close agreement is observed between the results estimated from the present study and reported earlier (refer Figure 1).

Table 3 Parameters and operating conditions used for validation

a (m)	b (m)	E (GPa)	v	ρ (kg/m³)	ω (rad/s)	n	T_a (K)	T_b (K)
0.04	0.1	72	0.33	2800	1570	0	0	0
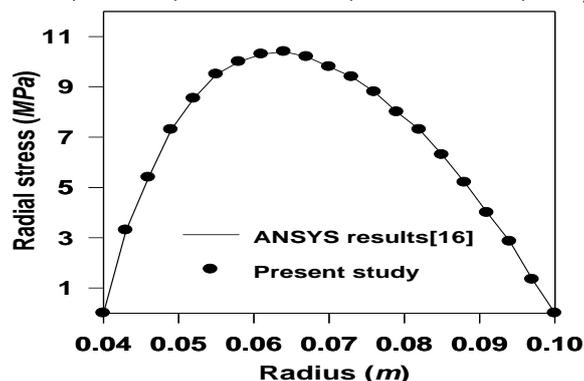
Fig. 1: Comparison of radial stress in disc: Present study vs ANSYS results

4.1   Effect of varying disc thickness profile on elastic stresses and strains

The purpose of this section is to compare elastic stresses and strains in FGM disc having radially increasing thickness with $k= 0.5$ (Disc D1), constant thickness disc $k= 0$ (Disc D2) and radially decreasing thickness with $k= -0.5$ (Disc D4), as mention in Table 1. The variation of disc thickness (h) with radius (r) for the above mentioned three discs is depicted in Fig. 2. For comparison, average thickness (t) of all the FGM discs is kept same as 5 mm.
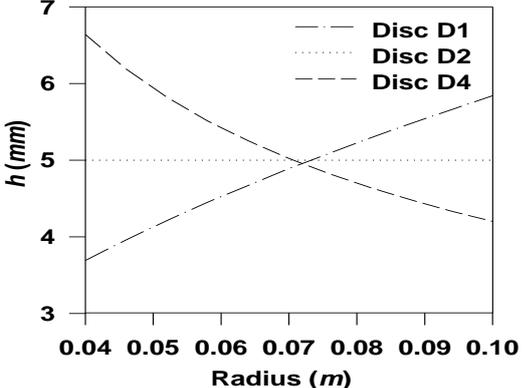
Fig. 2: Variation of disc thickness

The radial stress in all the FGM discs, Fig. 3a, increases from zero at the inner radius, reaches a maximum, before decreasing to zero again at the outer radius, under the imposed boundary conditions given in equation (21). As compared to uniform thickness disc (D2), the radial stress in FGM disc D1 is relatively higher, but in the FGM disc D4, it is relatively lower. The variation noticed in value of radial stress in various FGM discs is more towards the inner radius than noticed near the outer radius. Similar to radial stress, the tangential stress (Fig. 3b)in FGM disc D4, having radially decreasing thickness profile, is significantly lower than the constant thickness FGM disc D2 and FGM disc D1 with radially increasing thickness.
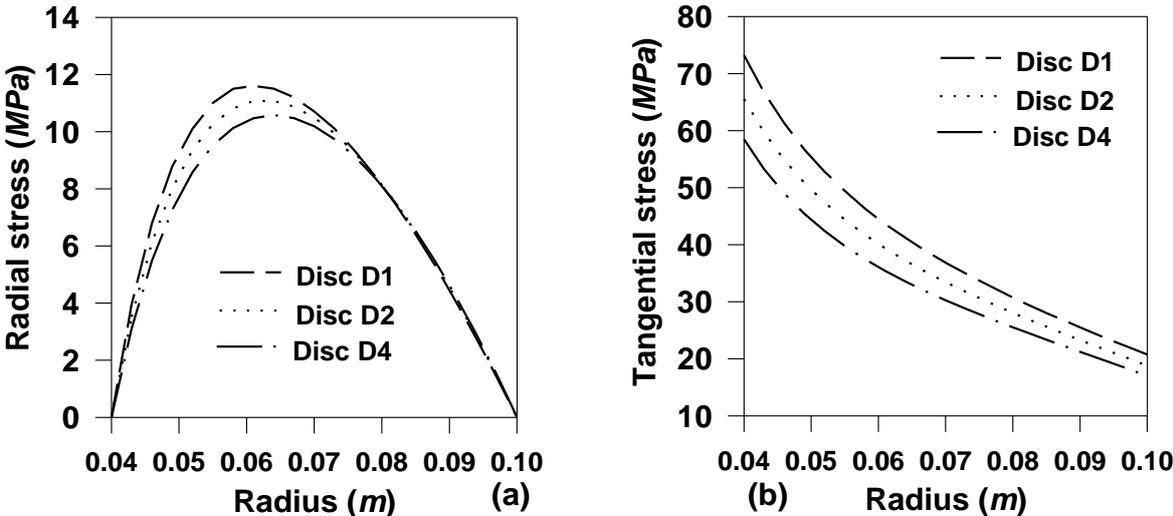
Fig. 3: Variation of: (a) Radial and (b) Tangential stresses in FGM discs.

The radial strain in the FGM discs remains compressive, except for some tensile value in the middle of FGM disc D4 (Fig. 4a). The radial strain in FGM disc D4 is relatively lower than the FGM discs D1 and D2. Similar to radial strain, the tangential strain in FGM disc D4 is lower than the FGM discs D1 and D2 (Fig. 4b). Thus, it is evident that the elastic response of the FGM disc D4, having radially decreasing thickness, is superior to any other FGM discs.
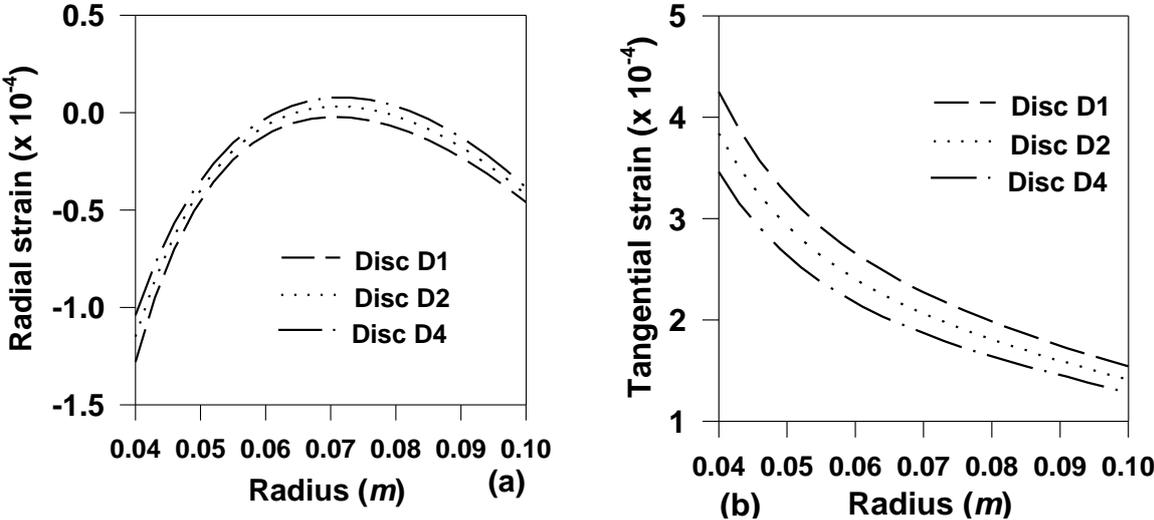
Fig. 4: Variation of: (a) Radial and (b) Tangential strains in FGM discs.

4.2   Effect of varying disc thickness gradient on elastic stresses and strains

It is reflected from section 4.1 that the FGM disc with radially decreasing thickness (k= -0.50) exhibits the lowest stresses and strains. Therefore, in this section we have made an attempt to investigate the effect of varying this kind of radially decreasing disc thickness gradient by varying k from -0.25 to -1. It is revealed from Fig. 5 that on decreasing k from -0.25 to -1 the disc thickness gradient [TG=($h_a - h_b$)] increases and as a result the SiC$_p$ gradient, defined as ($V_i - V_o$), decreases slightly (refer Table 1).
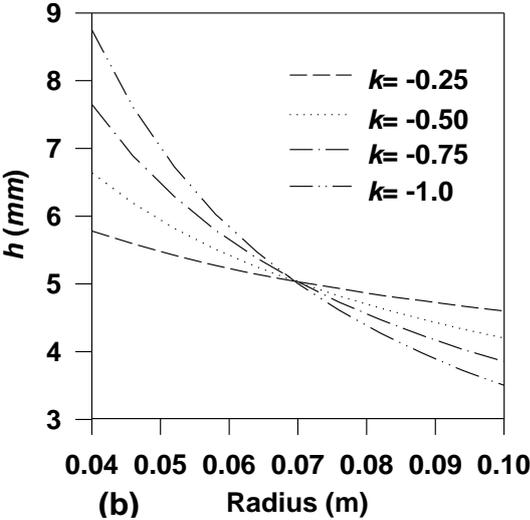
Fig. 5: Variation of disc profile with varying k from -0.25 to -1.0.

With the increase in disc thickness gradient (TG) of the FGM disc, the radial as well as tangential stresses (Figs. 6a and 6b) are observed to decrease over the entire disc. The decrease observed in radial stress is more somewhere in the middle of the disc. The tangential stress on the other hand exhibits relatively higher decrease near the inner radius than that observed towards the outer radius.

The effect of increasing TG on the radial and tangential strains in the FGM disc is shown in Figs. 7a-7b. It is revealed that the radial as well as tangential strain decreases with the increase in TG. It is also evident that with increasing TG, the distributions of strains become relatively uniform.
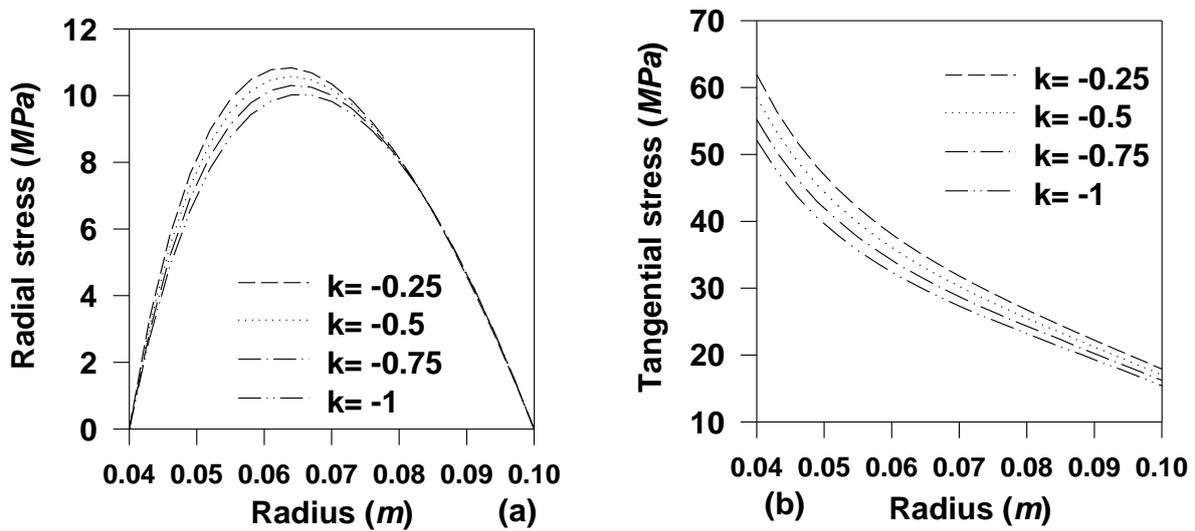
Fig. 6: Effect of increasing disc thickness gradient on (a) Radial and (b) Tangential stresses.
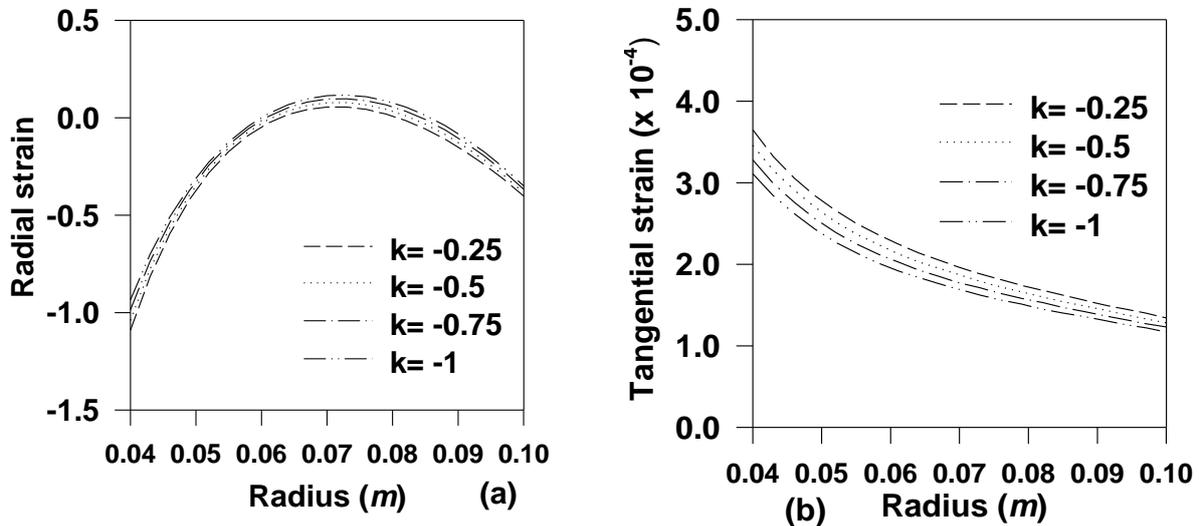
Fig. 7: Effect of thickness gradient on (a) Radial and (b) Tangential strains

4.3   Effect of different temperature profiles on elastic stresses and strain

This section investigates the effect of imposing three different kinds of radial thermal gradients, viz. linearly decreasing; linearly increasing and uniform temperature (refer Table 4), on the elastic stresses and strains in rotating FGM disc. The temperatures at different radial locations are estimated from equation (9). In all the three cases, the average temperature has been kept same as 12.5 K. The FGM disc-T1, operating under a radially decreasing temperature, exhibits the lowest radial stress (Fig. 8a) whereas the disc operating radial increasing radial temperature gradient shows the

highest radial stress. The tangential stress is the lowest in FGM disc T1, near the inner radius, but towards the outer radius it is the lowest in FGM disc T2 (Fig. 8b). The maximum value of tangential stress in FGM disc T1 is significantly reduced as compared to FGM discs T2 and T3 and in addition the distribution of tangential stress is more uniform in disc T1. Upon imposing a radially decreasing thermal gradient in FGM disc (*i.e.* FGM disc T1), the radial strain (Fig. 9c) increases near the inner radius but decreases towards the outer radius, when compared to radial strain in constant temperature FGM disc T3. In some portion, towards the outer radius of the FGM disc T1, the nature of radial strain become compressive. The imposition of radially increasing thermal gradient, as in FGM disc T2, reduces the radial strain near the inner radius but increases its value towards the outer radius. Except for some portion near the inner radius, the radial strain in FGM disc T2 is always tensile. The tangential strain (Fig., 9b) is the highest in FGM disc T1 and the lowest in FGM disc T2, except for some portion near the outer radius where the trend is just opposite (Fig. 9b).

Table 4 Description of FGM disc under thermal distribution

Disc notation	T_a (K)	T_b (K)	T_{avg} (K)
Disc (T1)	25	0	12.5
Disc (T2)	0	25	12.5
Disc (T3)	12.5	12.5	12.5
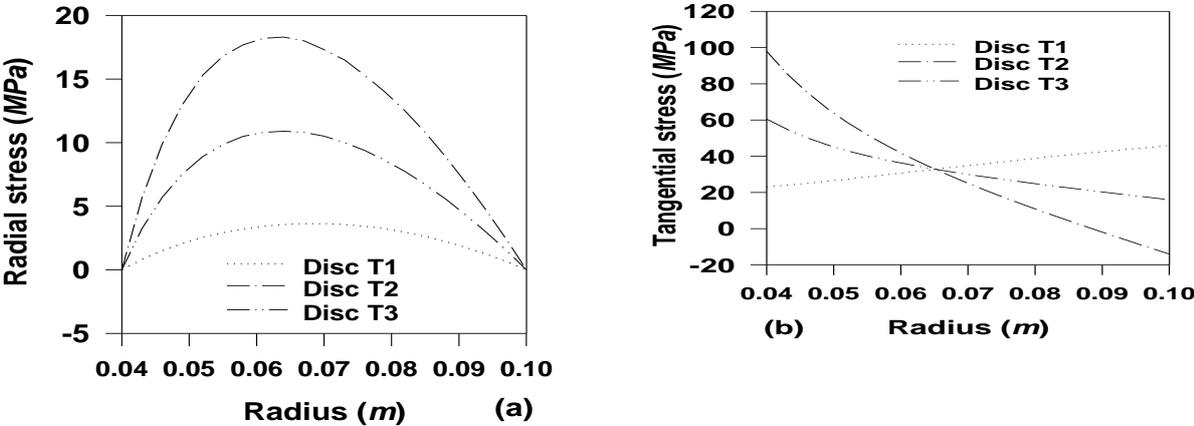
Fig. 8: Effect of temperature profiles on stresses in FGM disc
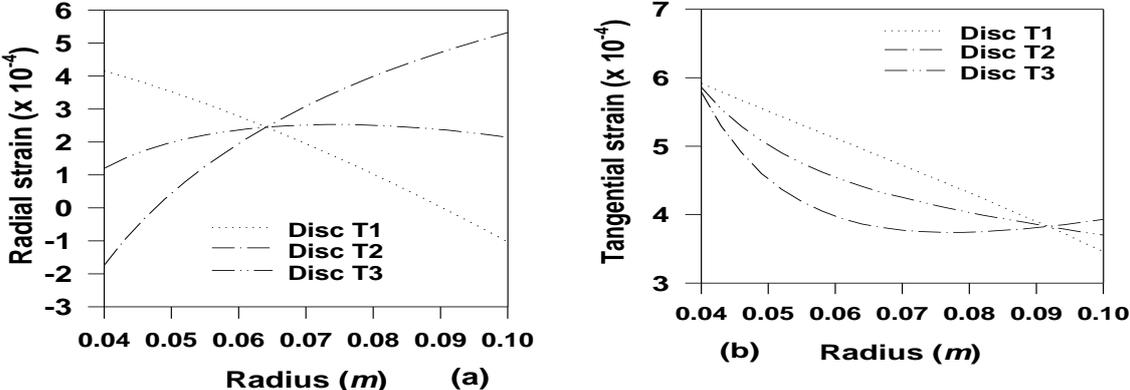
Fig. 9: Effect of temperature profiles on strains in FGM disc

5. Conclusions

The study has led to the following conclusions:

   i. The elastic stresses and strains in rotating FGM disc could be reduced by employing disc having radially decreasing thickness profile. The stresses and strains in the FGM disc are further reduced with the increase in disc thickness gradient.

  ii. The radial stress (over the entire disc) and tangential stress (near the inner radius) are lower in FGM disc operating under a linearly decreasing radial thermal gradient as compared to FGM disc operating under linearly increasing radial thermal gradient or constant temperature. However, the FGM disc operating under a linearly increasing radial thermal gradient shows the lower tangential stress towards the outer radius.

 iii. The radial strain near the inner radius is the lowest in FGM disc operating under a radially increasing temperature profile but towards the outer radius it is lowest in FGM disc operating under a linearly decreasing temperature. The tangential strain in FGM disc operating under a radially increasing temperature is the lowest, except for some portion towards the outer radius where the it is the lowest in FGM disc subjected to radially decreasing temperature.

References

1. Reddy T Y, Srinath H, *Int J Mech Sci* **16** (1974) 85.
2. Gurushankar G V, *J strain anal Eng***10** (1975) 137.
3. Gupta V K, Singh S B, Chandrawat H N and Ray S, *Eur J Mech A-Solid***23** (2004) 335.
4. Jahed H, Farshi B and Bidabadi J, *Int J Pres Ves Pip***82** (2005) 35.
5. Timoshenko S P and Goodier J N, *Theory of Elasticity*, McGraw Hill, California (1970).
6. Ugural A C and Fenster S K, *Advanced Strength and Applied Elasticity*, Elsevier, New York (1981).
7. Groves J F and Wadley H N G, *Compos Part B-Eng***28** (1997) 57.
8. Gupta V K, Singh S B, Chandrawat H N and Ray S, *J Eng Mater-T ASME* **127** (2005) 97.
9. Birman V and Byrd L W, *Appl Mech Rev***60** (2007) 95.
10. Horgan C O and Chan A M, *J Elasticity***55** (1999) 219.
11. Durodola J F and Attia O, *Mater Sci Tech***16** (2000) 919.
12. Yeh K Y and Han R P S, *J Appl Mech***61** (1994) 186.
13. Zenkour A M, *J Mater Sci***42** (2007) 9717-9724.
14. Zenkour A M, *J Mater Process Tech***209** (2009) 3511.
15. Callioglu H, *Adv Compos Lett***17**(2008) 147.
16. Callioglu H, Bektas N B and Sayer M, *Acta Mech Sin***27** (2011) 950.
17. Afsar A M and Go J, *Appl Math Model***34** (2010) 3309.
18. Peng X L and Li X F, *J Mech Sci Technol***26** (2012) 1483.
19. Callioglu H, Sayer M and Demir E, *Indian J Eng Mater S***18** (2011) 111.
20. Garg M, Salaria B S and Gupta V K, *Mater Sci Forum***736** (2012) 183.
21. Garg M, Salaria B S and Gupta V K, *Procedia Eng* **55** (2013) 542.

Modeling creep in a variable thickness composite disc with thermal residual stresses

[1]Dharmpal Deepak,[2]Manish Garg, [*3]V.K. Gupta

[1,3] Mechanical Engineering Department,,Punjabi University, Patiala-147002 (Pb.), India

[2].S.D. College, Barnala -148101 (Pb.), India

*Corresponding Author
E mail ID: guptavk_70@yahoo.co.in,
Phone: +91-9501007560, +91-175-2280166, *Fax* : +91-1753046333

Abstract

Creep analysis of a rotating disc with linearly varying thickness in the presence of residual stress, induced due to processing, is presented. The disc under investigation is made of 6061Al–SiCw. The creep behavior of the composite has been described by threshold based creep law by assuming a stress exponent of 5. The effect of different yield stresses of the composite under tension and compression has been investigated on the creep deformation of rotating disc. Theradial and tangential stresses in the composite disc are slightly affected by the presence of tensile residual stress. However, in the presence of thermal residual stresses, the steady state strain rates in the composite disc increase significantly as compared to those obtained in a similar disc but without residual stresses. In order to improve creep performance of the composite disc some stress relieving treatments must be performed on the composite disc before using it in actual practice.

Keywords: Creep, Composite, Variable thickness disc, Residual stresses

1. Introduction

Rotating disc is a common component in steam and gas turbine rotors, turbo generators, pumps, compressors, flywheels, automotive braking systems, ship propellers, computer disc drives and in a number of other dynamic applications [1–4]. In most of these applications, the disc has to operate under elevated temperature and is simultaneously subjected to high stresses caused by the rotation of the disc at high speed [5]. As a result of severe mechanical and thermal loadings, the material of the disc undergoes creep deformations and thereby affecting its performance [1, 6–7]. For example in turbine rotor, there are chances that heat from the external surface transmits to the shaft and then to the bearings, which poses adverse effects on its functioning and efficiency [8].

Under these conditions, the rotating disc made of monolithic material may not perform well. The excellent mechanical properties like high specific strength and stiffness, and high temperature stability offered by aluminium matrix composites reinforced with SiC particles, whiskers or fibers make them suitable for rotating disc applications exposed to elevated temperature [1, 9–10].

Processing of metal matrix composites often involves cooling from higher temperatures which induces residual tensile thermal stresses in metal matrix, due to mismatch in coefficient of thermal expansion between the matrix and the reinforcement phase. The magnitude of thermal residual stresses is estimated by determining the difference in yield strength of composite under tension and compression [11–14].

Singh and Ray [15] analyzed the effect of thermal residual stresses on the steady state creep in a constant thickness rotating disc made of whisker reinforced metal matrix composite. The study indicates that the presence of thermal residual stresses in the composite disc leads to higher strain rates as compared to a similar disc but without residual stresses. Sen and Aldas [4] estimated thermal stresses in a thermoplastic composite disc using finite element method. The magnitude and distributions of thermal and residual stresses are observed to be significantly influenced by the increase in linear temperature loads.

Some of the studies [16-18] indicate that the stresses in rotating discs having variable thickness, with more thickness at the centre than the periphery, are much lower than that observed in a constant thickness disc operating at the same angular velocity. By using variable thickness disc, the plastic limit angular velocity increases and the magnitude of stresses and deformations in the disc reduces [18]. The use of variable thickness disc helps in minimizing the weight of disc used in aerospace applications [19]. Gupta et al. [20] also observed that a rotating disc having radially decreasing density and thickness is much safer in comparison to a flat disc with radially variable density. Deepak et al. [21] observed that the stresses and strain rates in a rotating disc made of isotropic composite can be significantly reduced by selecting linearly varying thickness profile as compared to hyperbolic or constant thickness profile.

The present study is an attempt to investigate the effect of residual stresses in a 6061Al-SiCw (subscript w stands for whisker) composite rotating disc having linearly varying thickness on its steady state creep behavior. A mathematical model is developed to investigate the steady creep behavior of a variable thickness composite disc in the presence of thermal residual stresses. The stresses and strain rates are estimated and compared to that obtained for a similar disc but without residual stresses.

2.   Creep law and creep parameter

The disc under investigation is assumed to be made of aluminium alloy matrix reinforced with silicon carbide whiskers (SiCw). The material of the disc undergoes steady state creep according to following creep law [22–23],

$$\dot{\bar{\varepsilon}} = A' \left(\frac{\bar{\sigma} - \sigma_0}{E} \right)^n \exp\left(\frac{-Q}{RT} \right)$$

(1)

where $\dot{\bar{\varepsilon}}, \bar{\sigma}, \sigma_0, A', n, Q, E, R$ and T denote respectively the effective strain rate, effective stress, threshold stress, structure dependent parameter, true stress exponent, true activation energy, temperature-dependent young's modulus, gas constant and operating temperature.

The value of true stress exponent n in Eq. (1) is usually selected as 3, 5 or 8, which correspond to the following three well-documented creep cases for metals and alloys: (i) $n = 3$ for creep controlled by viscous glide processes of dislocation, (ii) $n = 5$ for creep controlled by high temperature dislocation climb (lattice diffusion), and (iii) $n = 8$ for lattice diffusion-controlled creep with a constant structure [22]. Though, a few research groups [24–26] have used a true stress exponent of 8 to describe the steady state creep in Al/Al alloy reinforced with SiCp,w (subscript 'p' for particle and 'w' for whisker) composites but a number of other research groups [27–34] have noticed that a stress exponent of either ~3 or ~5

provides a better description of steady state creep data of discontinuously reinforced Al–SiC composites. In this light, a stress exponent (*n*) of 5 is used to describe the steady state creep behavior of the composite disc in this study.

The creep law given by Eq. (1) may alternatively be written as:

$$\dot{\bar{\varepsilon}} = \left[M(\bar{\sigma} - \sigma_0) \right]^n \tag{2}$$

where $M = \dfrac{1}{E} \left(A' \exp \dfrac{-Q}{RT} \right)^{1/n}$

The creep parameters *M* and σ_o appearing in Eq. (2) are dependent on the type of material and the operating temperature (*T*). In a composite, the dispersoid-size (*P*) and content (*V*) are the primary material variables affecting the values of these parameters. In the present study, the values of *P*, *V* and *T* are taken respectively as 1.23 μm, 10 vol.% and 723 K. The creep parameters *M* and σ_0 for 6061Al–SiCw composites can be obtained from the following regression equations, as developed by Singh and Gupta [35],

$$M(r) = 0.02876 - \frac{0.00879}{P} - \frac{14.02666}{T} + \frac{0.03224}{V(r)} + dM_1 + dM_2 \tag{3}$$

$$\sigma_o(r) = -0.084P - 0.0232T + 1.1853(V(r)) + 22.207 + d\sigma_{o_1} + d\sigma_{o_2} \tag{4}$$

where the terms dM_1 and $d\sigma_{o_1}$ compensate the effect of incorporating SiC particles in 6061Al matrix instead of pure Al matrix and the additions of dM_2 and $d\sigma_{o_2}$ take into account the effect of incorporating SiC whisker instead of SiC particle in 6061Al matrix. The values of creep parameters *M* and σ_0 are estimated from Eqs. (3) and (4) respectively as 0.00931 s$^{-1/5}$/ MPa and 46.293 MPa for 6061Al–SiCw composite by taking P = 1.23 μm, V = 10 vol.% and T = 723 K.

3.   Mathematical formulation

The material of the disc assumed to be is isotropic that yields according to Hoffman's yield criterion which accounts for different yield stresses under compression (f_c) and tension (f_t) [36],

$$f(\sigma_{ij}) = \frac{1}{3} \left[(\sigma_{11}^2 + \sigma_{22}^2 + \sigma_{33}^2) - (\sigma_{11}\sigma_{22} + \sigma_{22}\sigma_{33} + \sigma_{33}\sigma_{11}) \right] + \frac{(f_c - f_t)}{f_c f_t} (\sigma_{11} + \sigma_{22} + \sigma_{33}) \tag{5}$$

The strain increment $d\varepsilon_{ij}$ of a yield surface $f(\sigma_{ij})$ is given by [37],

$$d\varepsilon_{ij} = d\lambda \frac{\partial f}{\partial \sigma_{ij}}$$

(6)

where $d\lambda$ is the proportionality factor depending upon σ_{ij}, $d\sigma_{ij}$ and ε_{ij} apart from strain history because of strain hardening.

Using the yield criterion given by Eq. (5) into Eq. (6), one gets the following constitutive equations in terms of principal strain increments $d\varepsilon_{11}$, $d\varepsilon_{22}$ and $d\varepsilon_{33}$ and principal stresses σ_{11}, σ_{22} and σ_{33},

$$d\varepsilon_{11} = \left[\frac{2}{3}\left(\sigma_{11} - \frac{(\sigma_{22} + \sigma_{33})}{2}\right) + \frac{(f_c - f_t)}{f_c f_t} \right] d\lambda$$

$$d\varepsilon_{22} = \left[\frac{2}{3}\left(\sigma_{22} - \frac{(\sigma_{11} + \sigma_{33})}{2}\right) + \frac{(f_c - f_t)}{f_c f_t} \right] d\lambda$$

(7)

$$d\varepsilon_{33} = \left[\frac{2}{3}\left(\sigma_{33} - \frac{(\sigma_{11} + \sigma_{22})}{2}\right) + \frac{(f_c - f_t)}{f_c f_t} \right] d\lambda$$

The effective stress $(\bar{\sigma})$ and the effective strain $(\bar{\varepsilon})$ are related as [37],

$$d\bar{\varepsilon} = \frac{2}{3} \bar{\sigma} d\lambda$$

(8)

Using Eq. (8) into Eq. (7), we get,

$$d\varepsilon_{11} = \frac{d\bar{\varepsilon}}{\bar{\sigma}}\left[\sigma_{11} - \frac{(\sigma_{22} + \sigma_{33})}{2} + \frac{3(f_c - f_t)}{2 f_c f_t} \right]$$

$$d\varepsilon_{22} = \frac{d\bar{\varepsilon}}{\bar{\sigma}}\left[\sigma_{22} - \frac{(\sigma_{11} + \sigma_{33})}{2} + \frac{3(f_c - f_t)}{2 f_c f_t} \right]$$

(9)

$$d\varepsilon_{33} = \frac{d\bar{\varepsilon}}{\bar{\sigma}}\left[\sigma_{33} - \frac{(\sigma_{11} + \sigma_{22})}{2} + \frac{3(f_c - f_t)}{2 f_c f_t} \right]$$

Integrating above set of equations, we get,

$$\dot{\varepsilon}_{11} = \frac{\dot{\bar{\varepsilon}}}{2\bar{\sigma}}[2\sigma_{11} - (\sigma_{22} - \sigma_{33}) + Y]$$

$$\dot{\varepsilon}_{22} = \frac{\dot{\bar{\varepsilon}}}{2\bar{\sigma}}[2\sigma_{22} - (\sigma_{11} - \sigma_{33}) + Y]$$

(10)

$$\dot{\varepsilon}_{33} = \frac{\dot{\bar{\varepsilon}}}{2\bar{\sigma}}[2\sigma_{33} - (\sigma_{11} - \sigma_{22}) + Y]$$

where $\quad Y = \dfrac{3(f_c - f_t)}{f_c f_t}$

The generalized constitutive Eqs. (10) for creep in an isotropic composite with different yield strength in tension and compression takes the following form when the reference frame is along the principal directions r, θ and z of the composite disc,

$$\dot{\varepsilon}_r = \frac{\dot{\bar{\varepsilon}}}{2\bar{\sigma}}\left[2\sigma_r - (\sigma_\theta + \sigma_z) + Y\right]$$

$$\dot{\varepsilon}_\theta = \frac{\dot{\bar{\varepsilon}}}{2\bar{\sigma}}\left[2\sigma_\theta - (\sigma_r + \sigma_z) + Y\right]$$

(11)

$$\dot{\varepsilon}_z = \frac{\dot{\bar{\varepsilon}}}{2\bar{\sigma}}\left[2\sigma_z - (\sigma_r + \sigma_\theta) + Y\right]$$

where, $\dot{\varepsilon}_r, \dot{\varepsilon}_\theta$ and $\dot{\varepsilon}_z$ and $\sigma_r, \sigma_\theta, \sigma_z$ are respectively the strain rates and the stresses along r, θ and z directions.

Let us assume a composite disc made of 6061Al–10 vol.% SiCw with the inner and outer radii a and b respectively, having variable thickness (h) and rotating at an angular velocity of ω (radian /sec). The analysis carried out is based on the following assumptions:

(i)   The disc material is incompressible and isotropic.
(ii)   Stresses at any point in the disc remain constant with time i.e. steady state condition of stress is assumed.
(iii) Elastic deformations in the disc are small, therefore, neglected as compared to creep deformations.
(iv)   The axial stress (σ_z) is zero throughout the disc.

Let A and A_0 denote respectively the area of transverse section of the disc element with outer radii r and b respectively but with the same inner radius a. The A and A_0 are expressed as,

$$A = \int_a^r h\,\mathrm{d}r \quad \text{and} \quad A_0 = \int_a^b h\,\mathrm{d}r$$

(12)

Similarly, the polar moment of area I and I_0 of these disc elements may be expressed as,

$$I = \int_a^r hr^2 \mathrm{d}r \qquad \text{and} \qquad I_0 = \int_a^b hr^2 \mathrm{d}r \tag{13}$$

The average tangential stress $(\sigma_{\theta_{av}})$ in the disc is given by,

$$\sigma_{\theta_{av}} = \frac{1}{A_0} \int_a^b h\sigma_\theta \mathrm{d}r \tag{14}$$

Under biaxial state of stress (i.e. $\sigma_z = 0$), the set of Eqs. (11) becomes,

$$\dot{\varepsilon}_r = \frac{\dot{\bar{\varepsilon}}}{2\bar{\sigma}}[2\sigma_r - \sigma_\theta + Y]$$

$$\dot{\varepsilon}_\theta = \frac{\dot{\bar{\varepsilon}}}{2\bar{\sigma}}[2\sigma_\theta - \sigma_r + Y] \tag{15}$$

$$\dot{\varepsilon}_z = \frac{\dot{\bar{\varepsilon}}}{2\bar{\sigma}}[-\sigma_r - \sigma_\theta + Y]$$

According to Hoffmann's yield criterion given by Eq. (5), the effective stress $(\bar{\sigma})$ in a rotating disc subjected to biaxial state of stress may be expressed as,

$$\bar{\sigma} = [\sigma_\theta^2 + \sigma_r^2 + \sigma_r\sigma_\theta + q(\sigma_r + \sigma_\theta)]^{1/2} \tag{16}$$

where $q = (f_c - f_t)$. The yield stresses in compression (f_c) and tension (f_t) of 6061Al–10 vol.% SiCw composite are taken respectively as 218 MPa and 186 MPa, as reported by Badini [12].

Substituting the values of $\dot{\bar{\varepsilon}}$ and $\bar{\sigma}$ respectively from Eq. (2) and Eq. (16) into the first equation amongst set of Eqs. (15), one gets,

$$\dot{\varepsilon}_r = \frac{\mathrm{d}\dot{u}_r}{\mathrm{d}r} = \frac{[(2x-1)+(Y/\sigma_\theta)]}{2[(x^2-x+1)+(q/\sigma_\theta^2)(\sigma_r+\sigma_\theta)]^{1/2}}[M(\bar{\sigma}-\sigma_0)]^n \tag{17}$$

where $x(=\sigma_r/\sigma_\theta)$ is the ratio of radial and tangential stresses and $\dot{u}_r(=\mathrm{d}u/\mathrm{d}t)$ is the radial deformation rate.

Similarly, the second equation amongst set of Eqs. (15) becomes,

$$\dot{\varepsilon}_\theta = \frac{\dot{u}_r}{r} = \frac{[(2-x)+(Y/\sigma_\theta)]}{2[(x^2-x+1)+(q/\sigma_\theta^2)(\sigma_r+\sigma_\theta)]^{1/2}}[M(\bar{\sigma}-\sigma_0)]^n \tag{18}$$

139

Dividing Eq. (17) by Eq. (18) and integrating the resulting equation between limits a to r, we obtain,

$$\dot{u}_r = \dot{u}_a \exp\left[\int_a^r \frac{\phi(r)}{r} \, dr\right]$$

(19)

where $\dot{u}_a$ is the radial deformation rate at the inner radius and $\phi(r)$ is given by,

$$\phi(r) = \frac{(2x-1) + Y/\sigma_\theta}{(2-x) + Y/\sigma_\theta}$$

Substituting $\dot{u}_r$ from Eq. (19) into Eq. (18) and simplifying, we get the tangential stress (σ_θ) as,

$$\sigma_\theta = \frac{\dot{u}_a^{1/n} \psi_1(r)}{M} + \psi_2(r)$$

(20)

where,

$$\psi_1(r) = \frac{\psi(r)^{1/n}}{[(x^2 - x + 1) + (q/\sigma_\theta^2)(\sigma_r + \sigma_\theta)]^{1/2}} \; ; \quad \psi_2(r) = \frac{\sigma_0}{[(x^2 - x + 1) + (q/\sigma_\theta^2)(\sigma_r + \sigma_\theta)]^{1/2}}$$

(21)

and,

$$\psi(r) = \frac{2[(x^2 - x + 1) + (q/\sigma_\theta^2)(\sigma_r + \sigma_\theta)]^{1/2}}{[(2-x) + (Y/\sigma_\theta)]} \exp\left(\int_a^r \frac{\phi(r)}{r} \, dr\right)$$

(22)

Considering the equilibrium of forces acting on an element of the disc having varying thickness (h), the force equilibrium equation may be written as [16],

$$\frac{d}{dr}(hr\sigma_r) - h\sigma_\theta + \rho\omega^2 r^2 h = 0$$

(23)

where ρ is density of the composite disc.

If the disc is fitted over a splined shaft where small axial movement is allowed, a free-free condition applies [38]. Therefore,

$$\sigma_r = 0 \text{ at } r = a \text{ and } \sigma_r = 0 \text{ at } r = b$$

(24)

Integrating Eq. (23) between limits a to b under the imposed boundary conditions given in Eq. (24), we get,

$$\int_a^b h\sigma_\theta\,\mathrm{d}r = \rho\omega^2 I_0 \tag{25}$$

Multiplying Eq. (20) by $h\mathrm{d}r$ and integrating the resulting equation between limits a to b, we get,

$$\frac{\dot{u}_a^{1/n}}{M} = \frac{A_0\sigma_{\theta_{av}} - \int_a^b h\psi_2(r)\,\mathrm{d}r}{\int_a^b h\psi_1(r)\,\mathrm{d}r} \tag{26}$$

where $\sigma_{\theta_{av}} = \dfrac{1}{A_0}\int_a^b h\sigma_\theta\,\mathrm{d}r = \dfrac{\rho\omega^2 I_0}{A_0}$, as evident from Eqs. (14) and (25).

Substituting the value of $\dfrac{\dot{u}_a^{1/n}}{M}$ from Eq. (26) into Eq. (20), we get σ_θ as,

$$\sigma_\theta = \frac{\psi_1(r)\left[A_0\,\sigma_{\theta av} - \int_a^b h\psi_2(r)\,\mathrm{d}r\right]}{\int_a^b h\psi_1(r)\,\mathrm{d}r} + \psi_2(r) \tag{27}$$

Integrating equilibrium Eq. (23) between limits a to r, we obtain,

$$\sigma_r = \frac{1}{hr}\left[\int_a^r h\sigma_\theta\,\mathrm{d}r - \rho\omega^2 I\right] \tag{28}$$

The tangential and radial stresses at any point within the composite disc are estimated from Eqs. (27) and (28) respectively. Thereafter, the strain rates $\dot{\varepsilon}_r$ and $\dot{\varepsilon}_\theta$ are estimated respectively from Eqs. (17) and (18).

4.   Disc thickness

The thickness (h) of the composite disc is described by the following linear function,

$$h = h_b + 2C(b-r) \tag{29}$$

where $C = \dfrac{(h_a - h_b)}{2(b-a)}$ is a constant, h_a and h_b are the disc thickness at the inner and outer radii respectively.

The average disc thickness (h_{avg}) is given by,

$$h_{avg} = \frac{\int_a^b 2\pi\, rh\, \mathrm{d}r}{\pi(b^2 - a^2)} \tag{30}$$

Substituting h from Eq. (29) into Eq. (30), we get,

$$h_a = \frac{3(b+a)h_{avg} - h_b(2b+a)}{(b+2a)} \tag{31}$$

The values of a and b are taken respectively as 31.75 and 152.4 mm. The average disc thickness (h_{avg}) is assumed to be 25.4 mm. The dimensions of the disc assumed are similar to the work reported by Bhatnagar et al. [16].

By assuming h_b = 13.97 mm, a = 31.75 mm, b = 152.4 mm and h_{avg} = 25.4 mm, we get h_a = 43.22mm from Eq. (31).

5.   Numerical computations

Following analytical procedure outlined in Section 3, the stresses and strain rates are evaluated in the composite disc by an iterative numerical scheme described in Fig. 1. To begin with, we estimate average tangential stress in the composite disc from equation: $\sigma_{\theta av} = \dfrac{\rho \omega^2 I_0}{A_0}$. To find first approximation of x, to be used in Eq. (22), we assume that $\sigma_\theta = \sigma_{\theta av}$ in Eq. (28) and obtain the first approximation of σ_r i.e. $[\sigma_r]_1$. The subscript represents the iteration number. Dividing $[\sigma_r]_1$ by $\sigma_{\theta av}$, we get $[x]_1$, which on substituting in Eq. (22) for x gives $[\psi]_1$. Using $[\psi]_1$ in Eq. (21), $[\psi_1]_1$ and $[\psi_2]_1$ are estimated, which are used in Eq. (26) to get $(\dot{u}_a^{1/n})_1$. Substituting $[\psi_1]_1$, $[\psi_2]_1$ and $(\dot{u}_a^{1/n})_1$ in Eq. (27), we get $[\sigma_\theta]_1$. Using $[\sigma_\theta]_1$ for $[\sigma_\theta]$ in Eq. (28), the second approximation of σ_r i.e. $[\sigma_r]_2$ is obtained, which is used to estimate the second approximation of x, i.e., $[x]_2$. The iteration process is carried out till the process converges and yields the values of stresses at different points along the radius. For rapid convergence, 75 % of the value of σ_θ estimated in the current iteration has been mixed with 25 % of the value of σ_θ estimated in the previous iteration and the resulting value is used in the next iteration. Knowing σ_r and σ_θ, the radial and tangential strain rates in the composite disc are estimated respectively from Eqs. (17) and (18).

6.   Results and discussion

On the basis of mathematical formulation presented in Section 3, a computer code has been developed to calculate the distribution of stresses and strain rates in the rotating composite discs with and without residual thermal stresses.

6.1.   Validation

Before estimating the results in this study, it is imperative to validate the analysis carried out and the software developed. In order to achieve this goal,the radial and tangential creep strains have been computed for a rotating steel disc by using the current analytical procedure. The results obtained are compared with the available experimental results for steel disc [39]. The operating conditions, dimensions and creep parameters used for steel disc are summarized in Table 1. To obtain creep parameters M and σ_0 for steel disc, the creep law given in Eq. (2) is integrated between limits of t from 0 to t;

$$\bar{\varepsilon} = [M(\bar{\sigma} - \sigma_0)]^n \int_0^t f(t)\,\mathrm{d}t$$

(32)

where $\bar{\varepsilon}$ is the effective strain and $f(t)$ is a function of time t. The function $f(t)$ is assumed to be unity in this study, similar to those described in the study of Wahl et al. [39]. Wahl et al. [39] noticed that the average strain at the end of 180 hrs corresponding to a mean stress $(\bar{\sigma})$ = 25 150 psi is 0.0109 in/in and at a mean stress $(\bar{\sigma})$ = 29 450 psi, the strain is 0.029 in/in. Using these values in Eq. (32), the creep parameters M and σ_0 for steel disc are obtained respectively as 2.05×10^{-4} $s^{-1/5}$/ MPaand 35.98 MPa. These parameters are used in the developed software to compute the distribution of tangential and radial creep strains in the steel disc. A close agreement is obtained between the analytical and the experimental results reported by Wahl et al. [39], Fig. 2, which inspires confidence in the analysis carried out and the software developed.

6.2 Distribution of stresses and strain rates

The steady state creep stresses and strain rates have been computed for a composite disc made of 6061Al– 10 vol.% SiCw and having residual thermal stress of magnitude 32 MPa. The yielding is described by Hoffman's yield criterion, which in the limiting case, when $f_c = f_t$, converges to von Mises yield criterion. The results are also estimated for a similar composite disc but without residual stress (*i.e.* $f_c = f_t$).

The radial stress, shown in Fig. 3a increases from zero at the inner radius, reaches maximum before dropping to zero again at the outer radius under the imposed boundary conditions given in Eq. (24). The radial stress in the composite disc with thermal residual stress is slightly higher than those observed in a similar composite disc but without residual stress. The maximum variation observed in radial stress between both the discs is around 1.97 MPa at a radius of 51.86 mm. The effect of residual stresses on tangential stress is shown in Fig. 3b. In the presence of residual stress, the tangential stress increases slightly near the inner and outer radii but decreases marginally in the middle of the disc, when compared with a similar composite disc without residual stress. The maximum variation observed in tangential stress between both the discs is around 8.91 MPa at inner radius.

The presence of residual stress in composite disc leads to increase in the effective stress in the disc, Fig. 3c. The increase observed is slightly higher near the inner radius than that observed towards the outer radius. The maximum increase observed in effective stress is around 23.3 MPaat the inner radius of the disc. Therefore, it is quite evident from the above discussion that the presence of residual stress leads to increase the values of stresses in the disc, except for a slight decrease observed in tangential stress in the middle of the disc.

The strain rates in the composite disc are dependent on the effective strain rate ($\dot{\bar{\varepsilon}}$), which is a function of stress difference $(\bar{\sigma} - \sigma_0)$, as revealed from the creep law given by Eq. (1). Therefore, to investigate the effect of residual stress on the creep rates, the distribution of $(\bar{\sigma} - \sigma_0)$ is represented in Fig. 4. The effect of residual stress on stress difference $(\bar{\sigma} - \sigma_0)$ is similar to those noticed for effective stress in Fig. 3c.

As a result of higher $(\bar{\sigma} - \sigma_0)$ in the composite disc with thermal residual stress, the radial as well as tangential strain rates in this disc is significantly higher than that observed in a similar composite disc without residual stress as evident from Fig. 5a and 5b. The presence of residual stress in the composite disc increases the radial (compressive) as well as tangential (tensile) strain rates by an order of about 6 than that observed in a similar composite disc without residual stress. Therefore, the presence of residual stress of 32 MPa in the 6061Al–10 vol.% SiCw disc leads to marginal increase in the magnitude of stresses but it causes a substantial increase in the order of strain rates in the composite disc. In order to counter the ill effects of residual thermal stress on creep performance of the composite disc, attempts should be made to reduce the magnitude of residual stress in the disc by subjecting it to the heat treatment process prior to using it in applications involving severe thermo-mechanical loads.

7.   Conclusions

Theradial, tangential and effective stresses in the composite disc are marginally increased in the presence of tensile residual stress, except for a slight decrease observed in the tangential stress somewhere in the middle of the disc. The radial as well as tangential strain rates in the composite disc are significantly increased in the presence of thermal residual stresses as compared to those obtained in a similar composite disc without thermal residual stresses. In order to improve creep performance of the composite disc, the stress relieving treatment, such as, heat treatment must be carried out prior to using such components in real life applications.

References

Gupta V K, Singh S B, Chandrawat H N, and Ray S, *J. of Engg. Mater. Tech.***127** (2005) 97.
You L H, You X Y, Zhang J J, and Li J, *Z. angew. Math. Phys.***58** (2007) 1068.
Hojjati M H, and Hassani A, *Int. J. of Pressure Vessels and Piping***85** (2008) 694.
Sen F, and Aldas K, *Advances in Engineering Software***40** (2009) 813.
Farshi B, and Bidabadi J, *Int. J. of Pressure Vessels and Piping***85** (2008) 507
Laskaj M, Murphy B, and Houngan K, Improving the efficiency of cooling the front disc brake on a V8 racing car, *Project report*, Monash University, Melbourne (1999).

Farshi B, Jahed H, and Mehrabian A, *Comp. Struct.***82** (2004) 773.

Bayat M, Saleem M, Sahari B B, Hakouda A M S, Mahdi E, *Mech. Res.***35** (2008) 283.

Nieh T G, *Metall. Trans.***15A** (1984) 139.

Nieh T G, Xia K, and Langdon T G, *J. of Engg. Mater. Tech.***110** (1988) 77.

Shi N, Wilner B, and Arsenault R J, *Acta Metallurgica et Materialia***40** (1992), 2841.

Badini C, *Journal of Materials Science***25** (1990) 2607.

Arsenault R J, and Taya M, *Acta Metallurgica* **35** (1987) 651.

Williamson R L, Rabin B H, and Byerly G E, *Compos. Eng.***5** (1995) 851.

Singh S B, and Ray S, *Journal of Materials Processing Technology***143-144** (2003) 623.

Bhatnagar N S, Kulkarni P S, and Arya VK, *Nuclear Engg. Design***91** (1986) 121.

Eraslan A N, and Orcan Y, *Mechanics of Materials***34** (2002) 423.

Orcan Y, and Eraslan A N, *Mech. Res. Communications***29** (2002) 269.

Jahed H, Farshi B, and Bidabadi J, *International Journal of Pressure Vessels and Piping***82** (2005) 35.

Gupta S K, Sharma S, and Pathak S, *Indian Journal of Pure Applied Mathematics***31** (2000) 1235.

Deepak D, Gupta V K, and Dham A K, *International Journal of Materials Research***101** (2010) 780.

Tjong S C, and Ma Z Y, *Mater. Sci. Engg. R: Report***29** (2000) 49.

Ma Z Y, and Tjong S C, *Composites Science and Technology***61** (2001) 771.

Mishra R S, and Pandey A B,*Metall. Trans.***21A** (1990) 2089.

Pandey A B, Mishra R S, and Mahajan Y R, *Acta Metall. Mater.***40** (1992) 2045.

Gonzalez-Doncel G, and Sherby O D, *Acta Metall Mater***41** (1993) 2797.

Park K T, Lavernia E J, and Mohamed F A, *Acta Metall Mater***38** (1990) 2149.

Mohamed F A, Park K T, and Lavernia E J, *Mater. Sci Engg***150A** (1992) 21.

Cadek J, Oikawa H, and Sustek V, *Mater. Sci. Engg.***A190** (1995) 9.

Park K T, and Mohamed F A, *Metall. Trans.***26A** (1995) 3119.

Li Y, and Langdon T G, *Acta Materialia* **45** (1997) 4797.

Li Y, and Langdon T G, *Mater. Sci. Engg.***A265** (1999) 276.

Li Y, and Mohamed F A, *Acta Materialia***45** (1997) 4775.

Yoshioka H, Suzumura Y, Cadek J, Zhu S J, and Milicka K, *Mater. Sci. Engg.***A248** (1998) 65.

Singh T, and Gupta V K, *Composite Structures***93** (2011) 747.

Bicanic N, Pearce C J, Owen D R J,*Proceedings of International Conference on Computational Modeling of Concrete structures*, EURO-C. (1994) 185.

Singh S B, and S Ray, *Mechanics of Materials***34** (2002) 363.

Bayat M N, Saleem M, Sahari B B, Hamouda A M S, and Mahdi E, *Thin-Walled Structures***45** (2007) 677.

Wahl A M, Sankey G O, Manjoine M J, and Shoemaker E, *J. of Appl. Mech.***21** (1954) 225.

List of Figures

Figure 1: Numerical scheme of computation

Figure 2: Comparison of theoretical and experimental [39] strain rates in steel disc

      (Disc rpm = 15000, Creep duration 180 hrs).

Figure 3(a): Variation of radial stress

Figure 3(b): Variation of tangential stress

Figure 3(c): Variation of effective stress

Figure 4: Variation of stress difference $[\overline{\sigma} - \sigma_0(r)]$

Figure 5(a): Variation of radial strain rate

Figure 5(b): Variation of tangential strain rate

List of Tables

Table 1: Parameters and operating conditions for steel disc

<u>**LEGENDS:**</u>

ITER = Iteration no.

$$E_{RR} = \frac{[\sigma_\theta]_{ITER} - [\sigma_\theta]_{ITER-1}}{[\sigma_\theta]_{ITER-1}}$$

h = Limiting value of ERR (= 0.01)

ITM = Maximum no. of iteration (= 50)
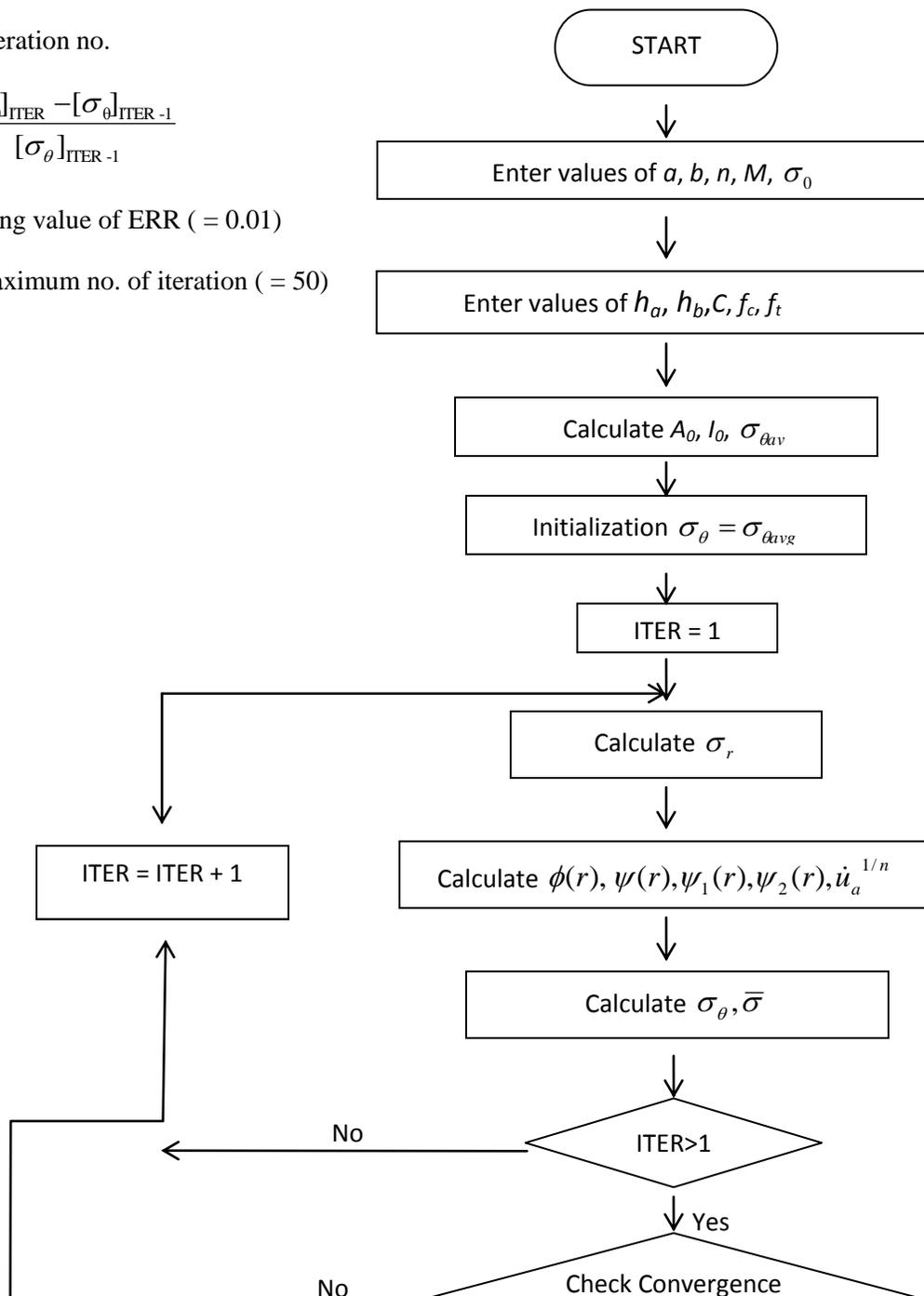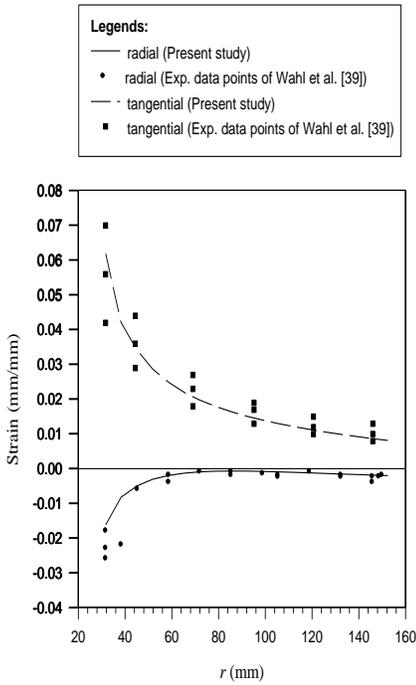
START

↓

Enter values of a, b, n, M, σ_0

↓

Enter values of h_a, h_b, C, f_c, f_t

↓

Calculate A_0, I_0, $\sigma_{\theta av}$

↓

Initialization $\sigma_\theta = \sigma_{\theta avg}$

↓

ITER = 1

↓

Calculate σ_r

↓

Calculate $\phi(r)$, $\psi(r)$, $\psi_1(r)$, $\psi_2(r)$, $\dot{u}_a^{1/n}$

↓

Calculate σ_θ, $\overline{\sigma}$

↓

ITER>1

No ←

ITER = ITER + 1

Yes ↓

Check Convergence

No

146

Figure 2: Comparison of theoretical and experimental [39] strain rates in steel disc (Disc *rpm* = 15000, Creep
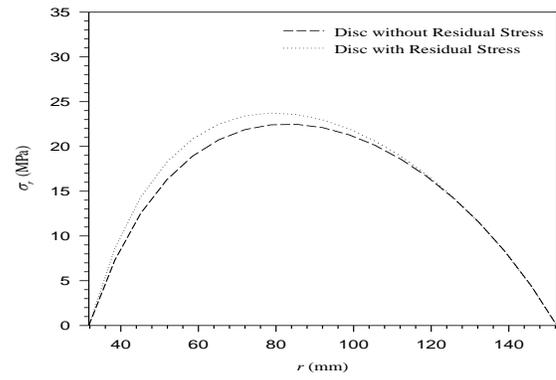
Figure 3(a): Variation of radial stress
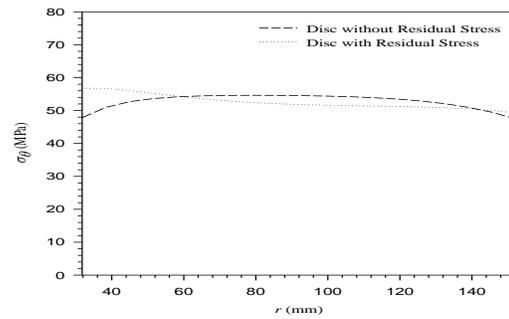
Figure3(b): Variation of tangential stress
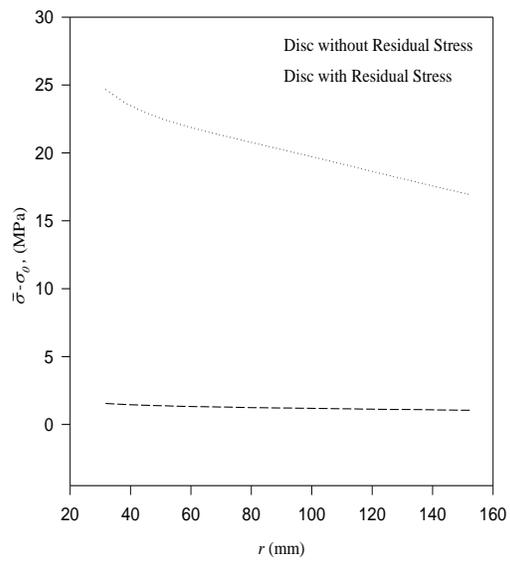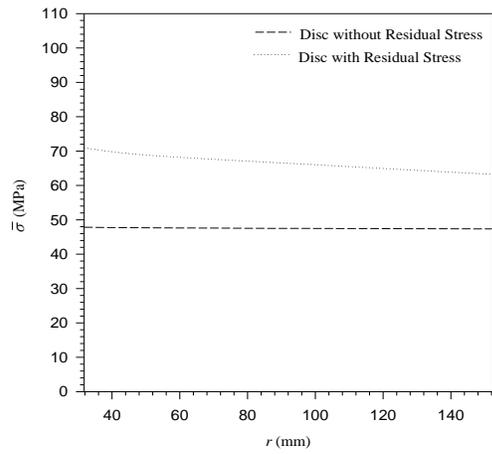
Figure 3(c): Variation of effective stress

Figure 4: Variation of stress difference
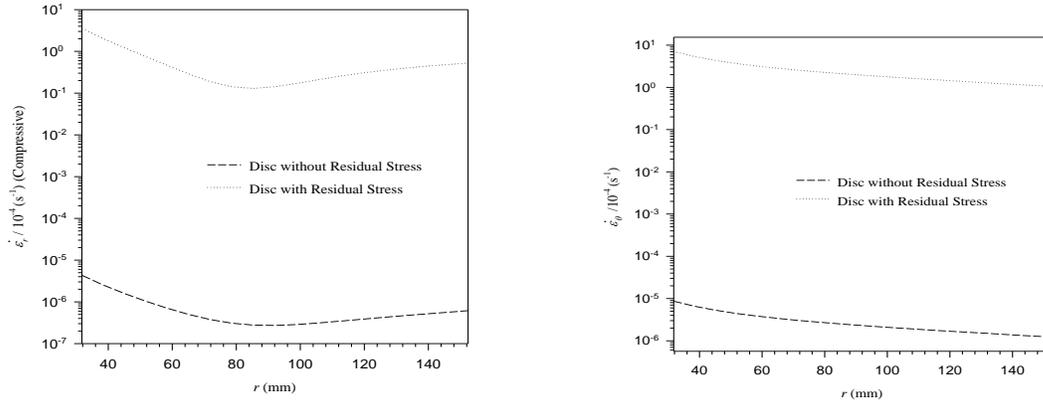
Figure 5(a): Variation of radial strain rate $(\overline{\sigma} - \sigma_0)$ **Figure 5(b):** Variation of tangential strain rate

Table 1: Parameters and operating conditions for steel disc

Parameters for steel disc:	Density of disc material (ρ) = 7823.18 kg m^{-3}
	Disc radii: a = 31.75mm, b = 152.4 mm
	Stress exponent: n = 5
	Creep parameters: $M = 2.05 \times 10^{-4}$ s$^{-1/5}$/ MPa
	σ_0 = 35.98 MPa
Operating conditions:	Disc *rpm* = 15 000
	Operating temperature = 810.78 K
	Creep duration = 180 hrs

Evaluation of tensile and flexural properties of hemp reinforced fresh/recycled polyethylene based natural fiber composites

[1]Navrattan Goyal, [*2]Dharmpal Deepak, [3]V.K. Gupta

Mechanical Engineering Department,Punjabi University, Patiala-147002 (Pb.), India
*Corresponding Author
E mail ID: deepakbass@yahoo.com,
Phone: +91-9815609794, +91-175-2280026
Fax: +91-175304633

Abstract

The tensile and flexural properties of hemp fiber reinforced high density polyethylene (HDPE) composite for varying amount of hemp fibers are evaluated. The specimens for tensile and flexural tests are fabricated in accordance to ASTM standards. Prior to fabrication of composite specimens, the surface of hemp fibers is chemically treated with 8% NaOH and 10% Maleic Anhydride solutions so as to improve the interfacial adhesion between hemp fibers and HDPE matrix. The results obtained by conducting tensile and flexural tests on composite specimens are compared with the specimens made of 100% virgin HDPE and 50-50 mixture of virgin and recycled HDPE. The study reveals that the tensile strength reduces when HDPE matrix is reinforced with hemp fibers. The tensile strength of the composite decreases respectively by 3.15 MPa and 6.21 MPa on reinforcing HDPE matrix (50% virgin and 50% recycled) with respectively 10% and 30% hemp fibers. However, the flexural strength increases with the reinforcement of hemp fibers into HDPE matrix, having equal proportion of virgin and recycled HDPE. The flexural strength of composite containing 10% and 20% hemp fibers are respectively higher by around 3.2 MPa and 1.79 MPa when compared with specimen made of 50-50 mixture of virgin and recycled HDPE. SEM observations of the tensile fractured surface of the composite specimens reveal that the fiber pull-out and fiber breakage are the primary failure mechanisms.

Keywords: HDPE, Injection Moulding, Hemp fiber, Recycled HDPE

1. Introduction

The natural living world provides food, fiber, timber and absorbs waste contributing to the well-being of humanity and sustainability of our future. The potential of natural fiber composites for the automotive industry especially for non-load bearing exterior applications is becoming widely recognised owing to their easy availability, low cost and density, high specific properties, non abrasive nature and biodegradable characteristics [1-2]. Plants, such as flax, cotton, hemp, jute, sisal, kenaf, pineapple, ramie, bamboo, banana, etc. are more often applied as the reinforcement in composites [3-4]. Hemp fiber (Cannabis sativa) is recently gaining attention as diversified reinforcing applications in composite industry, housing, railways and aerospace applications due to its high specific strength and stiffness [5]. Hemp offers excellent mechanical strength and Young's modulus [6-7].

Combining the incompatible hydrophilic natural fibers and hydrophobic thermoplastics into a single product results in a weak fiber/polymer adhesion and, as a consequence, unsatisfactory composite properties are anticipated. An intuitive approach of increasing fiber/matrix compatibility is to decrease the hydrophilicity of the fibers by chemical modification [8]. In recent times, environment safety has been on priority in the development of new materials leading to a recycling and reuse approach to conserve the

material resources [9]. The disposal ways of plastics contribute to local pollution and emission of greenhouse gases responsible for global warming. Moreover, low cost plastic wastes are normally available for an eventual matrix for hemp fiber incorporation [10].

In the light of these facts, it is decided to investigate the mechanical behavior of NaOH and Maleic Anhydride treated hemp fiber reinforced recycled polyethylene (PE) matrix composites. In the present study natural fiber composites, containing 10%, 20% and 30% chemically treated hemp fibers as reinforcement and 50-50 mixture of virgin and recycled high density polyethylene (HDPE) as matrix, have been fabricated. The tensile and flexural properties of the composites are evaluated and compared with samples made of 100% virgin HDPE and 50-50 mixture of virgin and recycled HDPE.

2. Experimental details

2.1. Material and Method

In this study hemp fibers are used as reinforcement in HDPE matrix (both fresh and recycled). For chemical treatments; chemicals used are sodium hydroxide (NaOH), maleic anhydride (MA) used as coupling agent and acetone used as solvent. Sisal fibers were purchased from Chandra Parkash and Company, Jaipur, Rajasthan. HDPE (both fresh and recycled) of moulding grade was procured from Goyal polymers, Chandigarh. Chemicals used for treatment viz. NaOH, MA and acetone was procured from Vivek chemical Industries, Ambala Cantt.

2.2 Chemical treatment of hemp fibers

The adhesion between hemp fiber and HDPE (fresh and recycled) matrix is improved by the chemical modification of hemp fiber. To fulfill our objectives, the chemical treatment suggested by Kaczmar et al. [11] is used in the present study for the modification of the hemp fiber composites. Firstly the hemp fibers of size 4 to 5 mm approx were washed with distilled water and then dried in oven at 20°C for 1 hour for the removal of oil, dust or foreign particles which will affect the properties of fiber and composites. Then hemp fibers are soaked in 8% NaOH for a period of 2 hours. The NaOH treated fibers were rinsed with distilled water to obtain pH=7 and dried in the oven at 105°C for 1 hour. Now after drying the hemp fibers are soaked in 10% Maleic Anhydride (MA) in acetone for a period of 2 hours. MA treated fibers were then rinsed with distilled water till the pH of the fibers reached 7.

2.3 Fabrication of tensile and flexural specimens

In order to investigate the influence of amount of hemp fibers on tensile and flexural properties of hemp fiber–HDPE composite, the specimens for tensile and flexural testing were prepared with the help of injection moulding process by varying content of hemp fibers as 10, 20, and 30 % (by wt.) in a matrix of HDPE (50 % fresh and 50% recycled) as depicted in Table 2 and 3. For the purpose of comparison, the samples, both tensile and flexural, were also prepared by taking 100% fresh HDPE and 50–50% (fresh and recycled) HDPE.

Table 1: Description of Tensile Specimens

Fiber (wt.%)	Sample Density (gm/cc)	Tensile wt. (gm)	Fiber wt. (gm)
10	0.991	8.85954	7.0876
20	1.042	9.31548	14.905

30	1.093	9.77142	23.451

Table 2: Description of Flexural Specimens

Fiber (wt.%)	Sample Density (gm/cc)	Flexural wt. (gm)	Fiber wt. (gm)
10	0.991	8.85954	7.0876
20	1.042	9.31548	14.905
30	1.093	9.77142	23.451

[Density of hemp fiber = 1.45 gm/cc, Density of FHDPE = 0.94 gm/cc, Density of RHDPE = 0.93 gm/cc,]

2.4   Testing of samples

The tensile tests of the fabricated samples were conducted according to ASTMD-638 standard and flexural tests were according to the ASTMD-790 standard in Central institute of plastic engineering & technology (CIPET) Amritsar on a Universal Testing Machine (UTM). Before performing the tests all the samples were conditioned by putting them in a controlled environment chamber (Make: KASCO industries, Pune) at 25°C and 50% RH. For tensile testing, dumbbell shaped samples were subjected to uniaxial tensile load by gripping their ends in UTM (Model: SS UTM 1250, Capacity 250 KN, Make: P.S.I sales Pvt. Ltd.) by keeping a gauge length of 57 mm. The results were obtained at two different points, as mentioned in Table 3 and 4 by testing five similar specimens corresponding to each composition which were averaged to estimate the tensile strength of composite specimens corresponding to different compositions. In order to estimate flexural strength of composites specimens the short beam shear tests were conducted. It is basically 3-Point bending test which leads to failure by inter-laminar shear strength. These tests were conducted on UTM over a spam length of 107 mm.

2.5   Examination of fiber surface and fractography

The analysis of the fractured surface of the tensile samples and surface morphology of the treated sisal fibers were done with the help of scanning electron microscopy (SEM). For SEM, JEOL scanning electron microscope (Model: JSM6510LV) has been used having maximum magnification of 1 Lac. The samples for SEM observation were prepared with the JEOL fine coater (Model: JFC-1600) by gold and platinum coating of 5 nm thickness.

3.   Results and discussion

3.1.   Mechanical properties of composites

The tensile and flexural strength of the different composites specimens, obtained by averaging the five readings for five similar specimens at each composition, are summarized in Table 3.

Table 3: Tensile strength of HDPE composite reinforced with treated hemp fibers

Composition	Tensile sample	Tensile Strength (MPa)	Flexural sample	Flexural strength (MPa)
100%HDPE	T0	17.39	F0	12.27
50% FHDPE+ 50% RHDPE	T1	21.60	F1	17.78
10% Hemp + 90% (FHDPE	T2	18.45	F2	21.00
20% Hemp + 80% (FHDPE	T3	19.28	F3	19.57
30% Hemp + 70% (FHDPE	T4	15.39	F4	17.72

The tensile strength of specimen-T1 consisting of virgin and recycled HDPE (50% each) is higher by 4.21 MPa than the specimen-T0 containing 100% fresh HDPE. Therefore, the addition of recycled HDPE into fresh HDPE enhances the tensile properties. The tensile strength of composite is increased by 0.83 MPa with the increase in fiber content from 10% to 20% when compared to specimens made of HDPE alone. The tensile strength of the composite is decreased by 3.89 MPa on increasing the fiber content from 20% to 30% (Fig. 1). The fiber content and fiber strength are mainly responsible for strength properties of the composite. However, the decrease in tensile strength for 30% hemp fiber composite (T3) may be due to the poor fiber-matrix adhesion.

Similarly the flexural test was carried out in an UTM machine in accordance with ASTM D 790 on all the four specimens of hemp fiber with FHDPE plus RHDPE combinations. The results are tabulated in the Table 3. Unlike tensile strength, the flexural strength of specimen-F1 is about 5.51 MPa higher than the specimen-F0 made of fresh HDPE alone. In general, on reinforcing hemp fibers into polymer matrix the flexural strength increases as shown in Fig. 2, except for a slightly lower flexural strength observed for specimen-F4. As compared to specimen-F1 (made of 50% fresh and 50% recycled HDPE), the flexural strengths of composite containing 10% and 20% of hemp fibers are respectively higher by around 3.22 MPa and 1.79 MPa respectively.
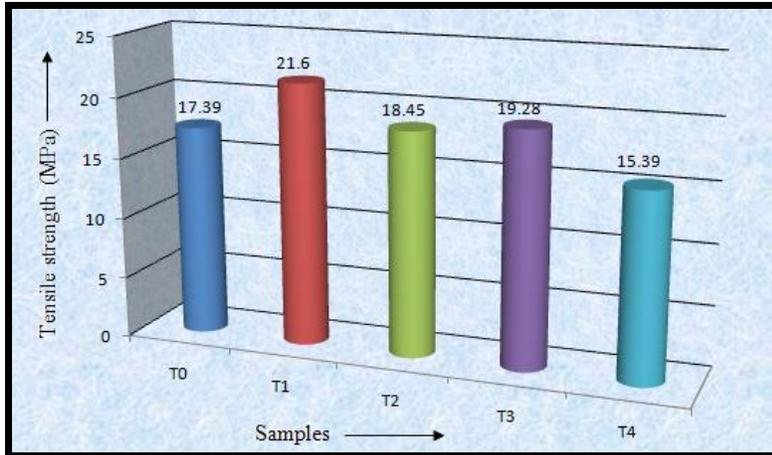
Figure 1: Tensile strength of various specimens
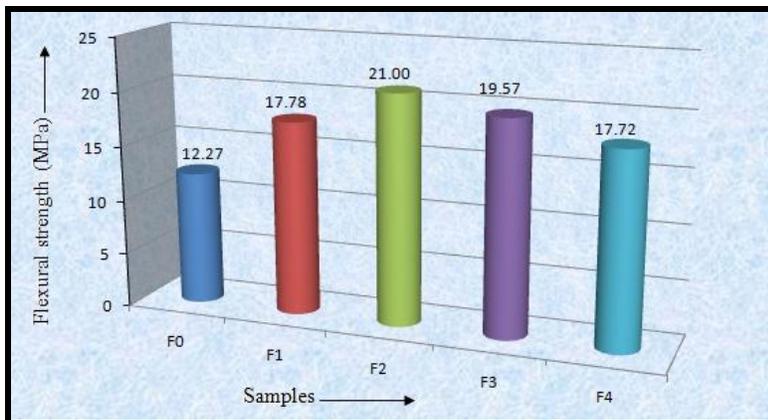
Figure 2: Flexural strength of various specimens

3.2. Scanning electron microscopy (SEM) analysis

SEM images of tensile fractured surface of hemp fiber reinforced PE composite samples are depicted in Figs. 3 to 4. The SEM image of 10% hemp composite shown in Fig. 3 reveals the presence of fiber pullout phenomenon in bundled form in the fractured composite specimens. The SEM image also reveals that hemp fibers are not uniformly distributed in HDPE matrix. As a result of which the fiber could not play a positive role in improving the performance of composite, especially for tensile strength, as observed in this study. The fiber pullout phenomenon observed in the fractured specimen reveals poor adhesion between the hemp fiber and the matrix that results into poor tensile strength of the composites.
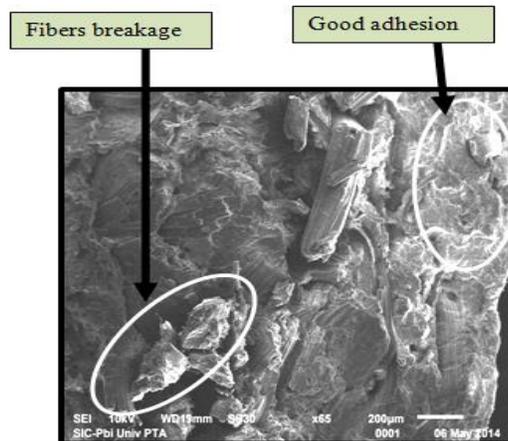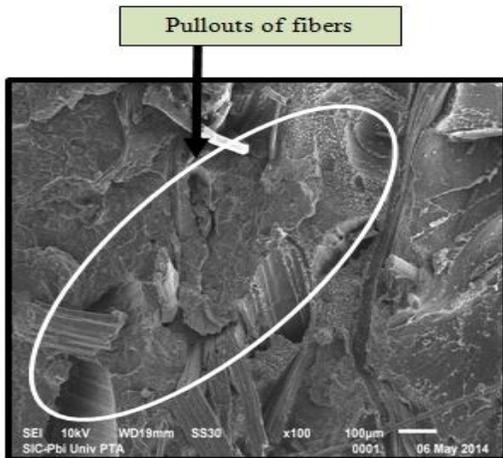
Figure 3: SEM of 10% hemp fiber composite **Figure 4:** SEM of 20% hemp fiber composite

SEM image in Fig. 4 shows that the bonding of fibers with HDPE (fresh and recycled) matrix increases to a large extent in the case of 20% hemp fiber composites.

4. Conclusions

- ❖ The hemp fibers treatment with NaOH+ distilled water and MA + acetone leads to remove the waxy substances from the surface of hemp fiber and leaves the roughness on the fiber surface.
- ❖ The addition of recycled HDPE into fresh HDPE enhances the flexural strength by 5.51 MPa.
- ❖ The tensile strength of chemically treated hemp fiber/HDPE (fresh and recycled) composite is lower than the HDPE (50% fresh + 50% recycled) sample. The tensile strength of the composite decreases respectively by 3.15 MPa and 6.21 MPa with the increase in fiber content of 10% and 30% respectively, when compared with specimen made of 50% fresh and 50% recycled HDPE. However, the composite with 20% hemp fiber is observed to have tensile strength lower by 2.32 MPa as compared to HDPE sample containing equal percentage of fresh and recycled HDPE.
- ❖ The reinforcement of chemically treated (viz. NaOH + distilled water and MA + acetone) treated hemp fibers into HDPE matrix (50% fresh + 50% recycled) leads to enhance the flexural strength. The flexural strength of composite containing 10% and 20% hemp fibers are respectively higher by around 3.2 MPa and 1.79 MPa respectively when compared with specimen made of fresh and recycled HDPE.
- ❖ The primary mechanism responsible for tensile fracture of the composite is fiber pull out with some amount of fiber delamination.

References

[1] Suddell B C, and Evans W J, *Seventh International conerence on woodfiber-plastic composites proceeding,* Madison 7-14 (2003).

[2] Kaewkuk S, Sutapun W, and Jarukumjorn K ,*Composites: Part B* **4**(2013) 544.

[3] Kumar R, Obrai S, and Sharma A, *Pelagia Research Library Der Chemica Sinica* **2** (2011) 219.

[4] Aruna M, *International Journal of Mechanical, Industrial Science and Engineering* **8** (2014) 84.

[5] Chen T, Liu W, and Qiu R, *BioResources* **8** (2013) 2780.

[6] Shahzad A, *Journal of Composite Materials* **46** (2011) 973.

[7] Hassan E, Wei Y, Jiao H, and Huo Y M, *International Journal of Engineering Science and Technology***4** (2012) 4429.

[8] Guinez D, Jasso C, Fuentes F, Navvaro F, Davalos F, and Ramos J, *Proceeding of the 8th Polymers for advanced Technologies international Symposium*, Budapest, Hungary (2005).

[9] Nayak S K, Dixit G, and Appukuttan K K,*International Journal of Plastics Technology* **16**(2012) 150.

[10]   Lima A C, Monteiro S N, and Satyanarayana K G, J Polym Environ **20** (2012) 245.

[11]   Kaczmar J W, Pach J, and Burgstaller C, *Polimery***56** (2011) 817.

Microstructure and Dry Sliding Wear Behavior of Al6061-6% SiC- 6% Graphite Particulate Reinforced Hybrid Composites

Madeva Nagaral[1], Shivanand B K[2], V Auradi[3] and S A Kori[4]

[1]Design Engineer, ARDC, HAL, Bangalore and Research Scholar, Department of Mechanical Engineering, SIT, Tumkur-572103, Karnataka, India

[2]Department of Mechanical Engineering, MVJ Polytechnic, Bangalore-560067, Karnataka, India

[3]R&D Centre, Department of Mechanical Engineering, SIT, Tumkur-572103, Karnataka, India

[4]R&D Centre, Department of Mechanical Engineering, Basaveshwar Engineering College, Bagalkot-587102 Karnataka, India

Abstract:

In this present work, the systematic study has been conducted to investigate the wear properties by introducing micro size Silicon Carbide and Graphite particulates into Al6061 alloy matrix. Al6061 alloy was taken as the base matrix to which SiC and graphite particulates were used as reinforcements. 6 wt. % of SiC and 6 wt. % of graphite were added to the base matrix. The Micostructural study was done by using optical microscopy, which revealed the uniform distribution of SiC and Graphite particles in matrix alloy.A pin-on-disc wear testing machine was used to evaluate the volumetric wear loss of prepared specimens, in which a hardened EN32 steel disc was used as the counter face. The results revealed that the volumetric wear loss was increased with increase in normal load, sliding speed and sliding distances for all the specimens. The results also indicated that the volumetric wear loss of the Al6061-6% SiC-6% Graphite composites were lesser than that of the Al6061 matrix. The worn surfaces were characterized by SEM microanalysis.

***Corresponding author:** Tel./fax: +919845452018, E-mail: madev.nagaral@gmail.com

1. Introduction

Metal matrix composites (MMCs) have been created to meet demands of lighter materials especially suited for applications requiring high strength to weight ratio with high specific strength, dimensional stability, structural rigidity, and stiffness for different applications like automotive, space, aircraft, defence, and in other engineering sectors [1-3].Aluminium is the most widely used matrix material for the preparation metal matrix composites. Aluminium alloys are broadly classified into cast alloys and wrought alloys. Major alloying elements in aluminium alloys are copper, manganese, silicon,

magnesium and zinc.Aluminium has been used as a matrix material due to its light weight, high strength, excellent wear resistance properties, high temperature, easy to prepare the composite and availability in abundance [4]. From fast few years aluminium matrix composites are widely used in numerous structural, non-structural and functional applications. The major benefits of aluminium based composites in transportation sector are low fuel consumption, less air borne emissions and lower noise.

Many ceramic materials like particulates of SiC, TiC, graphite, boron carbide are widely used reinforcements in aluminium alloy [5-6]. Aluminium alloy based particulate reinforced composites have a more number of engineering applications, reinforcing aluminium alloys with different hard ceramic particles is mainly due to wide availability. The most commonly used aluminium alloy matrices are 2024, 2014, 2219, 5083, 5052, 6061, 6068, 7010 and 7075 alloys.

Particulate reinforced aluminium composites are fabricated by solid or liquid state processes. These composites are less expensive as compare to continuous fiber reinforced composites. Mechanical and tribological properties of particulate reinforced composites are in line with short fiber or continuous fiber reinforced composites.The main advantages of particulate reinforced aluminium composites over other materials are their cost advantage, formability, improved corrosion and seizure resistance [7]. Hence, these aluminium based composites are used as cylinder blocks, disc brakes, calipers, connecting rods and structures for space applications. In most of these services the components are subjected to tribological loading conditions [8].

Several researchers have invetigated the wear behavior of Al based composites. Baradeswaran et al. [9] studied on mechanical and wear properties of Al7075-Al$_2$O$_3$-Graphite composites. Shown hardness, tensile strength and compression strength of the hybrid composites are found to be increased. The wear properties of hybrid composites containing graphite exhibited the superior wear resistance properties. Suresh et al. [10] have reported wear behavior of Al-TiB$_2$ composites using respnse surface methodology. Yuhai et al. [11] have invetigated the friction and wear behaviors of Al6061-B$_4$C composites. Composites were studied by considering the effect of sliding time, applied load, sliding velocity and heat treatment. Umanath et al. [12] conducted experiments on dry sliding wear behavior of Al6061-Al$_2$O$_3$-SiC habrid metal matrix composites.

In this study, an attempt has been made to prepare Al6061 alloy composites by adding 6 wt. % of SiC and 6 wt. % of Graphite particulates into matrix by using a novel two stage reinforcement addition method. The SiC and graphite content is limited to 6 wt. % to enhance the influence of graphite effect on wear behavior of composites. Further, the prepared Al6061-SiC-Graphite composites were studied for effect of load and sliding speed on the wear properties by using pin-on-disc wear testing machine.

2. Experimental Details

2.1. Materials Used

Metal matrix composites containing 6 weight percentage of SiC and 6 wt.% of graphite particles were produced by liquid metallurgy route. For the production of MMCs, an Al6061 alloy was used as the matrix material while SiC and graphite particles with an average size of 90-125μm were used as the reinforcements. The chemical composition of the alloy used in the present investigation is given in Table

Table1 Chemical composition of Al6061 alloy used

Element	Wt. Percentage
Magnesium	0.80
Silicon	0.64
Iron	0.23
Copper	0.17
Zinc	0.031
Manganese	0.072
Titanium	0.015
Chromium	0.014
Aluminium	Bal

The morphology of procured SiC and graphiteparticulates are shown in fig.1 which shows that the mixture of semi round and angular grains with sharp cornered morphology.

(a)   (b)

Fig. 1 Shows SEM microphotographs of (a) SiC particulates (b) Graphite Particulates

2.2. Preparation of composites

The SiC-graphite-particle reinforced Al6061alloy hybrid metal matrix composites have been produced by using a vortex method. Initially calculated amount of Al6061 alloy was charged into SiC crucible and superheated to a temperature 720˚C in an electrical resistance furnace. The furnace temperature was controlled to an accuracy of ±50 degree Celsius using a digital temperature controller. Once the required temperature is achieved, degassing is carried out using solid hexachloroethane (C_2Cl_6) to expel all the absorbed gases [13]. The melt is agitated with the help of a zirconia coated mechanical stirrer to form a fine vortex. A spindle speed of 250 rpm and stirring time 5-8 min. were adopted. The SiC and graphite particulates were preheated to a temperature of 600 degree Celsius in a pre-heater to increase the wettability. The pre-heated SiC and graphite particles introduced into melt in steps of two at constant feed rate of 1.2-1.4 g/sec. Two stage additions involve dividing entire weight of reinforcement into two equal weights and then individual weights are added to the melt in two steps rather than adding all at once. At every stage, stirring is carried out before and after introduction of reinforcement to avoid agglomeration and separation of particles and to ensure homogeneous dispersion of SiC and graphite particles in the melt. After holding the melt for a period of 5 min., the melt was poured from 710 degree Celsius into a preheated cast iron mould having dimensions of 120mm length x 15mm diameter. Wear specimen of size 25mm length and 8mm diameter was prepared by using castings made. Fig. 2 showing the machined samples for wear test.

Fig. 2 Shows wear test specimen

2.3. Dry sliding wear test

Dry sliding wear tests were carried out on Al6061 alloy and Al6061-SiC-Graphite composites using a pin-on-disc wear test apparatus. Cylindrical pin specimens of 8 mm diameter and 25 mm length were mounted vertically on a pin holder. The end of specimens were polished with abrasive paper of grit size 600 and followed by grade 1000. During the test the pin was pressed against the EN32 steel disc with hardness of 60 HRC. Prior to each run, the steel counter-face was ground with 320grit and then 600grit SiC abrasive for few minutes followed by cleaning with acetone. Test conditions included load-speed settings of 100, 200, 400 and 600 rpm under a 5kg normal load, and 1, 3 and 5kg loads at 400rpm speed. The initial weight of the specimen was measured in an electronic weighing machine with ± 0.01mg accuracy. Data collected and analyzed for volumetric wear loss in the form of weight loss. Further, volumetric wear loss was calculated.

3. Results and Discussion

3.1. Microstructural Anlysis

Fig. 3 a-b. Showing the Optical microphotographs of (a) as cast Al6061 alloy (b) Al6061-6%SiC-6% Graphite composites.

Fig. 3a-b shows microstructure of as cast Al6061 and Al6061-SiC-graphite composites. Silicon carbide and graphite reinforced aluminium composites have even distribution of reinforcement and this distribution can be seen in optical microscopy photograph (fig. 3b). Aluminium 6061 alloy matrices have grains with different sizes. This is due to the result of fast cooling during casting process. As it is examined in fig. 3b optical microphotograph of Al6061-SiC-graphite composites generally have equi-axed grains. Further these figures reveal the homogeneity of the cast composites. Further, in the case of

Al6061-SiC-graphite composites, the bonding between Al and SiC can be between layers of silicon atoms or carbon atoms in SiC and aluminium, and this will further influence the properties [14].

3.2 Wear Properties Evaluation

Fig. 4 shows the variation of volumetric wear loss with respect to load and Al6061 alloy and its composites. The results are observed for the maximum sliding distance of 2000m. The results clearly indicate that the increase of load increases the volumetric wear loss. Also the maximum wear is observed for unreinforced alloy.

Fig. 4 Shows the volumetric wear loss of as cast Al6061 alloy and its composites at constant sliding speed 400 rpm and varying loads

The variation of volumetric wear loss at constant 400rpm and varying loads of 1, 3 & 5kg is as shown in fig. 4. Applied load affects the wear rate of Al-alloy and the composites significantly and is most dominating factor controlling the wear behaviour. From the results, it has been asserted that the addition of 6 wt. % of SiC and 6 wt. % of graphite particulates to the matrix has a marked effect on the volumetric wear loss.

The improvement in the wear resistance of the composites with the addition of SiCreinforcement can be attributed to the improvement in the hardness of the composites and improved hardness results the decrease in the volumetric wear loss of the composites. Sudarshan et al.[15] reported that good interfacial bonding is necessary for better wear behaviour as load transfers occurs through interface and also debonding of reinforcement particles results in increase in wear rate at higher loads. The addition of 6 wt. % of graphite particulates into Al matrix plays very important role in the wear behavior of composites. Graphite acts as a lubricant and forms oxide layer between the steel counter part and pin.

Fig. 5 shows the variation of volumetric wear loss of Al-6061 matrix alloy and Al6061-6% SiC-6% graphitecomposite at constant 5kg load and varying sliding speeds. With an increasing speed i.e. 200, 400, and 600 rpm, there is an increase in the volumetric wear loss for both matrix alloy and its composites. However at all the sliding speeds studied, the volumetric wear loss of the composite was much lower when compared with the matrix alloy. Further increased wear rate with increased sliding speed is due to thermal softening of the composite. On the other hand the increased temperature at higher sliding speeds can cause severe plastic deformation of the mating surfaces leading to form high strain rate sub-surface deformation [16]. The increased rate of sub-surface deformation increases the contact area by fracture, and fragmentation of asperities. Therefore this leads to enhanced delamination contributing to enhance wear rate.

Fig. 5. Shows the volumetric wear loss of as cast Al6061 alloy and its composites at constant load

5kg varying speeds (rpm)

3.3 Worn Surface Study

(a)   (b)

Fig. 6 Shows the SEM microphotographs of worn surfaces of (a) as cast Al6061 alloy (b) Al6061-6%SiC-6%Graphite composites at 5kg load and 400rpm.

Wear surface analysis of hybrid composites were examined by scanning electron microscope. Fig.6a-b represents the wear surface of as cast Al6061 alloy and specimens containing 6 wt. % of SiC and 6 wt. % of graphite particles reinforced composite at 5 kg load and 400rpm sliding speed.

The examination of worn surface Fig. 6 a showed that the worn surfaces of base alloy are much rougher than composites.Cavities and large grooved surfaces are found on worn surface of Al6061 alloy. The indication of cavities and grooves supports the fact that soft Al alloy deformed at higher load of 5kg

and at 400rpm speed and pulled out from the surface. The wear track observation shows that adhesion and delamination are dominant wear mechanisms observed at higher loads. This is supported by the large sized delamination flakes and severe adhesion resulting in bulk removal of material at higher loads.

Fig.6b shows the SEM image of the worn surface of Al6061-6% SiC-6% Graphite composite tested at applied load of 5kg and 400rpm speed. The grooves are very small due to the hard nature of SiC reinforcement and poor wear losses.As the ceramic particles resist the delamination process, composites are found to have greater wear resistance. Worn surface shows less cracks and grooves mainly due to the presence of graphite particulates. The smeared graphite particles from the worn surface of composites form a thin rich tribolayer between sliding surfaces, which prevent direct metal contact.

4. Conclusions

The present work on processing and evaluation of Al6061-6% SiC-6% graphite metal matrix composite by melt stirring has led to following conclusions. Al6061 alloy based composites have been successfully fabricated by melt stirring method using two stage addition method of reinforcement combined with preheating of particles. The optical microphotographs of composites revealed fairly uniform distribution of reinforcement particulates in the Al6061 alloy metal matrix. The volumetric wear loss is dominated by load factor and sliding speed. The increase of loads and sliding speeds leads to a significant increase in the volumetric wear loss. The Al6061-6% SiC-6% graphite composites have shown lower rate of volumetric wear loss as compared to that observed in as cast Al6061 alloy matrix. SEM micrographs of worn surface revealed the presence of smooth grooves in the Al6061-SiC-graphite composite compared to the base matrix.

References

[1] SourabhGaratte, Rahul Upadhye, VenkateshDandagi, Shrikanth Desai, BhimappaWaghmode, "Preparation and Characterization of Al5083 alloy composites", Journal of Minerals and Materials Characterization and Engineering, 1, (2013) 8-14.
[2] RamkoteshwaraRao V, Ramanaiah N, Sarcar M,"Fabrication and investigation on properties of TiC reinforced Al7075 metal matrix composites", Applied Mechanics and Materials, Vols. 592-594, (2014) 349-353.
[3] Hamid Reza Ezatpour, SeyedAbolkarimSajjadi, Mohsen Haddad Sabzevar, Yizhong Huang, "Investigation of microstructure and mechanical properties Al6061 nano-composite fabricated by stir casting", Materials and Design, 55, (2014) 921-928.

[4] Srimant Kumar Mishra, SandyaraniBiswas, AlokSatapathy, "A study on processing, characterization and erosion wear behavior of silicon carbide particle filled ZA-27 metal matrix composites", Materials and Design, 55, (2014) 958-965.

[5] Baskaran S, Anandakrishnan, MuthukannanDuraiselvam V, "Investigations on dry Sliding wear behavior of in situ casted AA7075–TiC metal matrix composites by using Taguchi technique", Materials and design vol.60, (2014) 184-192.

[6] RamPrabhu T, Varma V K, SrikanthVedantam, "Effect of SiC volume fraction and size on dry sliding wear of Fe/SiC/graphite hybrid composites for high sliding speed applications", Wear vol.309, (2014) 1–10.

[7] Dora Siva Prasad, ChintadaShoba, "Hybrid composites – a better choice for high wear resistant materials", journal of materials and research technology, vol. 3(2), (2014) 172–178.

[8] Surendran R, Kumaravel A, "Study on Mechanical Properties and Wear Behavior of LM6 Aluminum / Nano Al2O3 Composites", Journal of Applied Mechanics and Materials, vols.592-594, (2014)1352-1356.

[9] Baradeswaran A, ElayaPerumal, "Study on mechanical and wear properties of Al7075-Al2O3-Graphite hybrid composites", Composites Part B, 56, (2014) 464-471.

[10] Suresh S, ShenbagaVinayaga Murthy, Vettivel S C, Selvakumar N, "Mechanical behavior and wear prediction of stir cast Al-TiB$_2$ composites using response surface methodology", Materials and Design, 59, (2014) 383-396.

[11] Yuhai Dou, Yong Liu, ZhipngXiong, Qingbing Xia, "Friction and wear behaviors of B$_4$C/Al6061 composite", Materials and Design, 2014.

[12] Umanath K, Palanikumar K, Selvamani S T, "Analysis of dry sliding behavior of Al6061-SiC-Al2O3 hybrid metal matrix composites", Composites Part B, 53, (2013) 159-168.

[13] MadevaNagaral, Auradi V, Kori S A, "Dry sliding wear behaviour of graphite particulate reinforced Al6061 alloy composite materials", Applied Mechanics and Materials, vol.592-594, (2014) 170-174.

[14] RavikiranA, Surappa M. K, "Effect of sliding speed on wear behavior of A356-Al30% wt. SiCp MMC", Wear, 206, (1997) 33-38.

[15] Sudarshan, Surappa M K, "Dry sliding wear of fly ash particle reinforced A356 Al composites", Wear, 265, (2008) 349-360.

[16] Babu J S S, Kang C G, Kim H H, "Dry sliding wear behavior of aluminium based hybrid composites with graphite nanofiber and alumina fiber", Materials and Design, 32, (2011) 3920-3925.

Microstructure and Mechanical Properties of Cu-Coated Al_2O_3 Particulate Reinforced 6061 Al Metal Matrix Composite

Mithun B R[1], Madeva Nagaral[2], Bharath V[3], V Auradi[4]

Department of Mechanical Engg, Siddaganga Institute of Technology, Tumkur- 572 103, Karnataka, India

In the present work an attempt is made to synthesize 6061Al – Cu coated Al_2O_3 particulate metal matrix composite by two stage melt stirring method. Ceramic particulates such as TiB_2, SiC, Al_2O_3, B_4C can be reinforced with aluminum matrix for better strength and wear resistance properties. In the present investigation 6061Al alloy were reinforced with copper coated Al_2O_3 particulate through two stage melt stirring process. Two stage melt stirring is adopted over single stage melting stirring process as this avoids agglomeration of particulates and results in better properties of MMC. The MMC is obtained by incorporating 6 wt. % of un-coated Al_2O_3 and Cu-coated Al_2O_3 with 6061 Al alloy. Microstructural analysis reveals that Cu coatings around Al_2O_3 particulates have improved the wettability at the interface resulting in better incubation and avoiding segregation of particulates in the melt which are evident from SEM microphotographs. Mechanical properties like density, hardness and tensile strength were studied for both copper coated and uncoated Al_2O_3 reinforced composite at room temperature. Significant increase in mechanical properties was observed for copper coated Al- Al_2O_3 composite due to improved wettability and uniform distribution of particulates within 6061Al matrix compared with Al- Al_2O_3 composite without Cu coatings.

*****Corresponding author:** Tel: +919901717522, E-mail:mithunbr44@gmail.com or madev.nagaral@gmail.com

1. Introduction

Aluminium alloys are extensively used in advanced engineering application such as aerospace and automotive industry due to its high strength, machinability, low density, easy availability and cost effectiveness compared to other materials. The scope of aluminium can be further extended by using it as a matrix material in the production of MMC. Aluminium metal matrix composites (AMMCs) possess significantly improved properties including high strength to weight ratio, higher elastic modulus, damping capacity and good wear resistance compared to unreinforced alloys [1] & [2].

Among aluminium alloys, 6061 Al is an Al-Si-Mg alloy widely used in structural and engineering applications due to its good strength to weight ratio, weldability, machinability, corrosion resistance, heat

treatability – forms precipitates on heat treatment and thus increasing strength with the cost of ductility. Harder ceramic particles such as B_4C, Al_2O_3 and SiC are widely used as reinforcement in composites. Among this, Al_2O_3 facilitates high strength and stiffness, good thermal conductivity, excellent size and shape capability and good wear resistance [3]. Al_2O_3 is most commonly used in the applications such as pistons, connecting rods etc., where tribological properties of the material are important [4]. But from studies and experiments it is observed that Al_2O_3 particle has poor wettability with 6061Al matrix.

Interface between the matrix and reinforcement strongly affect the properties of MMC's. Wettability between the matrix and reinforcement is the main factor which influences on the interfacial properties [5]. If the interface is not tailored properly it leads to lack of wettability, chemical reaction at the interface and degradation of reinforcement. Techniques used to obtain the desired interface include surface treatment of reinforcement, coating the reinforcement, optimizing process parameters and altering the matrix composition. Among the various techniques to improve the interface, coating is important one and widely investigated in the recent years [6] & [7].

Coating of the reinforcement restricts the diffusion of molten matrix material into the surface of the reinforcement. Thus, in the absence of diffusion chemical reaction at the interface is minimized [8]. Coating also plays an important role in increasing the wettability of the reinforcement in the molten matrix. Chemical vapor deposition, Physical vapor deposition, thermal spraying, electroless and electrolytic deposition etc., are the various techniques adopted to coat the reinforcement particles. Among these techniques electroless deposition is gaining importance due to its easy setup, low cost, uniform and continuous coating [9] & [10].

In present work an attempt is made to synthesize 6061Al based composites with reinforcements of un-coated Al_2O_3 / Cu-coated Al_2O_3 particulates with 6 wt. % by two stage stir casting route and to study the mechanical properties of the MMC.

2. Experimental Details

2.1. Materials Used

Aluminium 6061 alloy is an Al–Mg–Si alloy widely used due to its good strength, weldability, immunity to stress corrosion cracking as well as heat treatability, forming precipitates that increase the strength at the cost of somewhat reduced ductility. Alumina is used as the reinforcement which is one of the most widely used ceramic materials which are readily available and cost effective. It facilitates high strength and stiffness, excellent thermal conductivity, good size and shape stability, good wear resistance. In our present study Al2O3 with average particle size 100-125 µ is used.

Table 2.2: Properties of matrix and reinforcement

Components	Al	Mg	Si	Fe	Cu	Zn	Ti	Mn	Cr	Others
Amount (wt. %)	Balance	0.8-1.2	0.4-0.8	Max 0.7	0.15-0.40	Max 0.25	Max 0.15	Max 0.15	0.04-0.35	0.05

Table 2.2: Properties of matrix and reinforcement

Material/Properties	Density gm/cc	Hardness (HB500)	Strength (Tensile/Compressive) (MPa)	Elastic modulus (GPa)
Matrix – 6061 Al	2.7	30	115(T)	70-80
Reinforcement Al$_2$O$_3$ Particulate	3.69	1175	2100(C)	300

2.2. Electroless Cu-Coating

Electroless Cu-coating of Al$_2$O$_3$ particle is carried out as follows: Al$_2$O$_3$ is cleansed with acetone and acetone is separated. Cleaned Al$_2$O$_3$ is sensitized with stannous chloride & Conc. HCL and Al$_2$O$_3$ is separated from the mixture. Sensitized Al$_2$O$_3$ is treated with PdCl$_2$ and Conc. HCL to activate the surface of inactive Al$_2$O$_3$. In the activation process Pd is adsorbed on to the surface of Al$_2$O$_3$. Dried Al$_2$O$_3$ is dispersed in the electrolytic bath containing CuSO$_4$, distilled water, sodium hydroxide and Al$_2$O$_3$. 12-13 pH of the solution is maintained in the electrolytic bath. Thus Cu- coating is obtained on the surface of Al$_2$O$_3$ particulates.

2.3. Processing of MMC

Stir casting method is used to prepare the metal matrix composites of required dimensions. 6061Al alloy is melted in graphite crucible using resistance furnace. Meanwhile Al2O3 particles are preheated at 400°C for 30 minutes. The furnace temperature is maintained at 750°C, which is above the liquidous temperature of 6061Al alloy in order to increase the viscosity of the melt. Mechanical stirrer maintained at 200rpm is used to stir the melt to form the vortex. Once the vortex is created, the preheated Al2O3 particles are introduced in 2 stages. The melt is stirred for 10 minutes and the furnace temperature is maintained at 750°C i.e. pouring temperature. The melt is poured into cast iron permanent mould containing the cavity as per requirement. The test samples are prepared in the same procedure for different weight percentages.

2.4. Testing

Microstructure of prepared specimen is studied by taking the central part of the composite block. The face of the specimen to be examined is prepared by polishing through 220, 400, 600, 800 & 1000 grit emery papers and polished using diamond paste. The specimen is etched using Keller's reagent before it is examined using optical microscope and scanning electron microscopy. Specimen for hardness test and tensile test are prepared as per ASTM standards. Hardness test is done on the polished surface of the specimen using Micro- Vickers hardness testing machine consisting of diamond cone indentor and with the application of 30N load. Tensile test is done using computerized UTM as per ASTM standards and four specimens are tested for each composition of composite.

3.   Results and Discussions

3.1. Microstructural Studies

The properties of MMC's are mainly influenced by the dispersion of reinforcement in the matrix material. Homogeneous distribution of reinforcement leads to better mechanical properties. Fig 3.1 (a) show the SEM micrographs of 6061 Al alloy and Fig 3.1 (b) show the SEM micrographs of 6 wt. % of un-coated Al_2O_3 reinforced 6061Al alloy. The microstructure consists of Al_2O_3 particulates segregated at the inter-dendritic region of matrix alloy and also the presence of porosity which intern reduces the properties of MMC's.

Fig 3.1 (c) show the SEM micrograph of 6 weight% of Cu-coated Al_2O_3 reinforced 6061Al alloy. The SEM micrograph shows the homogeneous distribution of reinforcement in the matrix. By copper coating the Al_2O_3 particles, the interface between ceramic particle-metal matrix is replaced with lower surface tension of metal-metal interface. This homogeneous distribution of reinforcement shows that Cu-coating of the reinforcement has increased its wettability with the matrix material effectively.

<div align="center">(a)</div>

<div align="center">(b)</div>

<div align="center">(c)</div>
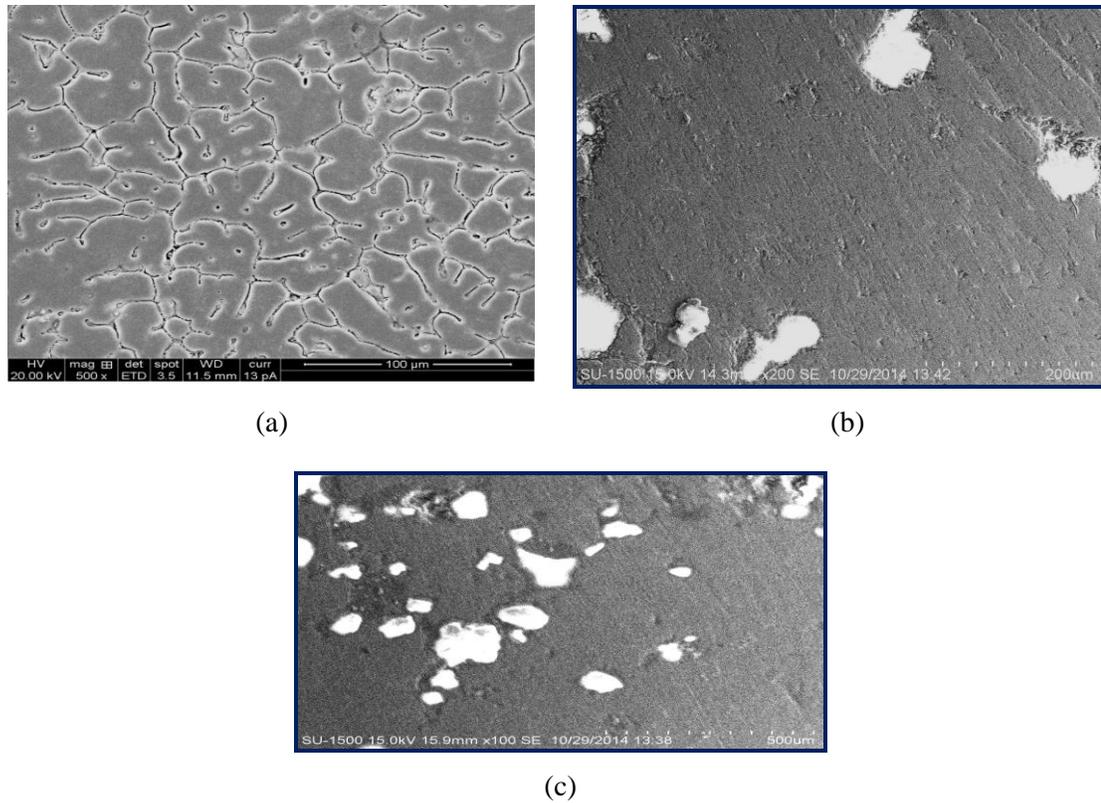
Fig 3.1: Shows the SEM micrographs of (a) 6061 Al alloy (b) 6061 Al reinforced with 6 wt% un-coated Al_2O_{3P} (c) 6061 Al reinforced with 6 wt% Cu-coated Al_2O_{3P}

3.2. *Hardness Observations*

Micro- Vickers hardness test is performed on the polished samples using diamond cone indentor. 30N load is applied on the polished samples and 3 reading are reported at different locations and average of these 3 reading is considered. The experiment is repeated for all the samples. Obtained hardness value of base material (6061Al alloy) and the prepared composites (6061Al reinforced Cu-coated Al_2O_3 / un-coated Al_2O_3) is plotted (Fig 3.2). The obtained values reveal that there is noticeable raise in the hardness value with increasing weight percentage of Al_2O_3 particles. It is observed that the hardness of prepared composite with Cu-coated Al_2O_3 is higher than that of composite containing non-coated Al_2O_3. The increase in hardness is due to the presence of stiffer and harder Al_2O_3 reinforcement particulates which acts as a constraint to plastic deformation of the softer matrix material. The presence of copper coating prevents the formation of brittle inter-metallic at the interface thus facilitating effective transfer of load from matrix to reinforcement.
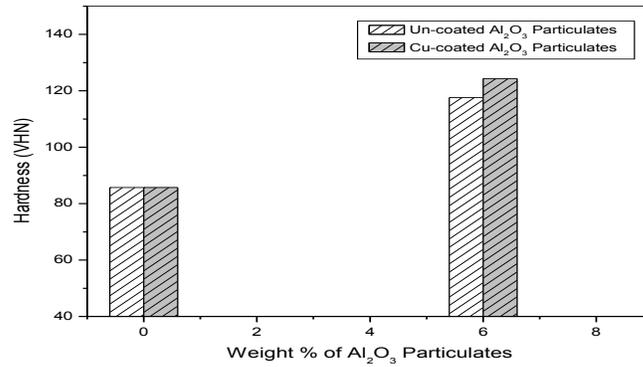
Fig 3.2: Shows the variation in hardness of 6061 Al and 6061 Al reinforced with 6 wt% of Un-coated/ Cu-coated Al_2O_3

3.3. *Tensile Properties:* Tensile test is conducted on computerized UTM as per ASTM standards to investigate the mechanical behavior of MMC. Four test specimens are used for each run. The tensile properties such as yield strength, percentage elongation and tensile strength are extracted from the test results. The test is carried out for the samples of base material and 6 wt. % of un-coated & Cu-coated Al_2O_3 particulates.

(a)

(b)
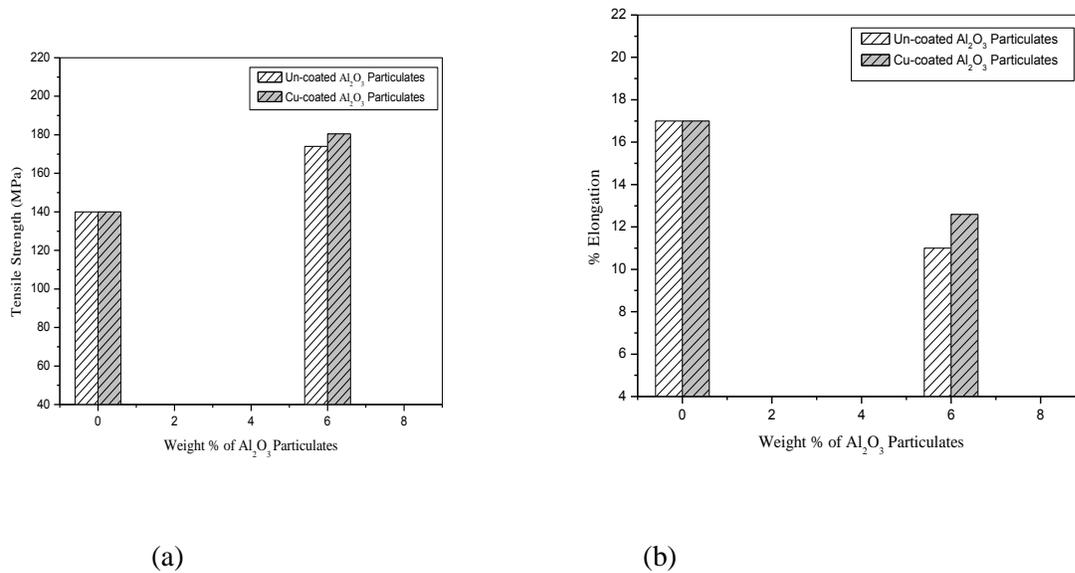
Fig 3.3: Show the tensile test result of 6061 Al base alloy before and after the addition of Un-coated / Cu-coated Al2O3 (a) Variation in ultimate tensile strength (b) Variation in % elongation.

The strength of the composite depends on the ability of the material to resist displacement motion. The harder and stiffer Al_2O_3 particle present restricts the plastic flow of softer matrix, thus enhancing tensile

strength of the material. The obtained results revels that there is appreciable increase in the tensile strength of composites but ductility of the material decreases when compared to 6061Al alloy. It is observed that composites of Cu-coated Al_2O_3 have more strength than that of the composites containing non-coated Al_2O_3. From the test results we can conclude that there is increase in tensile strength of the composites but the ductility of the material containing Cu-coated Al_2O_3 is higher than material containing non-coated Al_2O_3.

4. Conclusions

1. Successful synthesis of 6061 Al and un-coated/Cu-coated Al_2O_3 by two stage stir casting method.

2. Microstructural analysis reveals the uniform distribution of Cu-coated Al_2O_3 in matrix metal.

3. The hardness of composite containing Cu-coated Al_2O_3 is 7.9% greater than that of composite consisting non-coated Al_2O_3.

4. Tensile strength of the prepared composites with non-coated & Cu-coated Al_2O_3 is found to increases by 24.2% & 28.9% respectively.

5. Ductility of the MMC decrease with the addition of reinforcement but, ductility of Cu-coated Al_2O_3 reinforced 6061 Al matrix composite is increased by 9.33% than that of composite prepared with non-coated Al_2O_3.

References

[1] Rajeshkumar Gangaram Bhandare, Parshuram M. Sonawane, "*Preparation of Aluminium Matrix Composite by Using Stir Casting Method",* International Journal of Engineering and Advanced Technology (2013) 2249 – 8958

[2] Dr. Virupaxi Auradi*, "Composite material tutorials (2012)"*, Department of mechanical Engineering, Siddaganga Institute of Technology , Tumkur , Karnataka, INDIA.

[3] Bharath V, Madeva Nagaral, V Auradi, *"Preparation of 6061Al-Al₂O₃ Metal Matrix Composite by Stir Casting and Evaluation of Mechanical Properties",* International Journal Of Metallurgical & Materials Science and Engineering (2012) 2278-2516

[4] Prakash Gadade, Arun L.R, "*Characterization Of Aluminium-Flyash-Alumina Composite for Piston analysis By CAE Tools*" International Journal of Innovative Research in Science, Engineering and Technology (2013) 2319-8753

[5] Hashim. J, Looney. L, Hashim. M.S.J, "*The wettability of SiC particles by molten aluminium alloy*", Journal material processing Technology, Vol. 119 (2001)

[6] Rajan. T.P.D., Pillai. R.M., Pai. B.C, "*Review reinforcement coatings and interfaces in aluminium metal matrix composites*", Journal of Material Science, Vol.33 (1998)

[7] Rams. J, Urena. A, Campo. J, "*Sol-gel coatings as active barriers to protect ceramic reinforcement in aluminium matrix composites*", Advanced Engineering Materials, Vol.6 (2004)

[8] H. Beygi, S.A. Sajjadi, S.M. Zebarjad, "*Microstructural analysis and mechanical properties of aluminum matrix nano composites reinforced with uncoated and Cu-coated alumina particles*", Elsevier Journal of Material Science and Engineering (2014)

[9]R. Karthigeyan, S.Ezhil vannan, G. Ranganath, S.Paul vizhian, K.Annamalai, *"Effect of Coating Parameters on Coating Morphology of Basalt Short Fiber for Reinforcement Preparation of Al/Basalt Metal Matrix Composites*", International Journal of Electrochemical Science (2013) 10138 – 10148

[10]Burak Dikici, Cagri Tekmen, Mehmet Gavgali, Umit Cocen, *"The Effect of Electroless Ni Coating of SiC Particles on the Corrosion Behavior of A356 Based Squeeze Cast Composite*" Journal of Mechanical Engineering (2011)

Microstructure and Dry Sliding Wear Behavior of Al6061-6% SiC- 6% Graphite Particulate Reinforced Hybrid Composites

Madeva Nagaral[1], Shivanand B K[2], V Auradi[3] and S A Kori[4]

[1]Design Engineer, ARDC, HAL, Bangalore and Research Scholar, Department of Mechanical Engineering, SIT, Tumkur-572103, Karnataka, India

[2]Department of Mechanical Engineering, MVJ Polytechnic, Bangalore-560067, Karnataka, India

[3]R&D Centre, Department of Mechanical Engineering, SIT, Tumkur-572103, Karnataka, India

[4]R&D Centre, Department of Mechanical Engineering, Basaveshwar Engineering College, Bagalkot-587102 Karnataka, India

Abstract:

In this present work, the systematic study has been conducted to investigate the wear properties by introducing micro size Silicon Carbide and Graphite particulates into Al6061 alloy matrix. Al6061 alloy was taken as the base matrix to which SiC and graphite particulates were used as reinforcements. 6 wt. % of SiC and 6 wt. % of graphite were added to the base matrix. The Micostructural study was done by using optical microscopy, which revealed the uniform distribution of SiC and Graphite particles in matrix alloy. A pin-on-disc wear testing machine was used to evaluate the volumetric wear loss of prepared specimens, in which a hardened EN32 steel disc was used as the counter face. The results revealed that the volumetric wear loss was increased with increase in normal load, sliding speed and sliding distances for all the specimens. The results also indicated that the volumetric wear loss of the Al6061-6% SiC-6% Graphite composites were lesser than that of the Al6061 matrix. The worn surfaces were characterized by SEM microanalysis.

Keywords: Al6061, SiC, Graphite, Stir Casting, Wear Properties, Hybrid Composites

*__Corresponding author:__ Tel./fax: +919845452018, E-mail: madev.nagaral@gmail.com

5. Introduction

Metal matrix composites (MMCs) have been created to meet demands of lighter materials especially suited for applications requiring high strength to weight ratio with high specific strength, dimensional stability, structural rigidity, and stiffness for different applications like automotive, space, aircraft, defence, and in other engineering sectors [1-3]. Aluminium is the most widely used matrix material for the preparation metal matrix composites. Aluminium alloys are broadly classified into cast alloys and wrought alloys. Major alloying elements in aluminium alloys are copper, manganese, silicon, magnesium and zinc. Aluminium has been used as a matrix material due to its light weight, high strength, excellent wear resistance properties, high temperature, easy to prepare the composite and availability in abundance [4]. From fast few years aluminium matrix composites are

175

widely used in numerous structural, non-structural and functional applications. The major benefits of aluminium based composites in transportation sector are low fuel consumption, less air borne emissions and lower noise.

Many ceramic materials like particulates of SiC, TiC, graphite, boron carbide are widely used reinforcements in aluminium alloy [5-6]. Aluminium alloy based particulate reinforced composites have a more number of engineering applications, reinforcing aluminium alloys with different hard ceramic particles is mainly due to wide availability. The most commonly used aluminium alloy matrices are 2024, 2014, 2219, 5083, 5052, 6061, 6068, 7010 and 7075 alloys.

Particulate reinforced aluminium composites are fabricated by solid or liquid state processes. These composites are less expensive as compare to continuous fiber reinforced composites. Mechanical and tribological properties of particulate reinforced composites are in line with short fiber or continuous fiber reinforced composites. The main advantages of particulate reinforced aluminium composites over other materials are their cost advantage, formability, improved corrosion and seizure resistance [7]. Hence, these aluminium based composites are used as cylinder blocks, disc brakes, calipers, connecting rods and structures for space applications. In most of these services the components are subjected to tribological loading conditions [8].

Several researchers have invetigated the wear behavior of Al based composites. Baradeswaran et al. [9] studied on mechanical and wear properties of $Al7075-Al_2O_3$-Graphite composites. Shown hardness, tensile strength and compression strength of the hybrid composites are found to be increased. The wear properties of hybrid composites containing graphite exhibited the superior wear resistance properties. Suresh et al. [10] have reported wear behavior of $Al-TiB_2$ composites using respnse surface methodology. Yuhai et al. [11] have invetigated the friction and wear behaviors of $Al6061-B_4C$ composites. Composites were studied by considering the effect of sliding time, applied load, sliding velocity and heat treatment. Umanath et al. [12] conducted experiments on dry sliding wear behavior of $Al6061-Al_2O_3$-SiC habrid metal matrix composites.

In this study, an attempt has been made to prepare Al6061 alloy composites by adding 6 wt. % of SiC and 6 wt. % of Graphite particulates into matrix by using a novel two stage reinforcement addition method. The SiC and graphite content is limited to 6 wt. % to enhance the influence of graphite effect on wear behavior of composites. Further, the prepared Al6061-SiC-Graphite composites were studied for effect of load and sliding speed on the wear properties by using pin-on-disc wear testing machine.

6. Experimental Details

6.1. Materials Used

Metal matrix composites containing 6 weight percentage of SiC and 6 wt. % of graphite particles were produced by liquid metallurgy route. For the production of MMCs, an Al6061 alloy was used as the matrix material while SiC and graphite particles with an average size of 90-125μm were used as the reinforcements. The chemical composition of the alloy used in the present investigation is given in Table 1.

Table1 Chemical composition of Al6061 alloy used

Element	Wt. Percentage
Magnesium	0.80
Silicon	0.64
Iron	0.23
Copper	0.17
Zinc	0.031
Manganese	0.072
Titanium	0.015
Chromium	0.014
Aluminium	Bal

The morphology of procured SiC and graphite particulates are shown in fig.1 which shows that the mixture of semi round and angular grains with sharp cornered morphology.

177
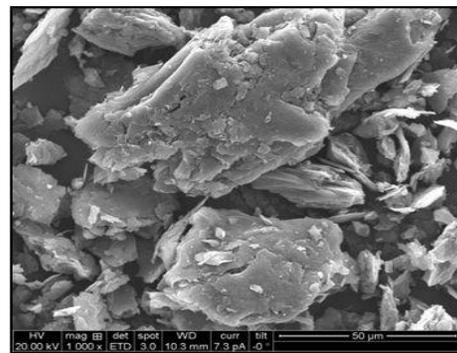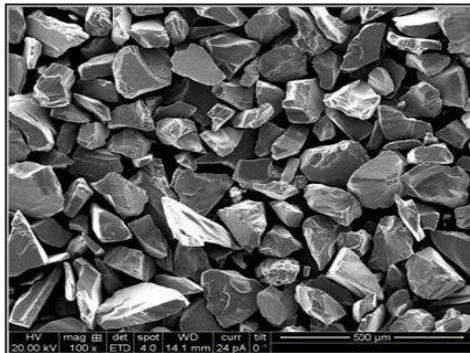
<div align="center">(b)   (b)</div>

Fig. 1 Shows SEM microphotographs of (a) SiC particulates (b) Graphite Particulates

6.2. Preparation of composites

The SiC-graphite-particle reinforced Al6061alloy hybrid metal matrix composites have been produced by using a vortex method. Initially calculated amount of Al6061 alloy was charged into SiC crucible and superheated to a temperature 720°C in an electrical resistance furnace. The furnace temperature was controlled to an accuracy of ±50 degree Celsius using a digital temperature controller. Once the required temperature is achieved, degassing is carried out using solid hexachloroethane (C_2Cl_6) to expel all the absorbed gases [13]. The melt is agitated with the help of a zirconia coated mechanical stirrer to form a fine vortex. A spindle speed of 250 rpm and stirring time 5-8 min. were adopted. The SiC and graphite particulates were preheated to a temperature of 600 degree Celsius in a pre-heater to increase the wettability. The pre-heated SiC and graphite particles introduced into melt in steps of two at constant feed rate of 1.2-1.4 g/sec. Two stage additions involve dividing entire weight of reinforcement into two equal weights and then individual weights are added to the melt in two steps rather than adding all at once. At every stage, stirring is carried out before and after introduction of reinforcement to avoid agglomeration and separation of particles and to ensure homogeneous dispersion of SiC and graphite particles in the melt. After holding the melt for a period of 5 min., the melt was poured from 710 degree Celsius into a preheated cast iron mould having dimensions of 120mm length x 15mm diameter. Wear specimen of size 25mm length and 8mm diameter was prepared by using castings made. Fig. 2 showing the machined samples for wear test.

Fig. 2 Shows wear test specimen

6.3. Dry sliding wear test

Dry sliding wear tests were carried out on Al6061 alloy and Al6061-SiC-Graphite composites using a pin-on-disc wear test apparatus. Cylindrical pin specimens of 8 mm diameter and 25 mm length were mounted vertically on a pin holder. The end of specimens were polished with abrasive paper of grit size 600 and followed by grade 1000. During the test the pin was pressed against the EN32 steel disc with hardness of 60 HRC. Prior to each run, the steel counter-face was ground with 320grit and then 600grit SiC abrasive for few minutes followed by cleaning with

acetone. Test conditions included load-speed settings of 100, 200, 400 and 600 rpm under a 5kg normal load, and 1, 3 and 5kg loads at 400rpm speed. The initial weight of the specimen was measured in an electronic weighing machine with ± 0.01mg accuracy. Data collected and analyzed for volumetric wear loss in the form of weight loss. Further, volumetric wear loss was calculated.

7.   Results and Discussion

7.1. Microstructural Anlysis

Fig. 3 a-b. Showing the Optical microphotographs of (a) as cast Al6061 alloy (b) Al6061-6%SiC-6% Graphite composites.

Fig. 3a-b shows microstructure of as cast Al6061 and Al6061-SiC-graphite composites. Silicon carbide and graphite reinforced aluminium composites have even distribution of reinforcement and this distribution can be seen in optical microscopy photograph (fig. 3b). Aluminium 6061 alloy matrices have grains with different sizes. This is due to the result of fast cooling during casting process. As it is examined in fig. 3b optical microphotograph of Al6061-SiC-graphite composites generally have equi-axed grains. Further these figures reveal the homogeneity of the cast composites. Further, in the case of Al6061-SiC-graphite composites, the bonding between Al and SiC can be between layers of silicon atoms or carbon atoms in SiC and aluminium, and this will further influence the properties [14].

3.4 Wear Properties Evaluation

Fig. 4 shows the variation of volumetric wear loss with respect to load and Al6061 alloy and its composites. The results are observed for the maximum sliding distance of 2000m. The results clearly indicate that the increase of load increases the volumetric wear loss. Also the maximum wear is observed for unreinforced alloy.

Fig. 4 Shows the volumetric wear loss of as cast Al6061 alloy and its composites at constant sliding speed 400 rpm and varying loads

The variation of volumetric wear loss at constant 400rpm and varying loads of 1, 3 & 5kg is as shown in fig. 4. Applied load affects the wear rate of Al-alloy and the composites significantly and is most dominating factor controlling the wear behaviour. From the results, it has been asserted that the addition of 6 wt. % of SiC and 6 wt. % of graphite particulates to the matrix has a marked effect on the volumetric wear loss.

The improvement in the wear resistance of the composites with the addition of SiC reinforcement can be attributed to the improvement in the hardness of the composites and improved hardness results the decrease in the volumetric wear loss of the composites. Sudarshan et al. [15] reported that good interfacial bonding is necessary for better wear behaviour as load transfers occurs through interface and also debonding of reinforcement particles results in increase in wear rate at higher loads. The addition of 6 wt. % of graphite particulates into Al matrix plays very important role in the wear behavior of composites. Graphite acts as a lubricant and forms oxide layer between the steel counter part and pin.

Fig. 5 shows the variation of volumetric wear loss of Al-6061 matrix alloy and Al6061-6% SiC-6% graphite composite at constant 5kg load and varying sliding speeds. With an increasing speed i.e. 200, 400, and 600 rpm, there is an increase in the volumetric wear loss for both matrix alloy and its composites. However at all the sliding speeds studied, the volumetric wear loss of the composite was much lower when compared with the matrix alloy. Further increased wear rate with increased sliding speed is due to thermal softening of the composite. On the other hand the increased temperature at higher sliding speeds can cause severe plastic deformation of the mating surfaces leading to form high strain rate sub-surface deformation [16]. The increased rate of sub-surface deformation

increases the contact area by fracture, and fragmentation of asperities. Therefore this leads to enhanced delamination contributing to enhance wear rate.

Fig. 5. Shows the
5kg varying speeds (rpm)

3.5 Worn Surface Study

(b)   (b)

Fig. 6 Shows the SEM microphotographs of worn surfaces of (a) as cast Al6061 alloy (b) Al6061-6%SiC-6%Graphite composites at 5kg load and 400rpm.

Wear surface analysis of hybrid composites were examined by scanning electron microscope. Fig.6a-b represents the wear surface of as cast Al6061 alloy and specimens containing 6 wt. % of SiC and 6 wt. % of graphite particles reinforced composite at 5 kg load and 400rpm sliding speed.

The examination of worn surface Fig. 6 a showed that the worn surfaces of base alloy are much rougher than composites. Cavities and large grooved surfaces are found on worn surface of Al6061 alloy. The indication of cavities and grooves supports the fact that soft Al alloy deformed at higher load of 5kg and at 400rpm speed and pulled out from the surface. The wear track observation shows that adhesion and delamination are dominant wear mechanisms observed at higher loads. This is supported by the large sized delamination flakes and severe adhesion resulting in bulk removal of material at higher loads.

Fig. 6b shows the SEM image of the worn surface of Al6061-6% SiC-6% Graphite composite tested at applied load of 5kg and 400rpm speed. The grooves are very small due to the hard nature of SiC reinforcement and poor wear losses. As the ceramic particles resist the delamination process, composites are found to have greater wear resistance. Worn surface shows less cracks and grooves mainly due to the presence of graphite particulates. The smeared graphite particles from the worn surface of composites form a thin rich tribolayer between sliding surfaces, which prevent direct metal contact.

8.   Conclusions

The present work on processing and evaluation of Al6061-6% SiC-6% graphite metal matrix composite by melt stirring has led to following conclusions. Al6061 alloy based composites have been successfully fabricated by melt stirring method using two stage addition method of reinforcement combined with preheating of particles. The optical microphotographs of composites revealed fairly uniform distribution of reinforcement particulates in the Al6061 alloy metal matrix. The volumetric wear loss is dominated by load factor and sliding speed. The increase of loads and sliding speeds leads to a significant increase in the volumetric wear loss. The Al6061-6% SiC-6% graphite composites have shown lower rate of volumetric wear loss as compared to that observed in as cast Al6061 alloy matrix. SEM micrographs of worn surface revealed the presence of smooth grooves in the Al6061-SiC-graphite composite compared to the base matrix.

References

[17] Sourabh Garatte, Rahul Upadhye, Venkatesh Dandagi, Shrikanth Desai, Bhimappa Waghmode, "Preparation and Characterization of Al5083 alloy composites", Journal of Minerals and Materials Characterization and Engineering, 1, (2013) 8-14.

[18] Ramkoteshwara Rao V, Ramanaiah N, Sarcar M, "Fabrication and investigation on properties of TiC reinforced Al7075 metal matrix composites", Applied Mechanics and Materials, Vols. 592-594, (2014) 349-353.

[19] Hamid Reza Ezatpour, Seyed Abolkarim Sajjadi, Mohsen Haddad Sabzevar, Yizhong Huang, "Investigation of microstructure and mechanical properties Al6061 nano-composite fabricated by stir casting", Materials and Design, 55, (2014) 921-928.

[20] Srimant Kumar Mishra, Sandyarani Biswas, Alok Satapathy, "A study on processing, characterization and erosion wear behavior of silicon carbide particle filled ZA-27 metal matrix composites", Materials and Design, 55, (2014) 958-965.

Best Compliments From:

Department Of Metallurgical & Materials Engineering

National Institute Of Technology, Srinagar